

**Towards Crystals of Crystals of
NanoCrystals:
A Self-Assembly Study**

Cover: Electron micrograph of 6 nm cobalt iron oxide nanoparticles self-assembled inside the spherical confinement of an emulsion droplet.

PhD thesis, Utrecht University, the Netherlands, Dec 2014.

ISBN: 999-99-999-9999-9

A digital version of this thesis is available at <http://web.science.uu.nl/SCM/>

Towards Crystals of Crystals of NanoCrystals: A Self-Assembly Study

Op weg naar Kristallen van Kristallen van Nanokristallen:
Een Zelforganisatie Studie

(met een samenvatting in het Nederlands)

Proefschrift

ter verkrijging van de graad van doctor aan de Universiteit Utrecht op gezag van de rector magnificus, prof. dr. G. J. van der Zwaan, ingevolge het besluit van het college voor promoties in het openbaar te verdedigen op maandag 1 december 2014 des middags te 4.15 uur

door

Bart de Nijs

geboren op 20 februari 1981 te Utrecht

Promotor: Prof. dr. A. van Blaaderen
Copromotor: Dr. A. Imhof

Contents

1	Introduction	1
1.1	Nanomaterials and self-assembly	2
1.2	Crystallization and crystal packing	2
1.3	Colloids and Colloidal Suspensions and nanoparticles	3
1.4	Emulsions, Surfactants and Ligands	6
1.5	Supraparticles	7
1.6	Presented in this thesis	8
1.7	Thesis Outline	8
2	Nanoparticle Synthesis and Characterization	11
2.1	Introduction	12
2.2	Nucleation and growth of nanoparticles	12
2.3	Properties of iron oxide	13
2.4	Experimental Details	16
2.4.1	Chemicals & Solvents	16
2.4.2	Equipment	16
2.4.3	Method 1: Iron oxide nanoparticles, Park <i>et al.</i> [51]	17
2.4.4	Method 2: Cobalt iron oxide nanoparticles, Bodnarchuk <i>et al.</i> [54]	17
2.4.5	Method 3: Maghemite (γ -Fe ₂ O ₃) iron oxide nanoparticles, Hyeon <i>et al.</i> [53]	19
2.4.6	Method 4: Gold nanoparticles, Turkevich <i>et al.</i> [49]	19
2.4.7	Method 5: Gold nanoparticles, Brust <i>et al.</i> [65]	20
2.4.8	Method 6: Cadmium selenite zinc sulfide core-multishell quantum-dots, Xie <i>et al.</i> [66]	20
2.4.9	Sample preparation and analysis	21
2.5	Results & Discussion	22
2.5.1	Spherical iron oxide and cobalt iron oxide nanoparticles (Methods 1, 2, and 3)	22
2.5.2	Au nanoparticles (Method 4 & 5)	37
2.5.3	Semiconductor (CdSe@ZnS) nanoparticles (Method 6)	40
2.5.4	Synthesis of non-spherical nanoparticles (Method 2 b,c&d)	41
2.5.5	High resolution TEM analysis of nanoparticles synthesized using Method 2a & b	46
2.6	Conclusion and Outlook	49
2.7	Acknowledgments	49

3	Supraparticle self-assembly	51
3.1	Introduction	52
3.2	High Power sonication	53
3.3	Droplet break-up of viscoelastic emulsions in a Taylor-Couette shear cell	53
3.4	Experimental Details	55
3.4.1	Chemicals & solvents	55
3.4.2	Equipment	56
3.4.3	Emulsion method: Self-assembly inside emulsion droplets	56
3.4.4	Induced solvophobic attractions method: Solvophobic interactions in the presence of PVP	56
3.4.5	Making water-free emulsion droplets	57
3.4.6	Silica coating of supraparticles	57
3.4.7	Sample preparation	57
3.5	Results & Discussion	58
3.5.1	Arrested nanoparticle self-assembly	58
3.5.2	Different methods of emulsification	60
3.5.3	Supraparticle size prediction	65
3.5.4	Small clusters	67
3.5.5	Water-free emulsion method	72
3.5.6	Stability of colloidal supraparticles	72
3.6	Conclusions & Outlook	73
3.7	Acknowledgments	74
4	Tomographic Analysis of Anisotropic Colloids and Nanoparticle Supraparticles	75
4.1	Introduction	76
4.2	Electron tomography in more detail	76
4.2.1	Work flow	80
4.3	Examples of colloidal model systems developed for self-assembly	82
4.3.1	Rod-shaped silica particles: bullets, spherocylinders & fluted shapes	83
4.3.2	3D structure analysis of supraparticles made from nanoparticles	84
4.4	Bending of rods	85
4.5	Experimental details	87
4.5.1	Equipment	87
4.5.2	Software	87
4.5.3	Chemicals	87
4.5.4	Synthesis of fiducial markers and sample preparation	88
4.5.5	Tomography, image analysis and visualization details	88
4.6	Results & Discussion	90
4.6.1	Comparison of the SIRT and BP algorithms used	90
4.6.2	Sphere-like particles	93
4.6.3	Rod-like particles	94
4.6.4	Nanoparticle assemblies	98
4.7	Conclusion & Outlook	103
4.8	Acknowledgments	104

5	Deformations of Supraparticles from Nanoparticles by drying forces	105
5.1	Introduction	106
5.2	Capillary forces	106
5.3	Experimental Details	110
5.3.1	Equipment and software	110
5.3.2	Sample preparation	110
5.4	Results & Discussion	112
5.4.1	Normal deformations	112
5.4.2	Lateral deformations	115
5.4.3	Self-assembly of cubic nanoparticles in emulsion droplets	118
5.5	Conclusion & Outlook	119
5.6	Acknowledgments	119
6	Entropy Driven Icosahedral Packing of Hard Spheres in Spherical Confinements	121
6.1	Introduction	122
6.2	Experimental Details	123
6.2.1	Chemicals & solvents	123
6.2.2	Equipment and software	123
6.2.3	Methods	124
6.2.4	Sample preparation	124
6.3	Results & Discussion	126
6.3.1	Colloidal experiments	126
6.3.2	Simulations	129
6.3.3	Size dependence crystal transitions	131
6.4	Conclusions	132
6.5	Acknowledgments	132
7	Luminescent, High-Quantum-Yield Quantumdot Supraparticles	133
7.1	Introduction	134
7.2	Refractive index and optical resonance modes.	135
7.3	Experimental Details	136
7.3.1	Chemicals	136
7.3.2	Equipment and software	136
7.3.3	Quantumdot synthesis	137
7.3.4	Quantumdot supraparticle synthesis	137
7.3.5	Growth of zinc oxide nanowires	137
7.3.6	Sample preparation	138
7.4	Results & Discussion	139
7.4.1	Photoluminescent quantumdot supraparticles	139
7.4.2	Quantum yield measurements	143
7.4.3	Power dependence and State filling	143
7.4.4	In air "suspended" SPs and Mie resonance modes	146
7.5	Conclusions & Outlook	147
7.6	Acknowledgments	147

References	149
Summary	162
Samenvatting	164
Acknowledgements	166
List of Peer-Reviewed Publications	168
Oral and Poster Presentations	169
Curriculum Vitae	170

Introduction

The self-assembly behavior of colloidal particles has been the subject of extensive studies, with topics such as the formation of photonic crystals as investigated by simulations, the drying properties of paints and coatings, and as a promising bottom-up approach for nanoscale functional components. As a result a lot is already known about the behavior of dense systems of such particles with a majority of the studies focusing on spherical constituents. However, much less is known about the phase behavior of such constituents in confined geometries. For such a case the simplest confining geometry is spherical as this is uniform in all directions and can be found commonly in nature as interfaces minimizing their surface area, e.g. emulsion droplets, gas bubbles and micelles.

In the presented research the self-assembly behavior of spheres confined to spheres is studied and a change in phase-behavior and the resulting superstructures is presented. To investigate this behavior of nanoparticles, micron-sized colloids and event driven molecular dynamics simulations were used to attain a scope on how the self-assembly behavior changes as a result of a confining geometry. The majority of the research was focused on the self-assembly of, mostly spherical, nanoparticles since they are hardly influenced by gravity and their fast Brownian motion allows for them to explore phase space and reach equilibrium on relative short timescales. In addition sub-100 nm nanoparticles often possess unique size dependent properties characteristic of the material but absent or strongly modified from those in bulk. The study of these properties is collectively called nanoscience. In this chapter we will first present a short introduction on the field of nanoscience and topics relevant to the self-assembly studied for this research.

1.1 Nanomaterials and self-assembly

Nanostructured materials are becoming more and more common in our modern day lives. They are present for instance in our TVs and in data storage devices. However, the functionality of nanostructured materials is much wider and can be applied in many more fields such as: ultra sensitive sensors [1, 2], high capacity batteries [3, 4], and medical applications [5, 6].

One of the advantages of nanostructured materials is that they require little energy to function, resulting in high efficiencies making these structures interesting for industry [7], where the main method for making nanostructured materials is lithography. This is a typical top-down method where larger objects are cut down to nanometer-sized components, but as components become smaller lithography starts to reach its physical limits and such top down methods become more complex and with it more expensive [8]. This opens up a field of previously unattractive alternative methods for making functional nanomaterials, amongst which are also bottom-up approaches. Self-assembly is a fundamental principle in which structural organization is generated from pre-existing components that come together and form larger systems without human intervention. Self-assembly is a widely applicable term and can be used from atomic and molecular scales to global weather patterns or even larger [9].

Utilizing self-assembly as an alternative "bottom-up" method for making functional nanomaterials can yield large quantities with little effort. Furthermore, since the method relies on free energy minimization generally few defects will be formed if the self-assembly is performed sufficiently slowly, or can even be repaired/healed given time. A simple example is self-assembled monolayers of magnetic nanoparticles forming long-range periodic structures [10]. These structures function similarly to conventional hard-disks but with smaller components thereby increasing the potential data storage capacity. Another great advantage of this method is the possibility of making 3D nanostructured materials, whereas lithography typically forms 2D structures as 3D structures are again complicated and expensive to make with this technique [11].

1.2 Crystallization and crystal packing

Bolhuis *et al.* showed that the face-centered-cubic (FCC) packing has the lowest free energy for hard spheres when equilibrium can be reached, with a minute free energy difference over the hexagonal-close-packed HCP phase [12]. Both the respective unit cells are depicted Fig. 1.1. Since the free energy difference is marginal, both crystal types will be present in most self-assembled structures with close to equal amounts. Typically, for hard spheres (particles without interactions other than excluded volume) the onset of crystallization occurs at volume fractions of $\phi = 0.494$ and the number of crystalline particles will in-

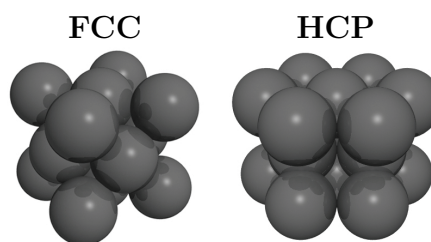


Figure 1.1: A 3D rendering of the FCC (**left**) and HCP (**right**) unit cell.

crease until the system is fully crystalline at a volume fraction of $\phi = 0.545$ and can be further compressed to ultimately reach a volume fraction of $\phi = 0.74$ [13–15].

Many more types of crystal structures are known, such as binary crystal packings consisting of two or more different types of constituents with some resembling ionic solids, but also single-type crystals of non-spherical components like simple cubic packing for cubes [16] and columnar packing for rod-like particles [17]. Interestingly, in general for such structures the free energy is lower than that of a disordered phase and they form through self-assembly instead of being actively built, if the process is sufficiently slow. This means the growth process does not consume energy and is independent of scale. In addition, since defects are often unfavorable, such systems have a propensic self-healing potential, permitted the components are capable of exploring phase space. Examples can be found in self-assembled molecular monolayers [18] and in perturbed colloidal membranes [3].

Classical nucleation theory

The nucleation and initial growth of such crystals can be described by classical nucleation theory according to which nuclei are formed continuously by thermal fluctuations, but most of the time melt again due to the high energy cost of the surface of the small crystallite exceeds the bulk energy gained by forming the nuclei. Ultimately the driving force behind crystal formation is the change in the Gibbs free energy ΔG , at least for homogeneous nucleation. The Gibbs free energy for such a system can be described by:

$$\Delta G = E_{Surface} - E_{Bulk} \quad (1.1)$$

Where $E_{surface}$ is the energy cost of the surface and E_{Bulk} the energy gain from the bulk phase. By substituting the appropriate surface and volume terms we get:

$$\Delta G = 4\pi r^2 \gamma - \frac{4\pi}{3} r^3 \Delta\mu n \quad (1.2)$$

Here r is the radius, considering a spherical shape for the nucleus crystal, and γ is the surface free energy per unit area of a crystal-liquid interface assuming each crystal plane has a similar surface tension. Then $\Delta\mu$ is the chemical potential difference between the liquid and the solid and n is the number density of the crystal. When the crystal reaches a sufficiently large size to overcome the maximum in ΔG , which is at the critical radius $r_c = 2\gamma/\Delta\mu n$, the crystal will continue to grow larger [19, 20]. However, for this we assume that the surface tension is sufficiently large and bulk free energies apply.

1.3 Colloids and Colloidal Suspensions and nanoparticles

For crystallization to occur the system must be able to explore the phase space of statistical mechanics. For this purpose it is essential that the particles move around to minimize the system's free energy. It is for this reason that colloidal systems are ideal for self-assembly and crystallization model studies as the components experience the necessary

Brownian motion as a result of collisions with the molecules or atoms of the dispersion phase. The size of the dispersed particles that are still referred to as colloids is in a loosely defined range from ~ 1 nm to ~ 1 μm . The lower limit of ~ 1 nm is set such that the dispersed phase is significantly larger than the dispersion molecules, so as to distinguish it from the study of individual molecules in a liquid medium. The upper limit is determined by the requirement that colloids are still subject to the characteristic Brownian motion. The latter behavior was first observed by Robert Brown in 1827 who studied the behavior of pollen grains in water exhibiting a random walk. A theoretical explanation for this behavior was later proposed by Albert Einstein [21] and supported by the findings of Jean Baptiste Perrin [22].

For colloidal systems the dispersed phase can consist of a gas, a liquid or a solid. The dispersing medium is typically a liquid since the dispersed phase must be able to execute Brownian motion. Due to this motion the particles will not fully sediment but remain partially suspended with a concentration gradient in the direction of gravity. This is referred to as the gravitational length, which is defined as the distance over which a single particle has to be moved in gravity to obtain 1 kT of gravitational potential energy [23]. Colloidal suspensions with components up to a few (~ 5) μm still exhibit significant Brownian motion. However, as these particles get bigger and heavier the time scales at which this Brownian motion is observed increases, the gravitational length decreases and the particles can only be made to self-assemble by non-thermal mechanics. Systems with particles large enough to not experience Brownian motion are classified as granular matter.

If particles in a suspension aggregate then their size increases and thus the Brownian motion decreases resulting in a shorter gravitational length and consequently sedimentation. Typically, to prevent this a repulsive potential is added to the components, such as a charge or a layer of sterically stabilizing molecules, to prevent the system from reaching the aggregated state keeping the system out of equilibrium. This is referred to as colloidal stability.

When objects or colloids are made small enough, $\ll 100$ nm, novel size dependent material properties can be found that are strongly different or sometimes even not present in the bulk phases of the respective materials. The study of these phenomenon is termed nanoscience and colloids within this size range are therefore typically named nanoparticles. These novel properties are not only strongly size dependent but also depend on the shape and surface termination of the nanoparticles making the geometry including surface features one of their most important characteristics.

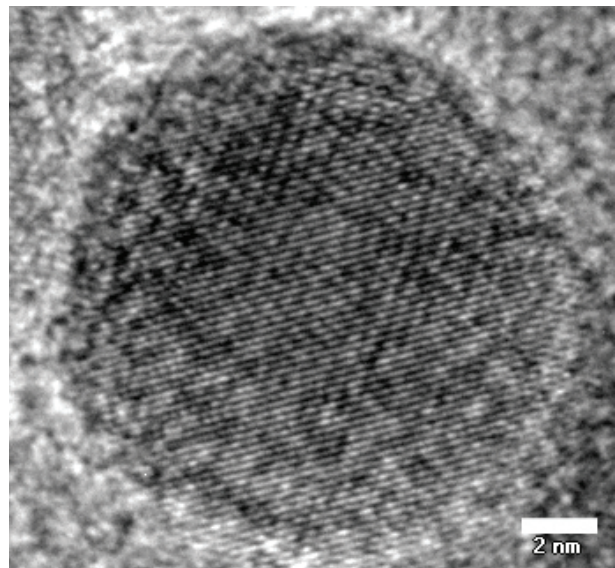


Figure 1.2: High resolution electron micrograph of a core@shell cobalt iron oxide ($\text{Fe}_x\text{O}@Co\text{Fe}_2\text{O}_4$) nanoparticle, showing atomic lattice fringes (scale bar = 2 nm).

A few examples of the unique properties found in nanoparticles are: superparamagnetism [6], localized plasmon resonance [24], and quantum confinement [25]. A nanocrystal is of the size of a nanoparticle but the internal atomic structure is crystalline. This crystallinity is common for metal, metal oxide and semiconductor nanoparticles but uncommon for micelles or organic nanoparticles. Most of the nanoparticles presented in this thesis consist of noble metals, metal oxides, or semiconductors and showed crystalline order, as in Fig. 1.2, and could therefore be referred to as nanocrystals. However, since the crystallinity was not determined for all samples and many of the results presented are also valid for non-crystalline particles, we will refer to them as nanoparticles.

Superparamagnetism

One of the interesting nanoparticle properties that arise due to the small size is superparamagnetism. If ferrimagnetic or ferromagnetic nanoparticles become sufficiently small the magnetization of the nanocrystals can randomly flip as a direct result of the influence of temperature. The time it takes for these nanoparticles to flip their magnetization and reverse its direction is called the Néel relaxation time after Liouis Néel whose studies on the magnetism of single-domain grains were published in 1949 and resulted in the Néel relaxation theory [26]. Without the influence of a magnetic field these nanoparticles will exhibit no net magnetization if the measurement time greatly exceeds the Néel relaxation time. When introduced to a magnetic field these nanoparticles will be magnetized similar to paramagnets, but with a higher magnetic susceptibility as described by Bean and Livingston [27]. Superparamagnetism is discussed in more detail in 2.3.

Localised Plasmon Resonance

Incident light on a metal can induce a surface bound collective motion, or wave, in the conduction electrons. This is a common occurrence in noble metals such as gold and silver. When exposed with light sufficiently close to the plasmon resonance frequency, e.g. visible light for Ag and Au, the electrons absorb the light and store the energy in a collective oscillatory motion. After a short time the energy is re-emitted in the form of light and the oscillation stops. However, a lot of this energy will be lost as the oscillation spreads like a wave over the surface dissipating its energy. Making the surface sufficiently small confines the plasmon, which prevents the energy from dissipating, and which results in stronger more localized plasmon resonances. This phenomenon typically occurs in noble metal nanoparticles in the visible light range and is used in bio-sensing and lab-on-a-chip devices.

Quantum Confinement

Perhaps one of the most intriguing size effects is the phenomenon of quantum confinement in semiconductor nanoparticles known as quantumdots (QDs). This quantum confinement is observed as a size dependent photoluminescence at a narrow bandwidth [28]. The small size of the QDs makes that there are a limited number of atoms to accommodate an excited electron, limiting the number of possible energy states, resulting in discrete energy levels more resembling that of molecules than that of bulk materials, and causes the energy

band gap between an ground and excited state to increase [29]. More on this will be discussed in Ch. 7.

Surface to volume ratio

The small size of nanoparticles makes that a large part of the particle's material is on the surface resulting in a large surface to volume ratio. This makes such particles ideal as catalysts since more reaction sites are available. However, due to this large surface area, if susceptible to oxidation, the particles will readily react and change their properties in the presence of oxygen or even water and need to be kept in an inert atmosphere. If the particles do not oxidize, they are considered chemically stable. Nanoparticles made from noble metals, such as gold, are chemically stable, whereas semiconductors are typically prone to photo-oxidation. There are of course still many more chemical processes other than oxidation that can still modify NPs through their surface, for example using acids, bases and with ligand bonding or complexation.

1.4 Emulsions, Surfactants and Ligands

In this thesis self-assembly in emulsion droplets plays a major role. The emulsion droplets act as a spherical confining geometry on the organization of constituents during the self-assembly. Emulsions are, like nanoparticles, a subcategory of colloidal systems where both the dispersed phase and the continuous phase are a liquid. To form an emulsion two or more immiscible liquids are mixed, where one phase is usually an aqueous or polar phase and the other an apolar one, so that both

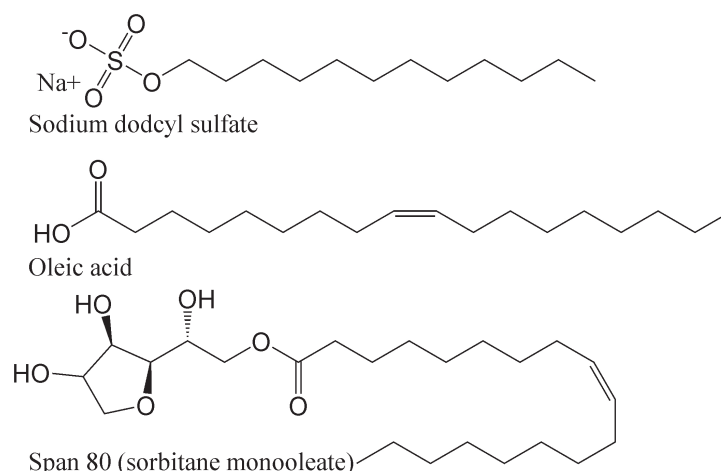


Figure 1.3: Common surfactants used in this thesis

liquids do not molecularly mix, with typically a surfactant added to stabilize the system. The dispersed phase can also be referred to as the inner phase and is often an organic liquid which is dispersed in an aqueous medium. If the inner phase is an aqueous phase and the continuous phase organic then the colloidal systems is referred to as an inverse emulsion. By agitating a mixture of two immiscible liquids the smallest phase will usually break up and form smaller droplets in the other one. As a result the surface area increases with a decrease in droplet size. Since the two liquids are immiscible the interfacial free energy increases with the contact area. Hence, the smaller the droplets are made, the more energy is needed to make them. Since the formation of droplets is thermodynamically unfavorable emulsions are not stable or meta stable. As mentioned, to stabilize emulsions surfactants or other surface active materials are added which lower the interfacial

free energy and prevent coalescence by, for instance, inducing (stronger) droplet charging, thereby stabilizing the emulsion. Ligands and surfactants are surface/interface-active molecules that most commonly consist of a polar "head" and an apolar "tail". The polar head adheres to polar phases and the apolar tail will prefer an a-polar phase. This behavior causes them to prefer interfaces and surfaces over a continuous phase. These molecules are typically referred to as surfactants or ligands. Common surfactants used in this thesis are oleic acid, sodium dodecyl sulfate (SDS) and Span 80, a schematic representation of each is shown in Fig. 1.3. Surfactants can be overall hydrophilic or hydrophobic depending on the ratio between the hydrophilic and the hydrophobic part of the molecules, which determines whether the molecule will prefer the water or the oil phase when not at an interface or surface. This is known as the hydrophile-lipophile balance (HLB), a measurement scale developed in the 1950s specifically for non-ionic surfactants by Griffin [30, 31]. To calculate the HLB the molecular weight of the hydrophilic segment is divided by the molecular weight of the hydrophobic segment. HLB values for oleic acid and span 80 are 1 and 4 respectively. HLB values below 10 are considered hydrophobic and above 10 hydrophilic. This is important for this research as we evaporate emulsion droplets and this will release surfactants from the interface. This HLB value will tell us whether they will move to the oil phase or the water phase. For the ionic surfactant SDS used in most of the experiments presented in this thesis, the ionic contribution was calculated to be 35 resulting in a HLB between 36 and 40 according to [32], meaning excess SDS will remain in the aqueous phase of an emulsion.

1.5 Supraparticles

The term supraparticle (SP) is as of yet not a well defined term, but typically refers to colloidal particles, built up from smaller particles, that in turn still experience Brownian motion meaning that they are redispersable as a colloidal suspension. A wide variety of different SPs have been reported in literature ranging from a few close packed spheres [33] to complex multi component aggregates [34]. Often such particles are of spherical shape as a result of the built-in size limiting mechanisms. Published SP formation routes include the self-assembly in or on the surface of emulsion droplets [33, 35, 36], a combination of electrostatic repulsions and van der Waals interactions [37], solvophobic interactions [38, 39] and directed molecular interactions [40]. However, most of these articles describe only the self-assembly behavior of a very limited amount (<100) of constituents and/or assume an attraction potential between the individual components [41]. Such SPs found in literature will be discussed in more detail in Ch. 3 and 6.

Several parallels to this field of research can be found in cluster science where the self-assembly behavior of atoms and small molecules is studied. Naturally, the interaction potentials between such constituents contain also attraction potentials as these are always present between atoms. Such knowledge is crucial in understanding how the properties of single atoms and molecules change into, and form the properties of, bulk materials. Nowadays it is well known that the ordering of atoms in any material greatly influences the materials properties. This ordering can influence anything from mechanical [42] and electronic [43, 44] properties to how the material interacts with light. One of the oldest

examples is the tempering of steel where induced defects in the crystal structure of steel increases its strength, e.g. Martensite. Therefore, it is crucial to understand the underlying mechanisms that cause such ordering behavior to allow for manipulating and even tailoring such properties to specific needs.

1.6 Presented in this thesis

In this thesis we will focus on the self-assembly of particles for which the most important interaction resembles that of hard spheres. In particular we studied how such particles self-assemble inside spherical confinements and show that this hard-sphere self-assembly in confined geometries leads to significantly different ordering with respect to bulk self-assembly as a result of the confinement alone. In addition to this packing difference, the clusters of these nanoparticles due to a spherical constraint form spherical assemblies, i.e. SPs, which in turn can be used as colloidal dispersions. Such SP suspensions not only have increased scattering properties but are visible with regular optical microscopy and in some cases still retain the individual nanoparticle properties such as a high light emission quantum efficiency, as will be shown in Ch. 7. There we show that using photoluminescent QDs, together with the spherical geometry and a high refractive index difference, leads to optical resonant modes on the surface of these assemblies (Mie resonances) which stimulate photon emission from the individual QDs at specific wavelengths. Such systems could be further developed to function as low threshold lasers and/or photonic resonators, which would be of major interest for practical applications in nanophotonics.

In addition, due to the fact that the formed SPs have sizes still in the colloidal domain, it is possible for these SPs to be self-assembled again. This opens the way to hierarchical self-assembly where ordering can be manipulated at different length-scales. Thereby opening up new possibilities in, for example, photonic crystals where the spheres of which the structure consists are self-assembled from or with functional nanoparticles with specific and unique light manipulating properties such as quantum confinement and/or localized plasmon resonances.

1.7 Thesis Outline

The thesis is organised as follows. In chapter 2 the syntheses of a range of different nanoparticle sizes and compositions, that were used in our self-assembly experiments, are presented. In chapter 3, two methods to self-assemble nanoparticles into colloidal SPs are discussed. In chapter 4 the use of electron tomography as a high resolution 3D analysis technique for colloidal systems is introduced and discussed. In chapter 5 we examine the influence of capillary forces, nanoparticles shape, magnetism and size on the self-assembly, or self-assembled structures, of nanoparticles. Then, in chapter 6, the self-assembly behavior of particles with hard-sphere like interactions in spherical confinement is studied in more detail and compared with event driven molecular dynamics simulations explaining the highly ordered structures formed in these self-assembly experiments. Finally, in chapter 7 we present the self-assembly of photoluminescent QDs into SPs and show how

the resulting structures influence the photoluminescent properties of the semiconductor nanoparticle constituents.

Nanoparticle Synthesis and Characterization

In this chapter we introduce the different methods, taken and adapted from literature, that were used and optimized for the nanoparticle synthesis. We will discuss the synthesis results in terms of polydispersity (PD), shape and size, and evaluate their suitability for the assembly methods described in the subsequent chapters. The different types of nanoparticles synthesized for this research included: iron oxide (FeO , Fe_2O_3 , Fe_3O_4), cobalt iron oxide core-shell ($\text{FeO@CoFe}_2\text{O}_4$), gold (Au), and cadmium selenite zinc sulfide core-multishell (CdSe@ZnS). The different shaped nanoparticles, other than spherical, that were synthesized and will be presented here included: cubes, octahedrons, and star-shaped nanoparticles all consisting of cobalt iron oxide.

2.1 Introduction

The key components in colloidal self-assembly studies are of course the individual building blocks, or particles. Their shape, size, surface coating and polydispersity (PD) will determine how they will behave during self-assembly. Therefore, a great deal of this study was focused on making nanoparticle "building blocks" and controlling their shape, size, PD and inter particle interactions. The results of that work is presented in this chapter. The ultimate goal of this work was to study, and use the structures resulting from, the self-assembly of nanoparticles in spherical confinements.

The technique that was used for self-assembly in spherical confinements was based on an oil in water emulsion technique as will be presented in Ch.: 3. This required the synthesized nanoparticles to not only be monodisperse to ensure crystalline ordering, but also for them to be robust in water and oxygen atmospheres at elevated temperatures (~ 68 °C).

2.2 Nucleation and growth of nanoparticles

In literature a myriad of nanoparticle synthesis methods are presented but most rely, in essence, on the same underlying nucleation and growth mechanism [48–50]. Of all these methods we focused on wet syntheses as these methods typically result in high yields and low PDs with a good control over the size, shape and surface coating [47, 51, 52]. Such wet syntheses typically start out with a homogeneously distributed precursor that, after for example heating or the addition of a reducing agent, dissociates into a concentrated solution of unstable ions (e.g. iron) or atoms (e.g. gold), referred to as monomer, which rapidly precipitates and nucleates into a colloidal suspension after which the nuclei continue to collect monomer causing them to grow [47, 49–54].

This rapid nucleation and growth mechanism was first described by LaMer *et al.* in 1950 [45–47] who showed that when monomer is continuously added to a solution at some point a supersaturation will be reached causing the monomer to "burst" nucleate and form seeds. As the monomer is incorporated in the formed seed the monomer concentration drops below the critical nucleation value and no new nucleation will occur. The seeds will continue to take up monomer as they grow further preventing the monomer concentration to reach supersaturation again. If supersaturation were to be reached again then a secondary nucleation step would occur resulting in a bi-disperse or polydisperse colloidal system. This nucleation and growth mechanism can be visualized by a LaMer

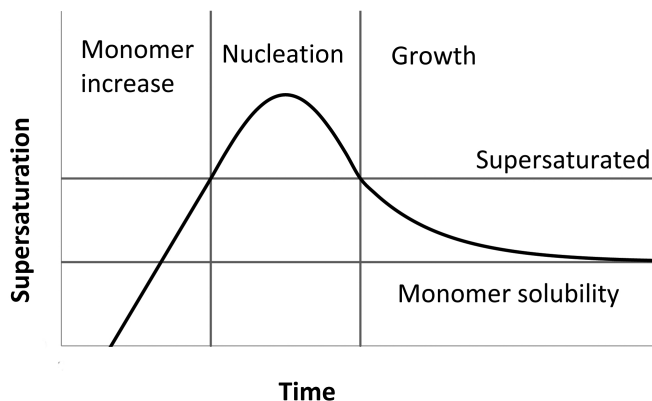


Figure 2.1: LaMer plot: Monomer saturation as a function of time during a nucleation experiment as described by LaMer [45–47].

plot as shown in Fig. 2.1 where the monomer concentration is shown as a function of time on arbitrary axes. Most methods for nanoparticle synthesis rely on this same mechanism and only differ in which way the monomer is introduced to the system. The most common ways are: thermal decomposition of a metal-precursor, the reduction of metal salts, and a non hydrolytic sol-gel method which is popular for water soluble oxide metal nanoparticles [47].

After nucleation, and during the growth, it is important to prevent aggregation of the formed seeds and the subsequent nanoparticles as a result of Van der Waals forces that increase with the size of the particles. A possible method to prevent aggregation is by introducing molecules that anchor to the surface of the particles providing steric stabilization [55] and are commonly referred to as ligands. If these ligands bind too strongly further growth is (kinetically) frustrated. By utilizing this effect the shape of the nanoparticles can be controlled to some extent [56–58]. By adding directing ligands the growth of a specific crystal facet is inhibited, promoting the growth of the remaining uninhibited facets resulting in nanoparticles that have shapes that are different from that as predicted using a surface tension minimization, such as for instance done in a Wulff construction based on the core properties alone [59].

2.3 Properties of iron oxide

For the majority of this research iron oxide and cobalt iron oxide nanoparticles were chosen since they can reproducibly be made with low PDs on large scales [51, 54] and are chemically stable in the presence of water and oxygen [60]. However, iron oxide nanoparticles are more commonly studied for their characteristic magnetic properties. These magnetic properties depend on the internal crystal structure and composition, which in turn strongly depends on the oxygen content and synthesis conditions. In nature the three most common crystal compositions are: FeO(wüstite), Fe₂O₃, and Fe₃O₄ (magnetite), of which the last is a combination of FeO and Fe₂O₃. Fe₂O₃ can be found in a range of different polymorphs, including α -Fe₂O₃ (hematite), β -Fe₂O₃, γ -Fe₂O₃ (maghemite) and ϵ -Fe₂O₃ [61], of which α and γ are the most common polymorphs [62]. The most relevant crystal structures are shown in table 2.1 with their magnetic properties and the size of their respective unit cells.

Paramagnetism is caused by unpaired electrons in the atomic structure. This means an atomic or molecular orbital filled with only one electron which can align its magnetic moment in any direction. This means that when a magnetic field is applied a paramagnetic material will align its magnetic field with the applied field and thereby reinforcing it. Ferromagnets are similar to paramagnets, and possess unpaired electrons as well, but in addition to aligning to a magnetic field the unpaired electrons also align parallel with their neighbor spins to maintain a lower energy state. These can order in domains resulting in a net magnet moment even if no external field is present and have strong hysteretic properties. It is these hysteretic properties that can be used to store binary data in the form of either up or down magnetized domains. However, the size of these domains is limited as bigger domains are unfavorable since more magnetostatic energy would be stored in a large external magnetic field. So to minimize the internal energy, rather

Mineral name	Hematite	Magnetite	Maghemite	Wüstite
Composition	$\alpha\text{-Fe}_2\text{O}_3$	Fe_3O_4	$\gamma\text{-Fe}_2\text{O}_3$	FeO
Crystal structure	hexagonal	cubic	cubic or tetragonal	cubic
Type of magnetism	weakly ferromag. or antiferromag	ferrimag.	ferrimag.	antiferromag.
Cell dimensions (nm)	$a = 0.50356$ $c = 1.37489$	$a = 0.8396$	$a = 0.83474$	$a = 0.4302$ -0.4275

Table 2.1: Table showing the compositions, crystal structures, magnetism, and the unit cell size for each relevant iron oxide type as found in Ref. [61].

than one domain, two or more anti parallel domains are formed instead, resulting in an energetically favorable smaller external field. Nanoparticles on the other hand are small enough to permit a single crystalline domain resulting in a net magnetic moment over the particle and with it stronger ferromagnetic properties than their bulk counterparts.

On such small magnetic nanoparticles there are two mechanism that describe this magnetic reorientation: Brownian rotation and Néel relaxation. Brownian rotation describes the relaxation time as a function of the hydrodynamic radius r_h and the solvents viscosity η .

$$\tau_B = \frac{4\pi r_h^3 \eta}{k_B T} \quad (2.1)$$

Where k_B is the Boltzmann constant and T the absolute temperature. The Néel relaxation time described the rotation of the magnetic moment with respect to the crystal lattice of the nanoparticle:

$$\tau_N = f_0^{-1} \exp\left[\frac{KV_m}{k_B T}\right] \quad (2.2)$$

Where f_0 is the attempt frequency: a constant between 10^7 sec^{-1} and 10^{12} sec^{-1} , KV_m is the height of the energy barrier, a product from the anisotropic energy density K and the magnetic domain volume V_m [26] and the mechanism whichever is faster will determine the reorientation mechanism.

Note that both have a temperature dependency, but that increasing the temperature in magnetic materials will also cause atoms to be "agitated" causing the domains of aligned unpaired electrons to disappear. The temperature at which this occurs is a material property and is referred to as the Curie point temperature.

In anti-ferromagnetic materials the magnetic moments of neighboring atoms are anti-aligned meaning each magnetic moment of the atoms points in an opposite direction with

respect to its neighbor. This causes these materials to have no net magnetic moment. In ferrimagnets magnetic moments are aligned within a group or sublattice where neighboring sublattices have different magnitudes resulting in a net magnetic moment. [63].

2.4 Experimental Details

In this section the experimental details for each different literature method used for making nanoparticles are presented. All chemicals and solvents were used as received unless noted otherwise. All nanoparticle syntheses were performed in a fume hood using standard Schlenk line techniques except for the quantumdots (QDs) that were synthesized in a glove box with a water and oxygen free environment. All syntheses were performed in glassware cleaned with piranha and aqua regia and stirred using Teflon coated magnetic stirring beans (this may differ from the proposed synthesis methods since the agitation methods were not always mentioned by the authors).

2.4.1 Chemicals & Solvents

1-Eicosene (Sigma-Aldrich, 90 wt.%), 1-hexadecene (Sigma Aldrich, 99 wt.%), 1-octadecene (Sigma-Aldrich, 90 wt.%), acetone (Merck), cadmium acetate ($\text{Cd}(\text{Ac})_2$, Sigma-Aldrich, 99 wt.%), cobalt(II) chloride (Sigma-Aldrich, ≥ 98.0 wt.%), cyclohexane (Sigma-Aldrich, ≥ 99.8 wt.%), cyclohexane (Sigma-Aldrich, anhydrous, 99 wt.%), diethyl zinc (Et_2Zn , Sigma-Aldrich, 1.0 M solution in hexane), ethanol 96 (Baker Analyzed, 96 wt.%), ethanol 100 (Baker Analyzed, 100 %, absolute), gold salt (HAuCl_4 , Sigma-Aldrich, 99.999 %, trace metals basis), hexadecyltrimethylammonium bromide (Sigma-Aldrich, ≥ 96.0 wt.%), hexane mixture of isomers (Sigma-Aldrich), hexane (Sigma-Aldrich, anhydrous, 99.8 wt.%), hexadecane (Acros, 92 wt.%, technical grade), iron(III) chloride hexahydrate (Sigma-Aldrich, 99 wt.%), methanol (Sigma-Aldrich, absolute, HPLC), methanol (Sigma-Aldrich, anhydrous, 99.8 wt.%), octadecene (ODE, Sigma-Aldrich, 90 wt.%), octadecene amine (ODA, Sigma-Aldrich, 90 wt.%), oleic acid (OA, Sigma-Aldrich, 90 wt.%), selenium (Strem Chemicals, 99.99 wt.%), sodium hydroxide (Acros, pellets, extra pure), sodium oleate (ABCR, 95 wt.%), sulphur (Alfa Aesar, 99 wt.%), tetraoctylammonium bromide (TOAB, Sigma-Aldrich, 98 wt.%), trimethylamine oxide ($(\text{CH}_3)_3\text{NO}$, Sigma-Aldrich) was dried by dissolving in toluene and distilling off water, trioctylamine (Sigma-Aldrich, 98 wt.%), trioctylphosphine (TOP, Sigma-Aldrich, 90 wt.%), trioctylphosphine oxide (TOPO, Sigma-Aldrich, 99 wt.%), trisodiumcitrate sesquihydrate (Sigma-Aldrich, 99 wt.%), toluene (Fluka, ≥ 99.7 wt.%), toluene (Sigma-Aldrich, anhydrous, 99.8%). The anhydrous solvents were used for glove box syntheses. To precipitate nanoparticles from an organic phase 100 % ethanol was used instead of 96 % ethanol to prevent phase separation. For de-ionized water a Millipore Direct-Q UV3 reverse osmosis filter apparatus was used ($18 \text{ M}\Omega\cdot\text{cm}^{-1}$ at 25°C).

2.4.2 Equipment

For TEM analysis a Philips Tecnai 12 with a tungsten tip as an electron source, operating at 120 kV, was used. The centrifuge used for sedimentation was a Hettich zentrifugen Rotina 46 S. For high resolution TEM analysis a monochromated Tecnai TF20-ST microscope operating at 200 kV was used. For heating during nanoparticle syntheses a Electrothermal EMA 250/CEBX1 Stirring 250 mL heating mantle was used.

2.4.3 Method 1: Iron oxide nanoparticles, Park *et al.* [51]

For the synthesis of iron oxide Fe_xO_y nanoparticles a method proposed by Park *et al.* (Method 1) was explored [51]. This synthesis was published in 2004 where it yielded relatively monodisperse nanoparticles with a good control over the size. Nanoparticles produced with this method contain a combination of maghemite $\gamma\text{-Fe}_2\text{O}_3$ and magnetite Fe_3O_4 according to Park and his coworkers based on X-ray absorption and x-ray magnetic circular dichroism measurements. They showed that the ratio of maghemite to magnetite increases as the nanoparticles are grown larger [51]. The proposed synthesis method is a thermal decomposition of an iron oleate complex at elevated temperatures. The metal ion reacts with oxides from the decomposing oleates resulting in an iron oxide crystal structure. This synthesis was performed in two steps. The first step was the synthesis of the organometallic precursor. The second step was the nucleation and growth of the nanoparticles. This synthesis method was scaled down to 1/4 of the original scale.

Step 1: precursor

To prepare the organometallic iron oleate complex precursor 8.1 g iron(III)chloride (20 mmol) and 27.38 g of sodium oleate were dissolved in 40 mL of methanol, 30 mL of de-ionized water and 70 mL hexane in a 250 mL round bottom flask. The mixture was heated to 70 °C and stirred for four hours. The hexane top layer was separated and washed three times with 15 mL of de-ionized water using a separatory funnel. The concentration of the resulting iron oleate precursor was determined gravimetrically by drying 1.00 mL of solution and the precursor solution was then diluted to 0.40 mmol/mL using 1-hexadecene. The hexane was removed using a rotation evaporator.

Step 2: Spherical nanoparticles

To synthesize ~7 nm iron oxide spheres 2.54 g of oleic acid was combined with 54.0 mL of the iron oleate precursor solution in a 250 mL round bottom flask. The mixture was degassed using a vacuum pump and heating to 120 °C for 1.5 h. The mixture was then gradually heated (~2-4 °C min^{-1} based on heating rate from Ref. [51, 54]) under nitrogen to a reflux temperature of 290 °C, and stirred for 35 minutes. The reaction mixture was then cooled to room temperature (RT) and diluted with ~1 equivalent hexane. The nanoparticles were precipitated by adding ~1 equivalent ethanol (100%) and centrifuging at 4000 rpm for 1-2 hours. The remaining nanoparticle sediment was redispersed in cyclohexane. This last washing step was performed three times in total for each sample.

2.4.4 Method 2: Cobalt iron oxide nanoparticles, Bodnarchuk *et al.* [54]

The second synthesis method for making magnetic nanoparticles (Method 2) was proposed by Bodnarchuk *et al.* in 2009 [54]. This synthesis route is similar to Method 1 proposed by Park *et al.* However, this method used a mixture of two metal oleate complexes which results in the formation of core-shell nanoparticles [54]. For this research the scale of the synthesis was doubled to yield a higher amount of nanoparticles resulting in a comparable

scale as Method 1. The methods to synthesize star-shaped and octahedral nanoparticles are not mentioned in the article as this is a newly developed modification of this method. For the remaining details the synthesis was performed according to literature.

The proposed method was again a two step synthesis. The first step was the synthesis of the precursor mixture. The second step was the nucleation and growth step, it is in this step the shape of the nanoparticles could be influenced.

Step 1: precursor

To prepare the precursor mixture of iron oleate and cobalt oleate with a molar ratio of 2:1 for $\text{Fe}^{3+}:\text{Co}^{2+}$, 8.66 g $\text{FeCl}_3 \cdot 4\text{H}_2\text{O}$ (32 mmol) was dissolved in 80 mL of methanol and mixed with 2.08 g CoCl_2 (16.0 mmol) dissolved in 40 mL of methanol. 40.2 g oleic acid (128 mmol) was added to the mixture. 5.12 g sodium hydroxide (NaOH) dissolved in 320 mL methanol was added over 45 minutes to the mixture. The resulting brown viscous liquid was separated by decanting and washed three times with methanol and dissolved in 80 mL hexane (anhydrous). The hexane phase was separated using a separatory funnel and washed three times using warm (50 °C) de-ionized water. The concentration was determined gravimetrically by drying a 1.00 mL aliquote of the solution. A precursor solution with a concentration of 0.50 mol kg^{-1} was prepared by adding 1.48 g 1-hexadecene for each gram of mixed oleate used. The hexane was removed by rotary evaporation at 30°C.

Step 2a: spherical nanoparticles

For the synthesis of 7 nm spherical nanoparticles 9.6 g of the precursor solution (4.8 mmol of mixed oleate) was mixed with 0.76 g oleic acid (0.84 mL 2.4 mmol) and 13.72 g 1-hexadecene. The mixture was then degassed at 110°C for 1 hour and gradually ($\sim 2\text{-}4 \text{ }^\circ\text{C min}^{-1}$) heated to reflux, after 35 minutes the mixture was allowed to cool to RT. The resulting suspension was mixed with ~ 1 equivalent of hexane and ethanol (100%), and centrifuged at 4000 rpm for 1-2 hours. The resulting black sediment was redispersed in cyclohexane. This last washing step was performed three times in total for each sample.

Step 2b: cubic nanoparticles

As described by the authors cubic core-shell nanoparticles are synthesized by adding sodium oleate to the reaction. For a typical synthesis 9.60 g precursor solution, 0.76 g oleic acid, 1.46 g sodium oleate (4.8 mmol) and 6.26 g 1-hexadecene were combined. The mixture was then degassed at 110°C for 1 hour and gradually ($\sim 2\text{-}4 \text{ }^\circ\text{C min}^{-1}$) heated to reflux, after 35 minutes the mixture was allowed to cool to RT. The resulting nanoparticles were isolated by centrifugation at 4000 rpm for 1-2 hours with ~ 1 equivalent of ethanol (100%) and hexane.

Step 2c: octahedral nanoparticles

As an alternative to the cube synthesis, tetraoctylammonium bromide was used to make octahedral core-shell nanoparticles: For this synthesis 9.60 g precursor solution, 0.76 g

oleic acid, 2.00 g tetraoctylammonium bromide and 6.26 g 1-hexadecene were combined. The mixture was then degassed at 110°C for 1 hour and gradually ($\sim 2-4\text{ }^\circ\text{C min}^{-1}$) heated to reflux, after 35 minutes the mixture was allowed to cool to RT. The resulting nanoparticles were isolated by centrifugation at 4000 rpm for 1-2 hours with ~ 1 equivalent of ethanol (100%) and hexane.

Step 2d: star shaped nanoparticles

For the synthesis of star shaped nanoparticles 9.6 g precursor solution, 0.76 g oleic acid, 2.00 g tetraoctylammonium bromide and 1.05 g sodium oleate (4.80 mmol) and 6.26 g 1-hexadecane were combined. The mixture was then degassed at 110°C for 1 hour and gradually ($\sim 2-4\text{ }^\circ\text{C min}^{-1}$) heated to reflux, after 35 minutes the mixture was allowed to cool to RT. the resulting nanoparticles were isolated by centrifugation at 4000 rpm for 1-2 hours with ~ 1 equivalent of ethanol (100%) and hexane.

2.4.5 Method 3: Maghemite ($\gamma\text{-Fe}_2\text{O}_3$) iron oxide nanoparticles, Hyeon *et al.* [53]

To synthesize nanoparticles with a single type of crystal structure a method proposed by Hyeon *et al.* in 2001 was used [53]. The nanoparticles made with this synthesis route consisted of maghemite ($\gamma\text{-Fe}_2\text{O}_3$) according to the authors, based on X-ray diffraction [53]. This method is based on the reduction of ironpentacarbonyl by trimethylamine oxide at 100 °C. To synthesize 21 nm maghemite nanoparticles 0.20 mL (1.52 mmol) of iron pentacarbonyl ($\text{Fe}(\text{CO})_5$) was injected into a solution of 0.91 g (4.56 mmol) of oleic acid, 7.00 mL of di-octylether and 0.57 g (7.60 mmol) of dry trimethylamine oxide ($(\text{CH}_3)_3\text{NO}$) at 100 °C under a nitrogen atmosphere. The resulting mixture was allowed to react for 1 hour at 120 °C and was then refluxed at $\sim 287\text{ }^\circ\text{C}$ for 1 hour. The solution was cooled to RT and was precipitated using ethanol (100%) and centrifuging for 30 minutes. In the article the authors also annealed the particles to further modify the particles, this step was not performed in our synthesis method.

2.4.6 Method 4: Gold nanoparticles, Turkevich *et al.* [49]

A well-known synthesis of gold nanoparticles is the method proposed by Turkevich *et al.* in 1951 [49, 64]. It comprises the reduction of a gold salt (HAuCl_4) using citric acid in water, resulting in colloidal gold [49, 64]. The citric acid in this method functions as reductor and as ligand, stabilizing the nanoparticles after nucleation by inducing a negative charge. This method is simple and fast to perform. However, it yields low concentrations of nanoparticles since only a low starting concentration is used.

To synthesize 10 nm nanoparticles 8.0 mg of HAuCl_4 was dispersed in 150 mL of de-ionized water and heated to a 100 °C. when the solution reached 100 °C a solution of trisodiumcitrate sesquihydrate dissolved in 50 mL de-ionized water was added quickly. The resulting mixture turned black, blue, and then wine red over a period of seconds. The resulting suspension was then allowed to cool to RT.

2.4.7 Method 5: Gold nanoparticles, Brust *et al.* [65]

Gold nanoparticles with a higher yield and lower PD were synthesized by the method proposed by Brust *et al.* [65]. This method consists of a two phase system in which the gold is complexed to hexadecyltrimethylammonium bromide (CTAB), the HAuCl_4 exchanges with the bromide ions, and the gold is transferred to the organic phase, after which it is reduced using NaBH_4 .

To synthesize 5 nm Au nanoparticles a stock solution (S1) was made by dispersing 270 mg of HAuCl_4 in 22.29 mL of de-ionized water. A second stock solution (S2) was made by adding 1.90 g tetraoctylammonium bromide to 60 g toluene. 5.30 mL of S1 was combined with 15.00 mL of S2 and stirred until the water phase became colorless and the toluene phase dark red. 0.076 g of NaBH_4 dissolved in 4.86 g of cooled de-ionized water was added to the S1/S2 mixture. After 30 minutes 75 μl dodecanethiol was added. After stirring for another hour the organic phase was isolated and the sample was sedimented by adding 50 w/w% ethanol and centrifuging for 22 minutes.

2.4.8 Method 6: Cadmium selenite zinc sulfide core-multishell quantumdots, Xie *et al.* [66]

Since the nanoparticles in this research are used for self-assembly in emulsion droplets, they must be chemically stable in the presence of air and water. Semiconductor nanoparticles, or quantumdots (QD), are usually sensitive to air or water due to photo-oxidation [67]. Core-multishell QDs that were stable in the presence of water and oxygen were synthesized according to a method by Xie *et al.* [66].

Seed growth

All QD syntheses were performed in a nitrogen atmosphere with pre-dried chemicals and stored in a glovebox. Prior to the synthesis of the CdSe QDs 2 precursors were synthesized. OA (3.68 g), ODE (25.92 g), and $\text{Cd}(\text{Ac})_2$ (0.64 g) were mixed and heated to 150 °C, and kept under vacuum for 2 h to form $\text{Cd}(\text{OA})_2$. Selenium (4.25 g) was dissolved in TOP (22.5 g) at 50 °C, followed by the addition of ODE (35.7 g).

CdSe nanocrystal seeds were synthesized under inert atmosphere using a Schlenk-line. TOPO (1.11 g), ODA (3.20 g), and $\text{Cd}(\text{OA})_2$ -precursor (4.9 g) were mixed, heated to 300 °C. When this temperature was reached the Se-precursor (5.2 g) was added rapidly. The size of the quantum dots can be tuned via changing the reaction time, which was 30 seconds for the presented QDs which resulted in a seed size of 2.9 nm, after which the mixture was cooled to RT. The particles were diluted by adding 1 equivalent of hexane. The quantum dots were washed by adding 2 equivalents of methanol and collecting the upper hexane layer (coloured) and adding 1 equivalent of acetone to precipitate the QDs. Finally, the nanocrystal seeds were re-dissolved in toluene and stored inside a glove box under nitrogen atmosphere

Shell growth

Prior to the synthesis of the CdSe quantum dots three precursor solutions were prepared. A zinc precursor solution (0.1 M) was prepared by dissolving Zn(Et)₂ (0.494 g) in oleic acid (5.05 mL) and ODE (19.8 mL) at 310 °C. A cadmium precursor solution (0.1 M) was prepared by dissolving Cd(Ac)₂ (1.10 g) in oleic acid (10.83 g) and ODE (43.20 mL) at 120 °C under vacuum for 2 hours. A sulfur precursor solution (0.1 M) was prepared by dissolving sulfur (0.032 g) in ODE (10 mL) at 180 °C. The Cd-, Zn-, and Cd/Zn-precursor solutions were kept at about 80 °C, while the sulfur injection solution was allowed to cool to RT. For each shell growth, a calculated amount of a given precursor solution was injected with a syringe using standard air-free procedures. CdSe QDs (1·10⁻⁷M of 2.91 nm QDs), ODE (5.0 g) and ODA (1.5 g) were combined and heated up to 150 °C for 1 h to remove all toluene. The reaction temperature was increased to 240 °C and in steps with reaction periods of 30 minutes the precursors were added slowly to grow the cell half-monolayer by half-layer. For the amounts added for each shell growth see table 2.2. Afterwards the reaction mixture was cooled to RT and diluted by adding 1 equivalent of hexane. The quantum dots were washed by adding 2 equivalents of methanol and collecting the upper hexane layer (coloured) and add 1 equivalent of acetone to precipitate the QDs. Finally, the nanocrystal seeds were re-dissolved in cyclohexane and stored inside a glove box under nitrogen atmosphere.

Step	Total monolayers	Added Precursors	Amount (μL)
1	0.5	Cd+S	130
2	1	Cd+S	165
3	1.5	Cd+S	205
4	2.0	Cd+S	250
5	2.5	Cd+S	295
6	3	Cd+S	350
7	3.5	Cd+S	410
8	4	Cd+S	470
9	4.5	Cd+S	540
10	5	Cd+S	610
11	5.5	CdZn+S	690
12	6	CdZn+S	770
13	6.5	Zn+S	855
14	7	Zn+S	940

Table 2.2: Table showing the amount of precursor solution added for each consecutive shell growth in the core-multishell QD synthesis.

2.4.9 Sample preparation and analysis

For TEM analysis 200 mesh copper grids with a ~25 nm thick Solutia support film were used as sample support, carbon coated for ~7 seconds using a Cressington 208 carbon coater. To prepare samples for TEM analysis ~3 μL of sample was deposited on a TEM grid and allowed to dry.

TEM was used to measure the diameter and standard deviation (SD) of the nanoparticles. The sizes of the nanoparticles were measured as the diameter of the core e.g. iron oxide, cobalt iron oxide, or gold, as the capping layer is not visible in TEM images. The SD is calculated as follows:

$$SD = \sqrt{\frac{\sum_{i=1}^N (\sigma_i - \bar{\sigma})^2}{N - 1}} \quad (2.3)$$

The PD is calculated as the SD divided by the mean diameter, and gives a measure for the heterogeneity of the system [68]. Effectively the nanoparticles are larger as a result of the capping layer, this means that the PD is effectively lower, assuming that the capping layer is of uniform thickness. The thickness of this capping layer determines the distance of nearest approach between the cores, this distance was measured in 2D close packed nanoparticle arrays over ~ 10 nanoparticles dividing this distance by the number of nanoparticles resulting in an effective diameter, subtracting the mean diameter resulted in the distance of nearest approach.

To study the intrinsic crystal structures of 12 nm cubic and 15 nm spherical core-shell cobalt iron oxide nanoparticles, synthesized according to Method 2a and b, high resolution transmission electron microscopy was used. For this analysis 8 μL of sample solution was drop-cast on a MEMS micro-hotplate, and the samples were examined using a monochromated Tecnai 20F-ST. The crystal lattice spacing was determined by measuring 10 spacings and dividing by 10 [69].

2.5 Results & Discussion

In the first part of this section the different methods for making spherical metal oxide nanoparticles will be discussed. We will then move on to non-spherical metal oxide nanoparticles, spherical metal nanoparticles, and subsequently to spherical semiconductor core-multishell nanoparticles. Finally, we will take a closer look at the internal crystal structures of core-shell cobalt iron oxide nanoparticles using high resolution TEM.

2.5.1 Spherical iron oxide and cobalt iron oxide nanoparticles (Methods 1, 2, and 3)

Heating rates for Methods 1 & 2

For the thermal decomposition experiments the heating rate determines the speed at which the monomer is introduced into the system and, as described in section 2.1, this rate is an important factor in the formation of the nanoparticles. For example to prevent secondary nucleation the temperature above 200 $^{\circ}\text{C}$ must be raised gradually with $\sim 2\text{-}4$ $^{\circ}\text{C min}^{-1}$. Below this temperature the heating rate has little to no effect on the monomer concentration as thermal decomposition does not start below 200 $^{\circ}\text{C}$ as found by Park *et al.* by thermogravimetric analysis (TGA) [51]. But where the authors of Method 1 [51] suggested a

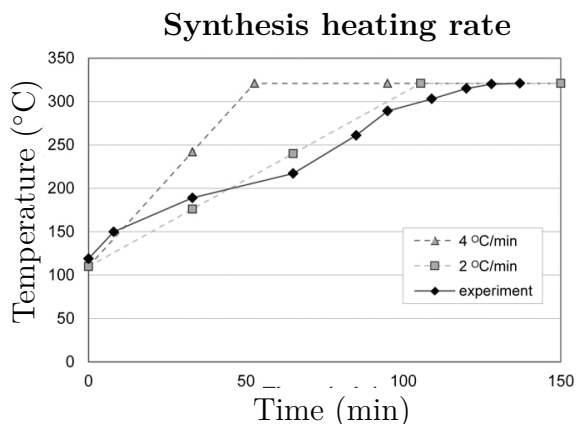


Figure 2.2: Heating rate used for nanoparticle synthesis compared to the suggested 2-4 $^{\circ}\text{C min}^{-1}$ [51, 54], thermal decomposition starts over 200 $^{\circ}\text{C}$ [51].

heating rate of $4\text{ }^{\circ}\text{C min}^{-1}$ for their method, the authors of Method 2 [54] use a heating rate of $2\text{ }^{\circ}\text{C min}^{-1}$ in their comparable synthesis method. For our experiments the heating rate had to be manually controlled by changing the power of the heating mantle. To get an idea of the heating rate the temperature was closely followed during the heating phase of a typical experiment, see graph Fig. 2.2. The heating rate, as depicted here, was close to the suggested $2\text{ }^{\circ}\text{C min}^{-1}$ by Bodnarchuck *et al.* However, it is likely that there were variations in the heating rates for different experiments as a result of the manual operation of the heating mantle.

Thermal decomposition of iron-oleate precursor (Method 1)

The first presented method for making metal oxide nanoparticles was presented Park *et al.*, [51]. According to the authors the size of the nanoparticles can be tuned by changing the synthesis temperature, where they controlled the temperature in their experiments by using solvents with different reflux temperatures. This has the advantage over conventional controlled heating in that there will be no overshoot in temperature and a smaller temperature gradient, either of which would result in a larger size distribution. The solvents chosen for these syntheses were: 1-hexadecene (bp $290\text{ }^{\circ}\text{C}$), 1-octadecene (bp $330\text{ }^{\circ}\text{C}$) and trioctylamine (bp $365\text{ }^{\circ}\text{C}$). Using these solvents in the syntheses resulted in 5.8 nm, Fig. 2.3a and 7.2 nm, Fig. 2.3b nanoparticles for 1-hexadecene, 18.8 nm nanoparticles for 1-octadecene 2.3c, and 38.3 nm nanoparticles for trioctylamine, Fig. 2.3d. This showed that the reflux temperature of the solvent indeed significantly influenced the nanoparticle size.

The nanoparticles made with this method are, according to the authors, a combination of meghamite and hematite [51]. In the article a typical PD of $<5\%$ was achieved. In our experiments the synthesis method yielded fairly monodisperse nanoparticles with PDs as low as $\sim 6\%$, as is shown in Fig. 2.4. Where Fig. a is 8%, b is 7%, c is 6%, and d is 6%. Although this is close to the value of the article it is not as good as the described $<5\%$.

Shortening the reflux time by ~ 10 minutes from ~ 35 minutes to ~ 25 minutes resulted in smaller 5.8 nm, Fig. 2.3a, instead of the 7.2 nm, Fig. 2.3b nanoparticles grown in 1-hexadecene over 35 min. The exact time at which the nucleation happens and when the growth stage occurs is unclear since the initial color change, indicating the formation of nanoparticles, difficult to distinguish from the dark precursor solution and the reflux temperature is only gradually reached over a time of ~ 15 minutes during which the burst nucleation happened and the growth started to occur. As a result the growth time has to be estimated since the exact time at which the nucleation occurred could not be accurately determined. The subsequent growth of the nanoparticles is then a compromise between size and PD [70]. An example of this was found in the comparison between these two batches of nanoparticles synthesized with a different growth time. The SD from the diameter for the samples were 0.5 nm and 0.5 nm. However, the batch with the shorter growth time (~ 25 min) had a PD of 8%, while the batch with the longer growth time (~ 35 min) resulted in a PD of 7% a result of the size difference. This suggests that the SD of the batch is predominantly determined during the nucleation and remains the similar or close to similar during the subsequent growth phase, lowering the PD. Typically, a low PD of 6.5% or less is required for the crystallization of hard spheres. However,

no crystallization was observed on TEM grids loaded with the two smallest batches of nanoparticles even though the PDs were close to the needed 6.5 % [68, 71]. The 18.8 nm and 38.8 nm nanoparticles with PDs of 6 % did show local ordering when deposited on the TEM grids as is shown in Fig. 2.3. The small, 5.8 nm and 7.2 nm nanoparticles were expected to crystallize even with a PD above 6.5 %, since the effective diameter is larger, likely close to ~ 8.6 nm based on the results shown in Fig. 2.10, resulting in an effective PD of 6%. The reason that no crystalline ordering was observed for these nanoparticle samples, besides the PD, could also be caused, amongst other factors, by an excess of surfactants (oleic acid) or residual high boiling solvents (hexadecane) remaining from the synthesis.

Note that using a more controlled drying method will most likely aid crystallization, e.g. drying on a TEM grid at an angle [72, 73], but since all iron oxide and cobalt oxide nanoparticles samples were deposited from cyclohexane on a TEM grid in a similar fashion it is possible to compare self-assembly behavior.

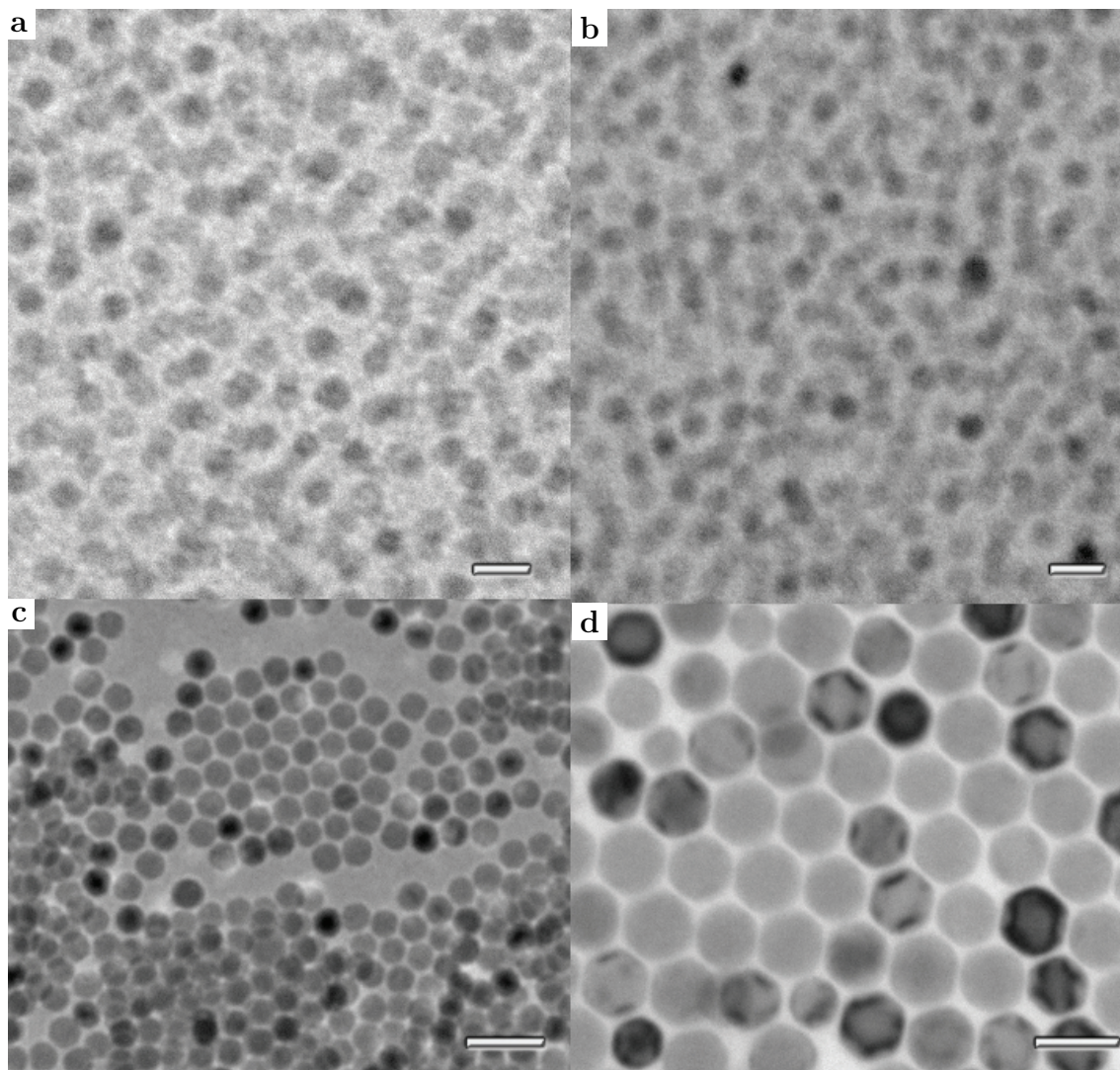


Figure 2.3: Transmission electron micrographs of iron oxide nanoparticles of sizes ranging from 5.8 nm to 38.8 nm synthesized according to Method 1 by Park *et al.* [51], which results in a combination of maghemite $\gamma\text{-Fe}_2\text{O}_3$ and magnetite Fe_3O_4 according to the authors. **a)** 5.8 nm nanoparticles synthesized in 1-hexadecene (bp 290 °C) (scale bar = 50 nm), **b)** 7.2 nm nanoparticles synthesized in 1-hexadecene (scale bar = 50 nm), **c)** 18.8 nm nanoparticles synthesized in 1-octadecene (bp 330 °C) (scale bar = 200 nm), **d)** 38.8 nm nanoparticles synthesized in trioctylamine (bp 365 °C) (scale bar = 200 nm).

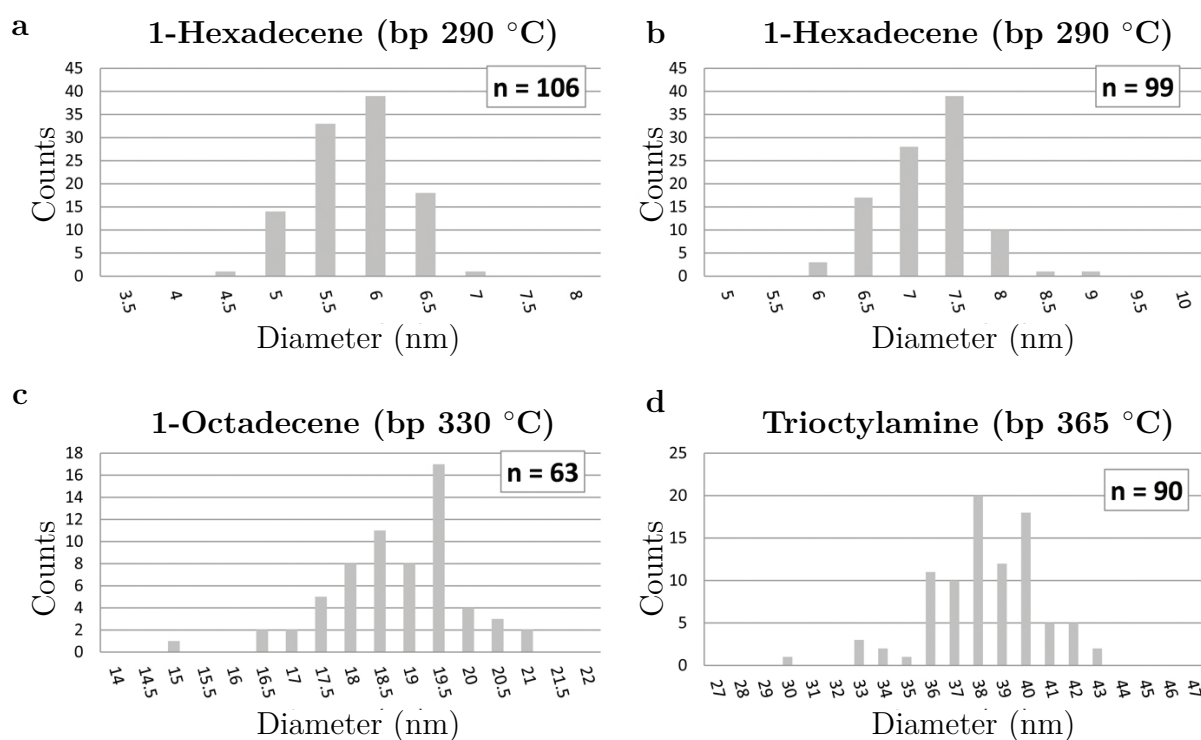


Figure 2.4: Size distributions shown in graphs for iron oxide nanoparticles synthesized according to Method 1 [51] in different solvents. **a)** 5.8 nm nanoparticles with a PD of 8 %, in 1-hexadecene for ~25 min. **b)** 7.2 nm nanoparticles with a PD of 7 %, in 1-hexadecene for ~35 min. **c)** 18.8 nm nanoparticles with a PD of 6 %, 1-octadecene. **d)** 38.3 nm nanoparticles with a PD of 6 %, trioctylamine.

Thermal decomposition of a mixed Cobalt/Iron-oleate precursor (Method 2a)

As described earlier, for hard-sphere crystallization a PD of less than $\sim 6.5\%$ is needed [71]. Since we want to study the crystallization of the particles, monodisperse batches of nanoparticles with polydispersities well under this value were preferred. Although the results of the previous method (Method 1) were promising, the documented polydispersities of $< 5\%$ were not obtained.

The method using mixed cobalt/iron oleate precursors (Method 2) showed promising monodisperse results in the literature and was therefore explored to see if this would result in lower PDs. Fig. 2.5 shows five of the best results obtained with this synthesis method showing large ordered domains of self-assembled nanoparticles.

The size of the nanoparticles was again influenced by varying the synthesis temperature by changing the solvent and the growth time similar as with the previous method. The respective size distribution graphs for these syntheses are shown in Fig. 2.6. Using 1-hexadecene and 1-octadecene as solvents and varying the synthesis time nanoparticles with mean size ranges from 6.0 nm to 19.6 nm and polydispersities around 4% were obtained. Using 1-hexadecene resulted in 6.0 nm nanoparticles with an SD of 0.3 nm and a PD of 5% 2.5a whereas with 1-octadecene nanoparticles of 10.8 nm 2.5b, 13.2 nm 2.5c, 14.9 nm 2.5d and 19.6 nm 2.5e were made, all with PDs of 4%. These results were consistently and significantly better than the results obtained with the previous method (Method 1) in terms of PD. The size difference between the nanoparticles synthesized in 1-octadecene was the result of varying the reflux time during the synthesis from ~ 25 minutes to ~ 40 minutes. However, again the time at which the reflux started is hard to determine as reflux is reached gradually and at varying speeds as a result of the manually controlled heating.

According to [74] the effective ionic radii of Fe^{2+} and O^{2-} are 0.55 Å and 1.40 Å respectively, implying a lattice spacing of 1.95 Å. which means that the SD of the radii of the most monodisperse nanoparticle sample (1.5 Å) is of the order of a single FeO lattice spacing. The effective PD of the nanoparticles is even lower if we assume a ligand layer with a uniform thickness. However, the thickness of this layer was different for each batch of nanoparticles and is elaborated on at the end of this section.

Also shown in Fig 2.5f is an example of a batch of nanoparticles which, most likely, experienced a secondary nucleation step during which a second batch of seeds was formed. This would mean the monomer concentration reached supersaturation again after the initial nucleation phase. The secondary seeds were formed later than the first batch and experience a shorter growth time, thus resulting in smaller nanoparticles. This was likely the result of a faster heating rate, unfortunately the actual heating rate is unknown as this is typically not logged during the experiments. To show that this is not just PD due to, for example, temperature gradients in the reaction the SD graph is plotted in Fig. 2.6 f. In this graph two distinct size distributions are visible with a size difference of $\sim 2 - 3$ nm.

When examining self-assembled layers of cobalt iron oxide nanoparticles both FCC and HCP packings were visible in layers with a thickness of three or more nanoparticles. This indicated that the nanoparticles self-assembled similarly to hard-spheres. Examples of these close-packed nanoparticles are given in Fig. 2.7 where **a** is an HCP and **b** an

FCC packing. Schematic representations of the types of packing are shown in **c** and **d**. According to Bolhuis and Frenkel the FCC crystal phase is thermodynamically favorable over the HCP phase [12]. However, in these samples no distinct preference was discerned for FCC nor HCP unlike in Ch. 6 where this type of cobalt iron oxide nanoparticles showed predominantly FCC packing in the form of tetrahedral crystalline domains separated by FCC twinning planes as a result of a spherical confinement.

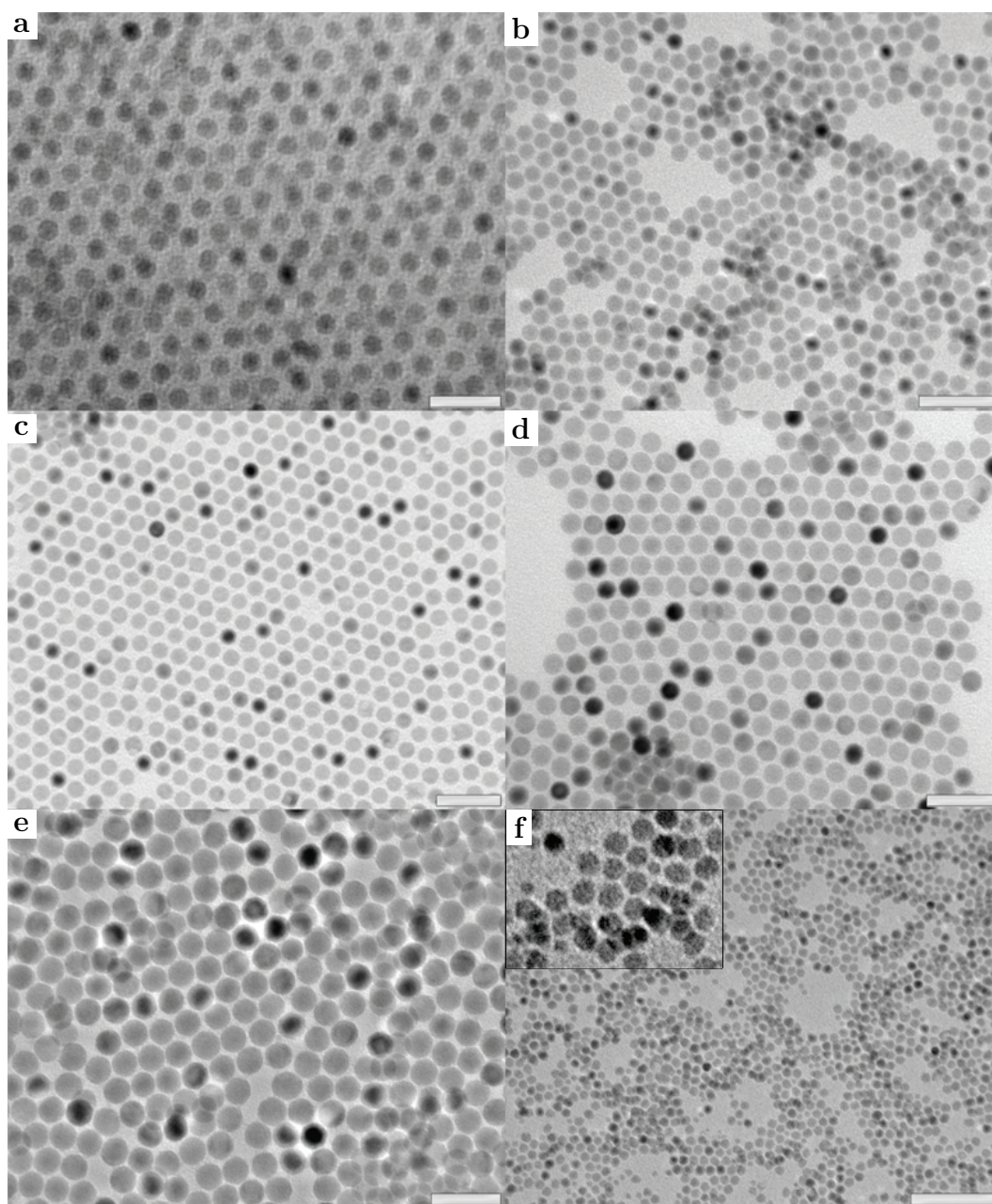


Figure 2.5: Transmission electron micrographs of nearly monodisperse core-shell nanoparticles with a cobalt iron oxide shell and an iron oxide core made according to Method 2a [54]. In these figures the nanoparticle sizes range from 6.0 nm to 18.8 nm. **a)** 6.0 nm nanoparticles synthesized in 1-hexadecene (scale bar = 20 nm). **b)** 10.8 nm nanoparticles synthesized in 1-octadecene, for ~25 minutes at reflux temperature (scale bar = 50 nm). **c)** 13.2 nm nanoparticles synthesized in 1-octadecene, ~35 minutes at reflux temperature (scale bar = 50 nm). **d)** 14.9 nm nanoparticles synthesized in 1-octadecene, ~40 minutes at reflux temperature (scale bar = 50 nm). **e)** 19.6 nm nanoparticles synthesized in 1-octadecene (scale bar = 50 nm). **f)** Bidisperse nanoparticles with sizes of ~7 nm and ~11 nm synthesized in 1-octadecene at reflux temperature for ~30 minutes (scale bar = 100 nm). Inset: zoomed in image of the binary sample.

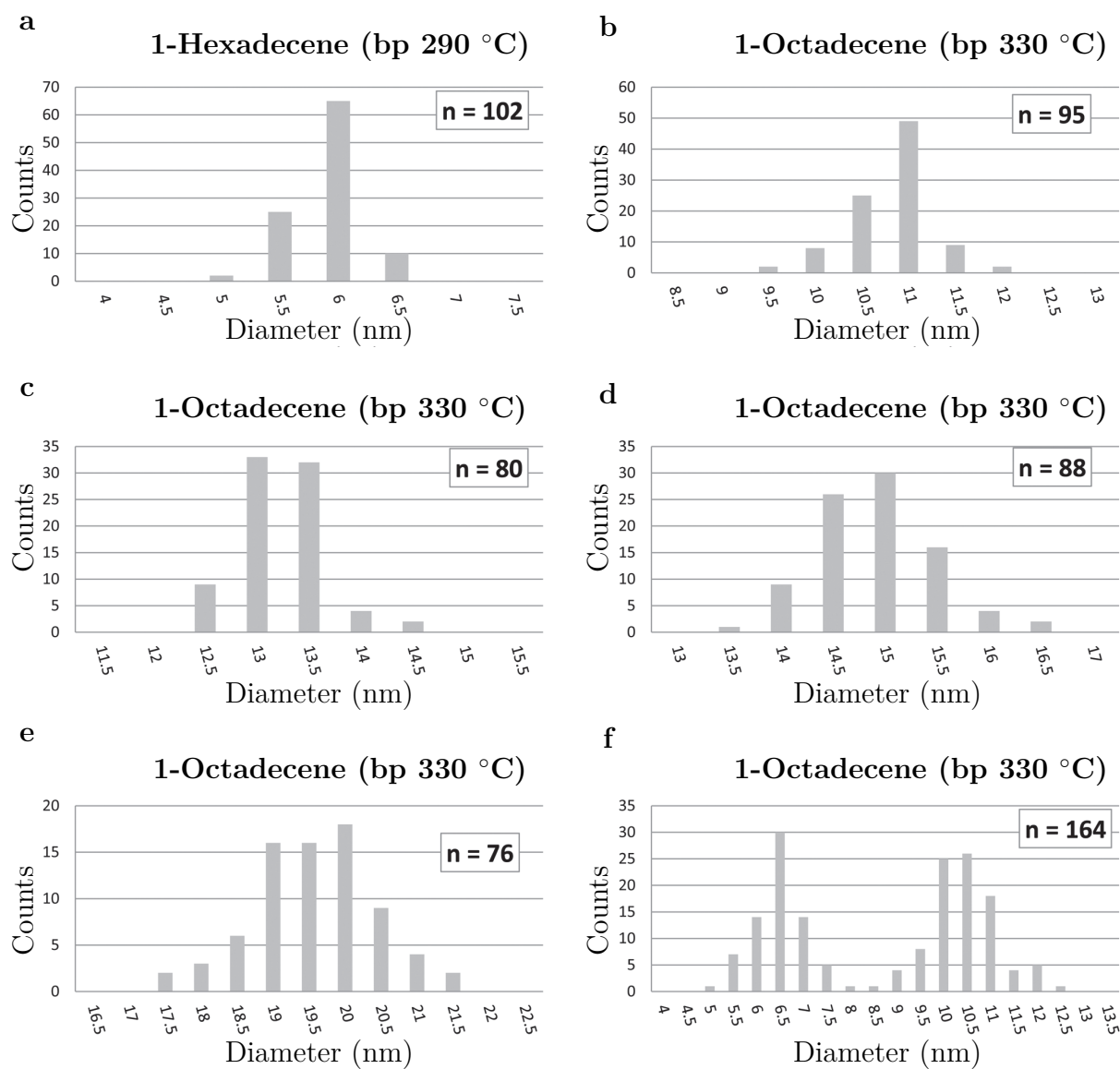


Figure 2.6: Size distributions of the cobalt iron oxide nanoparticles shown in Fig. 2.5 in the same respective order: **a)** 6.0 nm nanoparticles with an SD of 0.3 nm and a PD of 5 %, **b)** 10.8 nm nanoparticles with a SD of 0.5 nm PD of 4 %. **c)** 13.2 nm nanoparticles with an SD of 0.6 nm and a PD of 4 %. **d)** 14.9 nm nanoparticles with an SD of 0.6 nm and a PD of 4 %. **e)** 19.6 nm nanoparticles with an SD of 0.8 and a PD of 4 %. **f)** A bidisperse nanoparticles sample showing 2 distinct size distributions.

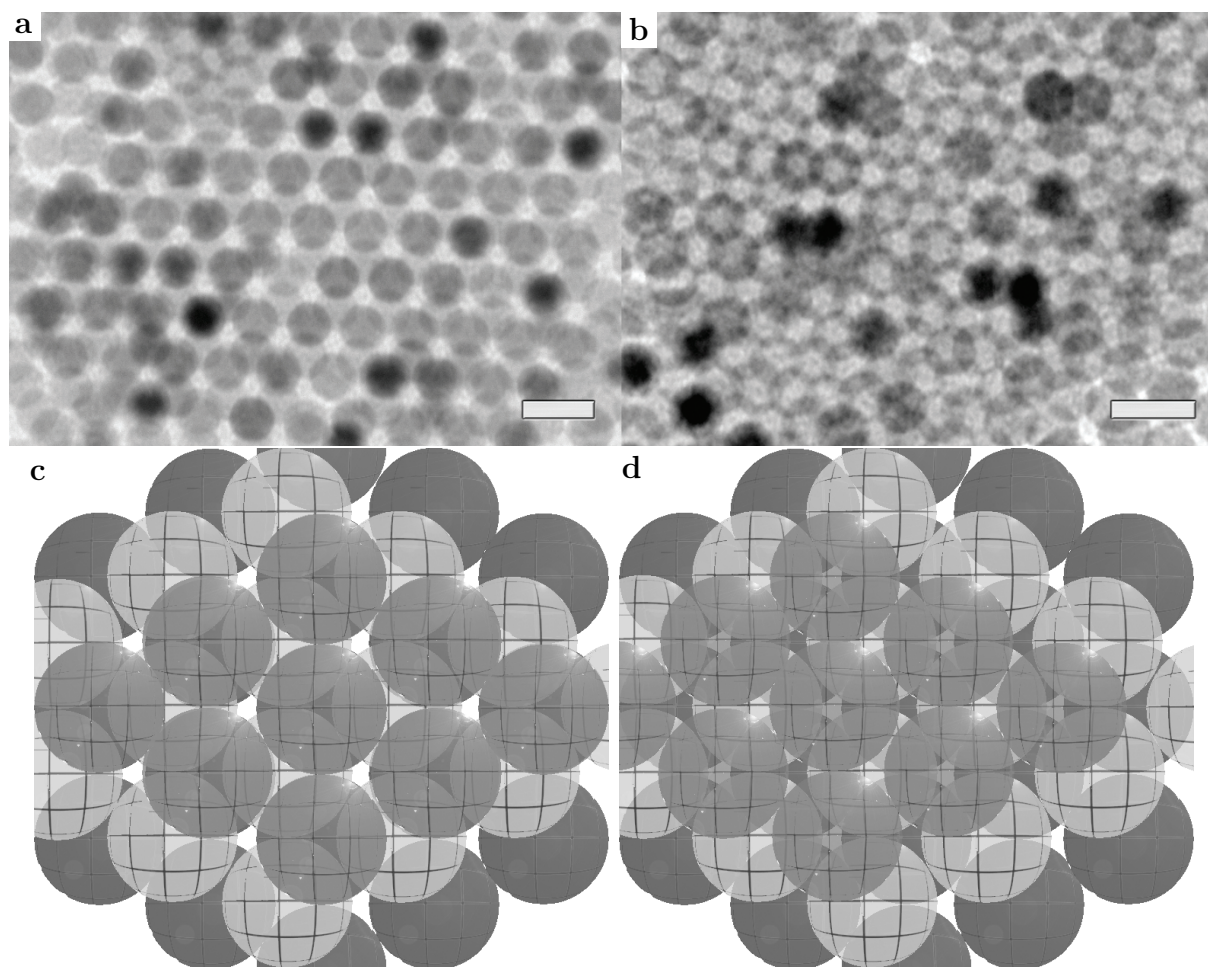


Figure 2.7: Transmission electron micrographs of close packed 13.2 nm cobalt iron oxide nanoparticles and schematic representations of the respective crystal structures. **a)** TEM image of nanoparticles self-assembled into three layers which if the ABAB sequence is repeated indefinitely forms an HCP crystal packing (scale bar = 20 nm). **b)** TEM image of nanoparticles self-assembled into three layers with an ABC stacking which if repeated forms an FCC crystal packing (scale bar = 20 nm). **c)** Schematic representation of HCP packed hard spheres. **d)** Schematic representation of FCC packed hard spheres.

The synthesis methods described up to now were similar save for the difference in precursors and for both experimental methods the size was tuned by using solvents with different reflux temperatures. Fig. 2.8 shows the obtained sizes plotted against the boiling temperatures of the solvents for both methods. When examining the PDs of both methods fairly constant PDs, between 4 % and 8 %, were observed as is shown in Fig. 2.9. Strikingly, Method 2a, using a mixture of precursors, yielded consistently significantly more monodisperse nanoparticles than Method 1. The reason for this lower PD is not clear.

As mentioned earlier, the effective diameter of the nanoparticles, for purpose of crystallization, was larger than the core diameter since the particles were covered in a layer of ligand molecules acting as a steric stabilizer [75]. When fully extended the ligand molecule used, oleic acid, can reach a length of 1.97 nm [76].

Measuring the effective diameter and distance of nearest approach for these nanoparticles will give a measure for the extension and or interdigitation of the ligands, as described by Korgel *et al.*[75]. To determine the effective diameter the distance over n (typically 10) nanoparticles was determined in close-packed nanoparticles and divided by n . The difference between the mean and effective diameter gave the distance of nearest approach for the nanoparticles, see Fig. 2.10. In this graph the distances of nearest approach is plotted for each of the cobalt iron oxide nanoparticles against the diameter of the cores. As shown here, this distance of nearest approach was not constant but varied between ~ 0.5 nm to ~ 3 nm, and decreased with the increase of the nanoparticle size. This is odd, as one would, at first glance, expect that the stabilizers could interpenetrate somewhat more for particles with a smaller radius of curvature. This observed change in distance of nearest approach could be caused by an increase in the Van der Waals interactions as a result of the larger particle size, but could also result from larger drying forces between larger particles. Although this last effect does not come into play for particles in dispersions it will most likely also happen in dried supraparticles making this relevant for the self-assembled structures that will be presented in the coming chapters as well, and although error bars are not shown in this plot, because they are hard to estimate, it is clear with distances so close to the resolution of the method that they are not small and could very well be larger than 20%.

One has to note that this is measured on systems in a dried state and these distances will likely change significantly with solvent molecules present.

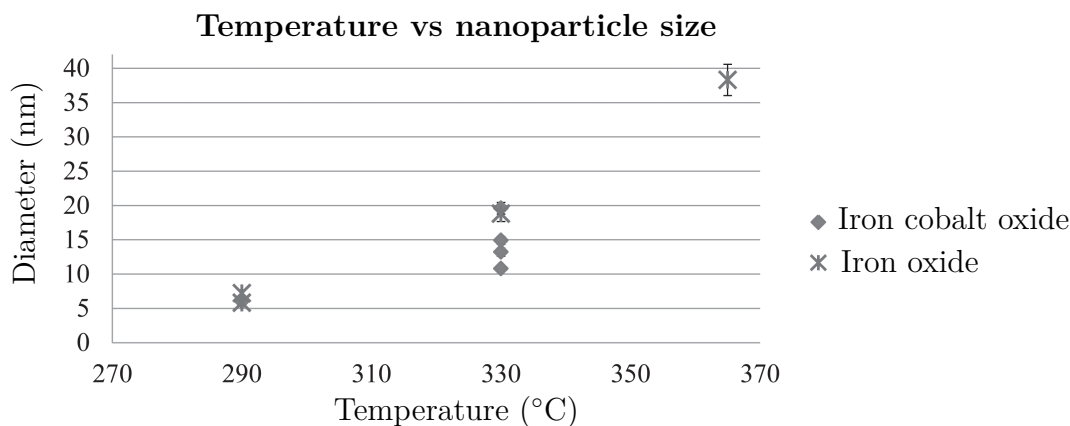


Figure 2.8: Graph showing the nanoparticle size as a function of the synthesis temperature for both the iron oxide and cobalt iron oxide nanoparticle syntheses.

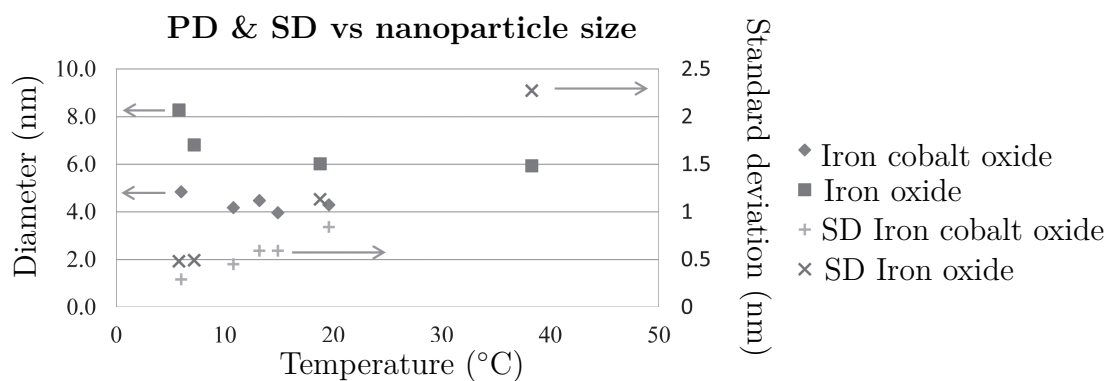


Figure 2.9: Graph showing the polydispersities of the particle cores versus the mean core diameters of the nanoparticles on the left *y* axis, and the standard deviation versus the mean core diameters of the nanoparticles on the right *y* axis.

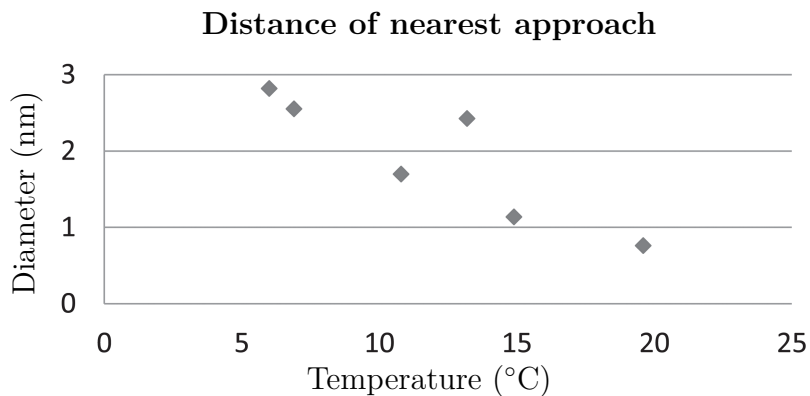


Figure 2.10: Measured distance of nearest approach for nearly monodisperse nanoparticles as a function of diameter.

Maghemite ($\gamma\text{-Fe}_2\text{O}_3$) nanoparticles by reduction of iron pentacarbonyl (Method 3) [53]

The spherical nanoparticles discussed before were either a combination of maghemite and magnetite, according to literature (Method 1) [51], or possessed a core-shell structure where the core was anti-ferromagnetic wüstite with a ferrimagnetic shell (Method 2a) [54]. To investigate the effect of a single crystal type (only $\gamma\text{-Fe}_2\text{O}_3$) has on the shape and the magnetic properties of the nanoparticles a synthesis method was explored which formed only $\gamma\text{-Fe}_2\text{O}_3$ iron oxide according to the authors of Ref. [53]. The reason for the single crystal type is likely a combination of the starting reagents and the oxidizer [53]. The synthesis method is described in the experimental section as Method 3 and resulted in a batch with 20.9 nm nanoparticles as shown in Fig. 2.11. As is shown here a small shape anisotropy in the nanoparticles can be observed which was not seen in previous syntheses for spherical nanoparticles. Furthermore, the particles showed clearly stronger paramagnetic properties as they were pulled from the suspension and onto the stirring bean by its magnetic field as is shown in Fig. 2.11b. In this figure the nanoparticles were not only aggregated on the stirring bean but showed ferro fluidic behavior forming spikes of nanoparticles along the field lines of the stirring bean. This was not observed in previous syntheses for spherical nanoparticles (Method 1 & 2). As to why these particles exhibit such strong paramagnetic behavior is yet unclear and could be caused by the difference in crystal structure but could also be caused by the domain size of the intrinsic crystal structure or other property differences.

This batch consisted of 20.9 nm nanoparticles with an SD of 1.2 nm and a PD of 6 %, Fig. 2.12. The diameter was measured over the width of the nanoparticles. The shape anisotropy will likely hamper the crystallization, although the PD was not lower than obtained with Method 1. The magnetic properties of the nanoparticles were of secondary interest for the research of this Thesis. For these reasons this synthesis method was not further explored, and synthesis Method 2a was used to produce the majority of the spherical nanoparticles used for this research.

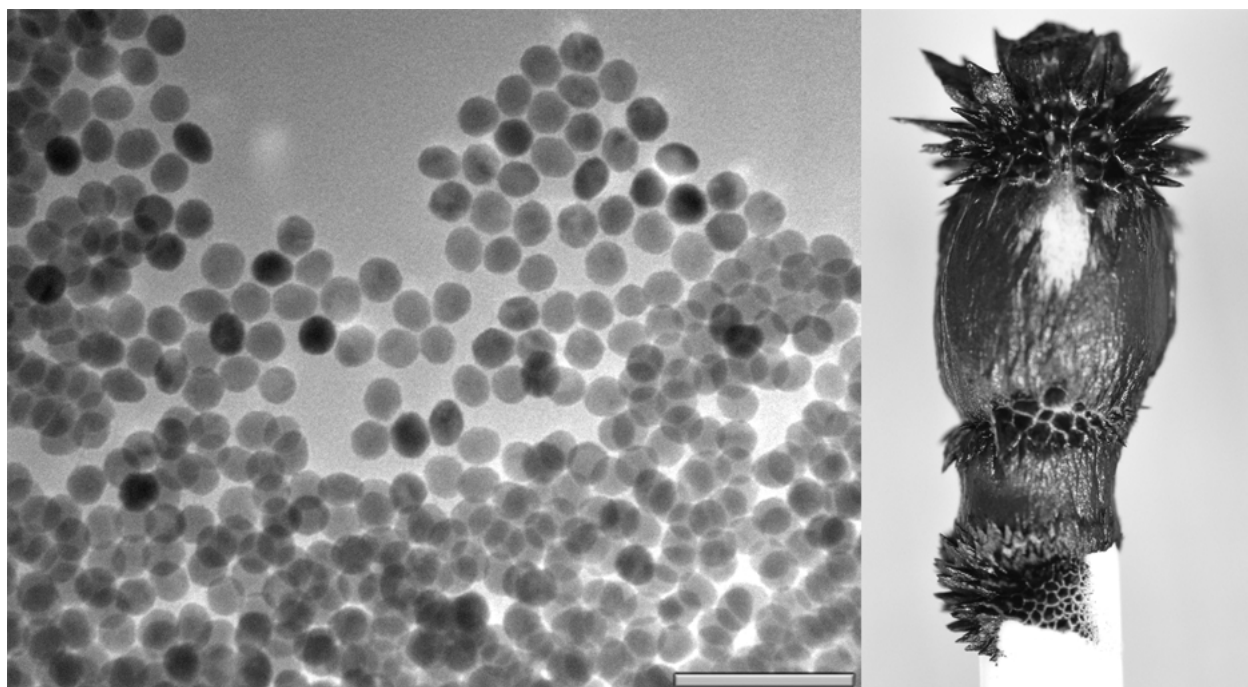


Figure 2.11: Electron micrograph and photograph of 20.9 nm maghemite iron oxide nanoparticles synthesized according to Method 3 [53]. **a)** Transmission electron micrograph showing 20.9 nm spherical nanoparticles with a shape anisotropy (scale bar = 100 nm). **b)** Photograph of a teflon coated magnetic stirring bean covered by these maghemite nanoparticles.

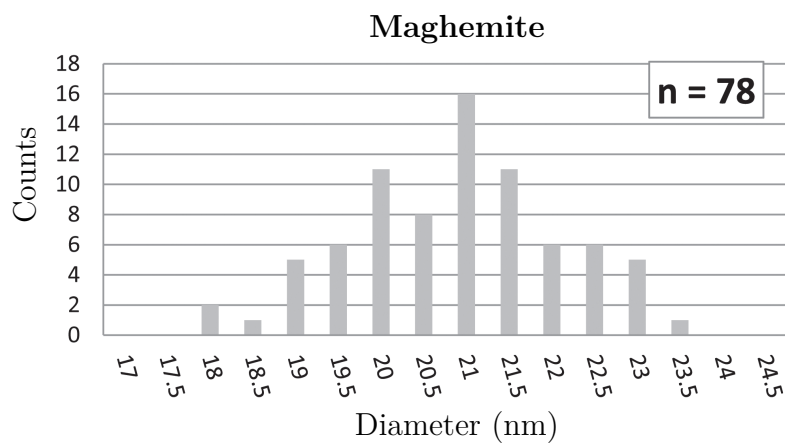


Figure 2.12: Size distribution graph of 20.9 nm spherical maghemite nanoparticles with shape anisotropy. The PD of the particles was 6 %. These particles were synthesized by the reduction of iron pentacarbonyl using trimethylamine oxide with the method proposed by Hyeon *et al.* [53].

2.5.2 Au nanoparticles (Method 4 & 5)

Gold nanoparticles were synthesized according to two different methods. However, one resulted in particles in polar solvents (Method 4), the other in apolar solvents (Method 5).

Turkevich *et al.*, Method 4

The best (monodisperse) batch of nanoparticles obtained with this method consisted of 16.4 nm gold nanoparticles with an SD of 1.8 nm (PD of 11 %). These particles were stable in the water phase and did not show sedimentation without centrifugation. An image of these nanoparticles is shown in Fig. 2.14 **a**, the corresponding size distribution graph is shown in Fig. 2.13 **a**. A drawback of this synthesis method is that it yielded low concentrations of particles since the initial H_{AuCl}₄ concentration had to be as low as 2 mM.

Brust *et al.*, Method 5

The method proposed by Brust *et al.* was explored to improve upon the PD and the concentration of the Au nanoparticles [65] as synthesized by previous methods such as described in Ref. [49, 64]. This method produced relatively monodisperse nanoparticles and particles made through this recipe were successfully used by Murray *et al.* for binary nanoparticle crystallization [77]. The initial H_{AuCl}₄ concentration used for the synthesis was 29.4 mM which was considerably higher than the concentration used for Method 4. The synthesis yielded 6.9 nm nanoparticles with an SD of 0.7 nm (PD 10 %) and is shown in Fig. 2.14 **b**. The corresponding SD graph is shown in Fig. 2.13 **b**. Three dimensional crystalline domains were observed in the sample after deposition even though this batch had a PD above 7 %.

Note that both methods resulted in significantly higher PDs compared to the spherical iron oxide and cobalt iron oxide nanoparticles presented earlier. It is true that for both these nanoparticle samples the PD can likely be significantly reduced by using size dependent precipitation, see e.g. Ref. [78], but this will lower the yield significantly as well. Possibly the methods need to be fine tuned for better results or different synthesis routes should be explored for the synthesis of Au nanoparticle with low PDs.

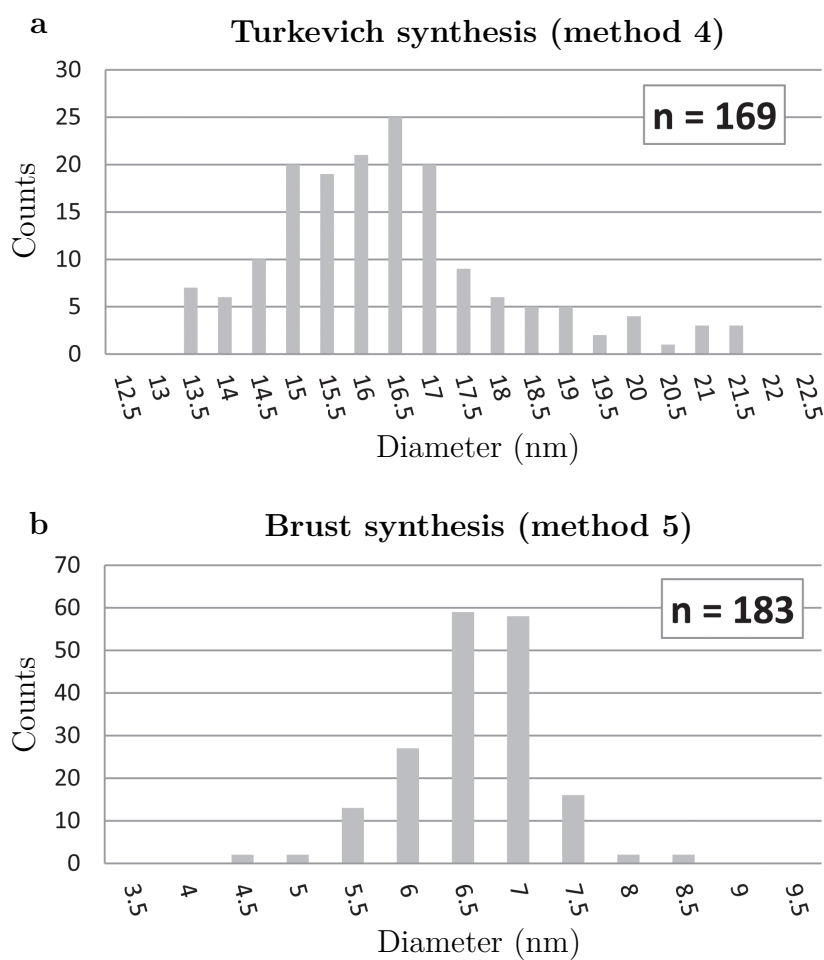


Figure 2.13: Size distribution graphs of gold nanoparticles synthesized with two different methods. **a)** 16.4 nm gold nanoparticles with a SD 1.8 nm, synthesized according to Method 4 [49]. **b)** 6.9 nm gold nanoparticles with a SD of 0.7 nm, synthesized according to Method 5 [65].

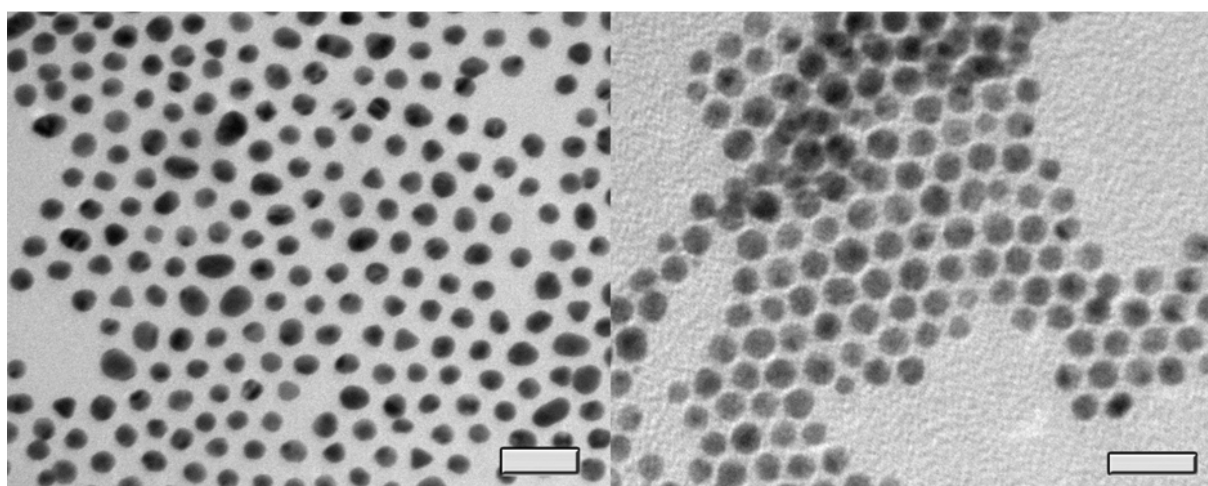


Figure 2.14: Transmission electron micrographs of gold nanoparticles **a)** gold nanoparticles synthesized according to Method 4 [49] (scale bar = 50 nm). **b)** gold nanoparticles synthesized according to Method 5 [65] (scale bar = 20 nm).

2.5.3 Semiconductor (CdSe@ZnS) nanoparticles (Method 6)

The synthesis of the batch of semiconductor nanoparticles shown here was performed according to Method 6 as proposed by Xie *et al.* [66]. The synthesis resulted in 12.4 nm QDs with an SD of 1.0 nm resulting in a PD of 8 %. The size distribution of this synthesis is shown in Fig. 2.15. These were orange in color and when excited with a 5 mW 305 nm laser emitted red light. The nanoparticles still exhibited this photoluminescence when exposed to air and when deposited on TEM-grids indicating that they remained chemically intact. These particles were used to make spherical assemblies which will be discussed in more detail in Ch. 7.

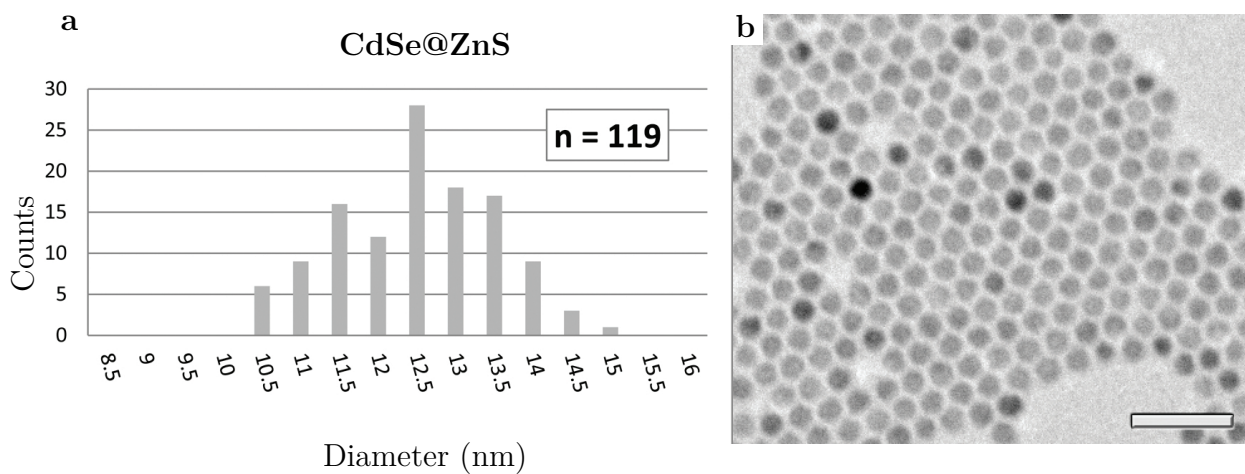


Figure 2.15: 12.4 nm CdSe@ZnS core-multishell quantumdots synthesized according to Method 6 [66]. **a)** Size distribution with an SD of 1.0 nm and a PD of 8 %. **b)** Transmission electron micrograph showing the particles in 2D ordering.

2.5.4 Synthesis of non-spherical nanoparticles (Method 2 b,c&d)

As mentioned before some control over the shape during the nanoparticle synthesis can be attained by changing the ligands. In this section the shape control of cobalt iron oxide nanoparticles is discussed. According to the authors the nanoparticles synthesized with their method possess a Wüstite crystal structure [54] which contains both cubic and octahedral facets for nanocrystals. In the synthesis of Ref. [54] oleic acid is used which likely coordinates in such a way to all facets of the nanoparticle during the synthesis that the resulting nano-crystals grew uniformly in all directions resulting in a spherical shape. Adding a ligand that coordinates significantly stronger to a specific facet will promote the nanoparticle to grow into a shape which contains the most of the inhibited facets. Adding sodium oleate cubic nanoparticles are expected and observed since the [100] facets are inhibited [54]. Adding tetraoctylammonium bromide, a positively charged ligand, resulted in octahedrally shaped nanoparticles, which would mean the [111] facet of wüstite was inhibited, similar as was observed for iron oxide nanoparticles [58]. Since we were curious what would happen if both the [100] and the [111] were inhibited, both ligands were combined which resulted in star shaped nanoparticles.

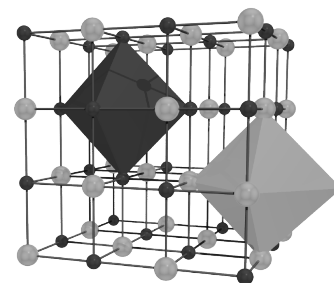


Figure 2.16: Schematic representation of a Wüstite crystal structure.

Cubic nanoparticles by addition of sodium oleate

Adding sodium oleate to Method 2 during the synthesis resulted in 13 nm cubic nanoparticles with a PD of 9 %, although with rounded corners, as shown in Fig. 2.17a, and are in accordance with the findings by Bodnarchuk *et al.* [54]. By increasing the amount of sodium oleate during the synthesis sharper, more pronounced 12 cubic nanoparticles with a PD of 11 % were obtained, Fig. 2.17b. This further indicates that the ligands influence the final shape of the particles. Interestingly a slight difference in packing behavior was observed when comparing sharp- and rounded cubes. In bilayers of 2D packed spheres the rounded cubes showed a correlation between, what are assumed, the top and bottom layer were ordered in the same direction at an offset. This was pervasive through each of the samples made with these cubes wherever two ordered layers were present, shown in Fig. 2.17c. In contrast, the sharp edged cubes did not show such a strong correlation between two ordered layers. Throughout the samples whenever multiple, generally two, layers were observed they were ordered at indiscriminate angles with no correlation between their adjacent top or bottom counterpart, see Fig. 2.17d.

Note that transmission electron microscopy is a 2D analysis technique. There is no distinction between nanoparticles on the top or bottom of the TEM grid support. A way of analyzing this would be by tilting the sample to high angles or by transmission electron tomography. However, if this would have been the reason for this difference in self-assembly behavior there would still have been some domains with clearly correlated ordering of the bilayers in the sample with the sharp edged cubes, and these were not observed.

Octahedral nanoparticles by addition of tetraoctylammonium bromide

Adding tetraoctylammonium bromide to Method 2 resulted in octahedral shaped nanoparticles as shown in Fig. 2.18a, b, and c. Where Fig. 2.18a shows an octahedral particle viewed from one of the sides and Fig. 2.18b viewed from one of the tips surrounded by several smaller octahedra. This showed that the octahedral shape of the intrinsic crystal structure was preferred over the cubic shape in these syntheses. Unfortunately PDs in all samples prepared using tetraoctylammonium bromide were well over 10% making them not suitable for crystallization experiments, Fig. 2.18c.

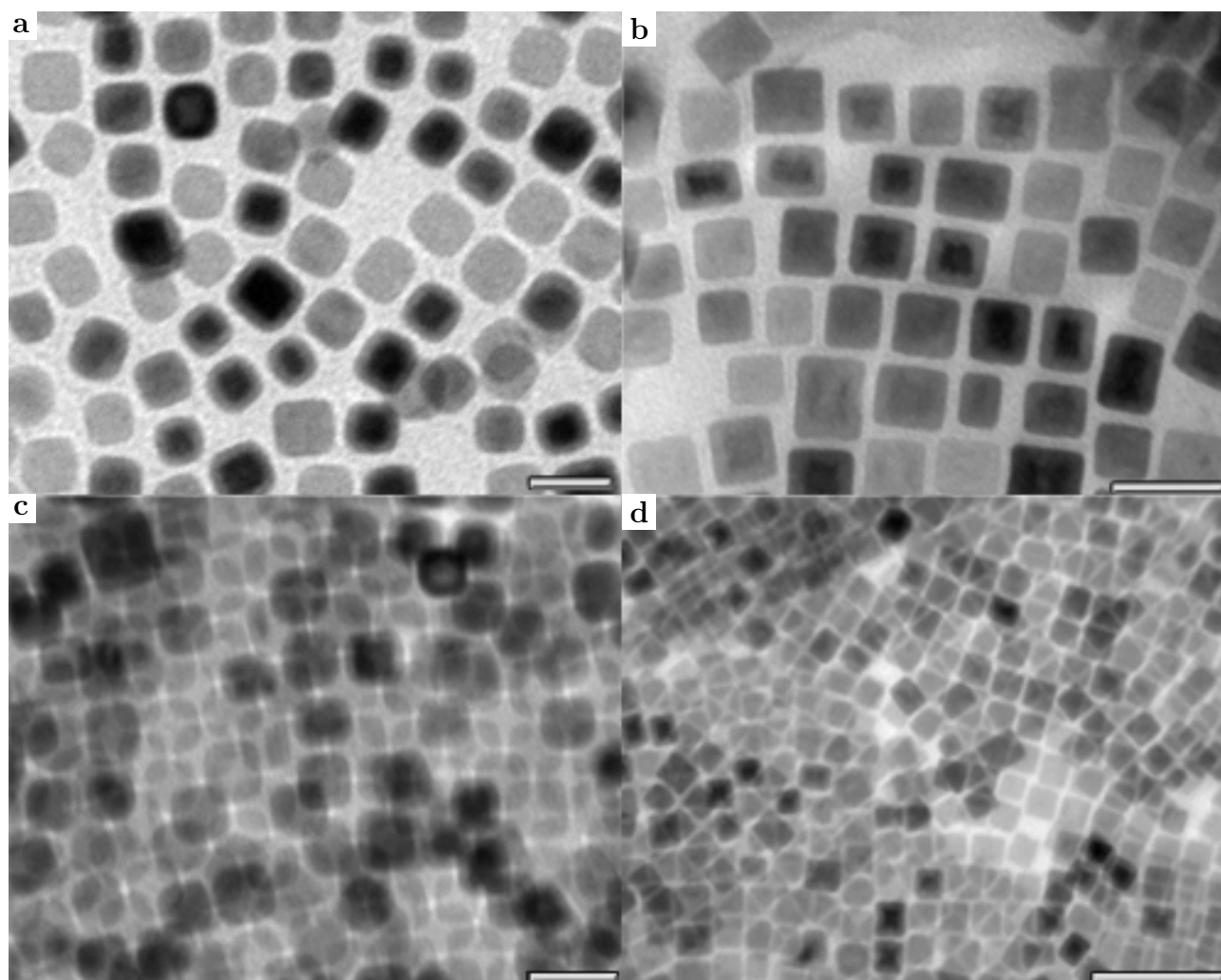


Figure 2.17: Transmission electron micrographs of cubic cobalt iron oxide nanoparticles synthesized according to Method 2b [54]. **a)** Rounded 13 nm cubic nanoparticles with a PD of 9 % (scale bar = 20 nm). **b)** Sharp 12 nm cubic nanoparticles with a PD of 11 % (scale bar = 20 nm). **c)** 2D ordered rounded cubic nanoparticles (scale bar = 20 nm). **d)** 2D ordered structure of sharp cubic nanoparticles (scale bar = 50 nm).

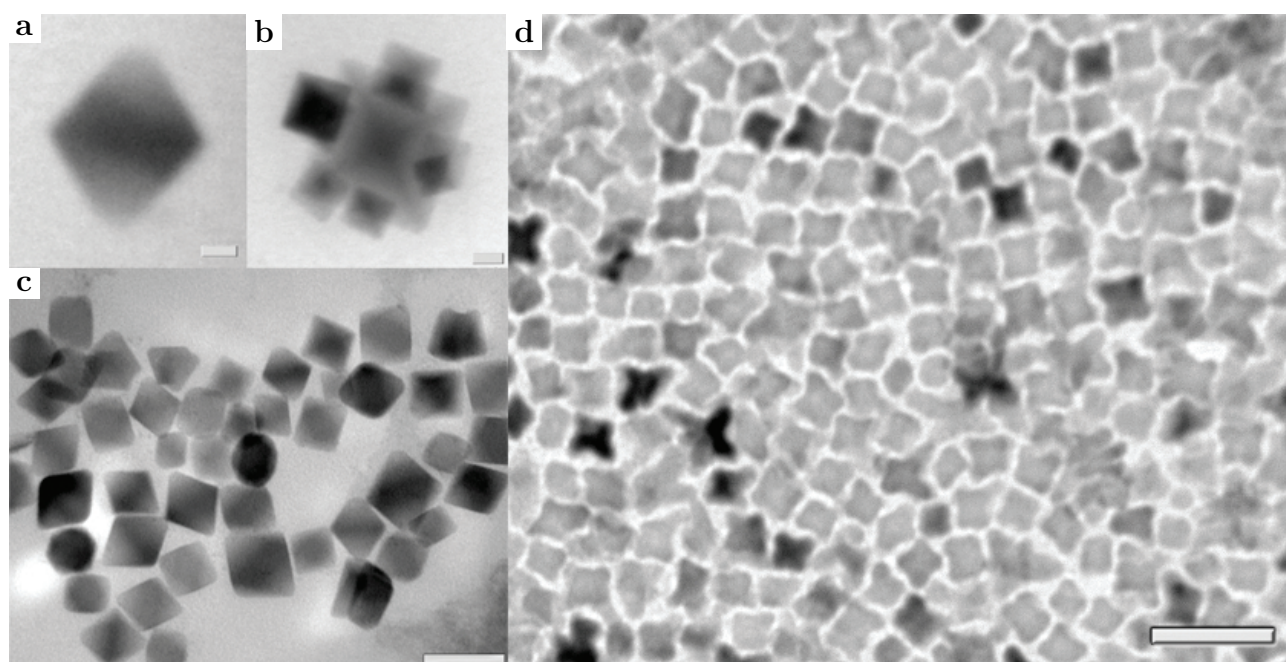


Figure 2.18: Transmission electron micrographs of octahedral and star-shaped cobalt iron oxide nanoparticles, synthesized according to a variation in stabilizing molecules used in Method 2 i.e. Method 2c. **a)** Octahedral nanoparticle viewed from one of the sides (scale bar = 20 nm). **b)** Octahedral nanoparticle viewed from one of the tips surrounded by six smaller particles (scale bar = 20 nm). **c)** Overview showing mostly octahedral nanoparticles with a high PD (scale bar = 50 nm). **d)** Star shaped nanoparticles made using both sodium oleate (cubic directing) and tetraoctylammonium bromide (octahedral directing) ligands during the synthesis, a variation on Method 2 i.e. Method 2d [54] (scale bar = 50 nm).

Star-shaped nanoparticles by adding two shape directing ligands, (Method 2d)

By adding both shape directing ligands, both the [100] and the [111] facets of the nanoparticles were likely inhibited, suppressing both the cubic and octahedral shape. This resulted in star shaped nanoparticles as shown in Fig. 2.18d. This shape could potentially be interesting for catalytic purposes due to the high surface to volume ratio with respect to the more common spherical and cubical shapes. The nanoparticles shown here have a mean diameter of 14.9 nm and an SD of 1.5 nm resulting in a PD of 10 % Fig. 2.19, although this of course is an approximation as one PD for this complex shape is not well defined. Star-shaped iron oxide nanoparticles have been observed before by O'Brien *et al.* [79]. However, not by using a combination of tetraoctylammonium bromide and sodium oleate but using pyridine n-oxide and oleic acid instead.

These findings combined show that indeed the ligands influence the shape of final nanoparticles during the synthesis. It is likely that inhibiting the growth of the facet is the mechanism with which these shapes are formed. An alternative mechanism, which could possibly be excluded by more accurate local chemical mapping than we had available to us at the time and therefore cannot be excluded at this time, is the incorporation of sodium or bromide ions into the crystal lattice preventing or modifying further growth. To determine which of these two mechanisms is really responsible further study will be necessary. What is clear is that by varying the coordinating ligands control over the shape can be attained albeit at the expense of monodispersity.

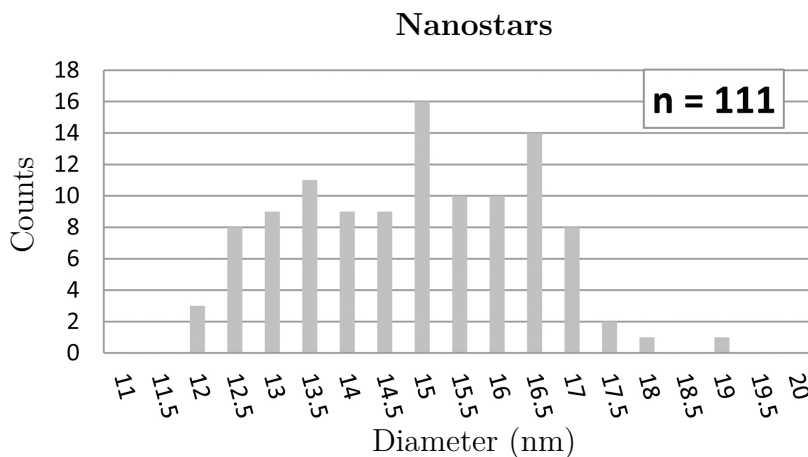


Figure 2.19: Size distribution graph of 14.9 nm nanostars with a PD of 10 % synthesized using Method 2d. Corresponding TEM image is shown in Fig. 2.18d.

2.5.5 High resolution TEM analysis of nanoparticles synthesized using Method 2a & b

For the cobalt iron oxide nanoparticles, synthesized according to Method 2, a core-shell intrinsic crystal structure was observed. As is shown in Fig. 2.20 where the cubic nanoparticles clearly show different attenuations for the inside and the outside. This is indicative of a core-shell structure with slightly different crystal lattices. According to the literature this difference is a 3° lattice mismatch between FeO (core) and CoFe_2O_4 (shell) [54]. At certain angles the interaction of the crystal lattice with the electron beam is different for the shell with respect to the core resulting in contrast differences between the inner and outer part of the nanoparticles. The angles at which these contrast differences are visible are small enough to appear and disappear during observation as a result of drift in the support, Fig. 2.21. In this figure the core or the shell can be seen as a darker attenuated part of the nanoparticles that disappears in the subsequent images. This suggests that all nanoparticles likely possess this core-shell structure but that this is only visible for a few particles at a time.

Using high resolution TEM to analyze these core-shell nanoparticles indeed showed highly crystalline structures, Fig. 2.22a [69]. However, this lattice mismatch between the core and the shell crystal structure could not be observed. In this figure the [400] and [040] lattice spacing of CoFe_2O_4 is highlighted in the position of the shell, and the [200] and [020] lattice spacing of FeO is highlighted in the core. The spacing was measured to be 0.22 nm which corresponds to half of the respective crystal lattices for Wüstite as discussed in table 2.1. In Fig. 2.22b a spherical cobalt iron oxide nanoparticle is shown with the crystalline structure visible together with the core shell structure. The core is darker for the same reasons as discussed earlier. This shows that the spherical cobalt iron oxide nanoparticles are mostly single crystalline, albeit for the core-shell structure, as well. A dark field image of the cubic nanoparticles is shown in Fig. 2.22c where the entire cubic particle is visible in the image, suggesting that there are crystalline domains that span the entire nanoparticle as they would otherwise not show up in a single dark field image of the nanoparticle.

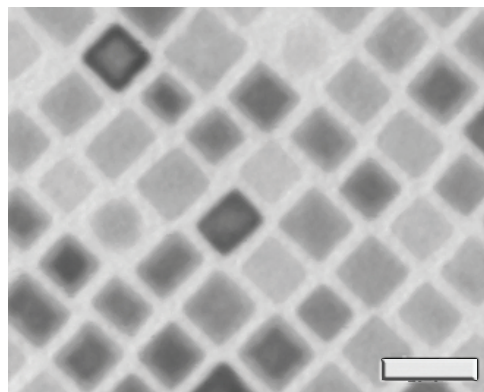


Figure 2.20: Cubic cobalt iron oxide nanoparticles exhibiting a core-shell structure, synthesized according to Method 2b.

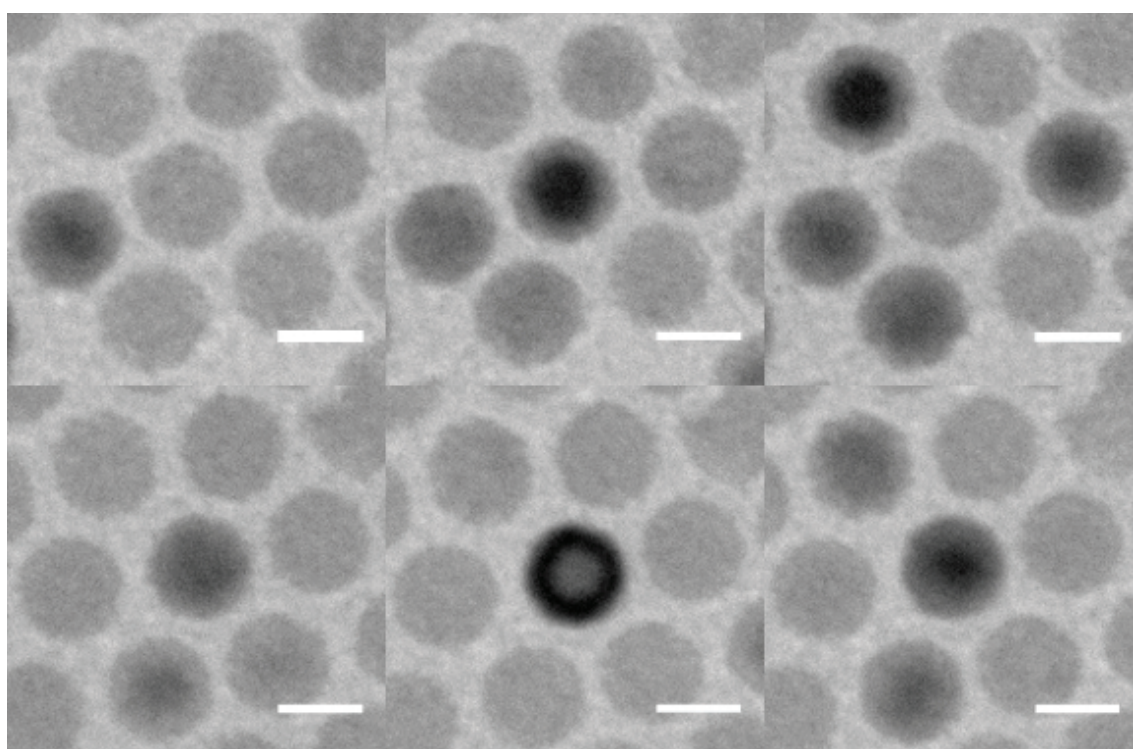


Figure 2.21: Transmission electron micrographs showing the contrast differences in the core and shell structure of 13.2 nm cobalt iron oxide nanoparticles (Method 2a), images are taken at several seconds interval with a drift in the sample (scale bars are 10 nm). *Note that the particle positions do not change with respect to these images.*

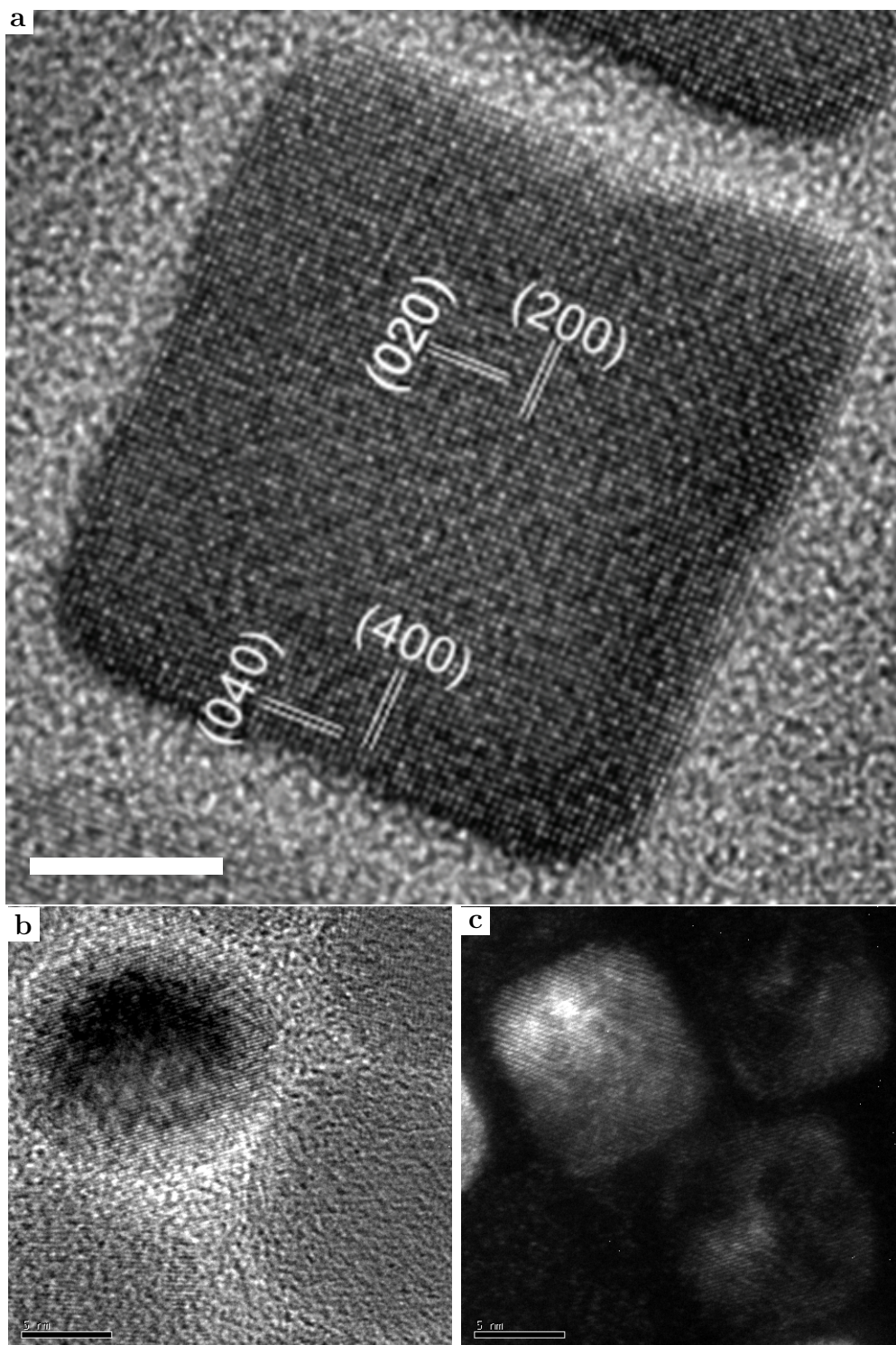


Figure 2.22: High resolution transmission electron micrographs (scale bars are 5 nm). **a)** Cubic cobalt iron oxide nanoparticle (Method 2b) showing the crystalline structure with the lattice spacings [040] and [400] for the CoFe_2O_4 lattice, and the [020] and [200] spacings for the FeO lattice highlighted, no lattice mismatch could be observed. **b)** Spherical particle (Method 2a) showing the crystalline pattern together with the light and dark gray of the core-shell structure. **c)** Dark field image of a cubic nanoparticle (Method 2b) showing single crystalline domains.

2.6 Conclusion and Outlook

In conclusion, nanoparticles consisting of iron oxide, cobalt iron oxide, gold, and cadmium selenite zinc sulfide were synthesized according to several published methods with sizes ranging from 6 nm to 38 nm. With PDs of <7 % for most spherical metal oxide syntheses, crystallization was readily observed on TEM grids and was therefore expected to also occur within spherical confinements. We also found that, when using a thermal decomposition method, the size of the nanoparticles was influenced by the reflux temperature of the solvents, although influences from the solvents other than reflux temperature cannot be excluded. These findings were in accordance with the results found by the initial authors of the method. We also found that limiting the reaction time for the metal oxide nanoparticles resulted in smaller diameters. In addition to controlling the size, it was found that the shape of the nanoparticles can be influenced by using different coordinating ligands during the synthesis. We found that cubic nanoparticles were formed when adding sodium oleate, octahedral particles when adding tetraoctylammonium bromide, and star-shaped nanoparticles when both ligands were added. The addition of the sodium oleate was presented in the original method, the use of tetraoctylammonium bromide instead of sodium oleate was not. These findings support the idea that the ligands, used to change the crystal shape away from spherical, anchor more strongly to specific crystal facets and reduce the local growth rate of this facet. We unfortunately also found that this resulted in higher polydispersities. We also observed a size dependence in the thickness of the oleic acid capping layer in cobalt iron oxide nanoparticles. Where in 2D ordered nanoparticles, as a function of particle diameter, this distance of nearest approach decreased.

From the high resolution transmission electron microscopy we also conclude that the synthesized metal oxide nanoparticles were mostly single crystalline, and that the lattice spacing was in close agreement with the reported crystal structures.

For the synthesis of gold nanoparticles we can conclude that a different method, or an alteration of the Turkevich *et al.* (polar medium) or Brust *et al.* (apolar medium) methods for gold nanoparticle syntheses is needed if a lower PD is desired, or that further fractionation e.g. such as in size selected precipitation steps are needed to obtain more monodisperse Au nanoparticles, see e.g. Ref. [78].

2.7 Acknowledgments

Hans Meeldijk, Marijn van Huis and Anil Yalcin are gratefully acknowledged for the high resolution TEM analysis of the FeO@CoFe₂O₄ nanoparticles, Carlos van Cats and Ben Ern  are thanked for their help on getting me started on the nanoparticle syntheses, Relinde Moes is gratefully acknowledged for performing the quantumdot synthesis and teaching me the method and Da Wang is thanked for helping with the cobalt iron oxide nanoparticle syntheses.

Supraparticle self-assembly

In this chapter we discuss the experimental methods we explored as ways halt the aggregation and growth of colloidal nanoparticle self-assemblies at a size still within the colloidal domain. Two promising methods, one involving slow drying of dispersed emulsion droplets the other a controlled aggregation into supraparticles (SPs) by inducing solvophobic attractions between the nanoparticle constituents, were taken from literature and investigated to examine which was most suitable in terms of size control and polydispersity (PD). The method with the best results, the technique using evaporating emulsion droplets consisting of oil dispersions of nanoparticles, was then optimized to obtain more control over the size and polydispersity (PD) of the SPs that resulted from the self-assembly and finally drying of the dispersions in the emulsion droplets.

3.1 Introduction

With the great advances that have been made in the recent years in nanoparticle synthesis and the characterization of their unique properties follows the search towards understanding their collective behavior and the subsequent fabrication of functional self-assembled nanoparticle superstructures. Such superstructures are already documented as sheets [80], binary superlattices [77] and supraparticles (SPs) [34, 36, 81]. Of particular interest to us are the SPs which can exhibit optical, magnetic and catalytic properties that differ both from the individual nanoparticles and their bulk assemblies [34]. In addition, if SPs are made monodisperse enough they in turn can be self-assembled into ordered structures, giving rise to hierarchical self-assembly [37]. This opens up the possibility of a powerful bottom-up fabrication method which mates the nanoparticle and SP properties with the characteristic properties of colloidal crystals. But to form hierarchical ordered structures, such as crystals of crystals of nanocrystals, SPs have to be made with a good control over their size, shape and PD. In this chapter we present our findings on nanoparticle self-assembly into SPs and how to control key factors such as size and PD.

To achieve self-assembled-systems for which the self-assembly can be stopped at a stage where the assembled structures are themselves still of a size within the colloidal domain, we explored initially, in preliminary experiments, two different processes described in literature: In the first process self-assembly was induced by increasing the osmotic pressure inside emulsions droplets made from a dispersion of nanoparticles and slowly letting the droplets shrink by evaporation [36]. The dried self-assembled SPs were rendered colloidally stable by the adsorbed surfactants and kept together by attractive van der Waals forces between the nanoparticles. In the second process solvophobic attractions between ligands on nanoparticle surfaces were induced by partially dissolving a second layer of surfactants on the nanoparticles in a polar dispersion medium containing a polymeric steric stabilizer which halted the self-assembly resulting in nanoparticle clusters [82].

The two methods that were explored, based on these processes, each utilized a different approach. The first method used nanoparticles dispersed in emulsion droplets of a low boiling solvent. The liquid-liquid interface functioned as a confinement and the volume fraction was increased by heating the system causing the droplet to evaporate [35]. The second method consisted of ligand stabilized nanoparticles, originally dispersed in chloroform, that were brought into a watery solution containing dodecyltrimethylammonium bromide (DTAB) as surfactant resulting in nanoparticles coated in a micelle of DTAB suspended in water. The nanoparticles were then injected into a solvent of a lower polarity (i.e. ethylene glycol) but still polar enough to be completely miscible with water, containing polyvinylpyrrolidone (PVP). The lower polarity caused the DTAB micelles to partially dissolve inducing nanoparticles aggregation through solvophobic interactions, the PVP molecules adsorbed on the aggregating nanoparticles sterically stabilizing the clusters [82].

In this chapter we will first compare results from both methods used to induce self-assembly, then different emulsification methods are discussed as a means to control the droplet size used for self-assembly in emulsion droplets. After this, a method for prediction the SP-size is described and an analysis of different sized SPs will be provided.

Finally, both of the presented methods include water in their self-assembly process which can pose a problem as nanoparticles such as CdSe and PbSe can react with water through photo-oxidation, quenching their photoluminescent properties [67]. For this reason we briefly looked into the possibilities of replacing water with an organic solvent and present here our preliminary results on making water-free emulsion droplets for nanoparticle self-assembly.

3.2 High Power sonication

In emulsions, for a constant volume, the inter-facial-area, and with it the inter-facial free energy, increases drastically with the decrease in droplet diameters as the number of droplets increase. This puts a limit on how small droplets in an emulsion can be made using classical mechanical emulsification techniques as the transfer of energy becomes less efficient at high energies. Ultrasonication, on the other hand, is a very effective method for making small ($d \ll 1\mu\text{m}$) emulsion droplets due to the generated, highly localized, extreme pressure fluctuations [83]. During ultrasonic emulsification as the diameters of the emulsion droplets decreases the surface free energy increases and the droplets become unstable and coalesce, while larger droplets have a higher probability of breaking up. This fusion and fission mechanism provides a natural limit to the size range of the emulsion droplets when using ultrasonic emulsification, resulting in relatively low PDs [84, 85]. In this chapter we will discuss both mechanical and ultrasonic methods for emulsification.

3.3 Droplet break-up of viscoelastic emulsions in a Taylor-Couette shear cell

For large ($>\sim 1\mu\text{m}$) and monodisperse emulsion droplets an emulsification method developed by the Bibette group [86–90], that uses droplet break-up of a viscoelastic emulsion in a Taylor-Couette shear cell, was chosen. This was a mechanical emulsification technique and for this purpose a rotor stator device was built with a small, 0.1 mm- 0.4 mm, gap spacing between the inner spinning rotor and the outer static cylinder, where the speed of the rotor could be varied from 0-7600 rpm. See Fig. 3.1 for a schematic representation of the shear cell, for an example of a Taylor-Couette shear cell in literature see [88]. By changing the rotor speed and the gap spacing the diameter of the resulting emulsion droplets could be set.

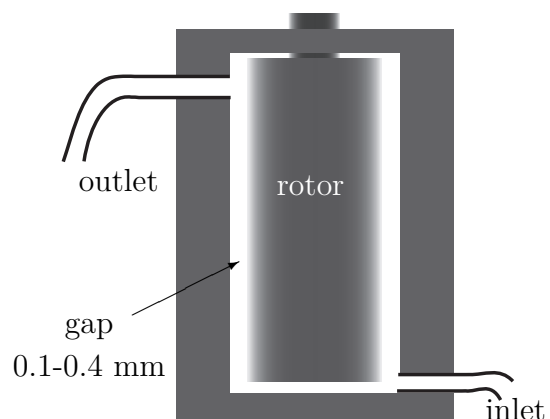


Figure 3.1: A schematic representation of a rotor-stator device with a 0.1 mm to 0.4 mm gap spacing.

Solvent	Viscosity mPa·s at 21 °C
hexane	0.313
cyclohexane	0.975
water	1.002
silicone oil	3.50

Table 3.1: Table showing the different viscosities of relevant liquids, the value for the silicon oil (poly(dimethylsiloxane)) was is taken from Ref. [87] where they mention they can change the viscosity by using different molecular weights (mol wt.) but fixed the viscosity at 3.5 mPa·s (the actual mol. wt. not mentioned).

To understand how such monodisperse emulsions can be formed in a viscoelastic emulsion it is important to understand how droplets are formed. However, describing the break-up of emulsion droplets due to shear is no trivial task [87–89]. The theory is usually limited to the rupturing of droplets in a viscous continuous medium at low shear velocities i.e. laminar flows where Reynolds numbers are low. In this low Reynolds regime the viscous forces play a larger role than inertial forces [91, 92] making predicting droplet break-up easier. The Reynolds number is given by Eq. 3.1:

$$Re = \frac{\rho v L}{\eta_e} \quad (3.1)$$

where Re is the Reynolds number, ρ is the density of the liquid, v is the speed of the rotor, L the gap spacing between the rotors, η_e the viscosity of the continuous phase. To deform a droplet the viscous shear stress of the continuous phase $\eta_e \dot{\gamma}$ must overcome the Laplace pressure $\sigma/r_{droplet}$ of the droplet. For an emulsion droplet to break-up, the capillary number (Ca), defined as the ratio between the shear stress $\eta_{eff} \dot{\gamma}$ and the Laplace pressure $\sigma/r_{droplet}$, must exceed a critical value of order unity [86, 93]:

$$Ca = \frac{\eta_{eff} \dot{\gamma} r_{droplet}}{\sigma} \quad (3.2)$$

Where $\dot{\gamma}$ is the shear rate, η_{eff} is the effective viscosity of the liquids (a combination of both the inner and the continuous phase), $r_{droplet}$ is the radius of the droplet prior to break-up, and σ is the surface tension. The shear rate $\dot{\gamma}$ is a function of the angular frequency ω in rotation per second (or the speed v of the moving plate) over the gap spacing L , in meters, between the moving walls:

$$\dot{\gamma} = \frac{2\pi r \omega}{L} = \frac{v}{L} \quad (3.3)$$

Where r is the radius of the spinning inner rotor.

However, for the self-assembly experiments the inner phase of the emulsion droplets was limited to low boiling organic solvents such as hexane (bp 68-69 °C) and cyclohexane (bp 80°C). Such solvents have low viscosities compared to the silicone oil used by Bibette and Mason (3.5 mPa·s) [86], see table 3.1. This means that according to Eq. 3.2 a higher shear rate is needed for a comparable droplet size, where on top of this the desired droplet size for self-assembly was typically even smaller than made by Bibette *et al.*. Both

a faster shear rate and a lower viscosity of the inner phase raises the Reynolds number to an estimated $Re = 1554$ (with: $\rho = 998 \text{ kg/m}^3$, $v = 15.6 \text{ ms}^{-1}$, $L = 0.0001 \text{ m}$, $\eta = 1.002 \text{ mPa}\cdot\text{s}$). The droplet break-up in such a system is much less predictable due to a more inhomogeneous shear flow and is likely to increase PDs. The Reynolds number can be lowered by increasing the viscosity of the continuous medium. For these experiments this was done by dissolving dextran in the water phase [94].

On a side note: Droplet break-up in viscous media typically results in the formation of small satellite droplets [95]. The formation of these "daughter" droplets has been studied and was found to be caused by an imbalance in capillary forces [96–98]. The volume of satellite droplets was found by Xiaoguang Zhang to be $<1\%$ V/V with respect to the parent droplet [97]. These satellite droplets were not taken into account when measuring the mean diameters since during a break-up up to ~ 19 small droplets per event can be created [95], and these droplets could readily be separated from the SPs by centrifugation [99].

3.4 Experimental Details

In this section the typical experimental details for the two different experimental methods is discussed. The nanoparticles used for this chapter consisted of either iron oxide or cobalt iron oxide capped with oleic acid. The effective diameter, based on the distances of nearest approach measured in section 2.5.1, was calculated for each of the nanoparticle sizes using table 3.2. The diameters of the spherical nanoparticles were estimated to be 7.2 nm (9.7 nm_{eff}) and 18.8 nm (19.8 nm_{eff}) for the iron oxide, 6.0 nm (8.8 nm_{eff}), 13.2 nm (14.6 nm_{eff}), 18.0 nm (18.8 nm_{eff}) and 38.8 nm (38.9 nm_{eff}) for the iron cobalt oxide. TEM images of these nanoparticles are shown in section 2.5.1.

Diameter	Nearest approach	Effective diameter
6.0	2.8	8.8
8.0	2.3	10.3
10.0	1.9	11.9
12.0	1.6	13.6
14.0	1.3	15.3
16.0	1.1	17.1
18.0	0.9	18.9
20.0	0.7	20.7

Table 3.2: Estimated effective diameters based on the distances of nearest approach in Fig. 2.10.

3.4.1 Chemicals & solvents

All chemicals were ordered from Sigma-Aldrich and used as received. Ammonium hydroxide solution (ammonia, $\sim 25 \text{ wt.}\%$ NH_3 , basis), chloroform (CHCl_3 , $\geq 99.5 \text{ wt.}\%$), cyclohexane ($\geq 99.8 \text{ wt.}\%$), Dextran from *Leuconostoc mesenteroides* (mol. wt. 1.500.000 g/mol - 2.800.000 g/mol), dodecyltrimethylammonium bromide (DTAB, $\geq 98 \text{ wt.}\%$), hexane mixture of isomers, methanol (absolute, HPLC), polyvinylpyrrolidone (PVP, average mol. wt. 40.000 g/mol), sodium dodecyl sulfate (SDS, $\geq 99.0 \text{ wt.}\%$), sodium silicate solution (reagent grade, $\sim 10.6 \text{ wt.}\%$ Na_2O , $\sim 26.5 \text{ wt.}\%$ SiO_2), tetraethyl orthosilicate (TEOS, 98 wt.%, reagent grade). For de-ionized water a Millipore Direct-Q UV3 reverse osmosis filter apparatus was used (18 M Ω at 25 °C).

3.4.2 Equipment

For the Taylor-Couette shear-flow a rotor-stator device was built [88–90] with variable inner rotor diameters of 39.75 mm, 39.55 mm and 39.15 mm, with gap spacings of $L=0.1$, 0.2, and 0.4 mm respectively 3.1. For optical analysis a Leica optical microscope with an Apo 63x oil immersion (NA=1.4) was used with a Nikon D90 digital camera and adapter lens. For TEM analysis a Philips Tecnai 12 with a tungsten tip as electron source was used, operating at an accelerating voltage of 120 kV. For high power sonication a Sonics Vibracell was used with a probe model CV33 at an amplitude of 23 %. For low power sonication a Branson 8510 sonic bath was used. The centrifuges employed for sedimentation were: a Heraeus Sepatech Labofuge Ae. For viscosity measurements an AND Vibro viscometer sv-10 was used.

3.4.3 Emulsion method: Self-assembly inside emulsion droplets

The nanoparticles used in this research were stabilized with oleic acid and as a result were stable in apolar solvents and did not disperse in water. By suspending the nanoparticles in an emulsion droplet of a low boiling solvent and heating the emulsion the nanoparticles were forced to self-assemble within the shrinking droplet as their volume fraction increased. According to Hoover *et al.* hard spheres will start to crystallize when the volume fraction reaches around 0.5 [13]. When the nanoparticles crystallize the curved interface acts as a hard spherical wall and affects the self-assembly as described in more detail in Ch. 6. See however also results of Ch. 5 where the nanoparticle shape and/or drying conditions of the emulsion influence the final SP shape that deviates from the shape of a sphere. This emulsion method was proposed by Li *et al.* in 2007 [35], who in their experiments self-assembled 6.9 nm BaCrO₄ and 9.8 nm Ag₂Se nanoparticles inside hexane droplets.

For a typical self-assembly experiment of nanoparticles into colloidal SPs 7 mg of 8.8 nm_{eff} cobalt iron oxide nanoparticles was dispersed in 1 mL of cyclohexane (approximately 0.3 volume % based on the effective diameter) and was added to 10 mL of de-ionized water containing 60 mg of SDS. The resulting mixture was then emulsified in either a Taylor-Couette-shear cell, by sonication or shaken by hand. The final emulsions was then heated to 68 °C and stirred for 4 hours evaporating the cyclohexane. In the experiments where dextran was used, 400 mg of dextran (mol. wt. 1.500.000 g/mol - 2.800.000 g/mol) was dissolved in the 10 mL of de-ionized water used for the continuous phase prior to adding the cyclohexane nanoparticle suspension.

3.4.4 Induced solvophobic attractions method: Solvophobic interactions in the presence of PVP

In a method proposed by Zhuang *et al.* in 2007, solvophobic interactions were utilized for controlled self-assembly [82]. Oleic acid capped iron oxide nanoparticles were encapsulated with an extra layer of the surfactant decyltrimethylammonium bromide (DTAB) forming a micelle around the nanoparticles and making them stable in the aqueous phase. The nanoparticles were then injected into an ethylene glycol solution containing polyvinylpy-

rolidone (PVP), which has a lower polarity than water. The mixture was then heated to 80 °C which caused the DTAB to dissipate and the micelles to break-up resulting in colloiddally unstable nanoparticles. These unstable nanoparticles aggregated forming SPs.

To self-assemble nanoparticles according to this method, a solution was prepared with a concentration of approximately 30 μM 19.8 nm_{eff} nanoparticles, synthesized as described in section 2.4 and presented in Ch. 2.5.1, in 1.0 mL of CHCl_3 . This solution was then combined with a 1.0 mL de-ionized water solution containing 65 mM DTAB. The chloroform was then evaporated by bubbling nitrogen through the solution for 3 hours which resulted in a clear nanoparticle suspension. The resulting mixture was then injected under vigorous stirring into a 20 mL counting bottle containing 5.0 mL ethylene glycol solution with 2.0 mM PVP (mol. wt. = 55000 g/mol). The mixture was then heated to 80 °C for 4 hours. The resulting SPs were isolated by centrifugation (Heraeus Sepatech Labofuge Ae at 100 rpm for 10 minutes) and washed prior to TEM analysis.

3.4.5 Making water-free emulsion droplets

Self-assembly of nanoparticles in oil-in-oil emulsion droplets was briefly explored where water was replaced by methanol (absolute). The methanol dissolved the cyclohexane inner phase, shrinking the droplets, forcing the nanoparticles to self-assemble similar to the emulsion method described in 3.4.5 but without heating and water-free. For a typical experiment 14 mg of 18.8 nm_{eff} nanoparticles was dispersed in 2 mL cyclohexane and injected at high force from a syringe into 100 % methanol containing 60 mg of SDS. The resulting colloidal suspension was allowed to sediment and was used as is for TEM analysis.

3.4.6 Silica coating of supraparticles

To coat SPs with silica, SPs were made according to the emulsion method described above but with the dextran substituted by PVP (mol. wt. 40.000 g/mol), using the same wt %, to provide an anchor layer for the silica [100]. The SPs were sedimentation and redispersed in 20 mL of de-ionized water. Then 5 mL of the SP-suspension was added to 80 μL of 0.54 wt.% sodium silicate solution and the mixture was left on a roller bank to react. After 4 days the reaction mixture was quenched by adding 7.5 mL of ethanol. The resulting silica layer on the SPs was grown further by taking 2.5 mL of the suspension, and 0.25 mL ammonia (25 % aq) and 25 μL TEOS was added. The reaction mixture was left to react for 3 days on a roller bank and the resulting suspension was washed by centrifugation (Heraeus Sepatech Labofuge Ae at 100 rpm for 10 minutes).

3.4.7 Sample preparation

For TEM grids 200 mesh copper grids were used with a ~ 25 nm thick Solutia support film carbon coated for ~ 7 sec using a Cressington 208 carbon coater. To prepare samples for TEM analysis ~ 3 μL of sample was deposited on a TEM grid and allowed to dry.

3.5 Results & Discussion

3.5.1 Arrested nanoparticle self-assembly

The first method, proposed by Zhuang *et al.* [82] and described in section 3.4.3, resulted in spherical SPs and hollow structures as is shown in Fig. 3.2a. The SPs were polydisperse and some shape anisotropy was observed for larger SPs. This method produced SPs with a mean diameter of 367 nm and a PD of 37 %. The resulting SPs were readily dispersible in water and showed colloidal stability. It should also be mentioned that if during this method not all the chloroform, used to create the nanoparticle micelles, is completely evaporated the complex procedure as described in Ref. [82] becomes a lot more like the emulsion method of Ref. [35].

The second method which was explored was the self-assembly of nanoparticles inside emulsion droplets as described by Bai *et al.* [35] and in section 3.4.5. As first emulsification method a sonic bath was used, which has a relatively low power sonication output compared to the sonic probe used later in this chapter. This method yielded SPs with a mean diameter of 90 nm, see Fig. 3.2b, with a PD of 23 %, which is lower than obtained with the previous method. Also, the SPs made with this method were easily redispersed in water and showed colloidal stability as well. The concentration used for this experiment was lower: 5 mg of nanoparticles in 2 mL of cyclohexane, which was initially done in an attempt to conserve nanoparticles.

However, some collapsed shells and hollow SPs were observed as well, as is shown in the right inset of Fig. 3.2b. These shell-like structures were typically observed for the larger SPs suggesting that not all cyclohexane was fully evaporated and more heating time was likely needed. From this we can derive that the evaporation may have been too fast. In addition, the concentration used for this initial emulsification experiment was lower, i.e. 5 mg of nanoparticles in 2 mL of cyclohexane. After this, based on these results and to prevent hollow structures from forming, the amount of nanoparticles was increased to 7 mg in 1 mL, as described in experimental section 3.4.3.

The emulsion droplet method of Bai *et al.* showed a lower PD than the micelle method of Zhuang *et al.* Together with an easier tune ability in droplet size (e.g. by shear stress) and a simple way of adapting the nanoparticle concentration, led us to choose the emulsion method to be further investigated for this chapter. However, it is interesting to note that a modified version of the method proposed by Zhuang, presented more recently, yielded interesting results, see Ref. [39]. In this article successful self-assembly of rods into anisotropic SPs due to solvophobic induced attractions was documented.

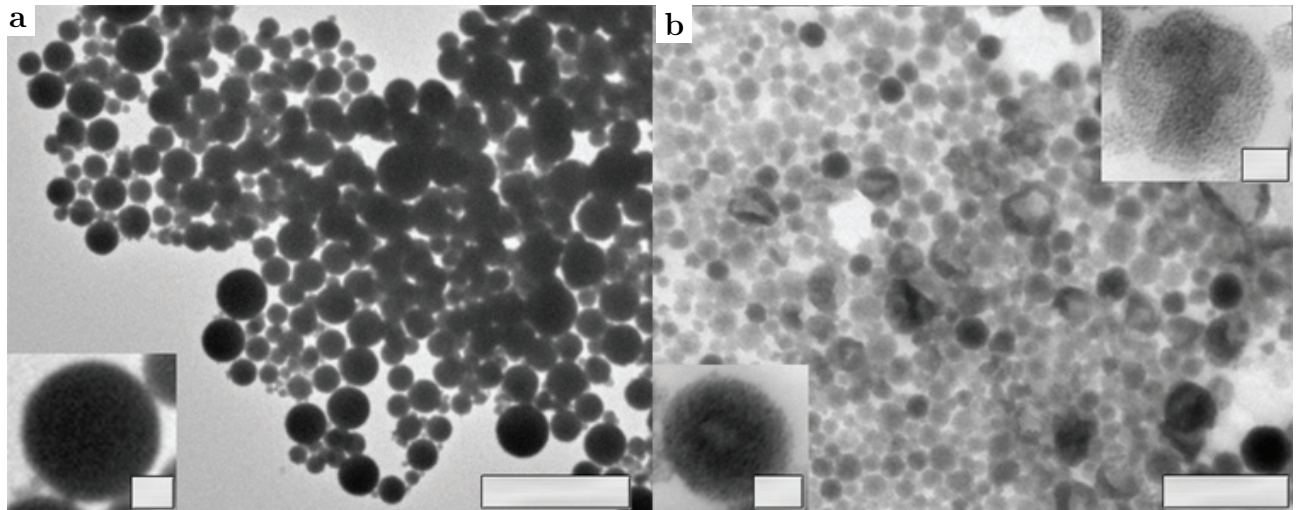


Figure 3.2: SPs made through self-assembly of iron oxide nanoparticles using two different methods. **a)** SPs with a PD of 37 % made through the induced solvophobic attractions method of Zhuang *et al.* [82] using 19.8 nm_{eff} nanoparticles (scale bar = $2 \mu\text{m}$), inset: enlarged SPs (scale bar = 200 nm). **b)** SPs with a PD of 23 % made in emulsion droplets according to the method of Bai *et al.* [35] using 9.7 nm_{eff} nanoparticles (scale bar = 500 nm), inset left: enlarged SPs, inset right: collapsed hollow shell of a nanoparticle adsorbed to the spherical interface (scale bars = 50 nm).

3.5.2 Different methods of emulsification

To explore the potential of this emulsion method several different emulsification techniques were explored. Shaking by hand as emulsification method was used as a reference to compare the results for each method with a PD baseline. The resulting SPs emulsified by shaking the oil water mixture by hand are shown in Fig. 3.4a. This resulted in a polydisperse (42 %) batch of $1.3 \mu\text{m}$ SPs. In addition, the majority of the sample consisted of hollow structures and broken shells.

Using high power sonication 132 nm SPs were obtained as shown in Fig. 3.4b, these clusters were larger than the SPs formed with a sonic bath, presented earlier, as a higher concentration of nanoparticles was used. These clusters were still small enough for the electron beam to have transmission through the entire cluster showing internal ordering suggesting a crystalline structure in the SPs. These SPs had a PD of 16 %, which is significantly lower than what was obtained by shaking the emulsion.

When using shear as an emulsification method, with a shear rate of $\dot{\gamma} = 1.56 \times 10^5 \text{ sec}^{-1}$ (7500 rpm), larger emulsion droplets were obtained compared to the high-power sonication and therefore resulted in larger 329 nm SPs as is shown in Fig. 3.4c. Furthermore, using this emulsification method resulted in a PD of 38 %. This was only slightly lower than the SPs made by shaking the emulsion by hand and significantly higher than the SPs from the sonicated emulsion. This could be the result of a turbulent flow in the shear cell since with a viscosity of water ($\eta = 1.002 \text{ mPa}\cdot\text{s}$) and a velocity of $v = 15.6 \text{ m}\cdot\text{s}^{-1}$ a Reynolds number in the turbulent regime is obtained as described in section 3.3 and Ref. [99]. To lower the Reynolds number the viscosity of the continuous water phase was increased by dissolving dextran, similarly as was done by the Bibette and Pine groups to create SPs consisting of only a few silica particles as described in Ref. [90]. When an emulsion with a dextran concentration of 40 mg/mL was sheared a batch of 753 nm SPs with a PD of 15 % was obtained which is a reduction of 23 % compared to the sample sheared without dextran. The resulting batch of SPs is shown in Fig. 3.4d. The size difference of these SPs is the result of the higher concentration of nanoparticles used for the sheared emulsion in dextran (5 mg/mL vs 7 mg/mL). An enlarged image of a SP from a similar SP assembly step is shown in Fig. 3.3. For that batch a lower concentration (5 mg/mL) of nanoparticles was used which resulted in smaller SPs, which allowed for better transmission electron microscopy analysis. On close examination an ordered internal structure was discerned together with a thin layer of low contrast (likely organic) material around the SPs. This thin layer was not observed in the SP syntheses without dextran. Therefore, it is likely

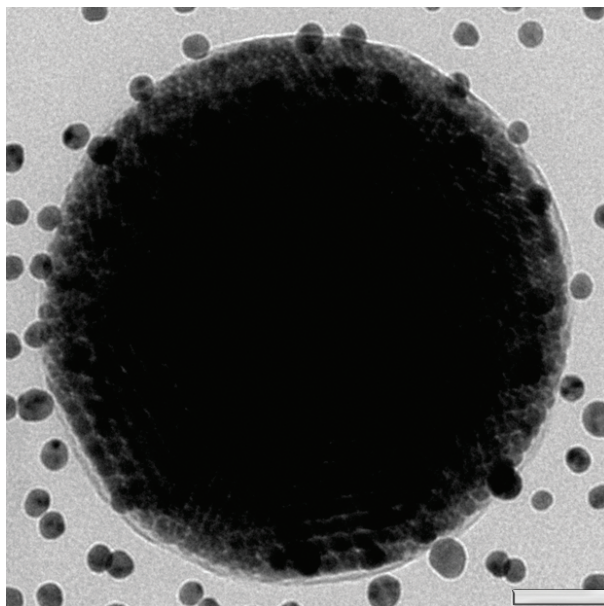


Figure 3.3: A spherical SP formed in a sheared emulsion with dextran and stabilized with SDS (scale bar = 50 nm).

that the dextran adsorbed to the surface of the SPs, in addition to modifying the viscosity, adding steric stabilization [55].

The size distribution (SD) graphs for each emulsification method are shown in Fig. 3.5. These graphs show that high power sonication resulted in a Gaussian SD, where this is less discernible in the shaken sample. The graphs of the sheared emulsions show a SD with a steep cut off for larger diameters, for these batches this cut off was at ~ 370 nm for **c** and ~ 1020 nm for **d**. These distributions can be improved by adding sedimentation steps to remove most of the smaller SPs.

To study this influence of the viscosity on the PD a series of mixtures with different dextran concentrations were sheared at 7500 rpm. The sizes of the emulsion droplets was measured and the results are shown in Fig. 3.6. This shows that increasing the dextran concentration did not significantly alter the mean diameter of the emulsion droplets, up to a concentration of 58 mg/mL at which the mean diameter was slightly reduced to < 3 μm . In contrast to the diameter, the PD of the emulsion droplets showed an immediate reduction upon addition of dextran. By adding dextran up to a concentration of 40 mg/mL a PD of 15 % was obtained, after which further increase in the dextran concentration showed no further decrease in the PD.

To determine at what viscosities the monodisperse (< 15 %) emulsions formed a series of water dextran mixtures were measured using a vibro viscometer, calibrated using water. Water mixtures were made containing 40 mg/mL (4 wt.%), 30 mg/mL, 20 mg/mL, 10 mg/mL and 0 mg/mL dextran (mol. wt. = 2.000.000 g/mol). The measured values were corrected for their respective densities using the values obtained from the ISCOTABLES handbook [101]. The resulting viscosities are plotted in graph 3.7. For a concentration of 40 mg/mL, at which the low PDs were found, a viscosity of $\eta = 6.6$ mPa·s was found. This would mean that the viscosity ratio P between the inner ($\eta = 0.97$) and the outer phase ($\eta = 6.6$) was $P = 0.15$ when the emulsions reach their lowest PDs. These findings agree with viscosity dependence of the PDs in emulsions found by Mabelle *et al.*, see Ref. [89], where the authors show a decrease in PD from 22 % to 17 % as the the viscosity ratio was lowered towards $P = 0.1$. However, their results do not explain the drastic decrease, from 32 % to 15 %, observed here, but this could be due to the higher PDs that were found in the experiments without dextran.

An additional factor which could influence the PD, as mentioned earlier, is the shear rate which, if high enough, becomes turbulent. For the concentration of 40 mg/mL, at which the lower PD starts, a viscosity of $\eta = 6.6$ mPa·s was found. This means that the Reynolds number for a typical emulsification experiment with 40 mg/mL dextran, sheared at 7500 rpm, with a gap of $L = 0.1 \times 10^{-3}$ m would be $Re = 236$. This is significantly lower than the $Re = 1554$ calculated for a similar experiment without dextran, resulting in a less turbulent flow regime [99], possibly explaining in part the high PDs difference in these experiments.

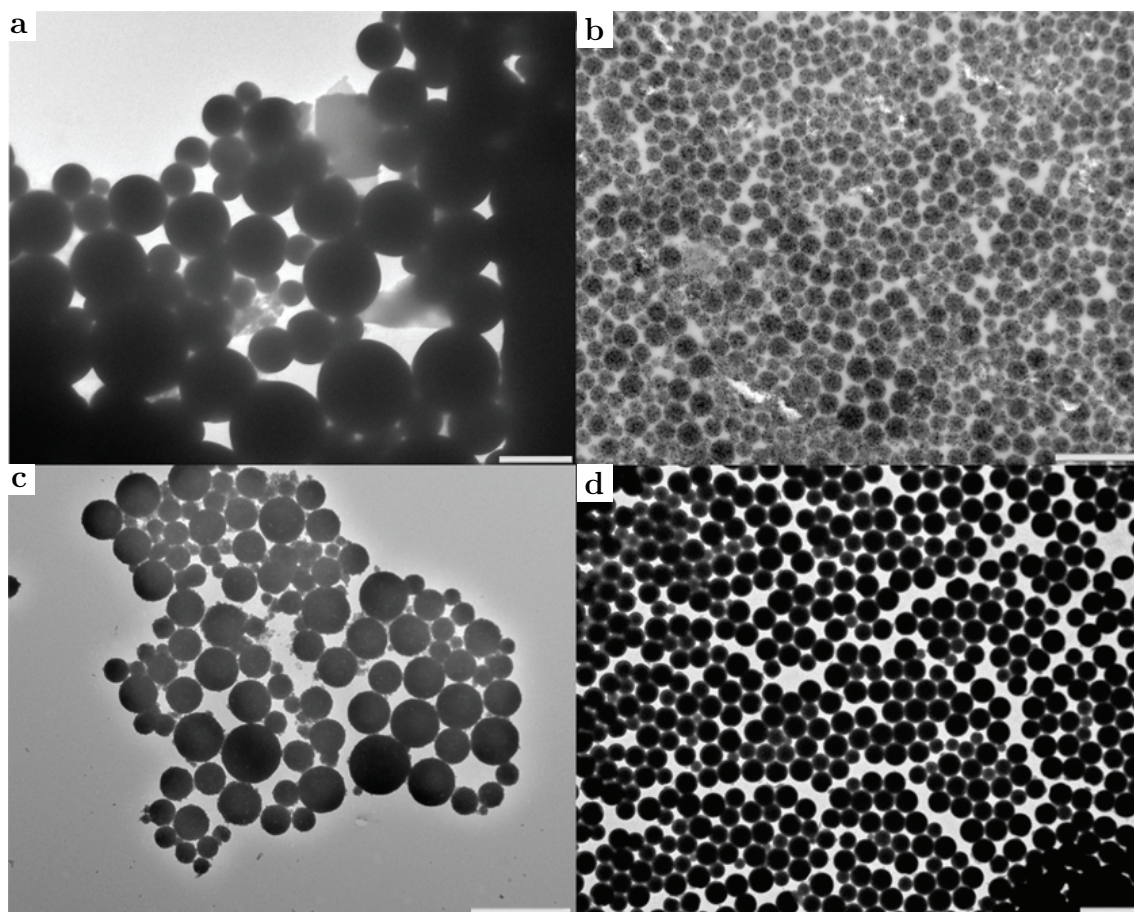


Figure 3.4: SPs formed in oil droplets made with different emulsification methods, for all methods shown here nanoparticles were dispersed in 1 mL of cyclohexane and added to 10 mL of water with sodium dodecyl sulfate (SDS). **a)** Cobalt iron oxide (7 mg/mL) SPs from a shaken emulsion (scale bar = 2 μm). **b)** Cobalt iron oxide (7 mg/mL) SPs from a sonicated emulsion (scale bar = 500 nm). **c)** Iron oxide (5 mg/mL) SPs made from a sheared emulsion (scale bar = 1 μm). **d)** Cobalt iron oxide (10 mg/mL) SPs made from a sheared emulsion with dextran (scale bar = 2 μm).

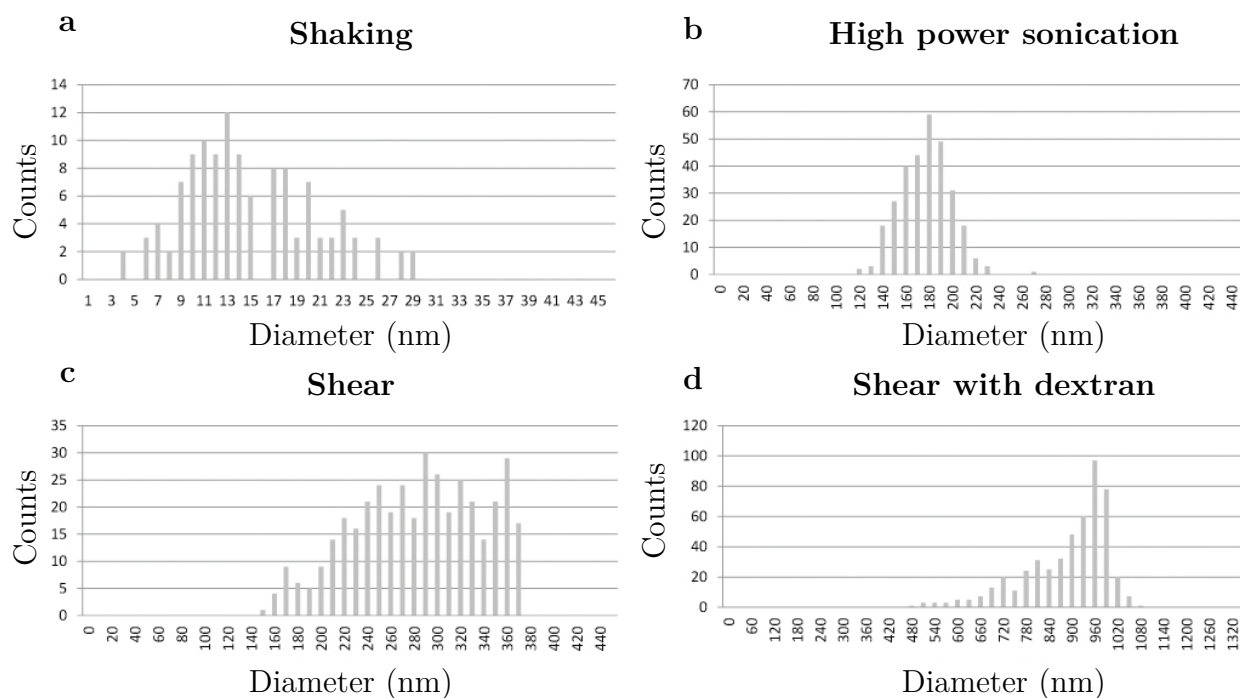


Figure 3.5: SD graphs comparing the distributions of supraparticles formed in emulsion droplets emulsified with four different methods. **a)** SP sizes from a shaken emulsion. **b)** SP from a sonicated emulsion. SPs made using the Bibette method for emulsification: **c)** without dextran and **d)** with dextran (40 mg/mL) [86].

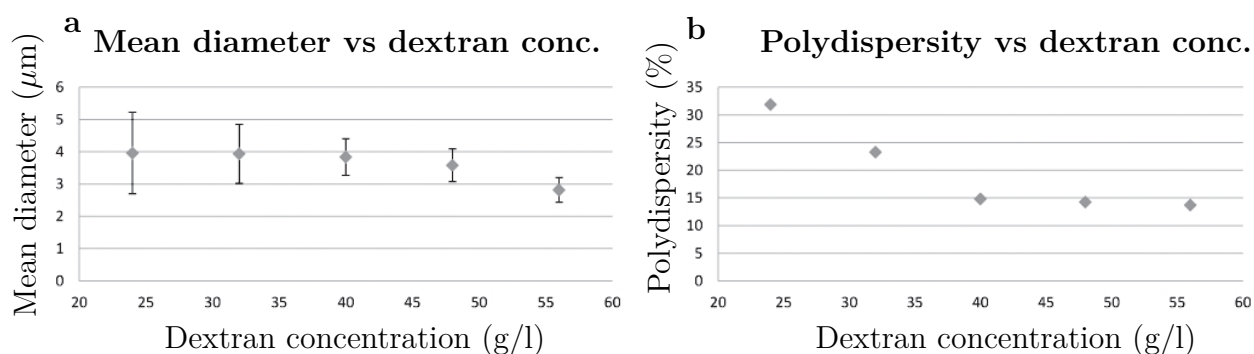


Figure 3.6: Graphs showing the effect of dextran on the size and PD of the emulsion droplets formed using a shear stress. **a)** The mean diameter as a function of the dextran concentration, error bars are the respective PDs, not the errors in the measurement. **b)** The PD as a function of the dextran concentration.

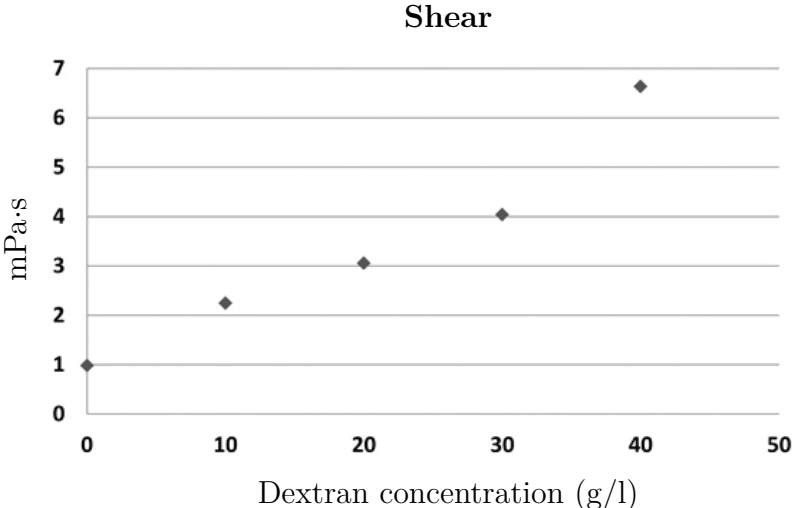


Figure 3.7: Graphs showing the viscosity of water in mPa.s as a function of the amount of dissolved dextran in g/L, as was measured using a vibro viscometer.

3.5.3 Supraparticle size prediction

As described here the emulsion droplets not only function as a spherical template for the self-assembly but also determine the size and PD of the final SPs. To gain more insight in this method, the predictability of the size of the SPs was studied. If we assume the number of nanoparticles per droplet remains constant throughout the experiment the final cluster size can be predicted based on the initial droplet size and the nanoparticle concentration. The amount of nanoparticles per droplet is a function of the nanoparticle concentration (c) and the droplet volume $V_{droplet}$.

$$n = cV_{droplet}. \quad (3.4)$$

Where n is the number of particles per droplet, c is number of particles per volume, $V_{droplet}$ is the volume of the droplets. The volume and diameter of the SP can then be predicted by:

$$V_{sp} = \frac{nV_{np}}{\phi} \quad (3.5)$$

Where V_{sp} is the volume of the SPs, V_{np} is the volume of the individual nanoparticles, and ϕ is the packing fraction of the individual nanoparticles. If we combine Eq. 3.4 and 3.5 we get:

$$r_{sp} = r_{droplet} r_{np} \left(\frac{4\pi c}{3\phi} \right)^{1/3} \quad (3.6)$$

Where r_{sp} is the radius of the SPs, $r_{droplet}$ the radius of the droplets, and r_{np} is the radius of the nanoparticles including the capping layer. With Eq. 3.6 we can now calculate the diameter of the SPs from the diameter of the initial emulsion droplets, which can be calibrated for the Bibette method [86–90]. For the packing fraction $\phi = 0.688$ was chosen, based on the calculations by Mackay for non-crystallographic dense packed spheres [102] and which is shown to be valid for nanoparticles interacting with a hard-sphere like potential and containing roughly less than 100.000 particles, as will be shown in Ch. 6. For larger SPs a value closer to the maximum packing density of hard spheres, is a better value. Then if we rewrite Eq.3.6 we get:

$$c = \frac{3\phi D_{sp}^3}{4\pi D_{np}^3 D_{droplet}^3} \quad (3.7)$$

To test if this holds true we first needed to understand how to control the size of the emulsion droplets. By varying the rotor speed in the Bibette method the size of the emulsion droplets could be set and since the PDs of these dextran emulsions was relatively low it was possible to compare the diameters. To test this a series (5) of emulsification experiments were performed where the rotor speed was varied from 3000 rpm ($\dot{\gamma} = 6.24 \times 10^4 \text{ sec}^{-1}$) to 7500 rpm ($\dot{\gamma} = 1.56 \times 10^5 \text{ sec}^{-1}$) with a gap spacing of 0.1 mm. The resulting droplet diameters were measured with optical microscopy and showed an exponential dependence on the rotor speed, see Fig. 3.8 and were in good agreement with the results found by Bibette *et al.* [86].

Note that the error bars show the standard deviation for each sample, not the error in the measurements.

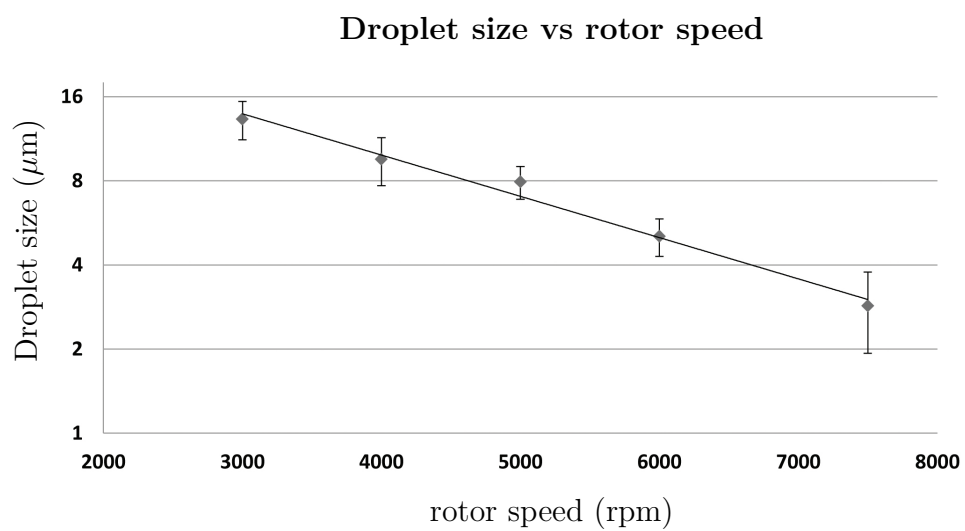


Figure 3.8: Droplet diameter as a function of rotor speed plotted in μm on a logarithmic scale, the error bars are the standard deviations of the droplet sizes.

To test equation 3.7 four dextran emulsions loaded with 7 mg/mL of 14.6 nm_{eff} nanoparticles were made and emulsified each with a different shear rate; $\dot{\gamma} = 1.56 \times 10^5 \text{ sec}^{-1}$, $\dot{\gamma} = 3.3 \times 10^4 \text{ sec}^{-1}$, $\dot{\gamma} = 2.3 \times 10^4 \text{ sec}^{-1}$ and $\dot{\gamma} = 1.8 \times 10^4 \text{ sec}^{-1}$. The resulting droplet diameters were measured using optical microscopy, and resulted in diameters of $3.8 \pm 0.4 \text{ }\mu\text{m}$, $5.1 \pm 0.9 \text{ }\mu\text{m}$, $7.6 \pm 1.3 \text{ }\mu\text{m}$, and $12.4 \pm 2.2 \text{ }\mu\text{m}$ respectively. After the inner phase was evaporated the sizes of the resulting SPs were measured using TEM, see Fig. 3.9. The smallest emulsion droplets with a mean diameter of 3.8 μm resulted in 557 nm SPs, the 5.1 μm droplets resulted in SPs of 795 nm and the 7.7 μm droplets resulted in SPs of 1228 nm. The largest emulsion droplets with a diameter of 12.4 μm did not result in SPs but formed broken shells/balloons covered in single, double or triple layers of crystalline packed nanoparticles instead. This was most likely the result of a too short drying time. We suspect that the nanoparticles at the outer layers form a solid/amorphous phase as a result of the fast drying of the droplet preventing correct SP self-assembly. Together with a larger volume which has to be evaporated, a much longer time in the heating step is thus likely needed to form the SPs. The results of the three successful SP syntheses were plotted against their diameter in Fig. 3.10.

Using the density of Fe₂O₃ (5,242 g/cm³) and oleic acid (0.895 g/cm³), considering a core diameter of 13.2 nm and a capping layer thickness of 1.4 nm, a weight of 6.7⁻¹⁸ g is approximated for the nanoparticles which would result in a concentration of $\rho = 1.05 \times 10^{18}$. Plotting this concentration in graph 3.8 using equation 3.7 showed that the SPs from the experiments turned out larger than the calculated size. This suggests that either the density of the nanoparticles was lower than what was assumed or, more likely, not all supraparticles were formed with a volume fraction of $\phi = 0.688$.

3.5.4 Small clusters

Since the SPs made with sonication were small (<150 nm), the ordered internal structure was readily observed using TEM and are discussed qualitatively similarly as in Ref. [41]. On close examination different crystalline patterns of dense packed 14.6 nm_{eff} cobalt iron oxide nanoparticles were discerned, as is shown in Fig. 3.11. Comparing the observed ordered structures with an icosahedral models of 5 layers of dense packed spheres (561 particles), built up as proposed by A. L. Mackay in 1962 [102], showed good correlations for each of the observed orientations. Comparing the proposed structure with the experimental clusters showed that typically nanoparticles seem to be missing from the corners, most likely, to better accommodate for the spherical confinement. Furthermore, this suggests that the nanoparticles in most of the clusters have the same internal ordering but only appeared different due to their orientation. Examining larger clusters formed by shearing instead of sonication showed similar ordering patterns, Fig. 3.12. After comparing these images with a larger model consisting of 7 shells (1415 particles) similar comparison was made, and again with particles missing from the corners of the SPs forming incomplete shells with respect to the icosahedral model. The ordering of nanoparticles inside SPs has been studied and described in more detail in Ch. 6, where by using tomography, particle tracking and simulations the internal structure was fully resolved.

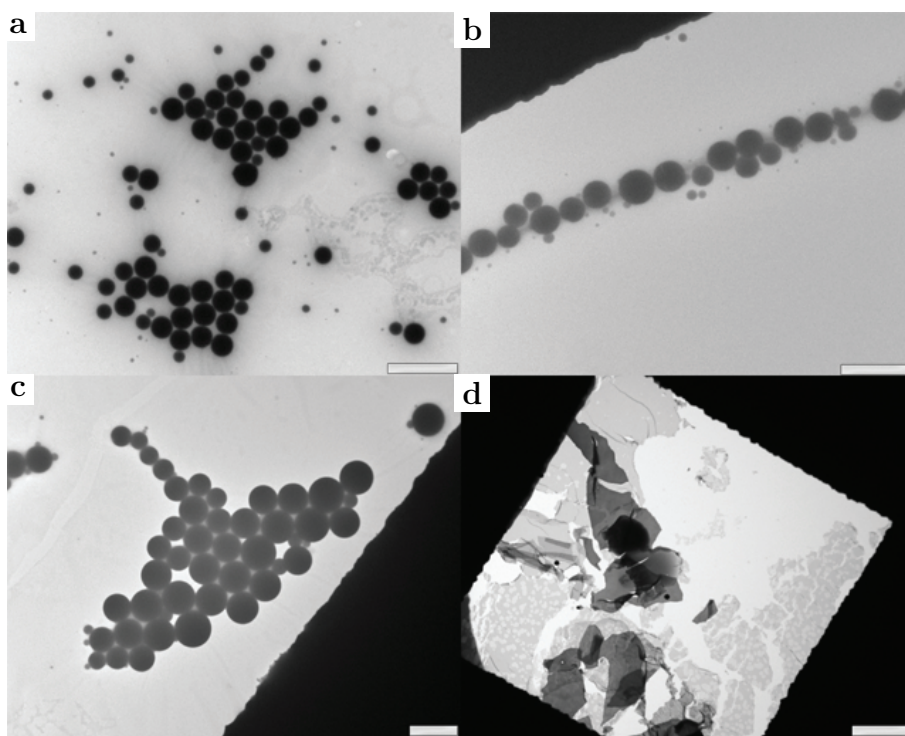


Figure 3.9: SPs of different sizes as a result of different emulsion droplet diameters made from 14.6 nm_{eff} cobalt iron oxide nanoparticles. **a)** 557 nm clusters with a SD of 96 nm and a PD of 17 % (scale bar = 200 nm). **b)** 795 nm clusters with a SD of 132 nm and a PD of 17 % (scale bar = 200 nm). **c)** 1228 nm clusters with a SD of 235 nm and a PD of 19 % (scale bar = 200 nm). **d)** Thin films with either one, two, or three layers of close-packed nanoparticles as a result of not fully evaporated emulsion droplets containing nanoparticles(scale bar = 10 μm).

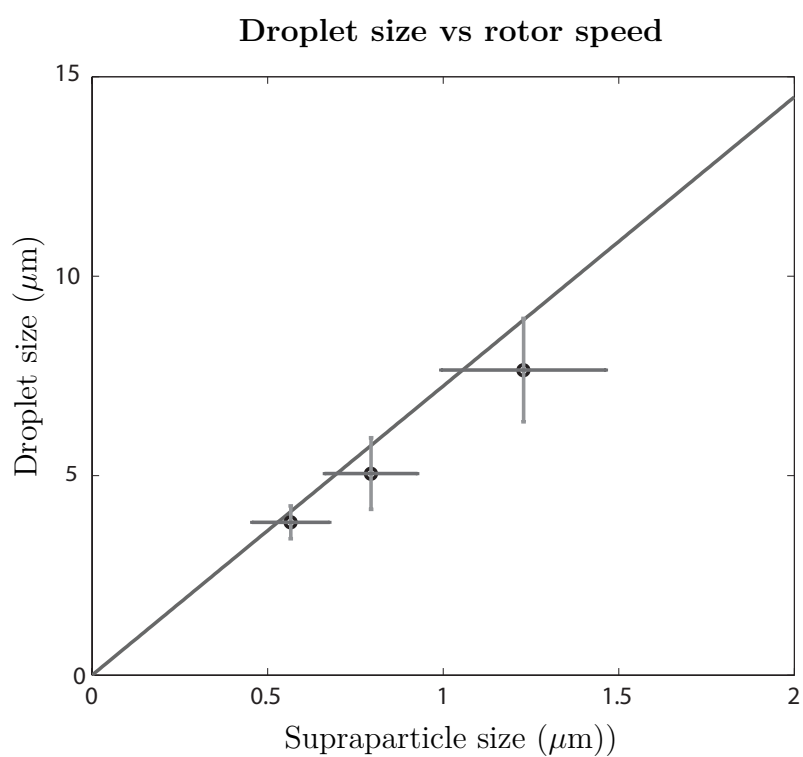


Figure 3.10: Plot showing the droplet size versus the final SP size self-assembled from 14.6 nm_{eff} cobalt iron oxide nanoparticles with a concentration of 2.1×10^{18} particles per liter, the error bars correspond to the SD. The line indicates where the supraparticles sizes should be for what droplet size according to equation 3.7.

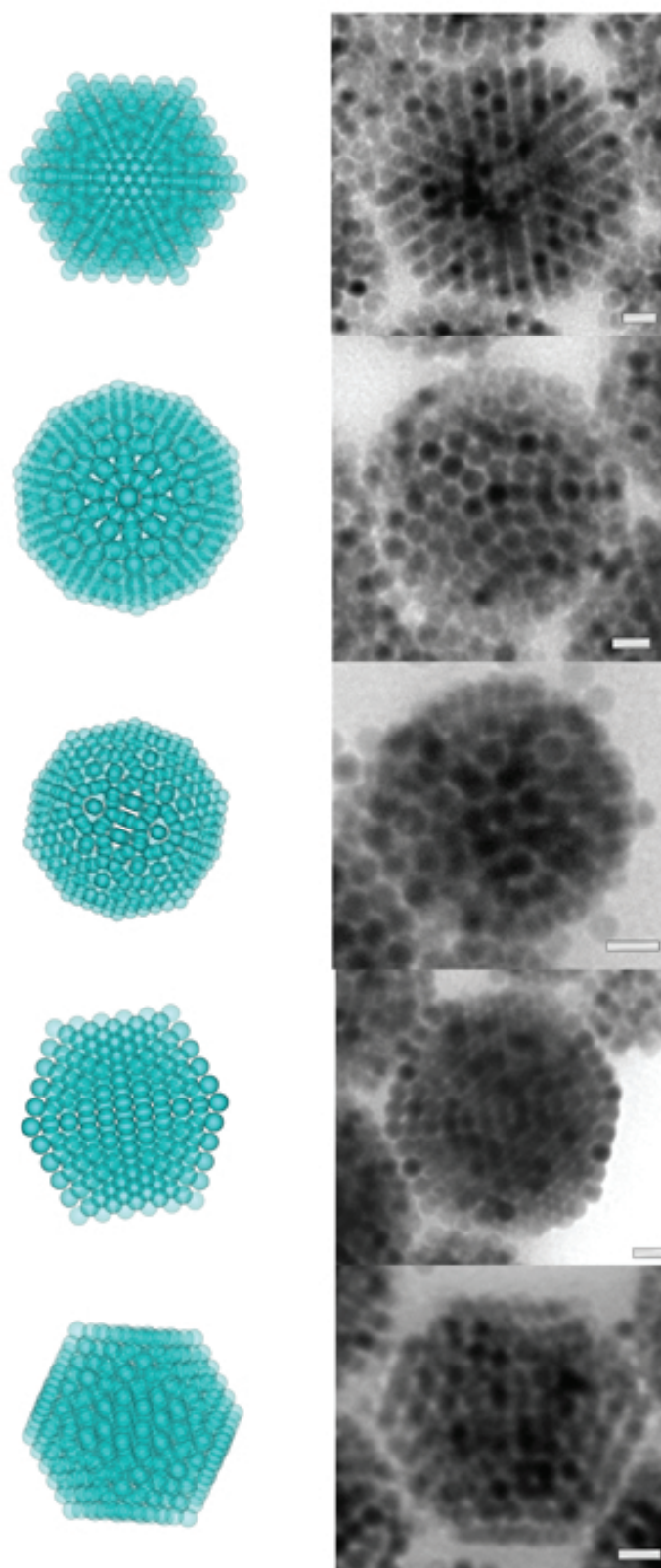


Figure 3.11: Model of a Mackay icosahedron at different orientations, paired with 14.6 nm_{eff} cobalt iron oxide nanoparticles self-assembled into SPs (scale bar = 20 nm).

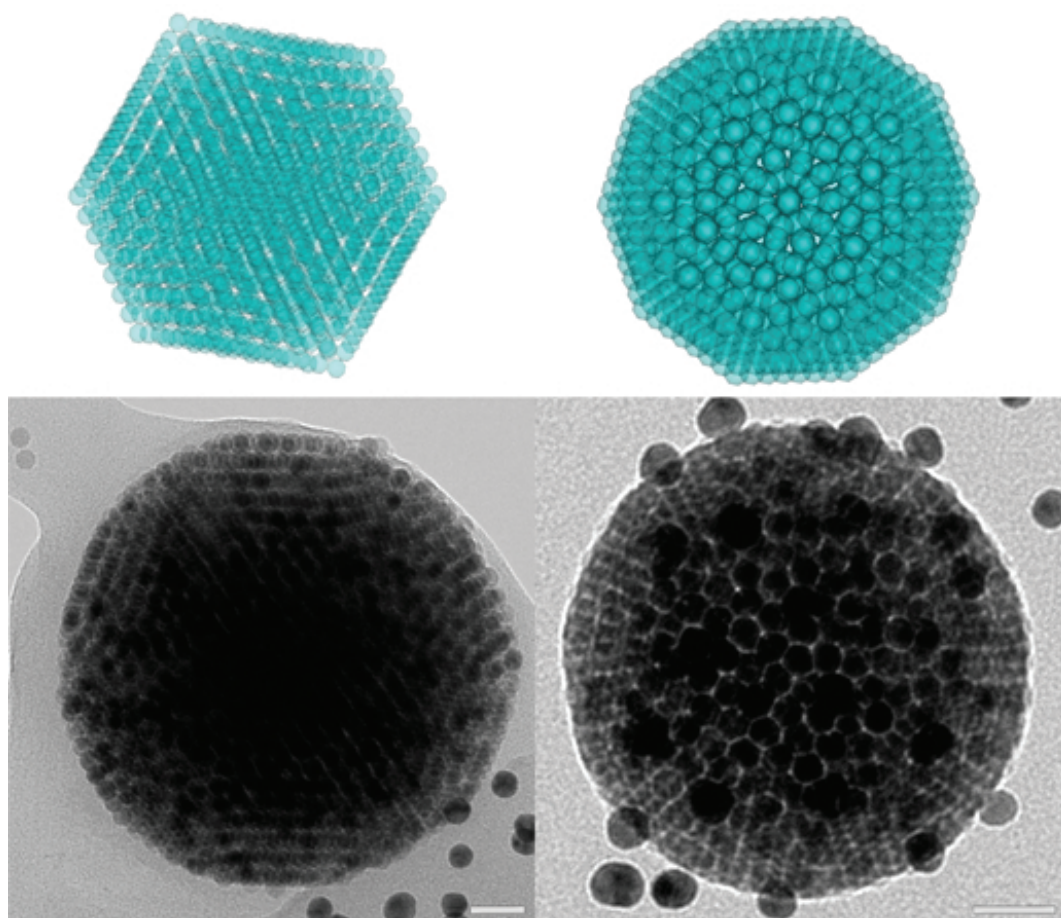


Figure 3.12: Large crystalline SPs built up out of 18.8 nm_{eff} cobalt iron oxide nanoparticles compared with an icosahedral model consisting of 1415 spheres. The nanoparticles visible alongside the SPs are gold markers used for tomographic analysis (scale bar = 50 nm).

By using larger nanoparticles with a diameter of ~ 38.9 nm_{eff} in the method with the sonicated emulsion, SPs with even fewer nanoparticles were made as is shown in Fig. 3.13. These clusters contained too few particles to form icosahedrons. These small clusters showed similar shapes for each cluster of the same size. The regular clusters showed the same packing when comparing the results found by Manoharan *et al.* for SPs made from micron-sized colloids [33].

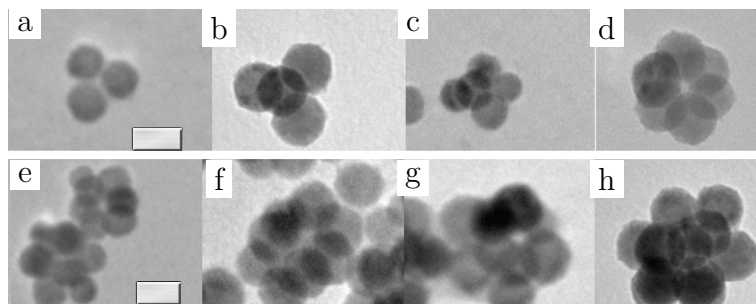


Figure 3.13: Small clusters of large (38.9 nm_{eff}) nanoparticles. **a)** Three nanoparticle cluster (scale bar = 50 nm). **b)** Four nanoparticle cluster. **c)** Five nanoparticle cluster. **d)** Six nanoparticle cluster. **e)** Seven nanoparticle cluster (scale bar = 50 nm). **f)** Eight nanoparticle cluster. **g)** Nine nanoparticle cluster. **h)** Eleven nanoparticle cluster.

3.5.5 Water-free emulsion method

To be able to apply this emulsion method to oxygen or water sensitive nanoparticles a different solvent combination was needed. To eliminate the water from the self-assembly process a hexane in methanol emulsion method was tested in preliminary experiments. When injected in methanol the hexane gets dissolved into the methanol resulting in the shrinking of the droplets. Since the inner phase of the emulsion droplets is more quickly dissolved the emulsion must be formed fast as well. Therefore, the nanoparticle suspension was injected at high force. However, this also resulted in a wide size distribution as is shown in Fig. 3.14. This method can be applied inside a glove-box since no water nor oxygen is present. Furthermore, this method does not require any heating making it more attractive for fluidics experiments as well. The downside of this method is the low control over the droplet size and the high speed at which the SPs were formed can prevent the system from reaching equilibrium and is therefore less likely to crystallize.

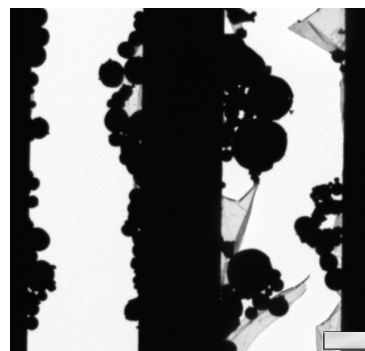


Figure 3.14: Supraparticles formed by injecting hexane nanoparticle suspensions in methanol with SDS (scale bar = 50 μ m).

3.5.6 Stability of colloidal supraparticles

The SPs made with the Bibette method and stabilized by dextran and SDS proved to be stable in water over the course of at least two years. When redispersed, the particles would sedimented slowly depending on their size, indicating colloidal stability. However,

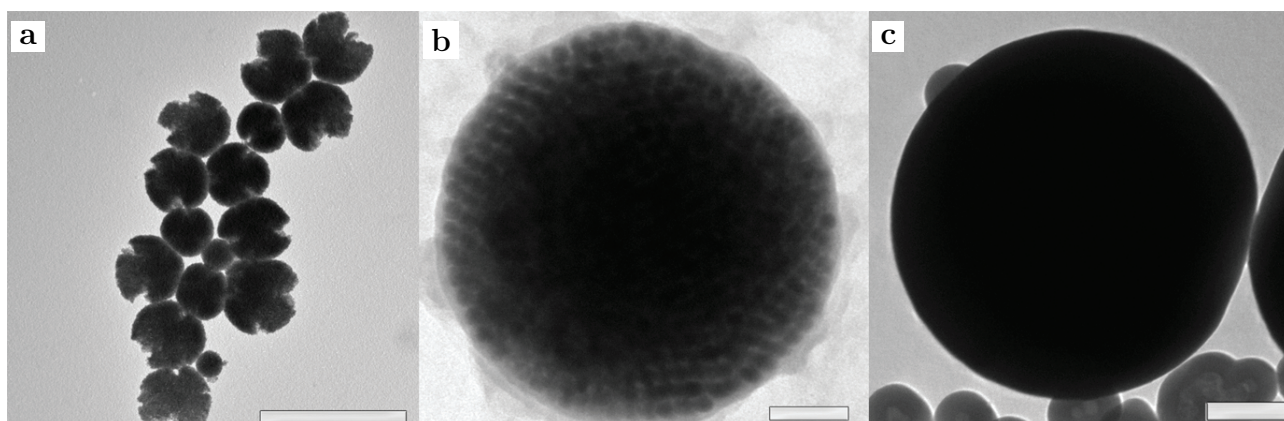


Figure 3.15: SPs made with the Bibette method dispersed in ethanol. **a)** Damaged dextran coated SPs as a result of ethanol (scale bar = 1 μm). **b)** Silica coated SP, made using waterglass, with no visible damage (scale bar = 50 nm). **c)** SP from the same batch but further coated with Stöber silica (scale bar = 200 nm).

washing the clusters too often with pure water resulted in flocculation. This was likely due to the removal of the surfactant in the suspension but could be reversed by adding SDS and slightly agitation, returning it to its original colloidal state. Adding ethanol as dispersion medium to the SPs caused them to break-up and deform immediately, as is shown in Fig. 3.15a. By replacing the dextran with PVP the SPs could be coating with silica using waterglass as described in the experimental details, and proposed by Graf *et al.* [100]. The resulting silica coated SPs did not break-up in the presence of ethanol and a layer of, what likely is silica was observed on the clusters as is shown in Fig. 3.15b. The SPs could consequently be grown larger using Stöber silica as described by [100]. The resulting SPs were increased in size from $\sim 220\text{nm}$ to $\sim 900\text{ nm}$, see Fig. 3.15c. This indicates that indeed silica can be grown on the particles further confirming that the layer observed in Fig. 3.15b is indeed silica as well.

3.6 Conclusions & Outlook

From the results in this chapter we can conclude that both methods selected from literature: slow drying of emulsion droplets and induced solvophobic interactions between the NPs, were successful methods for making SPs. The emulsion based methods were clearly more versatile and are less sensitive to exact details of solvents used and coatings on the NPs. Shaking by hand as emulsification method resulted in micron-sized SPs with a poor PD of 42 %. Whereas, using a sonic probe resulted in roughly ten times smaller supraparticles with highly ordered internal structures. These remarkable internal structure of the crystalline SPs resembled icosahedra of spheres, this is discussed fully in Ch. 6. Furthermore, the sonic probe resulted in a narrower size distribution than the shaking method with a PD of 16%.

Using a Taylor-Couette shear-cell to induce high shear rates in viscoelastic SDS stabilized oil in water emulsion systems using dextran as viscosity modifier resulted in a good control over the SP size and in a low PD of 15 %. We found that this lowest PD for this

method was reached with a dextran concentration of ~ 40 mg/mL. Further increasing the dextran concentration did not reduce the PD any further. These results were in agreement with the finding by Mabile *et al.* [89], except for the high PDs that were found for the emulsions with lower viscosities (no dextran). For this another explanation is needed, for example a turbulence in the shear flow, but is as of now not yet fully understood. Interestingly, the size of the emulsion droplets did not significantly change by adding dextran, only for high concentrations a slight decrease in diameter was observed.

We also found that calculating the SP-size from the emulsion droplets resulted in diameters close but slightly lower than the experimental values, and will be useful to predict the SP-size by choosing the right emulsification conditions and concentrations. It was found that by using this technique SPs consisting of tens of thousands of nanoparticles were formed while still exhibiting high degrees of order.

Using methanol instead of water resulted in emulsion droplets that formed SPs by dissolving the oils used, without heating, in a matter of seconds. This should be useful for water-sensitive nanoparticles, but is probably best slowed down by using partially saturated methanol solutions in follow up experiments to slow down the SP formation. Unfortunately, because of the high speed the size of the emulsion droplets was poorly controllable.

In future work it is also interesting to see how yet another way to arrive at monodisperse emulsion systems, microfluidics [103], can be used to make SPs with perhaps even narrower size distributions.

3.7 Acknowledgments

Simone Dussi is gratefully acknowledged for providing the Mackay cluster models, without these a comparison could not have been made. Marlous Kamp is gratefully acknowledged for her extensive research on coating SPs with silica, which I suspect will yield more nice results in the near future.

Tomographic Analysis of Anisotropic Colloids and Nanoparticle Supraparticles

In the following chapters the analysis technique of 3D electron tomography (ET) is extensively used to study self-assembled nanoparticle structures. With this technique transmission electron microscopy (TEM) images of a sample are taken over a wide range of angles from which a 3D representation of the object can be reconstructed with nanometer precision yielding detailed information on the packing, geometry and intrinsic structures. This chapter will introduce and present this technique in more detail for the 3D analysis of supraparticle (SP) structures built up from different types of nanoparticles, and for the 3D shape analysis of other colloidal model particles developed and intended to be self assembled. The colloidal systems that were analyzed for this chapter were: patchy colloids, block-copolymer stomatocytes, bowl-shaped and different kind of rod-shaped silica particles, binary superlattices, and spherical and cubical SPs.

4.1 Introduction

Electron tomography (ET) is a powerful 3D analysis technique where the high resolution of electron microscopy is combined with tomographic reconstructive algorithms to produce 3D reconstructions of objects with nanometer precision. This technique is typically used to study biological samples such as cells and their internal structure [104, 105], mitochondria [106], bacteria [107] but is also a suitable method to study the deposition of heterogeneous catalysts on supports [108]. But in more recent years this 3D imaging technique has found its way into soft-matter colloid science where it is now used to analyze for example: single, binary and ternary nanoparticle superlattices [109–111], large colloidal three dimensional gold nanoparticle assemblies [112, 113], the surface facets in gold nanorods with atomic resolution [114] and the self-assembly of silica coated micelles into unconventional mesoporous material [115].

In this chapter the methodology to study colloidal systems and their self-assembly behavior, which is as mentioned still only in its infancy in the analysis of structures relevant to colloid science, will be briefly explained. For a more detailed description on ET as an analysis technique the book "*The Radon Transform and Some of Its Applications*", and the chapter "*Introduction: Principles of electron tomography*" in the book "*Electron Tomography*" can be consulted [116, 117].

For this thesis ET was used to analyze several colloids that were interesting for self-assembly studies, nanoparticle assemblies and most importantly self-assembled nanoparticle SPs which are in turn amendable to further self-assembly steps themselves as well. With this method information on these colloids can be obtained with more detail than possible with conventional or confocal microscopy, which are powerful methods for quantitative 3D imaging of colloidal systems but lack the spatial resolution due to the diffraction limit [118–120].

4.2 Electron tomography in more detail

This 3D reconstructive technique had its greatest impulse when Hounsfield invented an 3D X-ray scanner for which he, together with Allan Cormack, received a Nobel prize in Physiology or Medicine in 1979. This technique is now widely used in medical diagnosis in the form of computer tomography (CT)-scanners. However, the mathematical framework for this technique stems from a paper published by Johan Radon in 1917 [121] who designed the theoretical basis for what is now known as the Radon transform. Radon also proposed an initial solution for the inverse transform which is needed to reconstruct the object from the Radon transform. ET was also greatly helped by the invention of the charge-coupled device (CCD) camera in 1983 [122], and the onset of digital data storage and increased computing power. Due to these developments the ET reconstructive technique rapidly developed into its own field of research [123].

As mentioned, ET and other tomographic reconstructive techniques are, in principle, based on the same mathematical framework where an object can be reconstructed using an inverse of the Radon transform. To describe the Radon transform for transmission electron microscopy (TEM), the process that forms the projection images must first be described mathematically. A single TEM image taken at angle θ is a projection made up out of a series of line integrals along angle θ passing through the object of interest. The line integrals describes the total attenuation (decrease in intensity) of the electron beam as it passes through the object. This integral is taken for each position on x' which results in the projected image $P_\theta(x')$. The attenuation for the electron beam through typical material occurs exponentially which can be described by the Beer-Lambert law. To show how this works let us consider a simple 2D object that can be described using a function dependent on x and y i.e. $f(x, y)$. The interaction of the electron beam with the material of that object can now be described as follows:

$$I = I_o \exp \left(- \int f(x, y) dy \right). \quad (4.1)$$

where I is the intensity of a single point on the projection along an angle of 0° . This point in the projection is taken for each point on x :

$$P(x) = \ln(I/I_o) = - \int f(x, y) dy \quad (4.2)$$

where $P(x)$ is the projection of $f(x, y)$ at an angle of 0° . To incorporate the tilting of the stage a tilted axes frame can be used:

$$P_\theta(x') = - \int f(x, y) dy' \quad (4.3)$$

where x' and y' are the tilted axes at angle θ described by:

$$\begin{bmatrix} x' \\ y' \end{bmatrix} = \begin{bmatrix} \cos \theta & \sin \theta \\ -\sin \theta & \cos \theta \end{bmatrix} \begin{bmatrix} x \\ y \end{bmatrix} \quad (4.4)$$

Now Eq. 4.3 can be rewritten as:

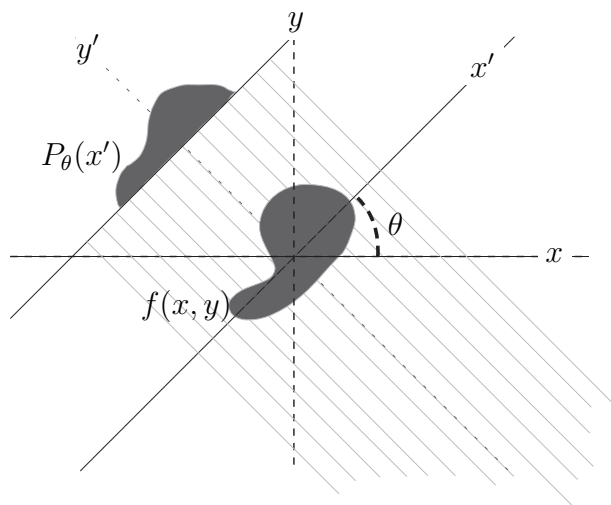


Figure 4.1: Schematic representation of a 2D object, described by a function $f(x, y)$, interacting with the incident electron beam where x' and y' are the axes of the tilted reference frame at angle θ . $P_\theta(x')$ is the integral over y' at position x' .

$$R_\theta(x') = \int_{-\infty}^{\infty} f(x'(x, y), y'(x, y)) dy' \quad (4.5)$$

This is known as the Radon transform with which the original object $f(x, y)$ can be reconstructed using an inverse of the radon transform based on the Fourier inversion theorem [124]. That the original object can be reconstructed from projection by using a solution for the inverse transform is proven by the projection slice theorem [125] that states: if a two dimensional object is projected onto an one dimensional line, the 1D Fourier transform of this line is equal to the 2D Fourier transform of a slice of the two dimensional object:

$$F_1 P = F_2 S \quad (4.6)$$

Here F_1 and F_2 are the 1- and 2- dimensional Fourier transform operators, and P is the projection and S is the slice of the two dimensional object. A short proof for the project slice theorem is given here. For ease of calculation again a two dimensional object will be considered. Let $f(x, y)$ again be the object. The projection p along the y axis is similar to Eq. 4.2 and can be written as:

$$P(x) = \int_{-\infty}^{\infty} f(x, y) dy \quad (4.7)$$

The Fourier transform of $P(x)$ results in:

$$F(k_x, k_y) = \int_{-\infty}^{\infty} \int_{-\infty}^{\infty} f(x, y) e^{-2\pi i(xk_x + yk_y)} dx dy \quad (4.8)$$

of which a single slice $S(k_x)$ is

$$S(k_x) = F(k_x, 0) = \int_{-\infty}^{\infty} \int_{-\infty}^{\infty} f(x, y) e^{-2\pi i x k_x} dx dy \quad (4.9)$$

by substituting Eq. 4.7 in Eq. 4.9 we get

$$S(k_x) = \int_{-\infty}^{\infty} P(x) e^{-2\pi i x k_x} dx \quad (4.10)$$

which, in turn, is the Fourier transform of $P(x)$. Thus proving that $F_1 P = F_2 S$ and that the 1D Fourier transform of a projection is equal to the 2D Fourier transform of a slice of the object. Therefore, the object can be reconstructed from projection data. This theorem is also true for higher dimensions and can be applied as such.

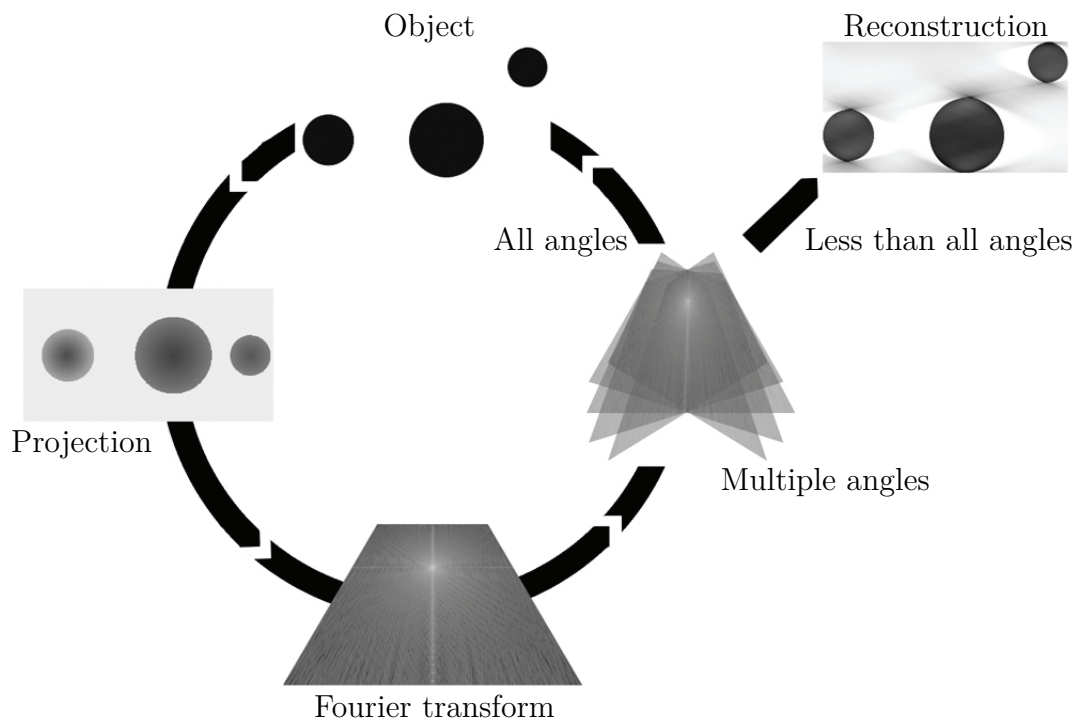


Figure 4.2: Schematic representation of the projection slice theorem. First a projection from an object is made. The projection is then Fourier transformed. This is repeated for all angles and the transformed projections are combined from which the original object can be reconstructed. If not all projections are available the image will lead to distortions, as is shown in the figure top right.

In theory, if an infinite number of projections are available over all angles θ a perfect reconstruction of the original object can be made. However, in practice typically for electron microscopy not all angles can be imaged since the copper support and the holder will eventually obstruct the view at high angles. As a result the reconstructed object will show distortions as a result of this missing wedge, as is shown in Fig. 4.2. In this figure the ideal reconstruction is shown in a circle diagram. An object, consisting of three spheres, is projected on a plane, from which a Fourier transform is made. This is done for all angles and the Fourier images are combined with which the original object can be reconstructed. If, however, a series of angles is missing, the reconstruction will show artifacts as a result of the missing data, shown in Fig. 4.2 as dark triangular shapes on the top and bottom of the spheres.

As stated earlier, to reconstruct $f(x, y)$ an inverse Radon transform (R^*) must be found for Eq. 4.5. There are several proposed solutions and these are known as reconstruction algorithms [126, 127]. One of the most common solutions is the Back-Projection (BP) algorithm by Crowther *et al.* [126].

$$B_{R^*x} = \frac{1}{2\pi} \int_0^{2\pi} R(\theta, x', y') d\theta \quad (4.11)$$

However, this method is prone to noise from the original data. An alternative algorithm, which is less prone to noise, is the simultaneous iterative reconstructive technique

(SIRT), as proposed by Peter Gilbert in 1972 [127]. With this technique, for each iteration, a trial tomogram is made and reprojected at the original tilt angles, the tomogram is then adjusted for the differences between the reprojection and the original projected images thereby improving the reconstruction. Both methods are compared in section 4.6.1.

4.2.1 Work flow

Using electron tomography (ET) has the great advantage of having both a nanometer resolution and a 3D imaging technique. However, ET is a time consuming process and for colloidal samples has for now only be done on dried samples. Here we will describe all the steps needed to make a ET reconstruction from TEM images using the IMOD 4.3 software package [128]. The work load can be separated in two major steps. The first is the acquisition of the tilt series which is done on an electron microscope. The second step is the actual ET reconstruction which can be completed anywhere on a sufficiently powerful computer, e.g. Intel i5-3210 8gb ddr3 nvidia Geforce GT630m 2gb, with a reconstruction software package. These steps are schematically represented in Fig. 4.3. For the acquisition the object of interest is first centered in view. The z-shift of the stage is adjusted until the objects position remains stationary during rotation. The stage is then tilted to ultimate angles to check for sufficient clearance; the object should be visible without obstruction at angles of $\sim 60^\circ$ in both positive and negative tilt, and preferably more. Reconstructions can be made with lower tilt angles if necessary, but the effect of the missing wedge will be more pronounced. The appropriate magnification is chosen such that the object and enough ($\geq \sim 10$) fiducial markers are visible in the view at the angle of 0° , and a high enough magnification to ensure that the desired level of detail can be obtained. The intensity is adjusted for sufficient and homogeneous illumination. If the option "auto-functions" is used then the pivot points have to be centered since the software uses these to auto-focus the object. During the acquisition of all projections the object must be kept focused and centered for each electron micrograph. Electron micrographs were typically taken as 8 bit images.

For the reconstruction the software package IMOD 4.3 was used [128]. This software package was developed by Kremer *et al.* and is freely available via the Boulder laboratory homepage ("bio3d.colerado.edu/imod/" at the time of writing). This software package contained the essential reconstruction software amongst which "ETomo", "MIDAS", and "3DMod". To align the data stack it was loaded in ETomo and coarsely aligned using an integrated cross correlation algorithm based on Fourier filtering. The alignment can be fine-tuned by hand using MIDAS if necessary. Then a fiducial model was made by selecting gold markers surrounding the object on the support film, and tracking these over the full tilt range of the series. The fiducial model was then fine-tuned by adjusting the tilt angle offset and by fixing large residuals (mismatch between the fiducial model and the actual markers). To center the object of interest in the ET reconstruction a trial tomogram was made and a boundary model encompassing the full object was determined by eye thereby centering the origin of the reconstruction near the center of the object. From the boundary model a z-shift and the pitch angles were calculated with which the final alignment was made. For the fine alignment the stack was typically binned down to 1024 by 1024 pixels. After this a ET reconstruction can be made using either the BP or

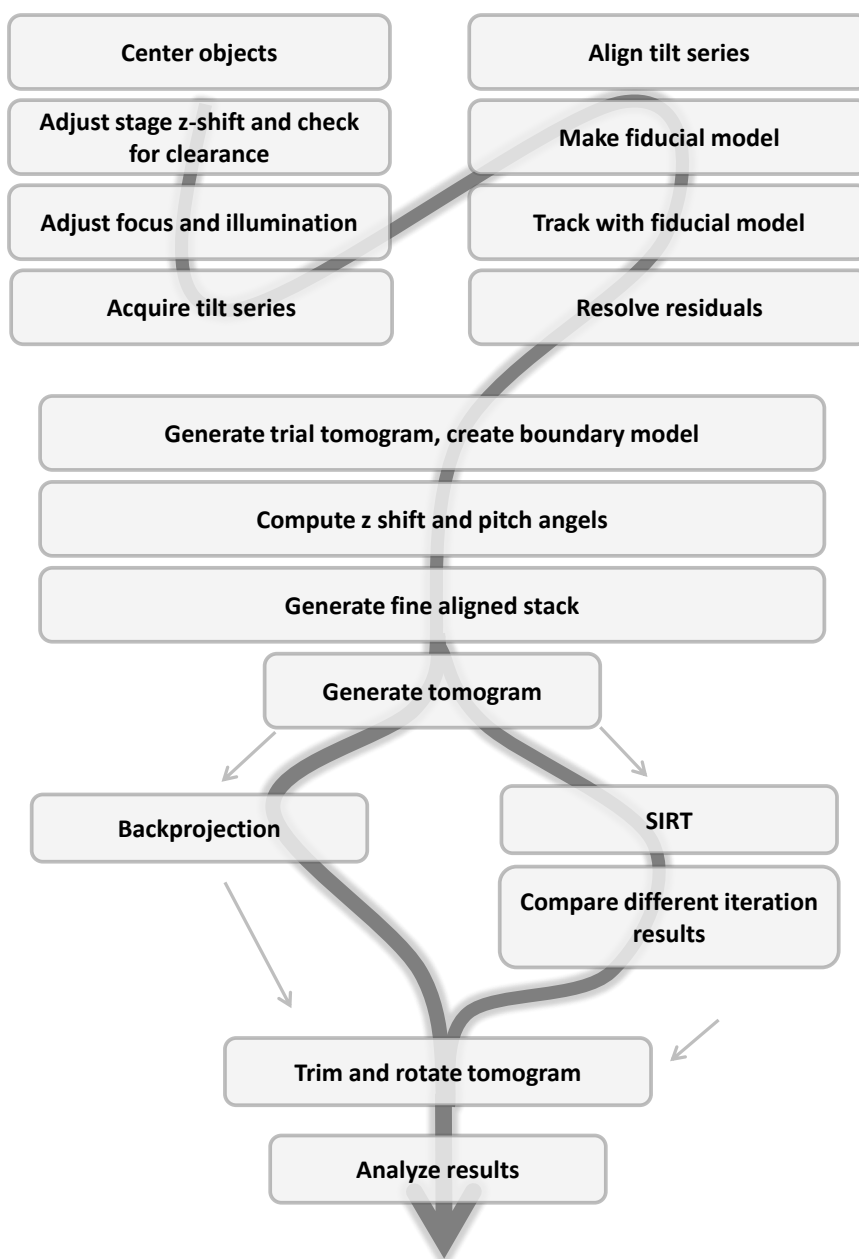


Figure 4.3: Flowchart depicting the work flow for making a ET reconstruction using IMOD 4.3.

SIRT algorithm. This is by far the most computational demanding step, using a graphics card (CUDA) significantly reduced the typical reconstruction time from 2 hours to 30 min, but this strongly depends on the desired resolution of the reconstruction. For SIRT a number of iteration steps between 5 and 20 was typically chosen as these yielded the best results. The resulting ET reconstruction was then trimmed down and used for data analysis.

4.3 Examples of colloidal model systems developed for self-assembly

Within the soft condensed matter (SCM) group a wide variety of new colloidal model systems were and are being developed [129]. These colloids were synthesized for a specific purpose within the field of self-assembly, in which the shapes and other properties affecting the interaction potential between the particles and thus their self-assembly played integral roles, for instance as in self-assembly induced by the use of external electric fields [130]. Thus the exact determination of the 3D shape of such colloids is an ideal test case to study the strengths and weaknesses of this 3D analysis method. In this section each of the different colloidal systems that were examined is introduced. The synthesis of these particles will only be touched upon briefly, mostly through references, as the focus of this chapter is on the ET reconstruction technique, including possible artifacts, and its 3D resolving power.

Sphere-shaped colloids: Patchy spheres, stomatocytes & Bowls

Three different types of quasi spherical colloidal particles were analyzed: The first type of colloid was Patchy spheres, which consisted of silica spheres with hemispherical silica patches distributed over its surface. These were made by coating dense packed colloidal crystals of silica spheres with the silane coupling agent 3-(trimethoxysilyl)propyl methacrylate (TPM). When redispersed the particles contained patches of non-coated area resulting from the regions where they were touching in the dense packed colloidal crystal or amorphous packing. On these non-coated areas silica was grown using tetraethyl orthosilicate (TEOS) according to a method developed by Wang *et al.* [131]. The goal of these particles is to make colloidal systems with inhomogeneous interactions which allows for extra control over the crystallization behavior of silica colloids. ET is quite useful for these systems. For instance, it is well known that for colloids with a hard potential the free energies for hexagonal-close-packed (HCP) and face-centered-cubic (FCC) ordered structures are close together (see also section 6.1). The patches resulting from a colloid in an FCC like surrounding are different from those surrounded by a HCP stacked close packed crystal, in addition polydispersity will lead to distortion of the lattice and particles not touching each other leading to missing patches. Ultimately if the polydispersity is too high, the resulting packing becomes amorphous and the regularity of the patches on each sphere is lost.

The second type of sphere-like particles was a type of colloid revert to as stomatocyte. The shape of this colloid consist of a spherical particles with a hollow cavity

inside connected to the surface through a narrow funnel. These particles were made from polyethylene glycol-polystyrene (PEG-PS) block copolymers which formed through self-assembly these hollow colloidal PEG-PS spheres. A platinum nanoparticle was then grown inside the hollow cavity to act as a catalyst to reagents present in the dispersion medium. These particles were developed and synthesized by Wilson *et al.* as self propelled particles in a liquid suspension containing hydrogen peroxide [132]. As such particles decompose the hydrogen peroxide a chemical potential gradient over the particle results in a force propelling the particle to a more hydrogen peroxide rich area, the exact mechanism of which is still debated in the literature, see for an overview and proposed mechanism e.g. Ref. [133]. The strength of ET for these structures lay in the ability to determine if there was indeed a catalytic nanoparticle inside the supra particle and that it was connected to the outside through the funnel.

The third sphere-like shape was bowl shaped: Bowl shaped or hollow hemispherical particles were formed by collapsing a hollow silica/siloxane particle in on itself by removing the inner phase. These particles were synthesized by crosslinking part of emulsions droplets of polydimethylsiloxane (PDMS) with tetraethoxysilane and by dissolving the uncrosslinked PDMS with ethanol. This method was developed by Zoldesi *et al.* [134, 135]. Again, ET was useful to determine the exact geometry of the bowl shaped particles and the thickness of the wall which can then be used for simulations on the phase behavior of these particles and for calculation involving the polarizability [130] and other interactions such as depletion induced effects.

4.3.1 Rod-shaped silica particles: bullets, spherocylinders & fluted shapes

The first rod-like shape that was analyzed was a bullet shape: Bullet shaped particles are rod shaped particles with one rounded and one flat end. These new micron-sized rod-shaped colloidal model particles were made from silica and were synthesized according to a method developed by Kuijk *et al.* [136], these particles were also optimized for real-space studies [137]. Using this method rods were grown from emulsion droplets which resulted in this non-symmetric shape. In one of these batches a seemingly concave tip was observed for the particles where a flat tip was expected based on previous examples (see Fig. 4.4). The strength of ET lay in the ability to analyze the exact geometry and the internal structure, determining whether the objects were hollow or not, if the flat tip was concave, convex or flat, and how sharp the edges of the bullets were. All of these properties can influence behavior of these particles [17, 138]. Furthermore, the shape

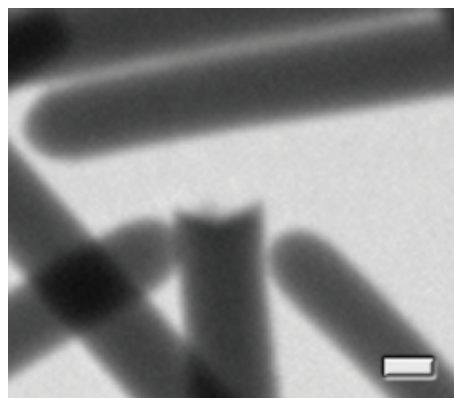


Figure 4.4: Electron micrograph of a bullet shaped rod-like particle with what seemed to be a convex tip (scale bar = 200 nm).

obtained from the ET reconstruction can be digitized and be used to study the behavior of these shapes adsorbed to liquid interfaces [139].

The second shape was a spherocylinder: Spherocylinders were rod shaped particles with two hemispherical tips. These particles were synthesized by growing a layer of silica around the bullet shaped particles introduced above, and the synthesis was performed as described by Peng *et al.* [138]. This modification was performed to study the influence of the geometry on the site specific growth of polymethylmethacrylate polymer at specific sites on the silica rods and how this depended on the particle shape.

The third rod-like shape was a fluted rod: Fluted rods are patchy silica rods where the silica patch is elongated over the full length of the rod. These particles were synthesized by coating rods similarly to the patchy spheres as described above, but instead with the silica rods assembled in a dried smectic or columnar crystal phase as formed by the rods. The rods were then coated with 3-(trimethoxysilyl)propyl methacrylate (TPM) and redispersed to grow silica on the un-coated region. This resulted in strips of silica on the areas where the rods were previously touching in the colloidal solid. Which was visualized using ET yielding information on how the rods are touching when in a smectic or columnar crystal phase.

4.3.2 3D structure analysis of supraparticles made from nanoparticles

In this chapter we will also discuss the use of ET for structural analysis of supraparticles (SPs) assembled from spheres, cubes and rods. Additionally, the ET analysis of preliminary experiments towards binary nanoparticle self-assembly in SPs is presented.

Spherical SPs were made according to the emulsion method described in section 3.4.5. By heating nanoparticle loaded emulsion droplets the inner low boiling oil phase was evaporated and the nanoparticles were forced to self assemble within the spherical confinement provided by the surface tension of the droplets. The SPs discussed in this chapter consisted of cobalt iron oxide nanoparticles with an effective diameter of 8.8 (effective polydispersity 4 %) nm and 14.7 nm (polydispersity 3 %) for the spherical particles 2.5.1, and a length of 13 nm for the cubic shaped nanoparticles 2.5.4. As rods silica coated gold nanorods with an aspect ratio of 1.8 were used with a length of 118.8 nm (polydispersity 8.2 %) and a width of 68.0 nm (polydispersity 3.1). The gold rods were synthesized according to Ye *et al.* [140]. After the synthesis the rods were first coated with a mesoporous silica layer using a method proposed by Gorelikov *et al.* [141] and then an OTMOS layer based on the method described in Ref. [142].

In order to investigate binary self-assembly of nanoparticles SPs, we first needed to demonstrate bulk binary crystallization. This was investigated using particles with a size ratio of 0.4, which if hard sphere-like interactions are assumed, is expected to give rise to a rock-salt crystal structure [143]. To make binary superlattices of nanoparticles 8.8 nm_{eff} (polydispersity 7 %) gold and 18.9 nm_{eff} (polydispersity 4 %) cobalt iron oxide with close to equal particle concentrations (number/mL) were combined in a glass vial and deposited on a TEM grid. The resulting structures showed binary crystalline structures and were analyzed using ET. The 6.0 nm gold nanoparticles were synthesized according to Zheng *et al.* [144], and 18.9 nm_{eff} cobalt iron oxide were synthesized according as described in

section. 2.4.4. Unfortunately, there was not enough time left to study the binary self-assembly behavior in spherical confinement.

4.4 Bending of rods

A deformation of the bullet shaped silica particles was observed with TEM and ET in samples that were allowed to dry at room temperature from a water phase. These deformations were observed as a bending of the silica rods in a direction perpendicular to the support and an indentation in the ~ 25 nm thick support film. This suggests that the rod and the film were pulled together during drying as a result of capillary effects, since neither of these deformations were observed in freeze dried samples.

To obtain an estimate of the forces exerted on these rods during this process, a mechanical engineering model for tensile strain was used. Using this model the minimal amount of forces needed to bend a rod and deform a plate (support film) to the observed curvature was calculated from the material properties. Although this is a rough estimate of the force that were applied, it does yield insights into the importance of freeze drying and the influence of these capillary effects.

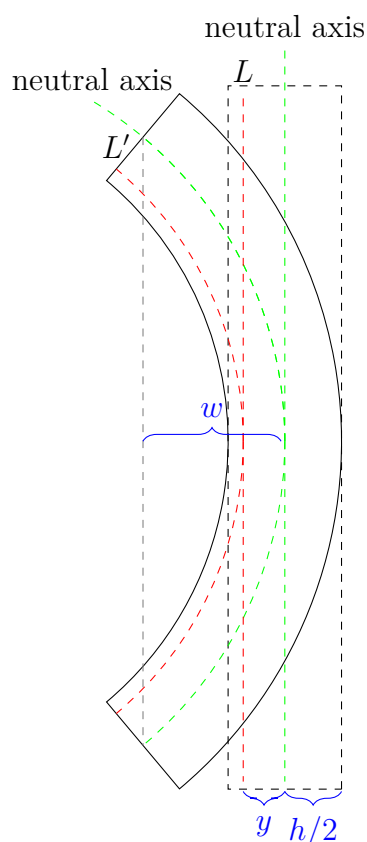


Figure 4.5: Schematic representation of the bending of a rod, as the rod deforms the inner part, here depicted left from neutral axis, will be compressed, whereas the outer part, right, will be stretched.

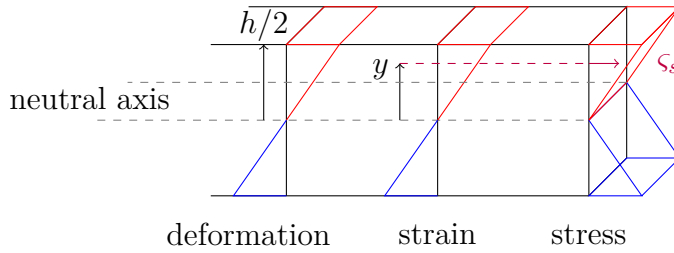


Figure 4.6: Schematic representation of the deformation, the strain, and the stress working on a beam during bending.

If an object is subject to stress it will experience strain i.e. an amount of deformation of the object 4.5. When the mechanical properties of the object are known an approximation for the applied forces can be used using a linear analysis if the observed strain is small enough. If this condition is met, the amount of bending remains in the elastic regime where the stress is proportional to the strain [145]. *Note that this means the rods would bend back once the forces have disappeared, which is not seen here, meaning that either the deformation is now held in place by other forces, e.g. as van der Waals, or a plastic deformation occurred instead.*

To approximate the force on a rod Eq. 4.12 was used which is a formula for the bending of a rod supported at both ends with a force applied homogeneously over the full length of the rod. *Note that the capillary effect is most likely weaker at the ends of the rods as the space between the length of the rod and the film is narrower than the space between the flat or rounded ends of the rod and the film.*

$$w = \frac{5}{384} \frac{pL^3}{EI_s} \quad (4.12)$$

Here w is the deflection of the center of the neutral axis from the point before bending. p is the pressure applied on the rod, L is the length of the rod, E is the Young modulus, and I_s is the area moment of inertia. The area moment is a property of a cross section that can be used to predict the resistance of rods to bending. As the rod bends the top of the rod is compressed and the bottom is elongated. This results in a positive strain on the top and a negative strain on the bottom. Over this area the moment must be calculated. The area moment of inertia I_s is defined as:

$$I_s = \int_A y^2 dA = \int_{-d/2}^{d/2} \int_{-h/2}^{h/2} y^2 dx dy \quad (4.13)$$

where y is the distance from the neutral axis plane, d is the width, and h is the height. For a cylinder gives:

$$I_c = \frac{\pi r^4}{4} \quad (4.14)$$

Where I_c is the area moment of inertia for a cylinder, and r is the radius of the cylinder. The Young modulus E is a function of the stress σ_s and the strain ε . The strain (ε) is the

change in length divided by the original length:

$$\varepsilon = \frac{\Delta L}{L_0} \quad (4.15)$$

Where ΔL is the change in length, L_0 is the original length, and ε is the strain. The stress is the force F applied on the initial area A_0 :

$$\varsigma_s = \frac{F}{A_0} \quad (4.16)$$

The Young modulus (E) is then equal to the stress divided by the strain:

$$E = \frac{\varsigma_s}{\varepsilon} = \frac{F/A_0}{\Delta L/L_0} \quad (4.17)$$

Using this method the minimum force needed to bend a rod a certain small amount can now be calculated. The obtained estimate will give some insight in the magnitude of the force working on these small structures, and indicate whether freeze drying is important or not.

4.5 Experimental details

4.5.1 Equipment

For centrifugation an Eppendorf Centrifuge 5415c was used. For TEM analysis a Tecnai 12 electron microscope operating at 120 kV with a tungsten electron source was used. For ET analysis a Tecnai 20 electron microscope operating at 200 kV in bright field (TEM) mode with an LaB₆ electron source, and for STEM analysis a Tecnai 20F electron microscope operating at 200 kV in scanning transmission electron microscopy (STEM) mode with a Field Emission Gun (FEG) as electron source. A Vitrobot Mark 2 plunge freezer was used to freeze samples for freeze drying and to carbon coat TEM grids we used a Cressington 208 carbon coater.

4.5.2 Software

Software used in this chapter was: Inspect 3D (FEI Company, Eindhoven), IMOD 4.3 (Boulder Laboratory, Colorado, including amongst others: MIDAS, ETomo, 3DMod, IMODauto, and IMODjoin).

4.5.3 Chemicals

Chemicals were obtained from Sigma-Aldrich unless noted otherwise and were used as received. Cylohexane (Sigma-Aldrich, $\geq 99.8\%$), Dextran from *Leuconostoc mesenteroides* (mol. wt. 1.500.000 - 2.800.000 g/mol), Ethanol 96% (Baker Analyzed, 96 %) PEG-thiol (Sigma-Aldrich, O-[2-(3-Mercaptopropionylamino)ethyl]-O'-methylpolyethylene glycol, MW 5.000), Sodium dodecyl sulfate (SDS, $\geq 99.0\%$). For de-ionized water a Millipore Direct-Q UV3 reverse osmosis filter apparatus was used (18 M Ω /cm at 25 °C).

4.5.4 Synthesis of fiducial markers and sample preparation

PEG-thiol coated gold nanoparticles served as fiducial markers. These nanoparticles were synthesized according to Method 4 presented in Ch. 2. The PEG-thiol coating was applied by adding 5 mg of PEG-thiol per ml of as-synthesized nanoparticle in water suspension and stirred for 16 hours. The resulting suspension was centrifuged at 12000 rpm for 30 minutes and the sediment was redispersed in 96% ethanol. To deposit the markers a drop was deposited on one side of the TEM grid and allowed to dry. The TEM grids that were used were copper 200 mesh with a ~ 25 nm thick Solutia support film carbon coated for ~ 7 sec. Samples were then deposited on the opposite site of the TEM grid as to not perturb the deposited gold nanoparticles using either of the following two methods.

For regular drop casting a small droplet ($\sim 3 \mu\text{L}$) of sample was deposited on the TEM-grid, which was then allowed to evaporate at room temperature (RT) at atmospheric conditions. To prepare freeze-dried samples TEM grids were first glow discharged using a carbon coater, making them hydrophilic, prior to gold markers and sample deposition. After the gold marker deposition the grid was loaded with $3 \mu\text{L}$ of sample. The deposited droplet was then blotted for 1.0 s. and plunged into liquid ethane at approximately -180°C using a Vitrobot. The sample was then kept under vacuum and heated to -90°C at $\sim 5^\circ\text{C}\cdot\text{m}^{-1}$, from there the sample was gradually heated to RT over a period of 3 hours, i.e. $< 1^\circ\text{C}\cdot\text{min}^{-1}$.

For a typical binary nanoparticle superlattice (BNSL) two types of nanoparticles, gold 8.8 nm_{eff} and iron cobalt oxide 18.9 nm_{eff} , were combined with a size ratio of 0.4 in a total volume of $100 \mu\text{l}$ of cyclohexane. A droplet of the mixture was then drop cast on a TEM-grid without fiducial gold markers as the gold nanoparticles in the structure were used instead. The sample was then allowed to dry at RT.

4.5.5 Tomography, image analysis and visualization details

Images were acquired up to the highest possible angles by tilting the stage along the x-axis in both directions. Images were taken with 1° intervals at high angles ($>30^\circ$) with respect to the normal, and with 2° for smaller angles. This typically resulted in a data stack (tilt series) with transmission data over $\sim 140^\circ$. To align these images fiducial markers were tracked in the tilt series using ETomo (part of the IMOD 4.3 software package), thereby determining the movement of the sample during tilting. The final reconstruction was made by either using the SIRT or the BP algorithm available in the IMOD 4.3 package.

The steps needed to make a 3D model and a 3D surface rendering outlining the particles shape are shown in Fig. 4.7 and are described in consecutive order but are specific for the IMOD 4.3 package and may vary for different reconstruction software packages. **a** TEM images were taken of the original object over all available angles. **b** A ET reconstruction of the object was made resulting in orthoslices of the object. **c** A threshold value was determined using the auto contours function in 3DMod, binarizing the image. **d** Contours were traced around the binarized model at the chosen threshold value using IMODauto (imodauto -l "threshold value" "reconstruction-name.mrc" "model-name.mod"). If multiple contours were traced using different threshold values, the models were merged using IMODjoin (imodjoin "model-in-1.mod" "model-in-2.mod" "model-out.mod"). Spherical or

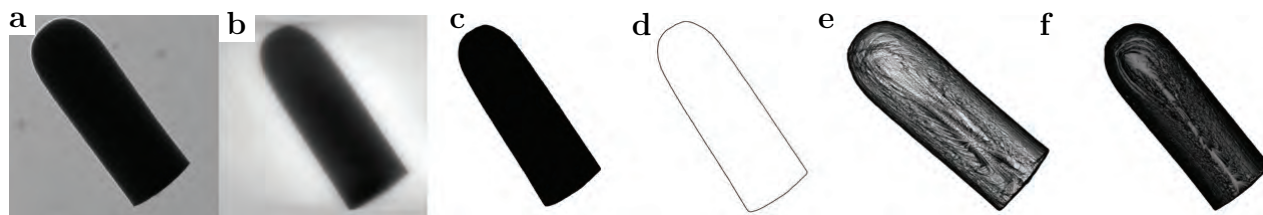


Figure 4.7: Steps used for making 3D models. **a)** Single image from a tilt series of an object. **b)** Orthoslice of the ET reconstruction made from the tilt series. **c)** Threshold based binarized image of an orthoslice. **d)** Contour traced around the binarized image. **e)** 3D wireframe model by combining all traced contours. **f)** Triangulated model by cross meshing the contours resulting in a solid object.

near spherical shapes were interpolated using 3Dmod's interpolator. **e)** Contours traced in each orthoslice are visualized in a 3D wireframe model. **f)** The model could then be cross meshed resulting in a 3D tessellated model of the original object. A 0.5 transparency wireframe model typically showed the information on identifying the shape and other geometrical properties the clearest and was therefore used in this chapter to show models of the analyzed objects.

4.6 Results & Discussion

The results of the ET analyses are presented in this section. The results are presented in three parts: The first part discusses results for different reconstruction algorithms used to determine the most suitable reconstruction algorithm for the tracing of 3D models. The second part presents the study of the geometrical properties of colloidal systems. The third and final part discusses the resolving power, and which mode of EM operation is most advantageous for ET, on SPs self-assembled from nanoparticles. Details on the structures that were found using the methodology described in this chapter of the nanoparticles in the SPs for the spherical particles are described in more detail in Chapter 6 and of the cubic particles in Chapter 5.

4.6.1 Comparison of the SIRT and BP algorithms used

To compare the two algorithm, Back-projection (BP) and simultaneous iterative reconstructive technique (SIRT), ET reconstructions with both methods were made and compared using a patchy silica spheres with a diameter of 300 nm and patches of roughly ~ 40 nm. To test the resulting reconstructions orthoslices of the least resolved angle were compared. This is parallel to the grid and perpendicular to the tilt angle where the effect of the missing wedge is the most pronounced.

These comparisons are shown in Fig. 4.8. The insets show the binarized versions of the images after thresholding, and represent the contour that is traced when a model is made of this ET reconstruction at the most optimal threshold (determined by eye). The BP reconstructions are shown in Fig. 4.8**a,b** and the SIRT reconstructions are shown in Fig. 4.8**c,d,e**, and **f**. In panel **a** a reconstruction based on 683 x 683 pixels is shown whereas a reconstruction from 1024 x 1024 pixels is shown in panel **b**. The three patches and the outline of the shape can clearly be identified in reconstruction from both algorithms. The reconstruction using BP shows a higher level of detail with sharper edges but also more noise, whereas the SIRT algorithm shows less detail and less noise. For the BP the higher pixel density result in less pronounced diagonal artifacts but also increased the overall noise as can be seen in the binarized insets. For the SIRT algorithm the difference in pixel density showed little change in the final reconstruction, 683x683 pixels shown in panel **c** 1024 x 1024 pixels shown in panel **d**. The reconstructions made with the SIRT algorithm showed the best results when binarized, shown as inset in **d**. Increasing the iteration steps, Fig. 4.8**e** 20 and **f** 50, emphasized the features of the structure but also increased diagonal artifacts reduced the contrast in the center of the structure, resulting erroneously in a hollow structure as can be seen in the inset if Fig. 4.8**e**. Based on these results, the SIRT method with 5 iteration steps was used to make the ET reconstructions of the remaining colloidal systems for this chapter.

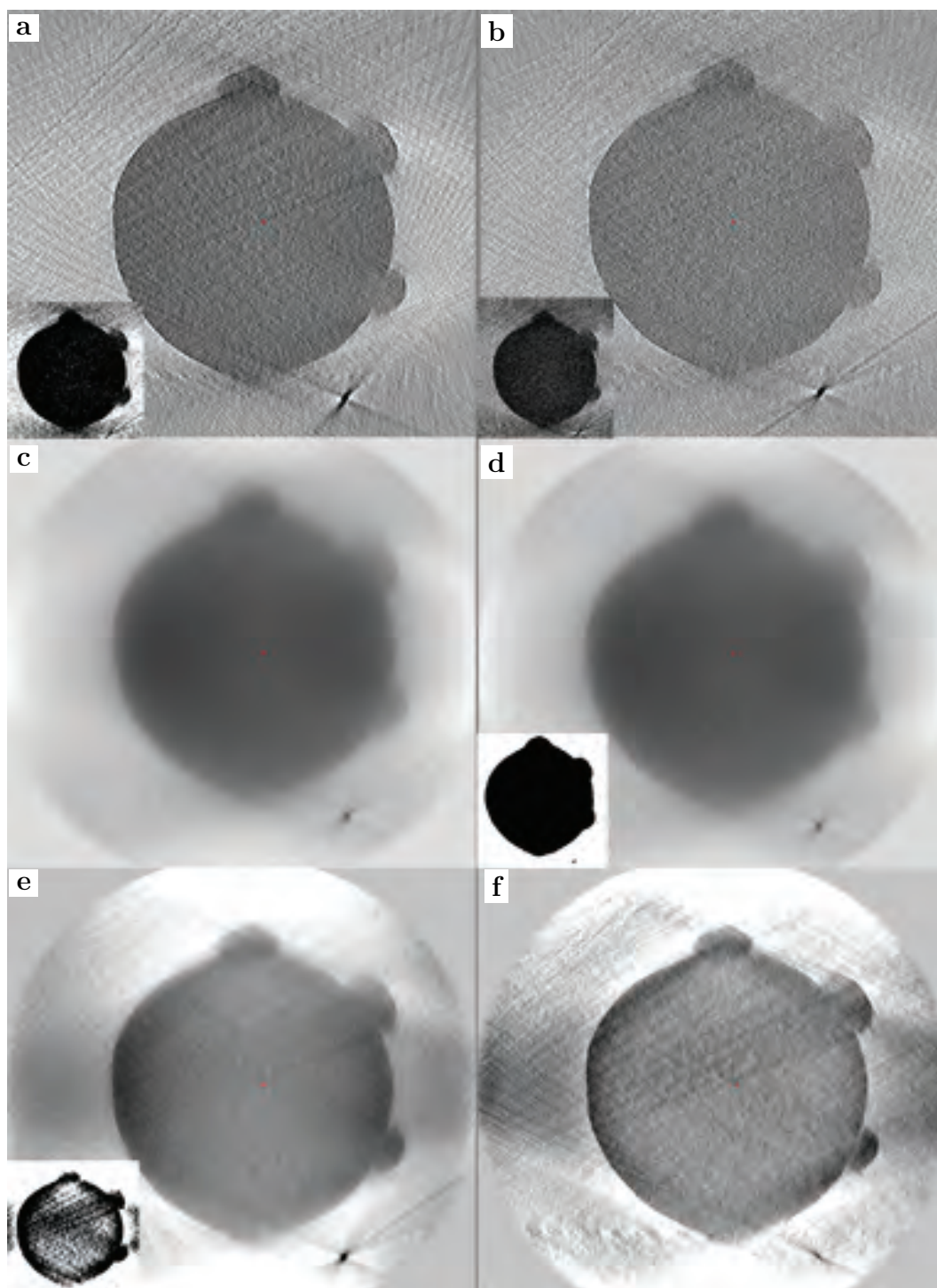


Figure 4.8: Different ET reconstruction techniques used to resolve the shape of a patchy sphere. Reconstructions are viewed from an angle of 90° with respect to the normal view. **a)** BP reconstruction with a data stack binned to 683×683 pixels. **b)** BP reconstruction with a data stack binned to 1024×1024 pixels. **c)** SIRT reconstruction using 5 iterations and a 683×683 pixels data stack. **d)** SIRT reconstruction using 5 iterations and a 1024×1024 pixels data stack. **e)** SIRT reconstruction using 20 iterations and a 683×683 pixels data stack. **f)** SIRT reconstruction using 50 iterations and a 683×683 pixels data stack. Insets show the binarized versions of the respective images.

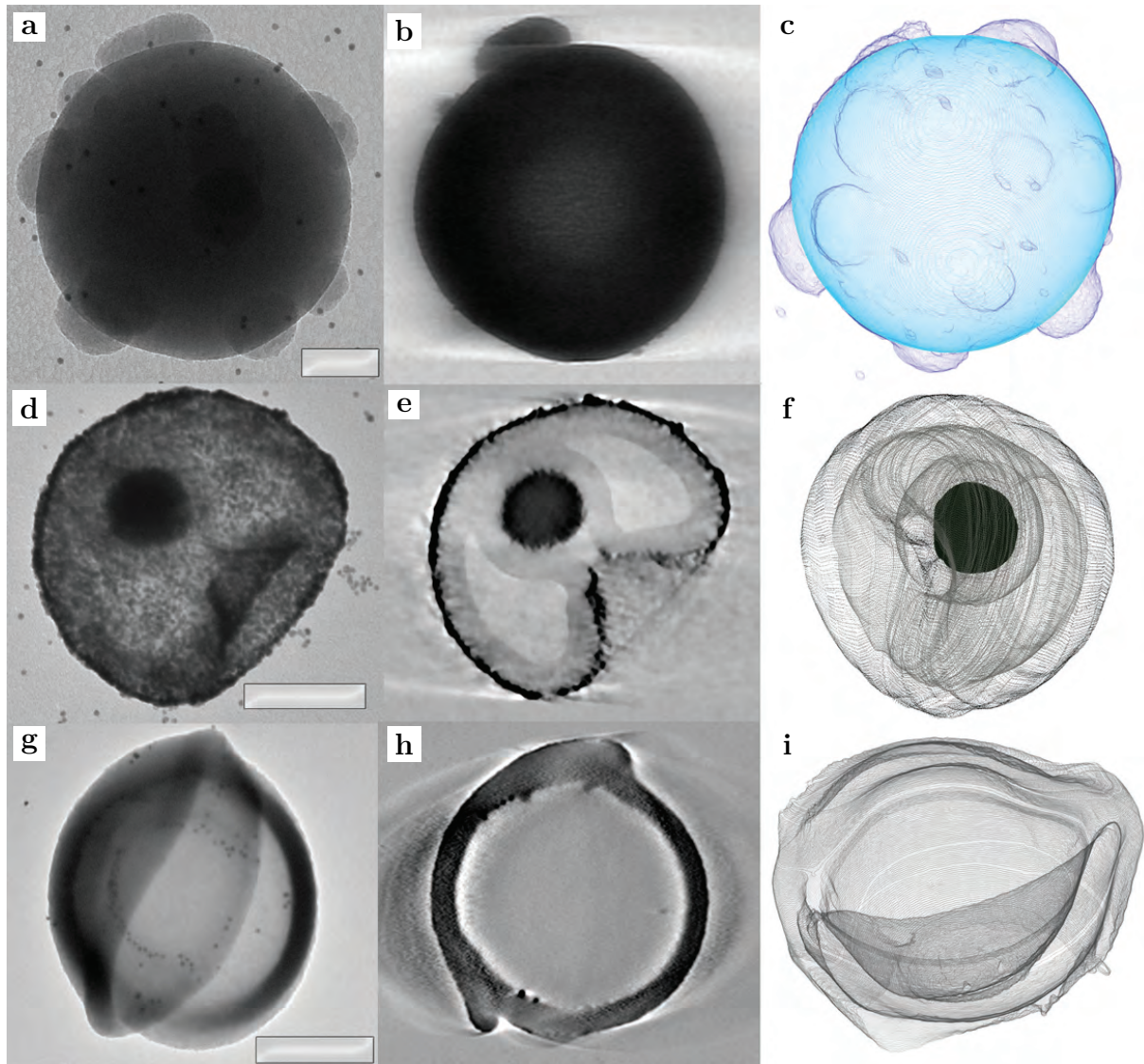


Figure 4.9: Electron micrographs, orthoslices, and 3D wireframe models of sphere-like particles (c, f, and i) are rotated. **a)** Electron micrograph of a 300 nm patchy silica colloid (scale bar = 100 nm). **b)** Orthoslice through a reconstruction of the patchy silica colloid. **c)** 3D wireframe model of the patchy silica colloid. **d)** Electron micrograph of a stomatocyte sequestering a platinum nanoparticle (scale bar = 100 nm). **e)** Orthoslice showing the internal structure of the stomatocyte. **f)** 3D wireframe model (nanoparticle is depicted solid). **g)** Electron micrograph of two bowl shaped particles packed close together (scale bar = 500 nm). **h)** Orthoslice through the reconstruction of the two bowls. **i)** 3D wireframe model of the two close packed bowls.

4.6.2 Sphere-like particles

Three different types of sphere-like particles or particles originating from spherical shells were analyzed. These particles were: patchy spheres, stomatocytes, and bowl shaped particles, and will be discussed in this order. Shown in Fig. 4.9a is a TEM image of a typical patchy silica sphere. The patches are visible as light gray protrusions on the spherical shape. In the orthoslice shown in Fig. 4.9b the spherical shape can be seen together with the single patch that was present at this height interval. This showed that the resolving power of the technique allowed for enough detail to determine the shape of these sub 100 nm patches. The 3D wireframe model shown in Fig. 4.9c showed that the silica of which the colloid was made resulted in enough contrast to trace the shape accurately. From this model a total of 10 patches were identified and their position and symmetry was available with high accuracy, and showed that the patches were not formed on a silica colloid in a face centered cubic (FCC) or hexagonal close packed (HCP) crystal structure. Similar results were found for each of the three patchy spheres from the same batch that were analyzed. This indicated that the silica colloids were in a defect rich or glassy state instead of a colloidal crystal at the time of the TPM coating.

The second analyzed shape was a so-called stomatocyte, of which a typical example is shown in Fig. 4.9d. This spherical colloid has a hollow cavity with a narrow opening connecting the cavity with the outside. A platinum particle was grown in the hollow cavity after the shape had been formed. The nearly spherical shape of the outside the dark platinum nanoparticle are clearly visible. The orthoslices taken from the ET reconstruction showed the position of the platinum nanoparticle and the funnel connecting the cavity with the outside, see Fig. 4.9e. The funnel together with the catalytic properties of the platinum core functioned as a propulsion system when introduced to a hydrogen peroxide rich environment as was shown by Wilson *et al.* [146]. Furthermore, the ET technique was able to resolve the double wall resulting from the formation mechanism where the particle is folded in on itself. However, where the inner and outer wall touch no edge could be discerned between the two layers. A 3D wireframe model shown in Fig. 4.9f visualizes the full colloidal structure in a single view. To trace this model the option "auto contours" in 3DMod was used to find the shape at several height intervals and the remaining shape was interpolated from these contours.

For the analysis of a bowl shaped particles an object consisting of two close packed bowl shaped particles was chosen. A TEM image of this object is shown in Fig. 4.9g. The orthoslice from the ET reconstruction, Fig. 4.9h, shows the circular shape of the inner particle with the outer particle attached on the left. However, due to the missing wedge the contrast over the sphere is inhomogeneous, which is an artifact of the reconstruction. Furthermore, where both particles touch the shapes can no longer be distinguished. This is clearly seen in the model shown in Fig. 4.9i where two touching bowl shaped particles merge together into a single shape. This resulted in an inaccurate representation of the colloidal shape and reveals some of the limitation of this technique. It was however, clear from these reconstructions that these bowl-shaped particles were still flexible since strong deformations in the shape as a result of the packing were visible.

These findings combined show that the shape and the internal structure of these colloidal structures was resolved in great detail using this technique, although, a contrast

difference is needed such as a gap or a spacer of a different material to accurately distinguish the objects shapes. In short, it is best to analyze separately lying particles where possible.

4.6.3 Rod-like particles

For rod-like particles three different types of shapes were examined. The analysis of the first type, the bullet shape particles, was performed to determine whether the end was curved, and if so, how much. The bullet shaped particles, shown in Fig. 4.10a, showed one hemispherical and one flat tip. Due to observation of a concave curvature as discussed in Section 4.3.2 some TEM images suggested that the flat tip might be slightly concave in all cases, since the rods are grown from droplets. Orthoslices taken from the ET reconstruction revealed that no curvature was present on the flat tips of each of the four examined bullet shaped particles, see Fig. 4.10b. The 3D wireframe model of the bullet shaped particle clearly shows the shape of the particle with both the rounded end and the flat end with a relatively sharp edge. These geometrical properties were a subject of study for the observed site specific attachment of methyl methacrylate (MMA) droplets on the flat ends of these bullet shaped particles [138].

To examine this adsorption behavior in more detail the bullet shaped particles were overgrown with silica using a seeded growth process with the silica particles as cores, see Fig. 4.10d. This was done to see how the observed droplet attachment behavior changed as a result of the altered geometry [138], but is generally also used to optimize fluorescent rods for 3D analysis with confocal microscopy [137]. In the orthoslice, shown in Fig. 4.10e, the convex shape of both tips can be seen showing the clear change in geometry. From the 3D wireframe model, shown in Fig. 4.10f, the nearly spherocylindrical shape can be identified confirming the change in shape as a result of the silica coating.

Fluted rods, rods with patches of silica grown along the length of the colloidal particle, were made using a similar method as used for the synthesis of patchy spheres, see section 4.3.2 for details. The resulting ridges of silica were visible in electron microscopy as protrusions along the length of the rods, as shown in Fig. 4.10g. From the orthoslices, shown in Fig. 4.10h, it was found that these rods had a slight conical shape and that the ridges typically spanned from the bottom, near the wider flat base, up to roughly two third of the rods and not all the way to the top. It is likely that due to this conical shape only the wider base was in contact with the neighboring particles during the modification step resulting in this shape. In the 3D wireframe models six fold symmetries were observed near the bottom of the particles when viewed along the length of the rod, Fig. 4.10i, for two of the three analyzed fluted rods suggesting a, at least local, hexagonal packing at the time of the patch formation.

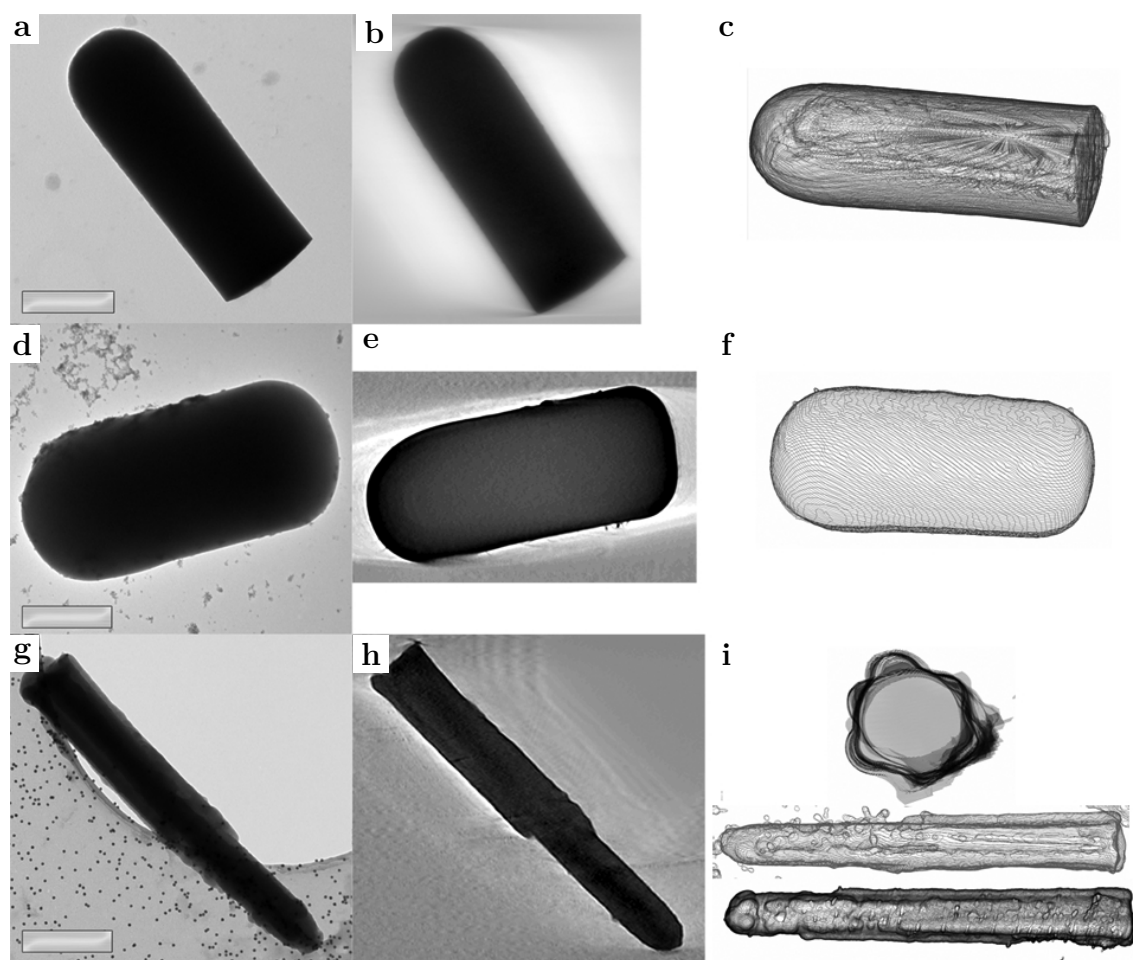


Figure 4.10: Electron micrographs, orthoslices, and 3D wireframe models of rod-shaped particles (scale bar = 500 nm). **a)** Electron micrograph of a bullet shaped silica rod. **b)** Orthoslice through the reconstruction of the bullet shaped rod. **c)** 3D Wireframe model of the bullet shaped particles showing a flat and a spherical tip. **d)** Electron micrograph of a bullet shaped particle overcoated with silica. **e)** Orthoslice of the silica coated bullet with two curved ends as result. **f)** 3D Wireframe model showing the nearly spherocylindrical shape of the silica coated rod. **g)** Electron micrograph of a fluted rod where patches of silica are grown along the length of the rods. **h)** Orthoslice through the fluted rod. **i)** 3D Wireframe model of the fluted rod.

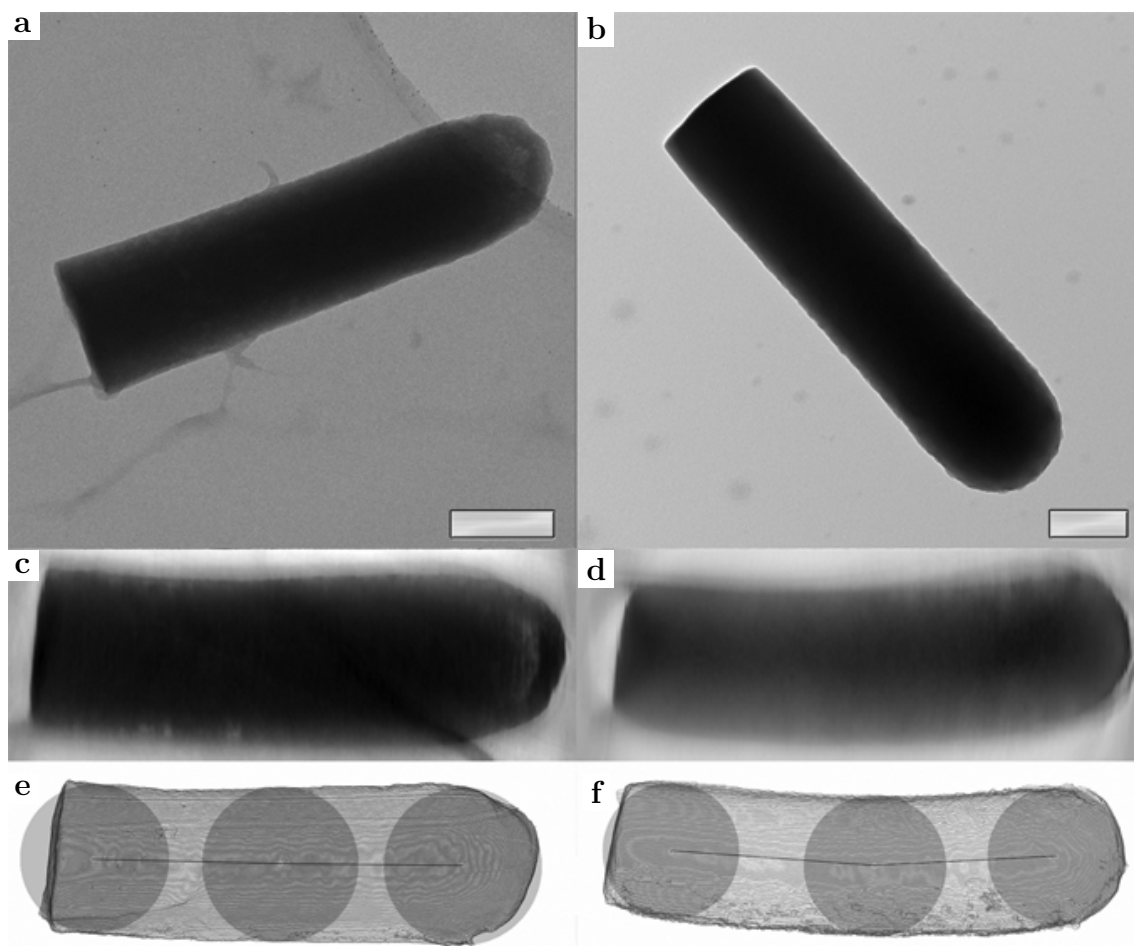


Figure 4.11: Electron micrographs and ET reconstructions of silica rods showing the differences between freeze and RT dried silica rods. **a)** TEM image of a freeze dried silica rod (scale bar = 100 nm). **b)** TEM image of a RT dried silica rod (scale bar = 200 nm). **c)** Tomographic reconstruction of the freeze dried silica rod viewed from an angle of 90° with respect to the normal viewing angle. **d)** Tomographic reconstruction of the RT dried silica rod at 90° with respect to the normal. **e)** 3D Wireframe model of the freeze dried silica rod. **f)** 3D Wireframe model of the RT dried silica rod. The bending of the rods was measured by determining the height of the respective centers of the rods in the middle and at each end as is shown in **e** and **f**.

Bending of rods

In Fig. 4.11 freeze dried (**a**), and RT dried (**b**) rods are shown. Both rods were bullet shaped particles with one flat and one hemispherical tip. In the reconstructions of the RT dried silica rods particle bending was observed as shown in Fig. 4.11d. These deformations were not observed in freeze dried rods, Fig. 4.11c. Therefore, this was likely caused by capillary effects during the drying of the liquid on the EM grid. To measure the extent to which these rods were deformed wireframe models were made of each ET reconstruction and the deflections were measured based on the respective centers at the middle and each end of the rods.

To get an estimate of the amount of force needed to bend a silica rod the deflection from the normal can be used, depicted in Fig. 4.11e and f. For the Young modulus of silica a value of 20 GPa was used based on the findings by Zhang *et al.* [147]. The lengths L for the rods were 1.29 μm , and 1.64 μm , and a width of 0.41 μm , and 0.58 μm was measured. However, a length of 0.98 μm and 1.33 μm was used since the center of the rods, needed to calculate the deflection w , could not be accurately determined at the tips. For the deformed rods a deflection w of 55 nm and 61 nm was measured. No significant deflection was measured for freeze dried rods, see Fig. 4.11e. With Eq. 4.17 this resulted in pressures of 286 MPa and 97 MPa that was needed to bend the rods to this extent. To calculate deformation in the support a beam, instead of a cylinder, with a length equal to the width of the rod and a width equal to the length of the rod was considered. The Young's modulus of the support was reported to be ~ 2.1 GPa according to the supplier Solutia (Pub.No. 2008084E). With a displacement of $w = 75$ nm a length of 310 nm and a width of 1.29 nm, a pressure of 44 MPa was found.

This shows that drying effects play a significant role and can affect the shape of objects, these forces are strong enough that it can not be ignored when using electron microscopy analysis. Therefore, freeze drying or another method that does not involve a liquid interface, like super-critical drying, is to be preferred to minimize artifacts.

Note that for these estimates a series of assumptions had to be made. First: with this equation the rod was considered to be suspended from both tips. Second: the force was considered to be applied uniformly over the entire rod. Third: an elastic deformation is described which would mean the particles bends back after the capillary effect disappears.

4.6.4 Nanoparticle assemblies

The two types of nanoparticle assemblies that were analyzed were: nanoparticle SPs consisting of either spherical, cubic or rod-like nanoparticles self-assembled inside emulsion droplets, and binary nanoparticle superlattices (BNSLs) composed of gold and cobalt iron oxide nanoparticles incorporated into a single crystalline structure.

Supraparticles self-assembled in confinement

All three of the different SP types that were analyzed with ET were self-assembled in emulsion droplets with dextran, see Ch. 3 for more details. The SPs built up from 8.8 nm_{eff} spherical nanoparticles resulted in ordered spherical SPs as shown in Fig. 4.12a. The orthoslice of the SPs showed inwards pointing wedge shaped crystalline domains, Fig. 4.12b, suggesting a higher order in the crystalline superstructure. This SP was analyzed and described in more detail in Ch. 6 in a study of ordering of the nanoparticles in spherical confinements with a focus on hard potentials. The SPs assembled from nanoparticles with a cubic geometry resulted in spherical and cubic shaped assemblies of which a cubic assembly is shown in Fig. 4.12c. These different shapes and their origin are discussed in more detail in Ch. 5. Analyzing these structures with ET showed a simple cubic packing of the 12 nm cubic nanoparticles, see Fig. 4.12d. Furthermore, the orthoslices showed that nanoparticles were missing from each of the corners of the cubic assemblies similar as was observed in section 3.5.4, likely to accommodate for the spherical geometry.

Shown in Fig. 4.13 is a SP self-assembled from 11 silica coated gold nanorods with an aspect ratio of 1.8, a length of 118.8 nm (polydispersity 8.2 %) and a width of 68.0 nm (polydispersity 3.1). The TEM image, Fig. 4.13a, shows a clear contrast difference between the gold nanorod and the silica coating which makes ET technique more effective. Using ET the shape, position and orientation of the gold nanorods within the SP were visualized by tracing the contours as is shown in Fig. 4.13b. The large separation between the nanorods and the high contrast difference with the silica results in well defined shapes for each of the nanorods. In addition, the ET reconstruction was used to demonstrate that the 3D tracking algorithm by Besseling *et al.*, developed for the real-space space tracking of concentrated rod-like colloidal systems [120], was also suitable for tracking the position, orientation and length of nanorods from ET data, Fig. 4.13c. Comparing the traced model, Fig. 4.13b, with the results of the particle tracking, Fig. 4.13c, shows a good agreement between the two techniques. These preliminary results show that it now is possible to also analyze SPs built up from rod-like nanoparticles for which the aspect ratio can be tuned. It will be especially interesting to see if differences of liquid crystal phase behavior known for bulk phases will be reflected and in what way in the spherically confined self-assembly.

Binary superlattices

Combining 8.8 nm_{eff} gold and 18.9 nm_{eff} cobalt iron oxide nanoparticles with roughly the same particle concentrations resulted in binary superlattices as shown in Fig. 4.14. These structures showed hexagonal close packed cobalt iron oxide nanoparticles together

with ordered gold nanoparticles. The packing of these few layers observed is compatible with what would be observed if the interaction potential between these particles was hard-sphere like as discussed in Section 2.5.1. Both the cobalt iron oxide nanoparticles and the gold nanoparticles showed regular patterning this combination of nanoparticles most likely was inclined to crystallize in a bulk binary crystal, but the crystal structure from just these few layers could not be obtained and looks similar as structures presented by Schevchenko *et al.* [77].

The ET reconstruction confirmed that these were BNSL with a NaCl packing as is shown in, Fig. 4.15a. For this figure the BNSL was rotated to show the large 18.9 nm_{eff} cobalt iron oxide nanoparticles surrounded by 4 small 7.7 nm_{eff} gold nanoparticles matching a NaCl crystal structure. The reconstruction showed that the BNSL consisted of 2 layers of cobalt iron oxide nanoparticles and 3 layers of gold nanoparticles. Orthoslices taken at each of these 5 layers, see Fig. 4.15b, show consecutively 6 gold (top), 3 gold (middle) and again 6 gold (bottom) nanoparticles around a cobalt iron oxide nanoparticles as we go through the structure. This suggests that the packing at the top and the bottom differed from that in the middle of the structure, which is often observed in surface reconstructed crystals and is most likely also influenced by the drying forces present at the interfaces.

We also analyzed a BNSL with 3 layers of cobalt iron oxide, Fig. 4.15, to get more hints of what kind of bulk and/or SP crystallization this system would prefer in equilibrium. For this ET analysis an electron microscope in scanning electron microscopy (STEM) mode was used since this is considered to result in better ET reconstructions [148]. Fig. 4.15a shows the structure scanned with high angle atomic diffraction (HAADF) detector (left) and a secondary electron (SE-STEM) detector, which only shows the surface of the structure. Where with HAADF-STEM transmission images are made, the SE-STEM mode only, but clearly, imaged the nanoparticles on the surface of the self-assembled structure. The orthoslices from the ET reconstruction shows 7 layers, alternating again between 6 gold nanoparticles at the top and bottom and 3 gold nanoparticles particles in the two middle layers.

Comparing the ET reconstructions from the two acquisition methods, TEM shown in Fig. 4.15 and HAADF-STEM shown in Fig. 4.16, showed that the gold nanoparticles were clearly visible in both ET reconstructions, but the cobalt iron oxide nanoparticles in the TEM reconstruction were better visible than in the STEM-HAADF reconstruction. Possibly the STEM-HAADF tomography could be improved by using more advanced electron microscopes, since in the literature STEM is considered more suitable for crystal structure analysis of atomic and molecular crystals using ET [149].

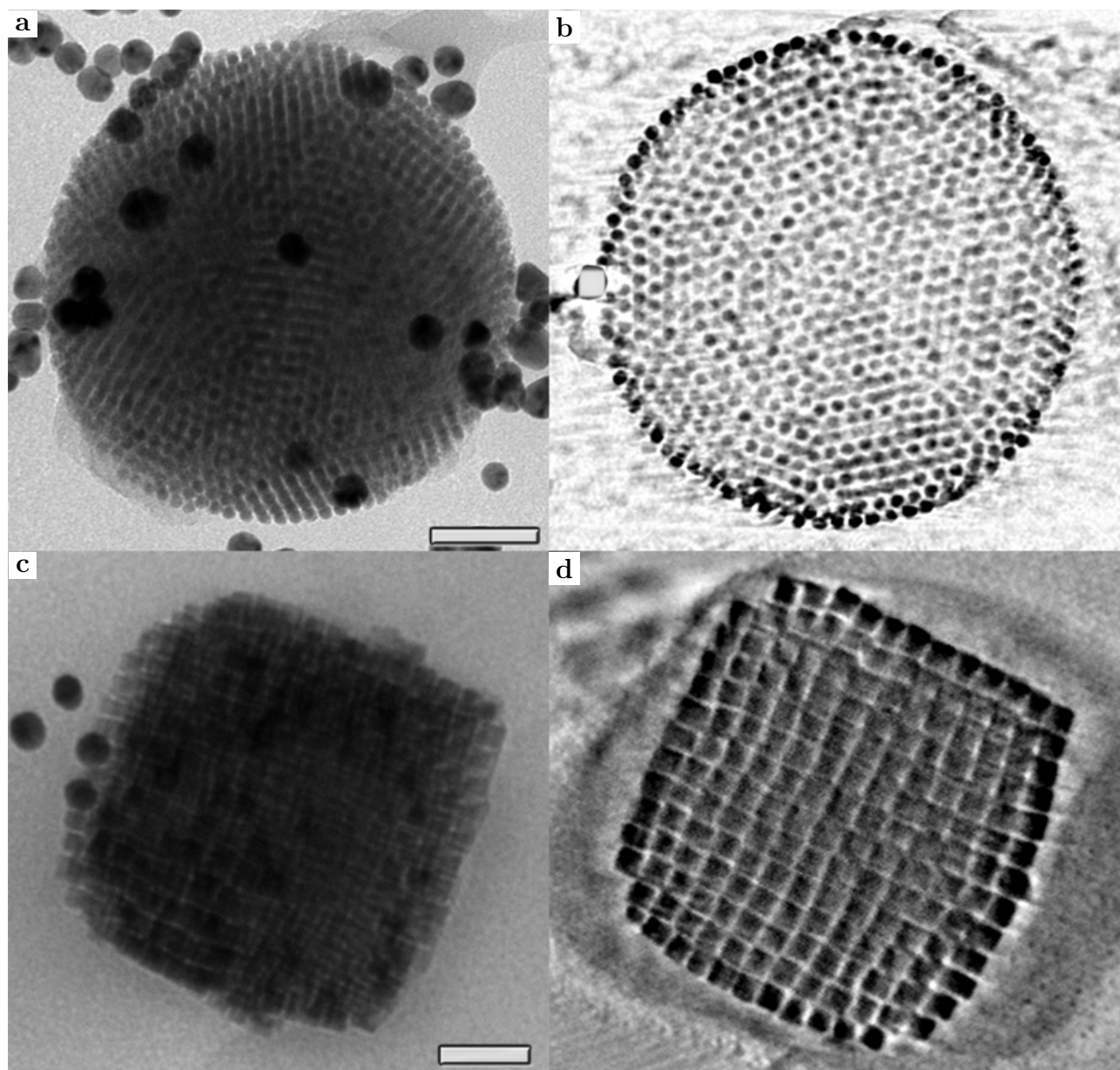


Figure 4.12: TEM images and ET reconstructions of two different types of supraparticles (SPs). **a)** A spherical SP made from 8.8 nm_{eff} iron cobalt oxide nanoparticles. The gold markers on the backgrounds are fiducial markers for the ET reconstruction (scale bar = 50 nm). **b)** Tomographic reconstruction of the SP showing high degrees of ordering in wedge shaped domains. **c)** Cubic SP built up from 12 nm cubic iron cobalt oxide nanoparticles (scale bar = 50 nm). **d)** Tomographic reconstruction of the cubic SP showing the ordering of the cubic nanoparticles.

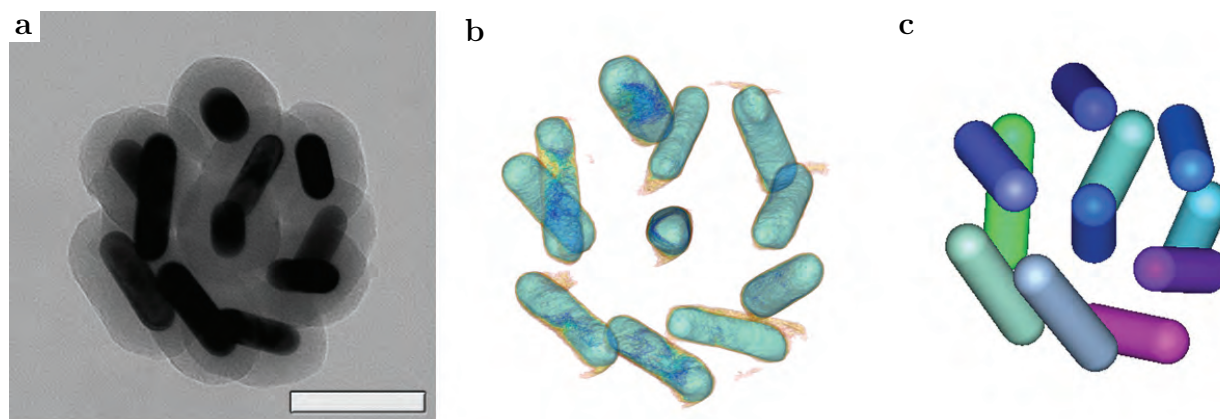


Figure 4.13: Supraparticle consisting of 11 silica coated gold nanorods (118.8 nm). **a)** Electron micrograph showing the clear intensity difference between the silica coating and the gold rods (scale bar = 100 nm). **b)** 3D model the SP as obtained from ET by tracing contours, showing the position, orientation and size of the gold nanorods. **c)** Particle positions, orientations, and lengths as obtained from a particle tracking algorithm developed for real-space rod-like particle tracking [120], here the colors indicate the orientation of the rods.

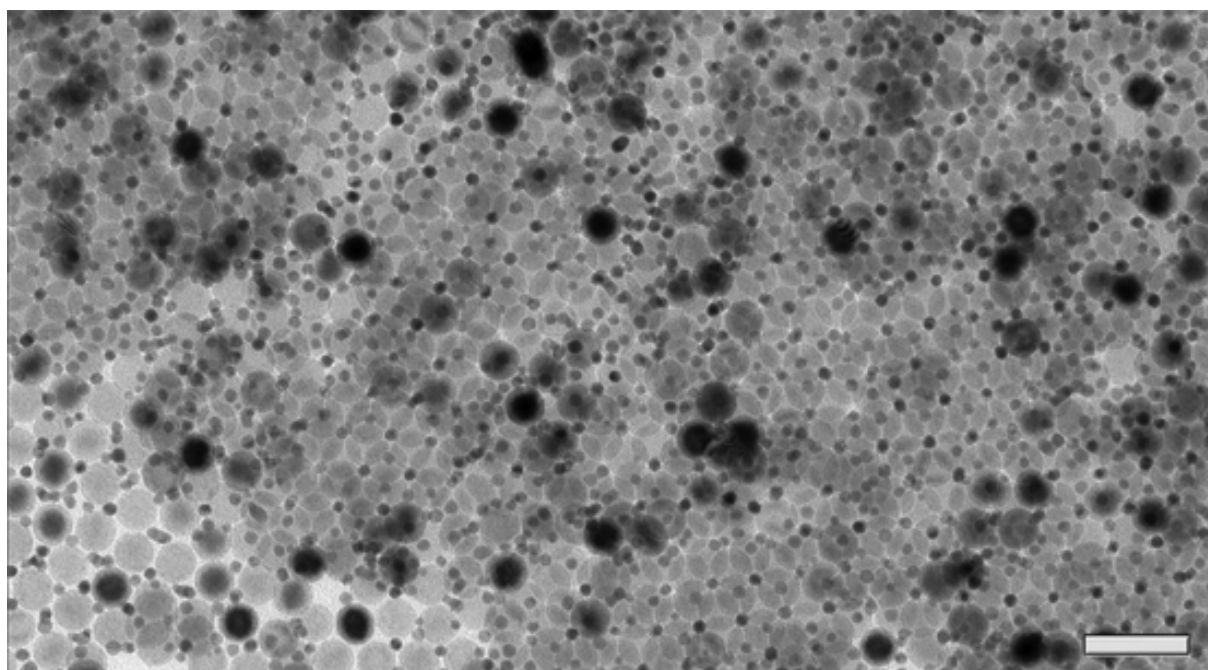


Figure 4.14: Electron micrograph of a binary superlattice consisting of 8.8 nm_{eff} gold and 18.9 nm_{eff} cobalt iron oxide nanoparticles self assembled on a TEM grid (scale bar = 50 nm).

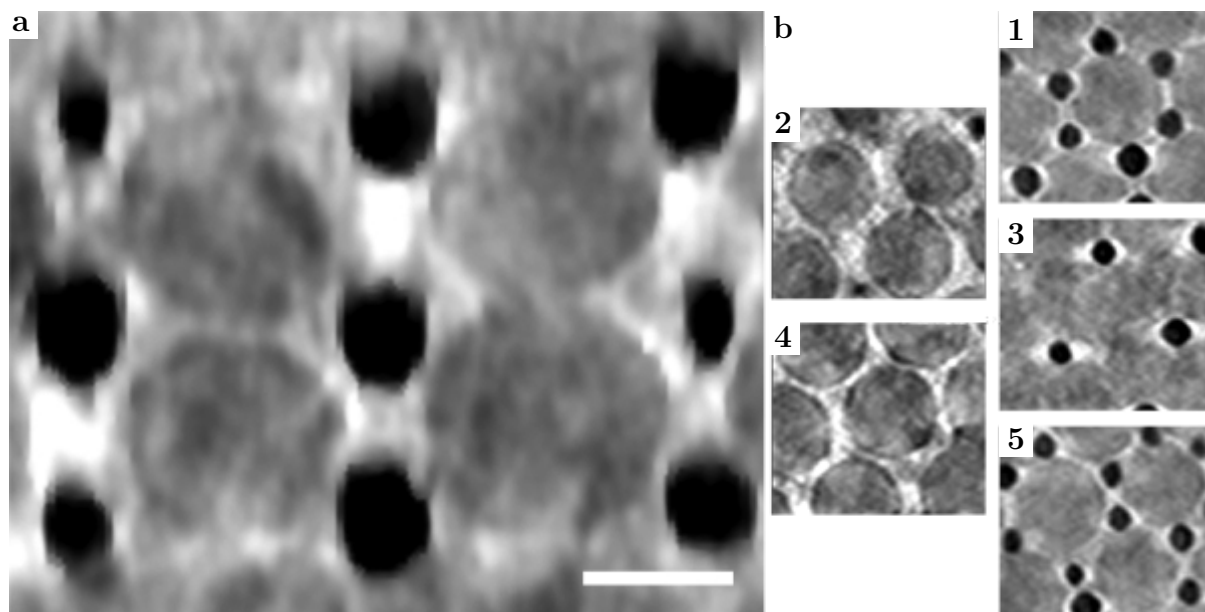


Figure 4.15: Orthoslices of a binary superlattice consisting of 8.8 nm_{eff} nm gold and 18.9 nm_{eff} cobalt iron oxide nanoparticles reconstructed from a tilt series acquired in bright field mode. **a)** Orthoslice of a part of the tomogram viewed from an angle of 90° with respect to the normal (scale bar = 10 nm). **b)** Orthoslices of the tomogram taken at 0° at 5 consecutive heights in the assembly.

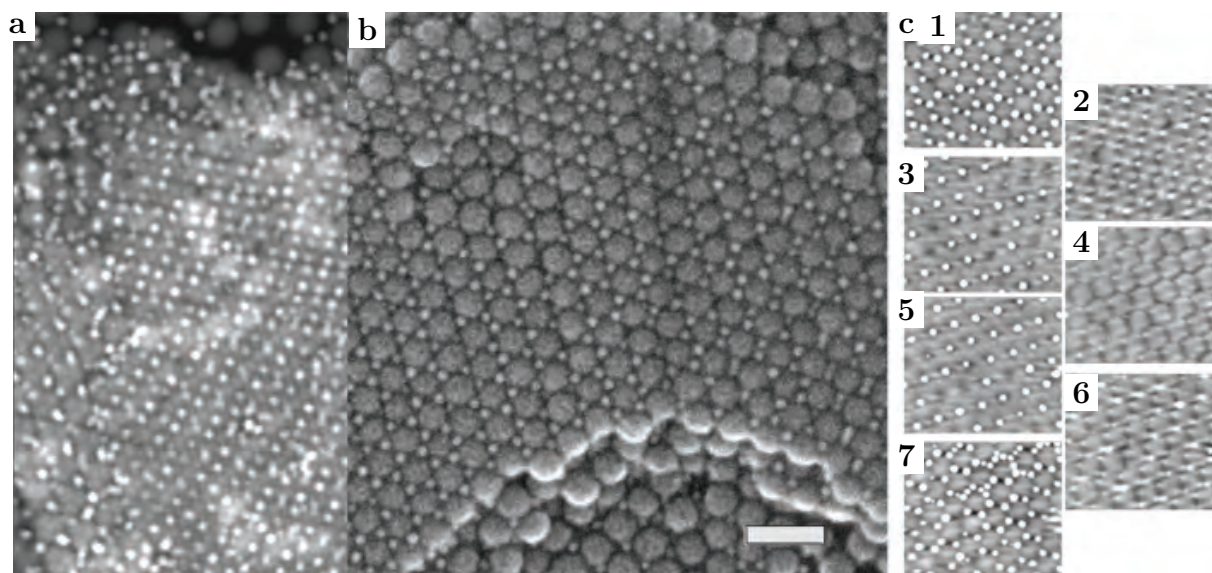


Figure 4.16: Electron microscopy images and orthoslices of a binary superlattice consisting of 8.8 nm_{eff} gold and 18.9 nm_{eff} cobalt iron oxide nanoparticles. **a)** HAADF-STEM image from the tiltseries, which was used for the ET reconstruction. **b)** A secondary electron STEM image of the same structure showing only the particles present at the surface of the structure (scale bar = 50 nm). **c)** Orthoslices of the tomogram taken at 0° (normal viewing angle) at 7 consecutive height intervals in the binary assembly.

4.7 Conclusion & Outlook

From the results presented in this chapter we can conclude that electron tomography (ET) reconstructions with nanometer precisions were made of colloidal particles synthesized for self-assembly, or self-assembled with another self-assembly step in mind. The ET reconstructions had enough resolution and contrast to resolve both the external and internal structure of these colloidal particles. It was found that the simultaneous iterative reconstructive technique (SIRT) algorithm resulted in less noise than the Back-projection algorithm, and using SIRT with 5 iterations was found to be the most suitable for tracing contours around the objects to make 3D models. Lowering the pixel density to speed up the reconstruction process had little impact on the quality of the reconstruction.

Using ET to analyze the placing and the number of patches on patchy silica colloids it was found that the positions of the patches were not in agreement with either a face centered cubic or a hexagonal close packed structure, indicating that during the surface coating step with 3-(trimethoxysilyl)propyl methacrylate the silica colloids were in a defect rich or glassy state instead of a colloidal crystal. For a stomatocyte the sequestered nanoparticle and the expected funnel could clearly be identified, showing that the core was indeed connected to the outside through a narrow opening. Two micron-sized bowl-shaped polydimethylsiloxane particles could, however, not be fully resolved as the contrast of the particles was weak and the spacing very small, if any. The analysis did show that the bowl shaped particles are flexible and can show strong deformation caused by drying. The analysis of rod-like particles showed that bullet shaped particles indeed had one flat end with a relative sharp edge and one convex end, and that coating this with silica resulted in a nearly spherocylindrical shape. For synthesized fluted rods we can conclude that the surface was indeed patterned with silica ridges over the lengths of the rods. In 2 of the 3 analyzed rods showed a hexagonal geometry in the ridge pattern was observed suggesting local hexagonal ordering of these rods at the time of the surface modification. The rods were found to be slightly conical shaped resulting in a wider base and a smaller top. Together with the observation that the patterning only spanned roughly half of the rods suggested that the rods were only touching with the wider base during the coating in the close packed structure.

Drying bullet shaped rods from a water phase at room temperature on a transmission electron microscopy grid resulted in deformations in the rods and the support films. These deformations were attributed to capillary effect caused by the drying water as they were not observed in freeze dried samples. Estimates, based on a linear elastic approximation, of the pressure needed to bend a silica rod to the observed deformation were on the order of ~ 100 MPa. This shows that for accurate ET analysis of colloidal system freeze drying or supercritical drying of the sample is needed to reduce artifacts.

The ET analysis of self-assembled nanoparticles showed for SPs consisting of spheres ordered wedge shaped domains of 8.8 nm_{eff} nanoparticles. Simple cubic packing of 12 nm cubes was observed in a cubic SP and a NaCl packing was observed for 8.8 nm_{eff} gold nanoparticles combined with 18.9 nm_{eff} cobalt iron oxide nanoparticles. Finally, it was shown that an algorithm designed for real-space tracking of colloidal rod-like particles was able to track 118 nm gold nanorods from an ET reconstruction.

From these findings we conclude that ET is a valuable method that can accurately resolve geometrical properties of colloidal particles and can yield valuable insights in their self-assembly behavior.

4.8 Acknowledgments

Bo Peng, Tian-song Deng, Marlous Kamp, Da Wang, and Daniela Wilson are gratefully acknowledged for providing the colloids and nanoparticle assemblies analyzed in this chapter. Hans Meeldijk and Chris Schneijdenberg are gratefully acknowledged for their help with the freeze drying experiments and tilt series acquisitions. Thijs Besseling is thanked for the 3D tracking of the silica coated gold nanorods.

Deformations of Supraparticles from Nanoparticles by drying forces

In this chapter the deformation from a spherical shape in nanoparticle supraparticles (SPs) is discussed in more detail. Deformations were observed as a result of capillary effects during drying, as a result of a magnetic field and as a result of using cubic nanoparticles instead of spherical ones.

5.1 Introduction

In literature, transmission electron microscopy (TEM) samples are typically prepared by drop casting, dip coating, or are scooped up from a liquid-liquid or liquid-air interface [40, 150–152]. Capillary effects during drying are prominent in such deposition techniques, as was shown in Ch. 4. Having such forces act upon nanoparticle structures can alter the geometry of the superstructure and can change the internal and surface ordering and/or the spaces between the particles, see e.g. Ref. [110, 153] for examples of such effects already mentioned in literature.

For this chapter deformations in supraparticles (SPs) were studied as model systems for deformations in 3D nanoparticle structures, and how the drying processes can be used to manipulated the formed structures. In the previous chapters it was presented that nanoparticles, in slowly drying emulsion droplets, can be self-assembled into ordered super structures. This ordering occurred as the volume fraction in the droplets increased during the evaporation of the inner phase. At the final stages of this drying process the oil-water interface would have to recline within the more or less compacted SP. At high volume fractions, the osmotic pressure inside the droplet would rise and the packing effects of, for instance, non-spherical particles could start to compete with the shape of the SP, which would be the shape that minimizes the droplets surface tension. In addition after the drying front would have gone inside the SP, as will be detailed below, the small radius of curvature of the meniscus inside the close packed structures would exert large directional forces onto the packing. As was already mentioned in the previous chapter depending on the shape of the nanoparticles this sometimes resulted in non-spherical SPs. Examples of these effects of the drying forces will be also shown in this chapter.

In the case that the SPs have already formed in the water phase, self-assembly has already occurred prior to deposition and a comparison between freeze dried (FD) and room temperature (RT)-dried SPs can be made. When a dispersion of such 'dried-of-oil' particles were made to dry on e.g. a TEM grid any deformation of the spherical shape would be the result of drying forces induced by drying of the water film, making them a suitable system to study the possible plastic deformations of such self-assembled structures. This will tell us how important the sample preparation is for an accurate representation of nanoparticle systems, but also how the drying processes can be used to manipulate the shape of the SPs. As the inorganic cores of the nanoparticles, making up the SP, have a high Young's modulus it is most likely that any plastic deformation of the spherical SP shape resulted from a deformation/motion within the interpenetrating steric stabilizer molecules.

5.2 Capillary forces

Before presenting the analysis providing simplified estimates of the drying forces acting upon the colloids it should be remarked that these estimates were made for drying forces acting on the polymer/surfactant coated outside of the spherical SPs. While it was already mentioned above that drying forces inside the porous SPs could have been in operation similarly as for the drying oil front, these forces are much more difficult to calculate, see

for example Ref. [154] where these forces are calculated for clusters of not more than 15 particles. The following estimates are based on the curvature of the SPs and should only be considered an upper estimate of the induced forces as the radii of curvature inside the SPs will most likely be smaller than those encountered on the outside.

During the drying the capillary forces arise at the liquid-vapor-solid interfaces and are, in general, proportional to the vapor pressure [155]. These forces are the result of tendencies of a system to minimize the sum of interfacial tensions. This gives rise to a preferential contact angle of the liquid solid interface as proposed by Thomas Young in 1805 [156]:

$$\gamma_{sv} - \gamma_{sl} - \gamma \cos \theta = 0 \quad (5.1)$$

This is called the Young's equation, where γ_{sv} is the surface tension between the solid and the gas phase, γ_{sl} is the surface tension of the solid and the liquid phase, γ is the surface tension between liquid-air interface, and θ is the equilibrium contact angle.

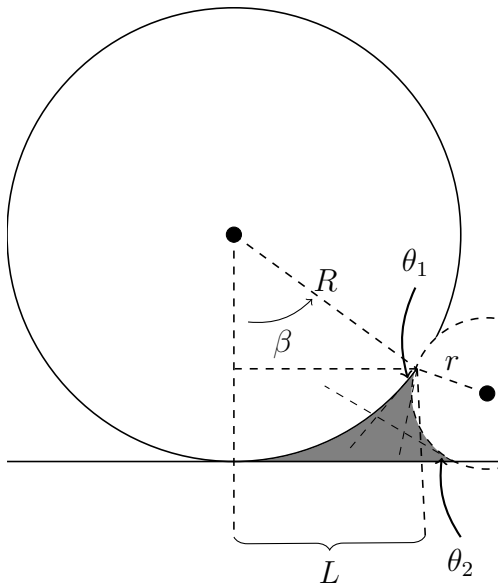


Figure 5.1: Schematic representation of the capillary force working on a sphere as a result of drying on a solid flat interface. β is the angle from the center of the sphere to the edge of the solid-liquid-air interface. θ_1 and θ_2 are the contact angles of the sphere and the substrate respectively. R is the radius of the sphere (object of interest), r is the size of an imaginary circle fitted to the curved interface of the liquid as a result of the contact angles.

To estimate the strength capillary forces exert on a sphere a model proposed by Butt en Kappl was used [157]. Butt and Kappl derived that the capillary forces on a sphere is given by:

$$F = \pi\gamma R \sin \beta \left[2 \sin(\theta_1 + \beta) + R \sin \beta \left(\frac{1}{r} - \frac{1}{L} \right) \right] \quad (5.2)$$

The level of the liquid between the colloid and the plane together with the contact angles determines the angle β . For this method the shape of the liquid-air interface

between the object and the plane is approximated to have a uniform curvature with a radius r , Fig. 5.1. The force F is in newton N , R is the radius of the colloid and D is the distance between the colloid and the plane in meters ($D=0$ in Fig. 5.1). The radius r is determined by both the contact angles θ_1 at the colloid and θ_2 at the plane and is calculated as follows:

$$r = \frac{R \sin(1 - \cos\beta) + D}{\cos(\theta_1 + \beta) + \cos\theta_2} \quad (5.3)$$

The distance L used in 5.2 can also be derived from this scheme as is shown in Eq. 5.4:

$$L = R \sin\beta - r[1 - \sin(\theta_1 + \beta)] \quad (5.4)$$

The resulting force as a function of angle β is plotted in Fig. 5.2. For this graph a spherical object with a radius $R = 0.5 \mu m$, and a distance between the object and the substrate of $D = 0$, and a surface tension of $\gamma = 0.0725$ were chosen since this chapter focuses on the drying forces and these forces are assumed to occur after the particles made contact with the support. As seen in this graph the strength of the forces is dependent on both the contact angle of the support and at surface of the object. In this graph contact angles θ_1 and θ_2 are plotted ranging from ideal wetting ($\theta = 0^\circ$) for both surfaces up to $\theta = 80^\circ$.

For the support contact angles anywhere between 25° and 75° are realistic, and dependent on how long ago the TEM grid was made and whether the support was glow-discharged or not. For the spheres the contact angles are harder to determine since these are a combination of dextran, SDS and possibly oleic acid at unknown concentrations. If the surface is assumed to be dextran then a contact angle between $\sim 50^\circ$ and $\sim 60^\circ$ can be assumed [158]. From the graph it can be seen that the force on the sphere increases as the liquid interface recedes during drying. A conservative estimate based on contact angles of 60° and a β of 30° yields a force of $50 \cdot 10^{-9}$ N working over an area of roughly $1.96 \cdot 10^{-13} m^2$, which is the equivalent of 2.6 kg pressing on $1 cm^2$ or 255 kPa.

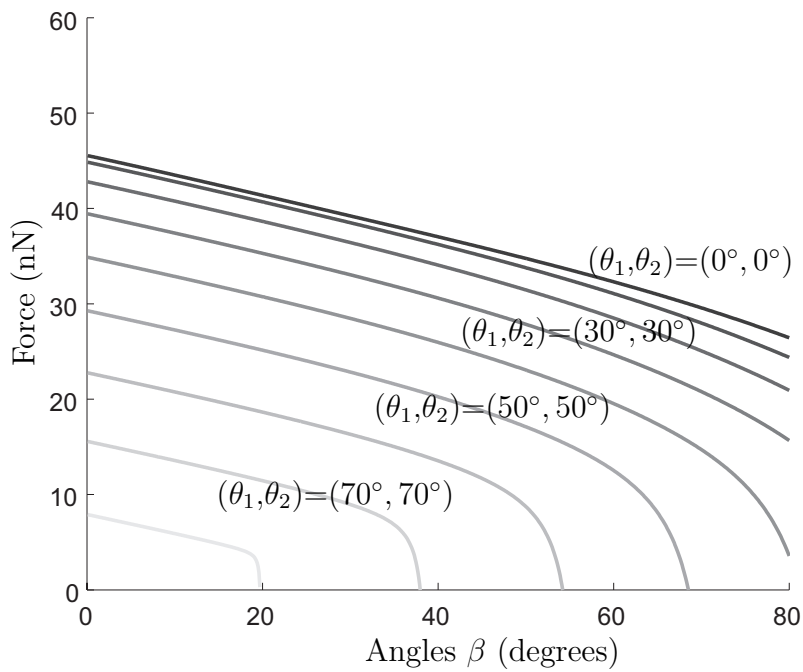


Figure 5.2: The strength of the capillary forces in nanonewton (nN) on a particle of radius $0.5 \mu\text{m}$ as a function of angle β in degrees. The colors represent different contact angles for the surface and the sphere. The graphs represent from top to bottom contact angles from $(\theta_1, \theta_2) = (0^\circ, 0^\circ)$ to $(\theta_1, \theta_2) = (80^\circ, 80^\circ)$.

5.3 Experimental Details

To study the influence of drying during sample preparation SPs were drop-cast from a water phase on a TEM grid and allowed to dry. The resulting samples were compared with freeze dried samples that were made as described in Ch. 4. For analysis TEM, electron tomography (ET), and scanning transmission electron microscopy (STEM) were used. For all experiments in this chapter cobalt iron oxide nanoparticles with low polydispersities, typically 4 % or lower, were used as constituents. These particles were synthesized as described in Ch. 2. The sizes used for the self-assembly in this chapter were 8.8 nm_{eff} (4 %), 12.6 nm_{eff} (4 %), and 20.4 nm_{eff} for spherical particles and 12 nm cubic nanoparticles.

5.3.1 Equipment and software

For TEM analysis a Fei Tecnai 12 with a tungsten tip was used, operating at 120 kV in bright field mode. For ET analysis a Fei Tecnai 20 with an LaB₆ filament operating at 200 kV was used. Freezing the samples for freeze drying was performed using a Vitrobot Mark 2 plunge freezer. To carbon coat TEM grids we used a Cressington 208 carbon coater. Tomographic reconstructions were done using IMOD 4.3 as described in Ch. 4. Centrifugation was done with an Eppendorf 5415c centrifuge operating at 1500 rpm for 30 sec.

5.3.2 Sample preparation

For TEM grids 200 mesh copper grids were used with a ~25 nm thick Solutia support film carbon coated for ~7 sec. Gold nanoparticles with a diameter of ~16 nm were used as fiducial markers in all samples as described in section 4.5.4. These were deposited on the support prior to sample preparation. All samples were washed prior to deposition by centrifuging 1 ml of sample in an Eppendorf tube, removing the supernatant and redispersing the sediment in ~10 μL water, this was done to remove excess dextran and SDS and to concentrate the sample. For the cubic nanoparticles a batch with cube dimensions of 12 nm was used, these are presented in section 2.5.4, and these nanoparticles have an approximate distance of nearest approach of 2.7 nm. However, the cube dimensions will not be given in effective diameters due to large variations in this distance.

Regular sample preparation, without freeze drying, was done by drop-casting; depositing a droplet of ~3 μL on a ~25 nm thick polymer film coated TEM grid (Solutia support) and allowing the water to evaporate. This will be referred to as room temperature drying (RT-drying).

For freeze drying (FD) the same sample preparation method was followed as described in Ch. 4: A droplet (~3 μL) of SP-suspension was deposited on a glow discharged (using a Cressington 208 carbon coater) TEM grid and blotted for 1 second using filter paper, and plunged in liquid ethane at roughly -170 °C. The samples were then FD by heating to -90 °C at ~5°C·m⁻¹ under vacuum and slowly heated at < 1°C·min⁻¹ to room temperature.

Deposition in a magnetic field

As described in Ch. 2 the cobalt iron oxide nanoparticles are ferrimagnetic and will become magnetized in the presence of a magnetic field. A SP-suspension self-assembled from ferrimagnetic nanoparticles was deposited in a magnetic field to study if this force was strong enough to deform the SPs and/or how this influenced the sample preparation. To achieve this the TEM grid was placed in the end of a self-closing tweezer with a ring ferrite speaker magnet attached to the other side ~5 cm away. This resulted in a magnetic field either from the magnet or at the tip of the tweezer in which the droplet was allowed to dry.

5.4 Results & Discussion

In SPs built up from spherical nanoparticles two types of deformations were observed. One was the deformations as a result of a contact between SPs and the support, so of SPs lying not in contact with others. These free deformations will be referred to as normal deformations, as these deformations were typically parallel to the normal viewing angle in the electron microscope. The second type of deformations was seen in close packed SP-assemblies where multiple SPs were in contact, either by drying forces or as a result of a magnetic field in combination with drying. This second type of deformation was visible using regular TEM as the forces were typically perpendicular to the normal viewing angle. These types of deformations will be referred to as lateral deformations.

Note that if lateral deformations occur it is likely that parallel deformations have occurred as well as there will be liquid between the particle and the surface as well as in between the particles.

5.4.1 Normal deformations

Normal deformations were parallel to the direction of the electron beam, and as a result were only visible at high tilt angles. For example analyzing RT-dried and FD SPs from an angle of 0° (normal viewing angle) no difference in their shape were discerned. In contrast, viewing the SPs from a side using ET revealed strong deformations in the RT-dried SPs where no deformations were observed in the FD structures, Fig. 5.3c, d. This pattern was observed in both of the examined SPs consisting of 8.8 nm_{eff} cobalt iron oxide nanoparticles.

In addition, the nanoparticles in the deformed SPs showed order through the entire assembly including near the most strongly deformed parts of the clusters. This indicated that the nanoparticle constituents were still able to reorder and adapt to the newly deformed shape and were not 'shear-melted' in the process. This meant also that these particles were still able to move in the dense structure as a result of the strain. The major differences in the crystal structures is a result of the number of nanoparticles in the SPs and will be discussed in more detail in Ch. 6.

Since the deformation was predominantly in one direction the aspect ratio can be used as a rough measure for the amount of deformation observed in the RT-dried SPs. This aspect ratio was measured for a total of 6 SPs, two for each nanoparticle size (8.8 nm_{eff} , 12.6 nm_{eff} , 20.4 nm_{eff}). It was found that SPs consisting of small (8.8 nm_{eff}) nanoparticles showed more deformation than SPs consisting of larger (20.4 nm_{eff}) nanoparticles; in which almost no deformations were observed. The aspect ratios found for the two SPs consisting of 20.4 nm_{eff} nanoparticles were both 1.00. For SPs consisting of 12.6 nm_{eff} nanoparticles aspect ratios of: 1.06, 1.09 were found. When using 8.8 nm_{eff} nanoparticles aspect ratios of: 1.16, 1.17 were measured. Plotting the measured aspect ratios versus the nanoparticle size reveals an inverse size dependence of the deformation, Fig. 5.4. The measured SPs were of roughly equal diameters 200-300 nm to account for differences in the capillary forces as a result of this. These findings suggest that the size of the nanoparticles that were used have a strong influence on the rigidity of the SPs. As already mentioned, this change in rigidity/plasticity is most likely a result of the higher surface

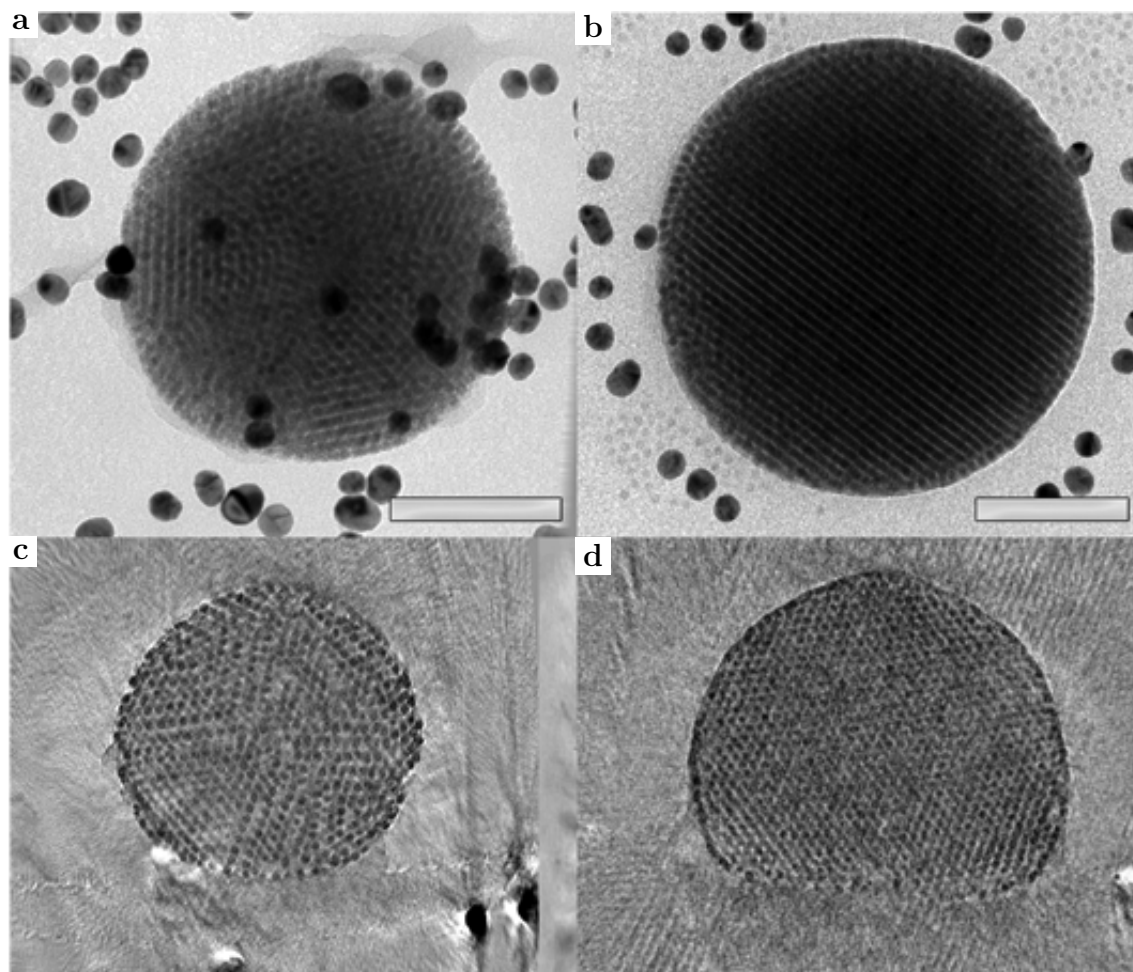


Figure 5.3: Electron micrographs and tomographic reconstructions showing the differences between room temperature dried (RT-dried) and freeze dried (FD) supraparticles (SPs) (scale bars are 50 nm). **a)** TEM image of a freeze dried SP viewed from 0° . **b)** A RT-dried SP viewed from 0° . **c)** Tomographic reconstruction of the freeze dried SP viewed from an angle of -90° . **d)** Tomographic reconstruction of a RT-dried SP viewed at an angle of 90° .

area for smaller particles and therefore a relatively larger amount of ligand molecules between the nanoparticles being able to providing the ability to transform ('lubricate') the transformations/deformations. In section 2.5 it was also determined that there was more interpenetration of the stabilizing molecules for larger core sizes, this could also have made the structures more rigid and less amendable to deformations for a similar force.

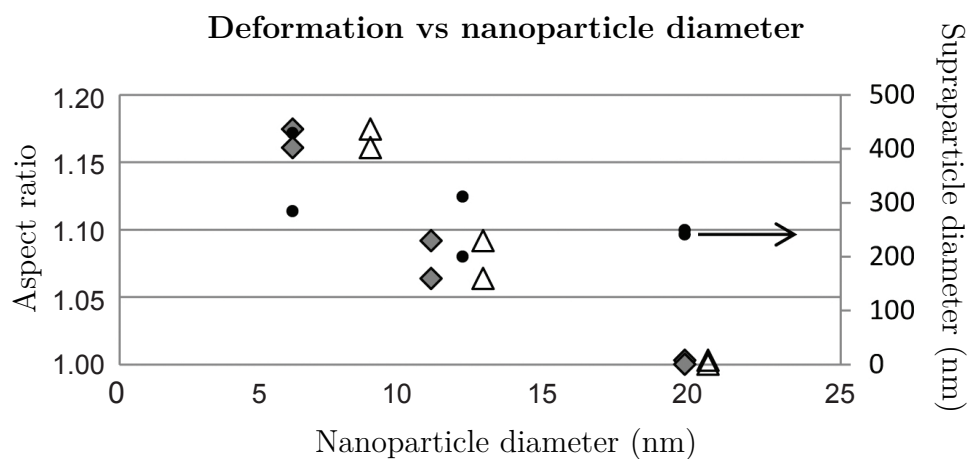


Figure 5.4: Graph showing the aspect ratio of RT-dried-SPs plotted against both the core and effective diameter of the constituent nanoparticles (left axis). Also shown in the graph are the respective SP sizes (right axis)

5.4.2 Lateral deformations

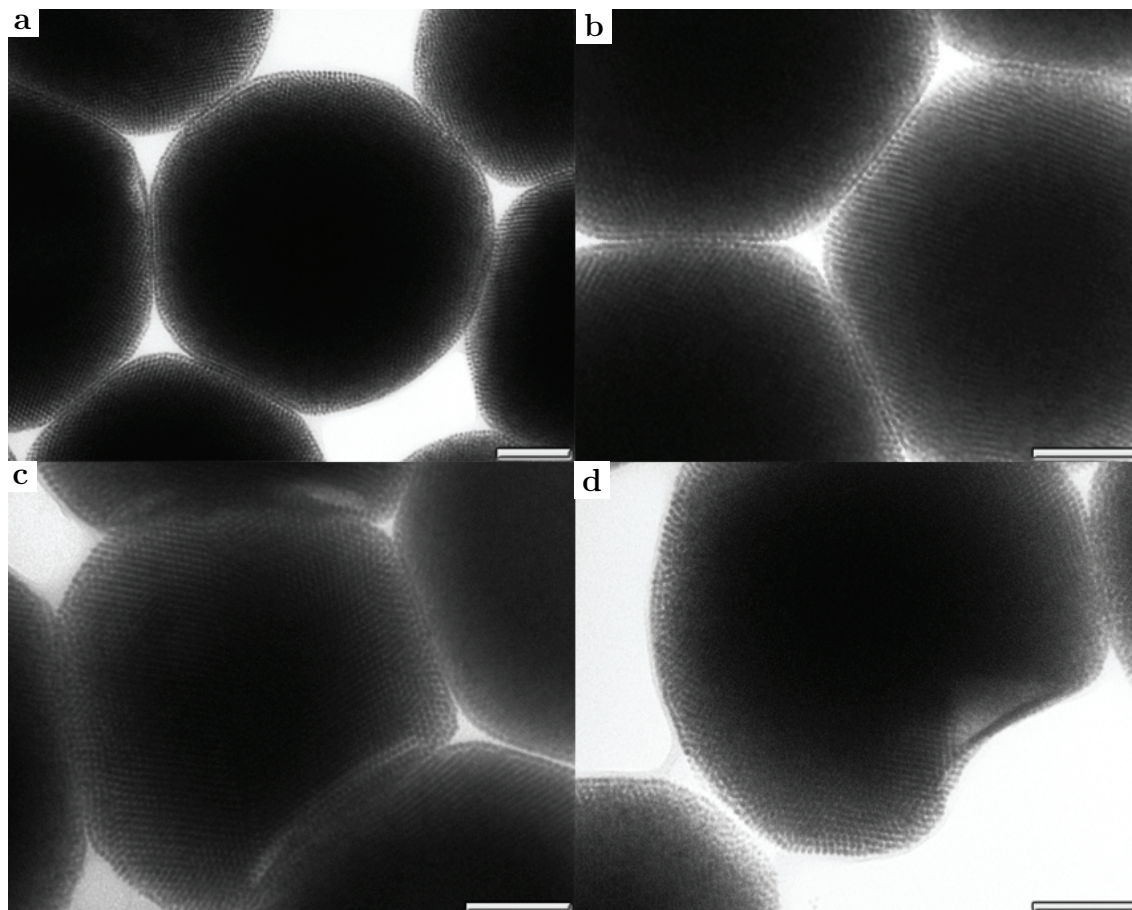


Figure 5.5: Transmission electron micrographs showing RT-dried SPs viewed from the normal viewing angle (scale bars are 100 nm). **a)** Small deformations in the central SP caused by the 5 neighbors. **b)** Large deformations in the central SP as a result of at least three neighbors. **c)** Indentation as resulting of an intruding neighboring SP. **d)** A indented SP with the intruding SP no longer present.

Lateral deformations were observed in RT-dried SPs when two or more SPs were in contact. In these assemblies deformations were observed from the normal viewing angle, Fig. 5.5. These deformations ranged from small flattened patches, Fig. 5.5a, to nearly hexagonally shaped SPs, Fig. 5.5b. The observations were in line with the previous findings, and here the internal constituents showed order through the entire structure also near the strongest deformations.

For some particles concave deformations were observed. These SPs appeared to have been intruded by a neighboring SP, Fig. 5.5c, where occasionally the protruding particle was missing, Fig. 5.5d. As expected with a plastic deformation, in SPs that experienced this deformation with the intruding SP removed did not return to their original shape but retained the concave feature except for a single layer of particles that seemed to be slightly puffed out, Fig. 5.5d. This most outer layer of nanoparticles was commonly observed on

the SPs and seemed to distinctively not follow the internal crystal structure, indicating that these layers had different mechanical properties. It is likely that these were particles stuck on the interface which formed a separate shell around the assemblies. Similar shell like structures, but then hollow, were observed, and are presented in Ch. 3.

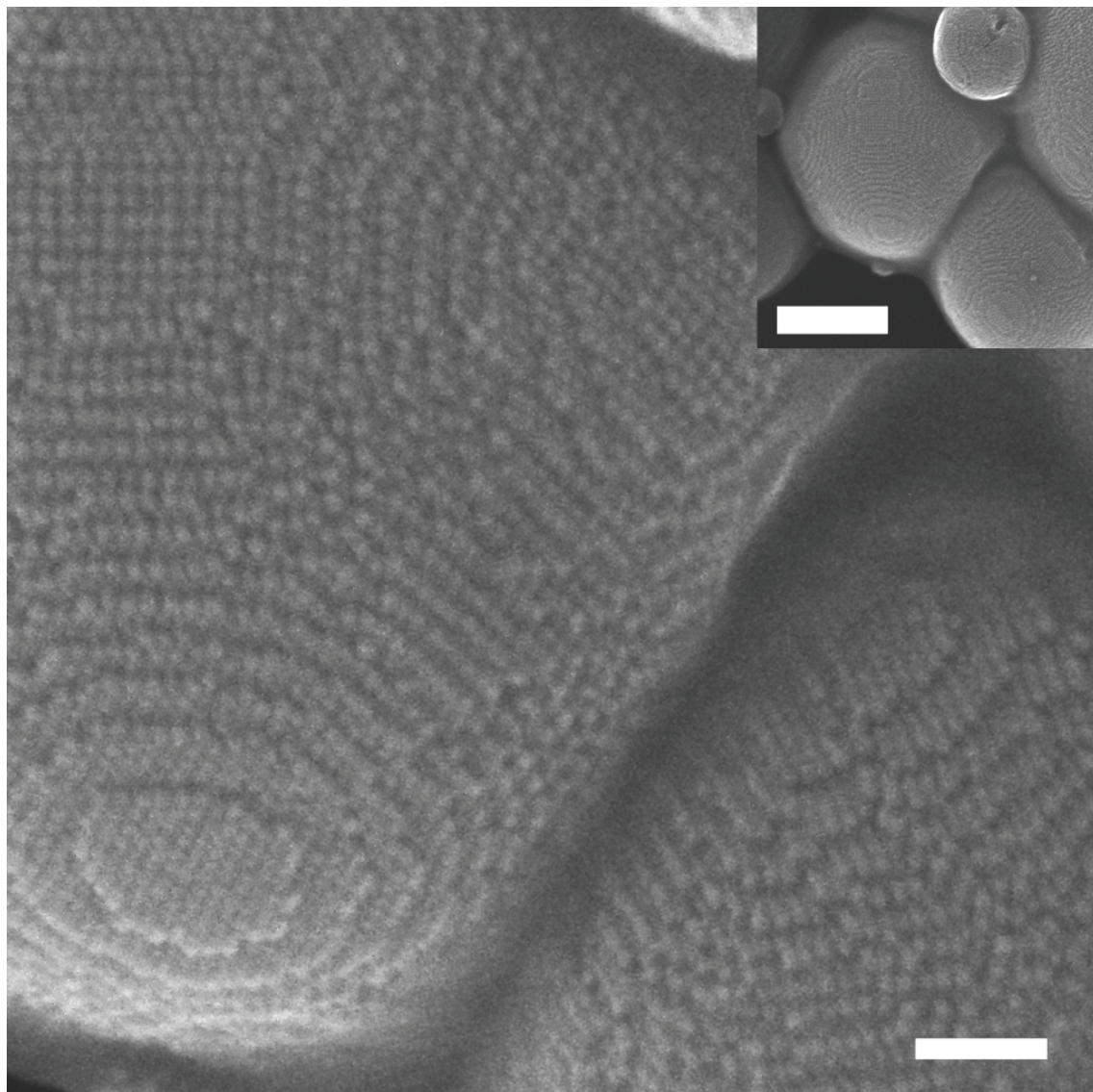


Figure 5.6: Secondary electron STEM electron micrographs showing the surface of two deformed SPs consisting of 8.8 nm_{eff} nanoparticles with highly ordered surfaces (scale bar = 50 nm). Inset: Lower magnification of the deformed colloids (scale bar = 250 nm).

The surface packing of the SPs was studied in more detail using secondary electron images recorded in STEM mode. It was found that these surface layers were highly ordered even though they were not or no longer part of the ordered internal structure as can be seen in Fig. 5.6. In this figure the nanoparticles on the surface of two SPs are shown. The nanoparticles are not only highly ordered but show square ordering (top left) and hexagonal ordering (bottom left). These types of ordering are consistent with the

FCC [100] and FCC [111] crystal planes. This suggested that these surface particles were part of the crystalline domains in the close packed SPs prior to deformation. During the deformation the nanoparticles retained their ordered respective positions on the surface but the surface was displaced with respect the internal crystalline structure. This FCC ordering of the surface is discussed in more detail in Ch. 6.

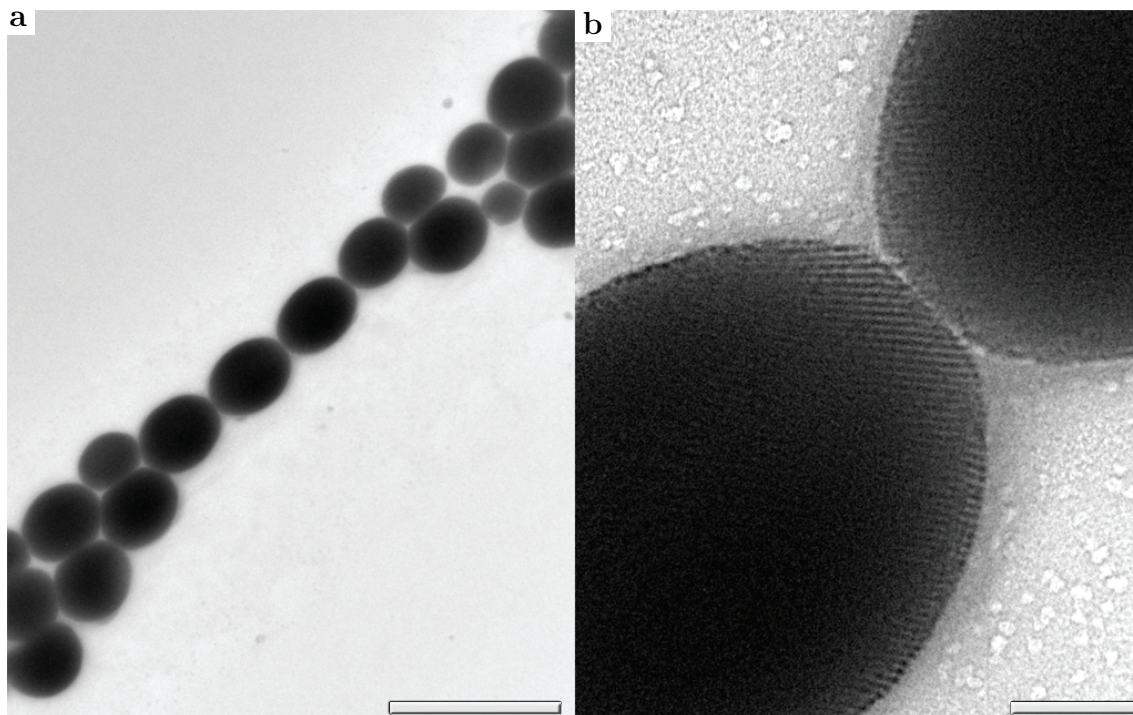


Figure 5.7: Transmission electron micrographs showing RT-dried 8.8 nm_{eff} SPs deposited in the presence of a magnetic field, resulting in string like assemblies of ellipsoidal SPs. **a)** The string like formations as observed after drying. **b)** Contact area between two deformed SPs showing ordered patterns of the nanoparticle constituents indicating (locally single) crystalline order.

Depositing the SPs, made up out of 8.8 nm_{eff} nanoparticles, on a TEM grid while subjected to a magnetic field resulted in string like formations of the SPs, Fig. 5.7a. This means that the SPs possess a magnetic dipole strong enough to induce the string formation as a result of the magnetic properties of the individual cobalt iron oxide nanoparticle constituents. Due to the string-like geometry the capillary forces working on the SPs were only present on either side of the assembly (and towards the support). This likely is what caused the resulting ellipsoidal SPs flattening at the tips, Fig. 5.7b, while the ellipsoidal shape is most likely the result of elongation of the SP in the magnetic field. Deformation of SPs as a result of purely the magnetic field without the capillary forces could not be observed since all SPs observed in such samples were in contact with at least a single neighboring SP when assembled in an magnetic field. These preliminary, but clear findings, open up the possibility to also deform SPs made from NPs of the size as shown here by electric fields as well [130].

5.4.3 Self-assembly of cubic nanoparticles in emulsion droplets

In a SPs self-assembly experiment 12 nm cubic iron cobalt oxide nanoparticles were used instead of the typical spherical nanoparticles. The emulsion was sonicated using a sonic bath. When the emulsion droplets were heated the cyclohexane evaporated and SPs were obtained similar to the previous experiments. However, TEM analysis revealed that the shape and the internal packing of the SPs was different from the spherical constituent counterpart. Several different SP shapes were identified: spherical, cubic, rectangular, and parallelepiped as shown in Fig. 5.8. The SPs showed ordered internal structures with simple cubic packing as was shown in the previous chapter where tomography was performed on these rectangular SPs. The rectangular and spherical shaped SPs were found side by side on the same grid after sample preparation indicating that the conditions in which they were formed were at the border of being influenced more by the nanoparticle shape or the surface tension of the emulsion droplet. The non-spherical shaped SPs were mostly observed for the larger SPs. More examples of these are shown in Fig. 5.9.

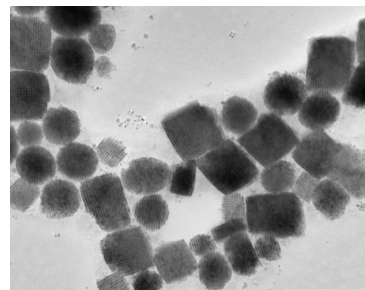


Figure 5.8: Transmission electron micrograph showing SPs of cubic nanoparticles, forming spherical and rectangular clusters (scale bar = 500 nm).

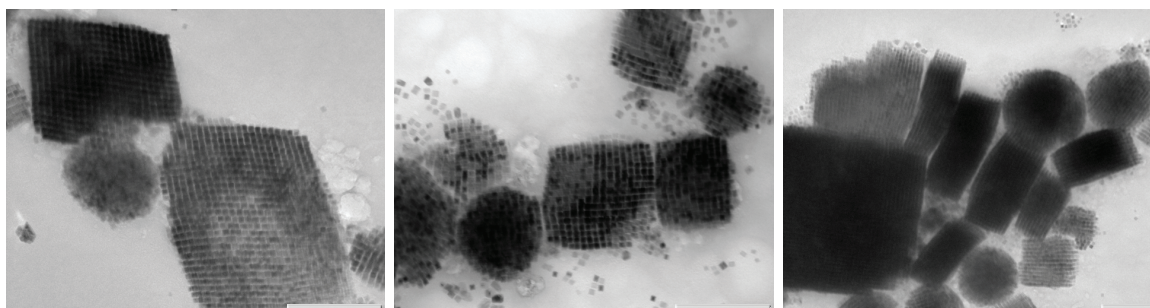


Figure 5.9: Transmission electron micrographs of spherical and rectangular clusters, consisting of cubic nanoparticles, self-assembled in emulsion droplets (scale bars are 200 nm).

5.5 Conclusion & Outlook

Lateral and normal deformations were observed in SPs consisting of cobalt iron oxide nanoparticles which were coated with the steric stabilizer which had a thickness of about ~ 1.5 nm. As explained in Ch. 2 these stabilizing molecules also partially interpenetrated with a core size dependency, as shown in Fig. 2.10. The normal deformations were the strongest in SPs consisting of 8.8 nm_{eff} nanoparticles, less in SPs consisting of 12.6 nm_{eff} nanoparticles and not observed in SPs consisting of 20.4 nm_{eff} nanoparticles. These deformations were most likely the result of an increased volume fraction of the stabilizers for the smaller particles, although the nanoparticle size dependent interpenetration of these molecules, as presented in Ch. 2, might be an influencing factor as well, as less interdigitated molecules are likely more mobile allowing more freedom of motion for the nanoparticles.

Studying the lateral deformations at contacts between SP neighbors showed strong deformations at the contact point between two or more SPs. These lateral deformations showed extensive reordering of the nanoparticles as well, showing that these interaction are not just with the substrate but also between the SPs, and that the nanoparticles are able to reorder and adapt to the deformed geometry.

We found that these SPs exhibit a paramagnetic behavior strong enough to align them in string like patterns. In these string like patterns the SPs deformed to ellipsoidal assemblies with flattened tips these shapes were most likely the result of the magnetic field (ellipsoidal shape) and of the capillary forces (flattening of the tips) working both to deform the SPs. It will be intriguing to induce similar effects with electric fields.

Using cubic instead of spherical nanoparticles resulted in the strongest deformations in the SP shapes, forming aside of spherical also cubic, rectangular, and parallelepiped shaped SPs. This shows that the influence from the cubic nanoparticles was bordering the influence from the surface tension of the emulsion droplets.

Finally, we can conclude that the forces working on assemblies of small ($< \sim 20.4$ nm_{eff}) nanoparticles are strong enough to move these constituents around and alter their superstructure. Therefore, to study such pre-assembled objects without deformations, as a result of capillary forces, freeze drying or supercritical drying is necessary.

5.6 Acknowledgments

Hans Meeldijk is gratefully acknowledged for the help with the freeze drying experiments. Naomi Winkelman is thanked for fruitful discussions on tomographic analysis.

Entropy Driven Icosahedral Packing of Hard Spheres in Spherical Confinements

In Ch. 3 we showed that the self-assembled nanoparticles in spherical confinements formed supraparticles resembling clusters with icosahedral symmetries. In this chapter, through 3D electron tomography (ET) analysis, confocal microscopy and event driven molecular dynamic simulations we confirm that these SPs have an icosahedral internal ordering if they consist of less than ~ 70.000 spheres. In addition, we show that entropy alone is enough for hard spheres to form supraparticles with icosahedral or surface reconstructed icosahedral symmetries when self-assembled inside a spherical confinement, showing that the self-assembly behavior we observe in this research is characteristic for hard-sphere like particles. We also show that the formation of these supraparticles and their final crystalline symmetries is determined by the number of spheres in the confinement.

6.1 Introduction

In 1952 Sir Charles Frank proposed that the most favorable local structures in simple liquids have short-ranged icosahedral symmetries [159]. Such ordering occurs when 12 particles are arranged around a central particle. Later it was found that this geometry tends to minimize attractive, Lennard-Jones-like, interactions and has shown to be entropically favorable [160, 161]. However, the characteristic five-fold symmetry of an icosahedra is not compatible with long-range positional order and inhibits the growth of large icosahedral clusters. And as a result, even though liquids often contain many local icosahedral centers [159, 162–164], they rarely grow out into a crystal [165]. The thermodynamically stable phase for hard spheres, the face-centered cubic (FCC) crystal, does not contain 5 fold symmetries. The FCC crystal structure maximizes the entropy at high densities, with a highest possible volume fraction of $\phi = 0.74$ at infinite pressure [12, 14]. Since locally the icosahedral ordering is favored and on long range the FCC crystal structure is favored, the question is raised over what length-scales this transition can be extended.

A dense non-crystallographic packing of spheres featuring a global icosahedral symmetry was theoretically proposed by Alan Lindsay Mackay in 1962 [102]. A 3D rendering of such a structure consisting of 147 spheres is shown in Fig. 6.1, a icosahedral wireframe is superimposed to accentuate the geometry of the structure. A Mackay icosahedron consists of 20 tetrahedral FCC packed domains pointing towards the center separated by FCC twinning planes. The structure has 12 vertices reflecting the smallest possible icosahedra, as mentioned before, consisting of a core particle with 12 surrounding particles. The Mackay structure has been observed and studied theoretically for atomic and molecular clusters [166–169], and clusters of nanoparticles [41, 170–172]. In these self-assembly studies the formation of structures with icosahedral ordering is mainly attributed to energetic interactions [41, 173, 174] together with kinetic effects [170], hierarchical self-assembly [168], or intricate growth mechanisms [171, 172]. In addition, Mackay icosahedra were found to correspond to minima in free-energy landscapes of Lennard-Jones clusters [175]. In hard sphere systems these interactions are not present and self-assembly is purely entropy driven. To make finite sized hard-sphere crystals a confinement can be used, e.g. such as presented in Ch. 3. It is known from theory and shown in experiments that such a spherical confinement can change the equilibrium phase of hard-spheres but only on small length scales [176, 177].

In this chapter we show that large icosahedral clusters can form by entropy alone when self-assembled in a spherical confinement, and show that the number of spheres inside the confinement determine whether the icosahedral or bulk-like FCC ordering is favorable. To show this self-assembly behavior nanoparticles, presented in Ch. 2, were self-assembled

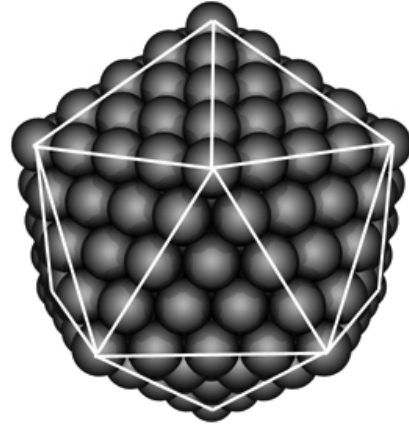


Figure 6.1: Icosahedron wireframe model superimposed on a 3D model of a Mackay icosahedron consisting of 147 spheres.

according to the emulsion method proposed in Ch. 3 and analyzed using electron tomography (ET), as described in Ch. 4. To show that this behavior is not characteristic for nanoparticles, self-assembly experiments of micron size colloids in emulsion droplets were performed as well. To analyze SPs built up from these larger colloids confocal microscopy was used.

6.2 Experimental Details

Colloidal self-assembly in spherical confinement was studied using SPs formed using the method described in Ch.3.4.3. The micron sized colloids were hydrophilic as opposed to the hydrophobic nanoparticles, to accommodate for this the emulsion method was changed to using a water in oil emulsion for these colloids instead. The internal packing of nanoparticle-SPs was studied using ET and the surface packing was studied using secondary electron scanning transmission electron microscopy (SE-STEM).

6.2.1 Chemicals & solvents

All chemicals were obtained from Sigma-Aldrich and used as received. Chemicals used were dextran from *Leuconostoc mesenteroides* (Sigma Aldrich, mol. wt. 1.500.000 - 2.800.000 g/mol), cyclohexane (Sigma Aldrich, 99.8 %), sodium dodecyl sulfate (SDS, Sigma Aldrich, 99.0 %), toluene (Acros, 99.7 %), 1-hexadecene (99 %), hexadecane (Sigma Aldrich, 99 %), Span 80 (Sigma Aldrich), oleic acid (Sigma Aldrich, 90 %), Fluorescein isothiocyanate (Sigma Aldrich, isomer I, FITC, 90 %), ethanol (Baker Analyzed, 99.9 %, absolute). For de-ionized water a Millipore Direct-Q UV3 reverse osmosis filter apparatus was used ($18 \text{ M}\Omega\cdot\text{cm}^{-1}$ at 25°C).

6.2.2 Equipment and software

For ET a FEI Tecnai 20 electron microscope was used with a LaB6 tip at an accelerating voltage of 200 kV in bright field mode. Transmission electron microscopy (TEM) was performed on a FEI Tecnai 12 with a tungsten tip, operating at 120 kV. For scanning transmission electron microscopy (STEM) a FEI Tecnai 20F with a Field Emission Gun was used, operating at 200 kV in secondary electron mode (SE-STEM) or in high-angle annular dark-field mode (HAADF-STEM). Confocal analysis was performed on a Leica SP2 confocal microscope with an 100x (NA = 1.4) oil immersion Leica confocal objective. For centrifugation of nanoparticles a Hettich zentrifugen Rotina 46 S @ 4000 RPM was used, while for centrifugation of nanoparticle clusters an Eppendorf centrifuge 5415c was used @ 1000 RPM. To carbon coat TEM grids we used a Cressington 208 carbon coater.

For ET Inspect 3D (FEI Company, Eindhoven) and IMOD 4.3 (Boulder Laboratory, Colorado) were used. To reduce noise in the ET reconstructions the following filter operations were performed. These filters are available in ImageJ 1.46R. The filters applied in consecutive order were: Invert, Subtract Background (50 px), Despeckle (Median 3x3), Bandpass (30 px high, 3 px low), Gaussian blur (3 px), Enhance Contrast (saturate 0.4 %).

6.2.3 Methods

Colloidal experiments

For the SPs presented in this chapter that are formed with nanoparticles the 6.0 nm (8.8 nm_{eff} cobalt iron oxide nanoparticles presented in section 2.5.1 were used. These were synthesized according to the method presented in section 2.4.4 for spherical nanoparticles but by using hexadecene as high boiling solvent in the synthesis. These nanoparticles were stabilized with a ~ 1.5 nm thick oleic acid capping layer. For a typical self-assembly experiment the method described in section 3.4.3 was used, i.e. 7 mg of 8.8 nm_{eff} cobalt iron oxide nanoparticles was dispersed in 1 ml of cyclohexane and added to 10 ml of de-ionized water containing 400 mg of dextran and 60 mg of SDS. The resulting mixture was then emulsified using a Couette flow with a shear rate of $\dot{\gamma} = 154 * 10^3 s^{-1}$. The formed emulsion was then heated to 68 °C for 4 hours during which the mixture turned less opaque as the emulsion droplets evaporated. The resulting SPs were retrieved by sedimentation and washed (sedimentation and redispersion in water).

Fluorescent core-shell particles were made using the dye fluorescein isothiocyanate (FITC) according to the method by van Blaaderen *et al.* [178]. The cores had a diameter of 434 nm and were used in seeded growth to arrive at a final diameter of 1.32 μm . Successive silica shells were grown on the cores according to the Giesche method [179]. TEM analysis showed silica colloids with a diameter of 1.32 μm with a polydispersity of 1.7 %. For a typical colloidal self-assembly experiment 5 mg of silica colloids were dispersed in 25 μL of de-ionized water. The suspension was then added to 150 μL of hexadecane containing 1.5 mg Span 80. The suspension was shaken slightly by hand. The inner water phase of the emulsion droplets was allowed to evaporate over 10 days with slight agitation (shaking) every 48 hours to prevent droplets from sticking to the glass vial. The resulting suspension was washed by sedimenting and redispersing in water.

6.2.4 Sample preparation

For electron microscopy analysis 200 mesh copper TEM grids with a ~ 25 nm thick Solutia support film were used, carbon coated for ~ 7 sec. Gold fiducial markers were deposited as described in sec 4.5.4. To prepare freeze-dried samples TEM grids were first glow discharged for 13 seconds using a Cressington 208 carbon coater, making them hydrophilic, prior to gold markers and sample deposition. After depositing the gold markers and allowing them to dry the grid was loaded with 3 μL of sample. The deposited droplet was then blotted for 1.0 second and plunged into liquid ethane at approximately -180 °C using a Vitrobot Mark 2 plunge freezer. The sample was then kept under vacuum and heated to -90°C at $\sim 5^\circ\text{C}\cdot\text{m}^{-1}$, from there the sample was gradually heated to RT over a period of 3 hours, i.e. $< 1^\circ\text{C}\cdot\text{min}^{-1}$.

Particle tracking and determining their crystal structure

To find particle positions in SPs in-house tracking software based on the tracking algorithm of Crocker and Grier [180] was used, but extended to 3D as for example schematically described in ref. [181].

To identify the crystalline domains in the SPs bond-orientational order parameters were used. These order parameters are able to differentiate between liquid and solid particles and identify crystalline domains. The bond-order parameters used for this chapter was first introduced by ten Wolde *et al.* in studies on nucleation and crystallization of Lennard-Jones particles in a fluid [182, 183]. These bond order parameters is commonly used for crystal nucleation studies; van Duijneveldt and Frenkel [184], ten Wolde and Frenkel [185], C.F. Auer and Frenkel [19], and Filion *et al.* [20]. In this algorithm "neighbors" are determined for each particle; for particle i the neighbors are all particles within radius r_c of particle i . This then results in the total number of neighbors $N_b(i)$. The bond-orientational order parameters $q_{l,m}(i)$ are defined as:

$$q_{l,m} = \frac{\frac{1}{N_b(i)} \sum_{j=1}^{N_b(i)} Y_{l,m}(\theta_{i,j}, \phi_{i,j})}{(\sum_{m=-l}^l |q_{l,m}|^2)^{1/2}} \quad (6.1)$$

where $\theta_{i,j}$ and $\phi_{i,j}$ are the inclinations and azimuth of the bond between i and j and $Y_{\theta,\phi}$ are spherical harmonics with $m \in [-l, l]$. A particle is considered solid when the number of connections per particle $n_{con}(i)$ is greater then the the critical number n_{con}^c [186]:

$$n_{con}(i) = \sum_{j=1}^{N_b(i)} H(d_l(i,j) - d_c) \quad (6.2)$$

where H is the Heaviside step function where d_c is a threshold value and d_l is defined as:

$$d_l(i,j) = \sum_{m=-l}^l q_{l,m}(i) q_{l,m}^*(j) \quad (6.3)$$

Each particle can only belong to a single cluster since all solid like particles which have solid like neighbors are incorporated in the same cluster. For this algorithm the following parameters are used: a neighbor cutoff r_c , a dot-product cutoff d_c , the critical number of solid-like neighbors n_{con}^c , and a symmetry index for the bond-orientational order parameters l . For the structures presented in this chapter thee l was set to 6 as the FCC crystal structure is the stable solid phase, a distance $d_l = 1.4\sigma$ was chosen, and the critical number of neighbors was set to $n_{con}^c = 7$ with a threshold value of $d_c = 0.6$.

6.3 Results & Discussion

In the first part of this section the results from the colloidal self-assembly experiments will be presented. Then these results will be compared to event driven molecular dynamic (EDMD) simulations of hard spheres. Finally, the effect of the number of constituents on the self-assembly behavior will be discussed.

6.3.1 Colloidal experiments

For the colloidal self-assembly in spherical confinements experiments at two different length scales were explored, with either nanometer or micrometer constituents. First type of experiments discussed is the nanometer length scale, then the micrometer length scale.

Self-assembly of 8.8_{eff} nm nanoparticles in cyclohexane droplets resulted in spherical highly ordered structures with three distinct geometries as is shown in Fig. 6.2. The observed geometries were: icosahedral **a**, rhombicosidodecahedral **b** and kink and ledge patterned bulk-like FCC packed spheres **c**. The smaller clusters closely resembled a Mackay icosahedron as proposed by Mackay [102], Fig. 6.2a. The fivefold symmetry characteristic for an icosahedron can clearly be seen in this figure. The second geometry, rhombicosidodecahedron, closely resembled the anti-Mackay icosahedral structure proposed Kuo [187]; a surface reconstructed Mackay icosahedron with truncated tetrahedra on each of the 20 facets with the spaces between the truncated tetrahedra filled with dense packed spheres. The third type of structures observed in these experiments were that of kink and ledge patterned spheres with hexagonal and cubic packed terraces Fig. 6.2c. These patterns are characteristic for FCC packed spheres.

Nanometer length-scale colloidal self-assembly

ET was used to study the internal crystal structure of the SPs with the rhombicosidodecahedron geometry. In total 7 different SPs were analyzed using ET and all showed similar packing patterns. A typical example is shown in Fig. 6.3 where in **a** a still from the tilt series is shown in which some order can already be identified. The particles outside the assembly are the gold markers used for aligning the tilt series. Panel **b** shows an orthoslice through the SP taken from the ET reconstruction near the respective center of the assembly. In the slice ordered wedge shaped domains can be discerned pointing to the center of the assembly. Using in-house tracking software the individual particle positions in the SPs were determined from the ET reconstructions. With the bond-orientational order parameters, discussed in section 6.2.4, the crystalline domains were identified **c**. This revealed tetrahedral shaped domains of mostly FCC packed spheres pointing towards the center of the SP. The tetrahedral domains combined formed a surface reconstructed icosahedral structure **c**. From these findings we see that the nanoparticles showed different self-assembly behavior from bulk when self-assembled inside spherical confinement. Similar results were found for 12.6 and 20.4 nm_{eff} nanoparticles suggesting that the size of the nanoparticles did not influence this packing behavior.

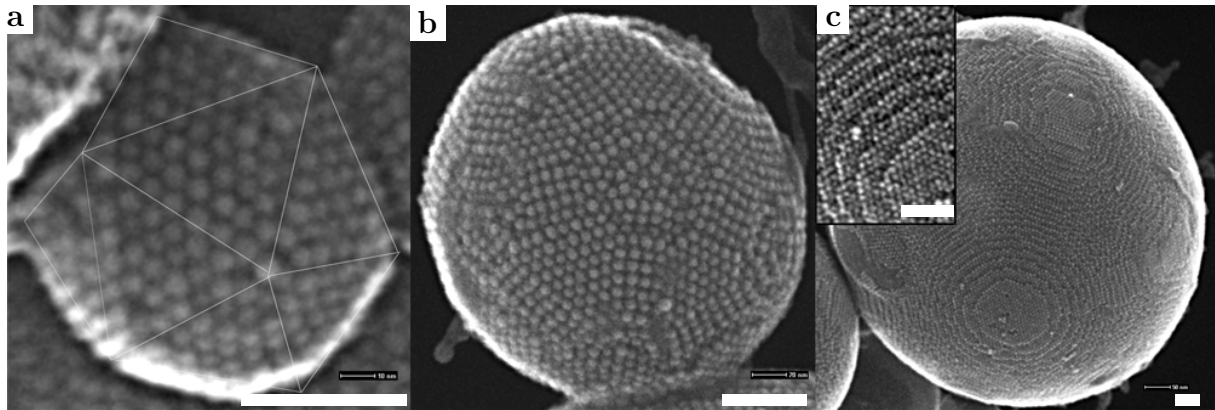


Figure 6.2: Electron micrographs made using secondary electron STEM of 8.8 nm_{eff} nanoparticles self-assembled in emulsion droplets (scale bars are 50 nm). **a)** ~ 700 Nanoparticles arranged in an icosahedral like geometry, closely resembling a Mackay icosahedron. **b)** ~ 7500 Nanoparticles packed together in a surface reconstructed icosahedron, closely resembling an anti-Mackay icosahedron. **c)** ~ 240.000 Close packed nanoparticles with kink and ledge patterns characteristic for FCC crystal structures. Inset: magnified image of the kink and ledge patterns on the surface.

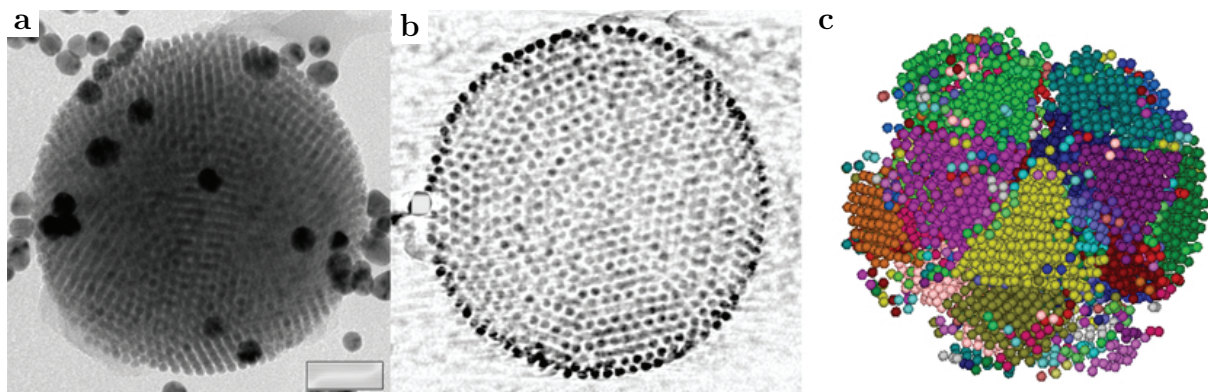


Figure 6.3: Tomographic analysis of a SP consisting of ~ 5.000 8.8 nm_{eff} cobalt iron oxide nanoparticles. **a)** Transmission electron micrograph of close packed nanoparticles taken from a tilt series for tomographic analysis, the angle is chosen such that the crystalline pattern of the nanoparticles is visible. The large black spots are 16 nm gold nanoparticles used as fiducial markers for the reconstruction (scale bar = 50 nm). **b)** Orthoslice taken from a tomographic reconstruction showing wedge shaped crystalline domains with their tips pointing to the center of the assembly, towards the edge of the assembly new domains can be discerned at 2-3 layers from the surface. **c)** Full reconstructed structure with the particles positions determined using an in-house tracking program and the crystalline domains determined using bond-orientational order parameters. In this image each domain has been assigned a color, the particles not belonging to a crystalline domain as determined by the order parameters are not shown.

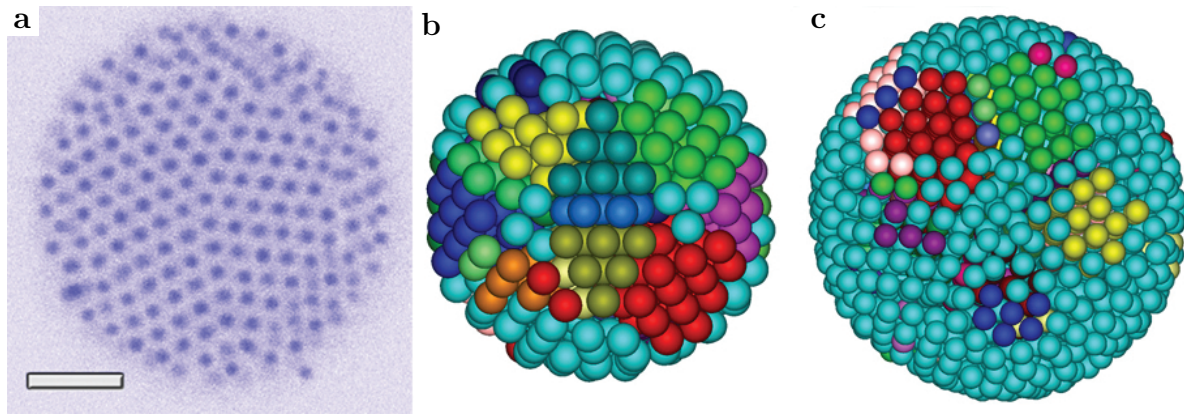


Figure 6.4: SPs self-assembled with $1.33 \mu\text{m}$ silica colloids formed inside water droplets. **a)** Confocal image of a silica colloid assembly of 3600 particles, taken close to the center. The colors of this image have been inverted (scale bar = $4 \mu\text{m}$). **b)** An icosahedral packed colloidal assembly consisting of 554 particles, where each of the domains is assigned a different color. **c)** An icosahedral colloidal packing consisting of 1614 particles, with surface termination.

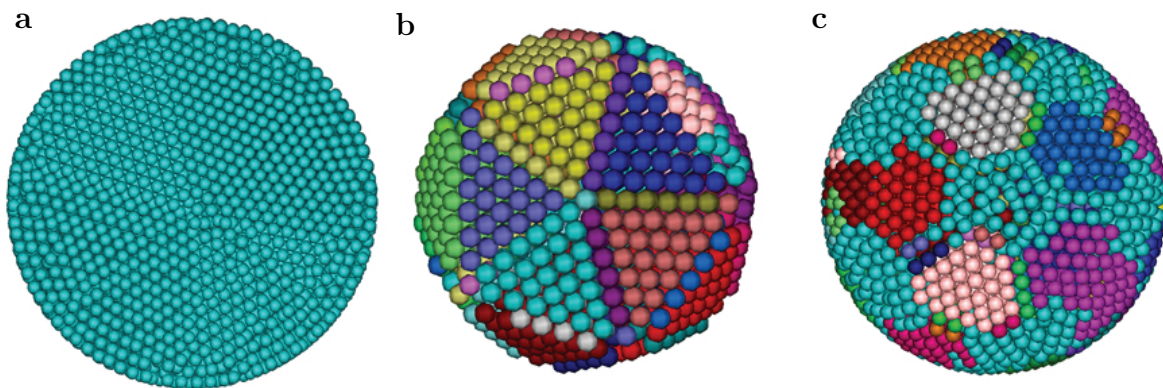


Figure 6.5: Crystalline assembly of 10,000 hard-spheres formed in EDMD simulations. **a)** Cut-through of the spherical assembly. **b)** The icosahedral packing inside the assembly with the view centered on a five fold symmetry. Colors depict different crystalline domains as determined by the order parameters. **c)** The surface termination on the assembly with the view centered on one of the five fold symmetries.

Micrometer length-scale colloidal self-assembly

To exclude the material properties, e.g. magnetic interactions, of the nanoparticles are the cause of the packing behavior, and to confirm that this behavior is independent of the constituent size, a similar experiment was performed using $1.32 \mu\text{m}$ silica colloids. The resulting SPs are shown in Fig. 6.4. Confocal images of the SPs, which is not to different from the orthoslices obtained with ET, showed similar wedge shaped crystalline domains as is shown Fig. 6.4a. The tracking software together with the order parameters found tetrahedral domains and partially icosahedral packings, Fig. 6.4b. The larger SPs showed similarities to the rhombicosidodecahedron geometries. However, typically these SPs showed only orderer in the, what is assumed, the bottom half of the structures. This was probably the result of the greater influence by gravity and the longer diffusion times as a result of the increased size and mass. The results from both experiments, although not identical, were still in good agreement. These findings show that this behavior was not a result of the size of the constituents nor its material properties. However, in colloidal experiments like these forces like van der Waals and gravity can never be completely removed and thus not be ruled out by indefinitely.

6.3.2 Simulations

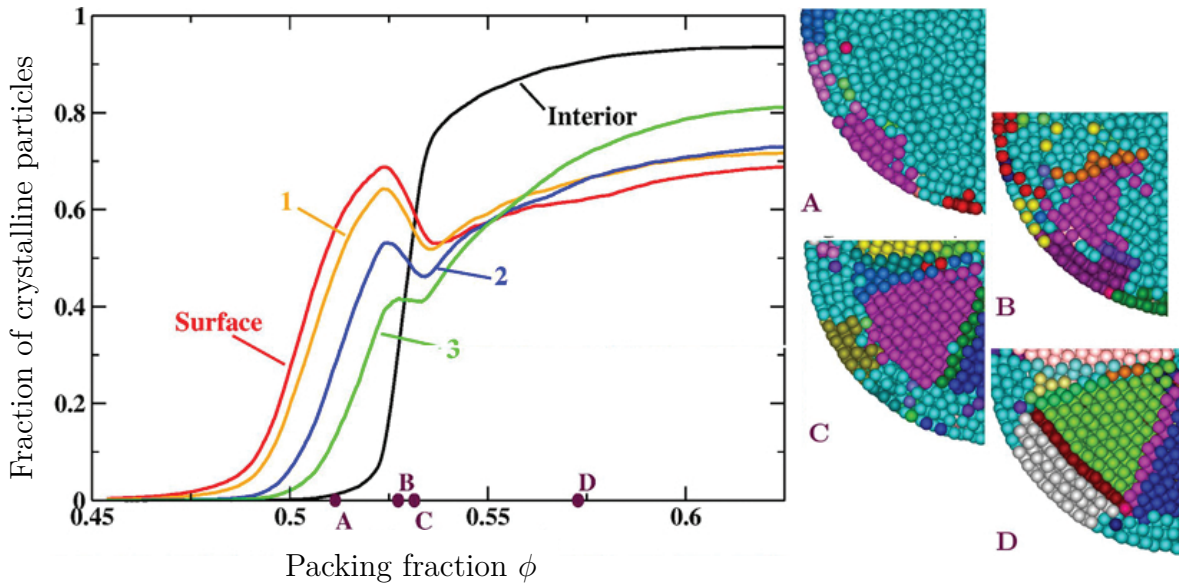


Figure 6.6: The evolution of crystalline domains showing the fraction of crystalline particles for each layer as a function of volume fraction. Inset: Snapshots taken at volume fractions **A**: $\phi = 0.511$, **B**: $\phi = 0.527$, **C**: $\phi = 0.531$, and **D**: $\phi = 0.573$.

To show that this is hard-sphere self-assembly behavior and thus purely entropic the experiments were simulated using EDMD. In these simulations hard spheres were compressed in a spherical cavity. The resulting structures of a simulation, using 10,000 spheres, are shown in Fig. 6.5, and are in good agreement with the colloidal experiments. The wedge shaped domains pointing to the center are visible in Fig. 6.5a. In Fig. 6.5b a nearly

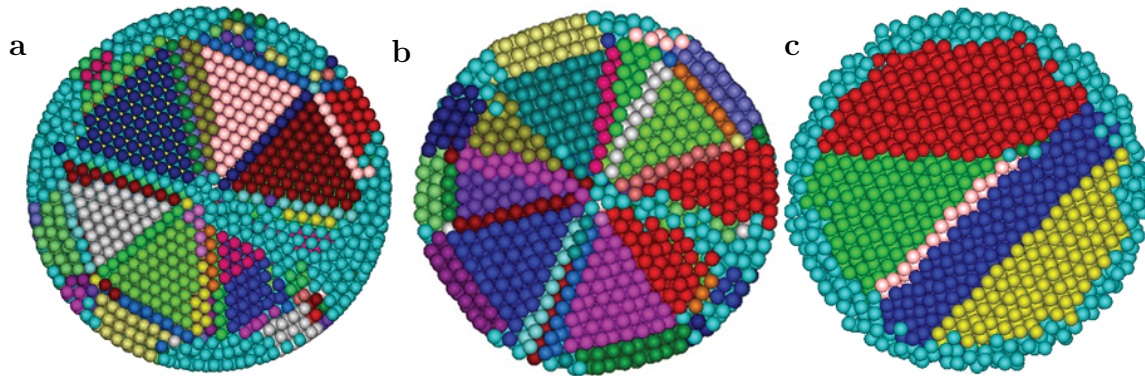


Figure 6.7: EDMD simulation showing the effect of a soft potential on the self-assembly of hard spheres in a spherical confinement. **a)** An assembly of 10.000 particles assembled in an confinement with a hard wall (no potential). **b)** An assembly of 8.000 particles formed with a soft potential with a range of 0.5σ . **c)** A self assembled structures of 10.000 particles formed with a long range repulsion ($> 3 \sigma$).

perfect Mackay icosahedron can be seen. The colors indicate the crystalline domains as determined by the bond-orientational order parameters, made visible by removing the outer layers of the structure. The rhombicosidodecahedron-like surface can be seen when viewing the full SP, Fig. 6.5c.

Since the confinement changed the self-assembly behavior it must have played an integral role in the self-assembly process. To study this influence in more detail the size and growth of crystalline domains near the interface was followed during the simulations. By measuring the fraction of crystalline particles in each layer as a function of the volume fraction ϕ the evolution of the structure was followed, Fig. 6.6. In this figure the fraction of crystalline particles in each surface layer (0 up to 3) and the interior are plotted, Fig. 6.6**Left**, and snapshots of the simulation at 4 different volume fractions are shown in Fig. 6.6**Right**. The graph shows that the crystallization started in the surface layer at a volume fraction of $\phi \approx 0.51$ followed shortly by layers 1, 2 and 3. At a volume fraction of $\phi = 0.527$ the interior of the assembly abruptly crystallized, nucleating inwards from the ordered surface layers, melting them in the process. Further increase in the volume fraction to $\phi \approx 0.55$ resulted in the recrystallization of the now disordered surface layers in the reverse order ($L_3 > L_2 > L_1 > L_0$), Fig. 6.6**left**. it was found that the crystallization of the interior phase started from the surface layers nucleating from the already present crystalline domains in these layers. Fig. 6.6 **right**.

Note that the outer most surface layer has the highest percentage (~69 %) of ordered spheres at a volume fraction $\phi \approx 0.52$ and does not reach this percentage again even at high volume fractions.

To further examine the influence of the confining two additional EDMD simulations were performed, one with a short range potential (0.5σ) and one with a marginally longer range potential ($> 3 \sigma$). Comparing the results from these simulations with the simulation results of the hard wall potential, see Fig. 6.7. Interestingly, the simulations with a short range repulsion on the wall the same icosahedral ordering, Fig. 6.7**b** as

observed for the hard-wall potential, Fig. 6.7, but with typically larger domains and less disordered particles. Increasing the repulsion on the wall to ($> 3 \sigma$) in non-icosahedra but bulk-like FCC packing, Fig. 6.7c. This shows that if the confining potential is too soft the influence of the wall on the self-assembly behavior disappeared.

6.3.3 Size dependence crystal transitions

In both nanoparticle and silica colloid self-assembly experiments and in EDMD simulations icosahedral structures were observed. These were mainly observed in SPs consisting of less than $\sim 18,000$ spheres. Where bulk-like FCC packing was typically observed in SPs consisting of more than $\sim 70,000$ spheres. This indicated that the number of spheres of which the SPs were self-assembled influenced the self-assembly behavior. To study this transition region in more detail 129 SPs consisting of anywhere between ~ 250 to $\sim 100,000$ 8.8 nm_{eff} cobalt iron oxide nanoparticles. For each of the SPs the geometry was determined

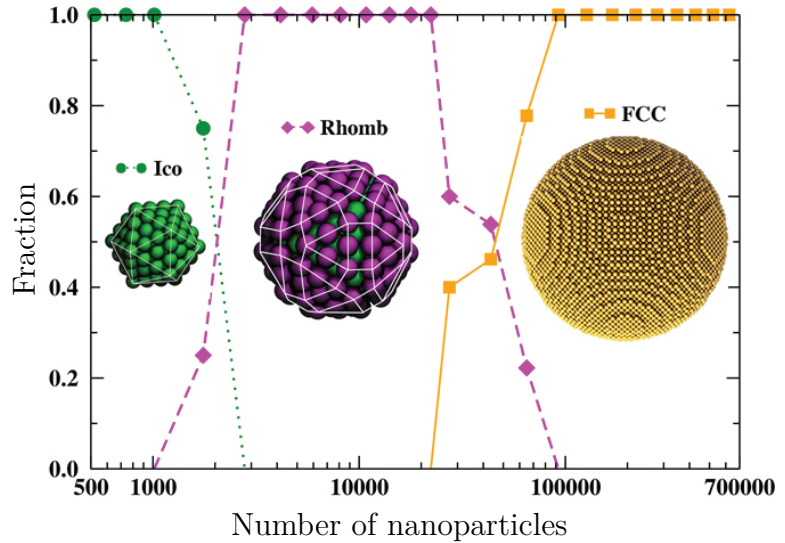


Figure 6.8: Shown here is the effect of the number of particles on the packing type of the clusters. **a)** Fraction of each of the three observed geometries (icosahedra, rhombicosidodecahedra and FCC), plotted against the estimated number of spheres per SP based on SP diameters and a volume fraction of $\phi = 0.74$.

using SE-STEM, as is for example shown in Fig. 6.2. The resulting geometries were plotted against the approximated number of constituent spheres based on the diameter and an assumed volume fraction of $\phi = 0.74$, see Fig. 6.8. From this graph three distinct regions for each of the geometries can be identified, below ~ 700 particles the SPs formed geometries with icosahedral symmetries, above ~ 700 up to $\sim 70,000$ resulted in SPs with rhombicosidodecahedral symmetries and larger clusters formed only SPs with bulk-like FCC packed spheres. Transition regions were found to be between ~ 700 and $\sim 2,000$, and between $\sim 18,000$ and $\sim 70,000$, see Fig. 6.8.

A similar trend was observed in the EDMD simulations ranging from 500 to 64,000 constituents, shown in Fig. 6.9. However, for the smallest clusters ($n = 500$) no icosahedral symmetries were observed. For these small clusters in EDMD to form icosahedral symmetries a short range repulsion on the wall was necessary. These findings are in line with the previous results on the soft-wall potential as mentioned earlier.

In both the nanoparticle and colloidal experiments short range repulsions on the interface are likely present as well, since particles can attach and detach from the surface allowing some movement at this interface at length scales comparable to individual constituents.

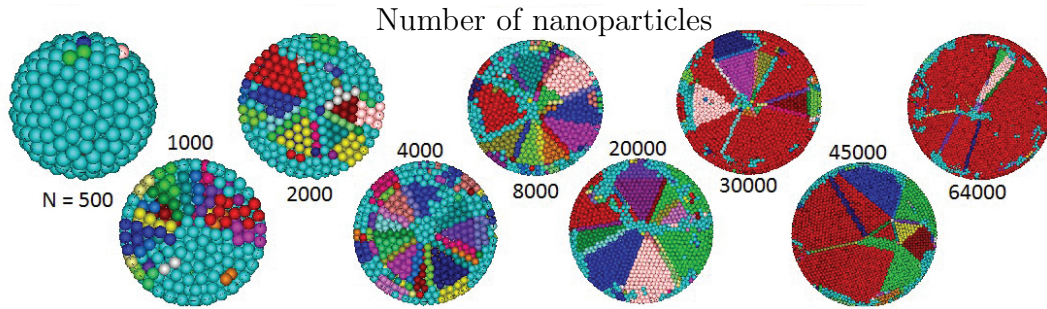


Figure 6.9: Crystalline domains of hard spheres in EDMD simulations for clusters consisting of $n = 500$ to $n = 6400$ particles.

6.4 Conclusions

In conclusion, in this chapter we showed that both cobalt iron oxide nanoparticles and micron sized silica colloids, when self-assembled inside emulsion droplets, form similar self-assembled ordered structures with either icosahedral, rhombicosidodecahedral symmetries or bulk-like FCC packings. It was also shown that these icosahedral and rhombicosidodecahedral structures form by entropy alone using simulations with hard-sphere interactions. This shows that entropy alone together with a spherical confinement is sufficient to form structures with icosahedral symmetries, and that interactions between the particles are not necessary in the formation of these geometries. Furthermore, we found that the nucleation starts at the wall of the confinement and the spheres crystallize inwards from there. A short range repulsion on the wall of the confinement did not change this self-assembly behavior, while a long range repulsion resulted in only bulk-like FCC packing. From SPs built up from 8.8 nm_{eff} cobalt iron oxide nanoparticles it was found that clusters with icosahedral symmetry formed in SPs consisting of up to 18.000 spheres, where rhombicosidodecahedral packing was observed in SPs containing up to 70.000 particles. SPs with more than 70.000 showed only bulk-like FCC packing.

6.5 Acknowledgments

Frank Smallenburg and Simone Dussi are gratefully acknowledged for their hard work on this research and performing the EDMD simulations. Dirk Groenendijk and Kyo Beyeler are thanked for their work on the self-assembly experiments of silica colloids in emulsion droplets. Michiel Hermes and Teun Vissers are thanked for providing the tracking and bond-orientational order parameters programs. Finally, Hans Meeldijk and Chris Schneidenberg are acknowledged for all their help and hard work with the freeze drying experiments, electron microscopy (both TEM and STEM) and tomographic analysis. Finally, Marjolein Dijkstra, Laura Filion, Alfons van Blaaderen and Arnout Imhof are thanked for their extensive efforts they put into this project.

Luminescent, High-Quantum-Yield Quantumdot Supraparticles

In this chapter SPs consisting of self-assembled photoluminescent quantumdots (QDs) are presented. Due to the use of QDs with a core@shell hetero structure the unique quantum confinement/size dependent photoluminescence was retained in the resulting micrometer sized dense packed assemblies. The resulting colloidal QD supraparticles (QDSPs) showed bright photoluminescence with comparable quantum yields as the individual constituents. Furthermore, preliminary local spectroscopic measurements on QDSPs "suspended" in air on a bed of zinc oxide nanowires used to excite the supraparticles, showed supraparticle specific modulated and strongly peaked emissions and photoluminescent hotspots that can tentatively be interpreted as the onset of laser-action. These observations of the specific enhancements of certain narrow emission frequencies are indicative of optical resonance modes (Mie modes) which could be the result of the high refractive index difference between the SPs and the surrounding air.

7.1 Introduction

In semiconductors the electrons are typically bound to atoms through covalent or ionic interactions (in the valance band), making it insulators. Electrons can be unbounded, leaving a hole behind, if they gain enough energy making it delocalized electrons (moving to the conduction band). This excited state is referred to as an exciton and introduces charge carriers to the material making the structure conductive. The amount of energy needed to generate an exciton, i.e. move an electron from the valance band to the conduction band, is called the energy gap (E_g) and is characteristic for the material.

Semiconductors can emit light by recombining an exciton (delocalized electron and hole) transferring its energy, typically equal to E_g , to a photon. For intrinsic semiconductors, e.g. cadmium selenide, zinc oxide, lead selenide, and aluminium nitride, no phonon is needed for this recombination, making such materials suitable light sources with high quantum efficiencies, i.e. the percentage of excitons that transfer their energy to a photon.

In semiconductor nanoparticle below ~ 10 nm the structure becomes small enough that the number of energy states for the excited electrons to occupy is limited resulting in discrete, molecular-like energy levels that are available to the electrons and holes [25, 188, 189]. As a result the E_g increases with a decrease in nanoparticle size, and is visible as a change in the wavelength of the photoluminescence. This phenomenon is known as quantum confinement and nanoparticles with such properties are referred to as quantumdots (QD) and have been the subject of extensive study in recent years as for example: light harvesters in solar cells [190–193], for biolabeling [194, 195], as LEDs or Lasers [196–198], and as single photon sources [199]. In addition to the change in E_g QDs show higher carrier-to-photon conversion efficiencies than their bulk material counterparts as a result of the quantum confinement as it prevents the long range carrier diffusion which typically occurs in semiconductor materials [200–202]. However, QDs suffer from non-radiative recombination when self-assembled in to close-packed structures as a result of exciton energy transfer by dipolar interdot interactions [203, 204].

For optical purposes QDs ideally should have quantum efficiencies near a 100 %, meaning: for each photon absorbed a photon is emitted. However, there are several mechanisms, in addition to the dipolar interdot interactions, that result in reduced quantum efficiencies. One example is caused by defects in QD crystal structure that create energy levels within the E_g providing non-radiative recombination pathways [205] and are typically present at the surface of the QDs. By growing a shell with a wider band gap E_g around the QDs a soft-well potential can be formed confining the exciton to the QD center, preventing it from reaching the defect rich surface [189, 206].

A second mechanism which lowers the quantum yield is Auger recombination. This happens when a recombining electron transfers its energy to a second already excited electron instead of a photon, thereby expelling the electron to the far field in the form of β -radiation [207, 208]. Not only does this results in an electron being radiated instead of a photon, it also leaves the QD with a charge. This charge has been partially assigned as the cause of blinking, the phenomenon of periodic intermission in the photoluminescence of QDs [209, 210]. Again this can be in part prevented by using soft-well potentials in QDs [211–213].

If Auger recombination is prevented, multiple excitons can be generated in a single QD while still exhibiting photoluminescence. As the number of excitons in the QD increases higher energy levels become occupied and photoluminescent recombination occurs from these elevated energy levels. This recombination can be seen in emission spectra as additional peaks at shorter wavelengths and is referred to as state-filling. These wavelengths correspond to the larger E_g between the electron-hole pair [213, 214].

In this chapter we present micron sized close packed supraparticles (SPs) built up out of the core-multishell CdSe@ZnS QDs and study if and how the optical properties changed as a result of the self-assembly. In addition, the SPs are investigated for any collective behavior of the QDs in their photoluminescence as a result of the large amount of QDs in the assembly and/or the spherical shape of the SP.

7.2 Refractive index and optical resonance modes.

In optical fibers light is contained by total internal reflection. The incident light through the fiber hits the inner wall and is reflected back into the fiber. This is a result of the light hitting the wall at angles larger than the critical angle. The critical angle depends on the refractive index difference between the carrier material and its surroundings, and is calculated as followed:

$$\theta_c = \arcsin\left(\frac{n_2}{n_1}\right) \quad (7.1)$$

Where θ_c is the critical angle above which incident light is fully reflected, n_1 is the refractive index of the material through which the light is propagating and n_2 is the refractive index of the refractive index outside the material. The higher this refractive index difference the steeper the angle of incident light can be. For an optical fiber this refractive index is $n_{core} = 1.62$ for the core and $n_{cladding} = 1.52$ for the cladding, and is surrounded by air $n_{air} = 1$ [215]. In a similar fashion an optical resonator can be formed by trapping light on the edge of a disk [216, 217], or the surface of a sphere [218]. In such a resonator the light is trapped and will travel over the edge/surface resulting in optical whispering gallery modes with constructive and destructive interference [217, 219].

Cadmium selenide (CdSe) and zinc sulfide (ZnS) are relative high refractive index materials with refractive indices, for example $n \approx 2.7$ and 2.6 respectively for $\lambda = 630$ nm and at room temperature. Self-assembling these into large SPs will lower the effective refractive index of the SP by the volume fraction ϕ of the cores and the size of the capping layer. Nevertheless, such spheres still possess a refractive index of $n_{SP} \approx 2$. This means that if these particles are sufficiently large the critical angle is high enough that light traveling along its surface is subject to total internal reflection. This would mean that a part of the photoluminescent light emitted from the QDs can be trapped on the surface forming an optical resonator, effectively forming a zero dimensional photonic crystal. And with each pass of the resonant light wave, through stimulated emission, the QDs are pushed to emit light at a wavelength similar to that of the passing wave intensifying the resonant mode. This will causes QDs to emit light at specific wavelengths depending on the size of the QDSP and effective index of refraction, and can even result in low threshold lasing [220]. It is important to mention here that the above 'light diffraction'

description is only an approximation as the size of the SPs and the wavelength of light are not too far separated making a classical optics description invalid. The correct Mie theory already developed about 100 years ago does treat the multiply scattered near and far field contributions in a correct way, but relatively simple analytical solutions only exist for (multiple core-shell) spheres in a homogeneous medium. Already the coupling to a half space with another dielectric contrast significantly complicates the calculation [221].

7.3 Experimental Details

In this section the chemicals, solvents, equipment and methods used in this chapter are discussed in more detail.

7.3.1 Chemicals

The following chemicals and solvents were ordered from Sigma-Aldrich and used as received. Cyclohexane ($\geq 99.8\%$), dextran from *Leuconostoc mesenteroides* (mol. wt. 1.500.000 - 2.800.000 g/mol), sodium dodecyl sulfate (SDS, $\geq 99.0\%$). For de-ionized water a Millipore Direct-Q UV3 reverse osmosis filter apparatus was used ($18\text{ M}\Omega\cdot\text{cm}^{-1}$ at $25\text{ }^\circ\text{C}$).

7.3.2 Equipment and software

The bright-field transmission electron microscopy (TEM) images were taken on a Fei Tecnai 12 electron microscope with a tungsten tip. Scanning transmission electron microscopy (STEM) and secondary electron (SE)-STEM measurements were made using a Fei Tecnai 20F using a field emission gun (FEG) as electron source. SEM images were obtained with an FEI Nova 600 Nanolab. For cathode luminescence a XL30S FEG electron microscope fitted with a cathode luminescence detector was used.

For optical measurements 4 different optical setups were used and are numbered for reference.

Optical setup 1: For quantum yield measurements a 445 nm diode laser and a Labsphere 6" integrating sphere with a fiber coupled spectrometer (USB 4000, Ocean Optics) were used.

Optical setup 2: A home-built luminescence microscope fitted with pulsed laser excitation (Spectra Physics Explorer, 349 nm, 10 ns pulse duration, 5kHz rep. rate) attenuated with neutral density filters and focused to an $50\text{ }\mu\text{m}$ full width half max spot coupled to a liquid nitrogen cooled spectrometer/CCD (Princeton instruments) was used to measure the exciton power dependence of the photoluminescence.

Optical setup 3: A Leica TCS SP8 confocal microscope fitted with an pulsed super continuum source (NKT Photonics, 5 ps pulse duration, 78 MHz rep. rate), focusing objective (63x/1.32 NA oil), and photo-multiplier-tube detection.

Optical setup 4: An Edinburgh instruments F900 double spectrometer was used to measure the photoluminescence and absorption of the QDs in solutions.

For centrifugation an Eppendorf centrifuge 5810 was used. A Philips Tecnai 20F electron microscope with a LaB₆ tip at 200 kV was used for electron micrographs. For

the Couette flow a rotor-stator device was used with an inner rotor size of 39.15 mm and a gap of 0.4 mm, as described in chapter 3.

7.3.3 Quantumdot synthesis

The QDs used for the self-assembly experiments presented in this chapter were synthesized as described in section 2.5.4 and the resulting QDs are presented in section 2.5.3. These particles had a 12.4 nm (14.8 nm_{eff}) diameter with a size distribution of 1.0 nm resulting in a polydispersity of 8 % (7 % eff.).

7.3.4 Quantumdot supraparticle synthesis

Quantumdot supraparticles (QDSPs) were made according to the emulsion method described in section 3.4.5. For a typical experiment 1 mL of cyclohexane loaded with $\sim 1 \times 10^{18} \text{ mol} \cdot \text{L}^{-1}$ of 12.4 nm QDs was added to 10 mL of de-ionized water containing 400 mg of dextran and 60 mg of SDS. The mixture was then shaken by hand and emulsified using a Couette rotor-stator device. Two self-assembly experiments were performed, one used a rotor speed of 7500 rpm and a gap spacing of 0.1 mm (shown in Fig. 7.2a and b), the second experiment used a rotor speed of 2600 rpm and a gap spacing if 0.4 mm (shown in Fig. 7.2c, d and , and all remaining figures). The mixture was then emulsified with a shear rate of $\dot{\gamma} = 9.7 \times 10^5 \text{ s}^{-1}$. The resulting emulsion was heated to 68 °C for 4 hours and sedimented by centrifugation and redispersed in de-ionized water.

An approximation of the refractive index of QDSPs was made based on the composition of the CdSe@ZnS QDs, the thickness of the organic capping layer and an the packing fraction. The CdSe@ZnS multi-shell QDs had a 12.4 nm diameter which is 60 % of the particles effective volume the 1.15 nm thick oleic acid capping layer accounts for the remaining 40 %. Assuming a refractive index of $n = 2.5$ for the cores based on 80 % CdS, 15 % ZnS and 5 % CdSe (at 630 nm and 20 °C), and a refractive index of $n = 1.46$ for the capping layer an effective refractive index of $n = 2.1$ can be approximated for each sphere. Since an ideal packing of spheres has a volume fraction of $\Phi = 0.74$ it is assumed that $\Phi = 0.26$ of the QDSPs consists of organic molecules e.g. cyclohexane or oleic acid. If the remaining volume fraction is cyclohexane then we estimate that the refractive index of the QDSPs is $n_{QDSPs} \approx 1.9$.

7.3.5 Growth of zinc oxide nanowires

Zinc oxide nanowires were used to suspend QDSPs into a medium with an as low as possible refractive index, while also being able to excite the SPs through the ZnO photoemission, and were synthesized with a method similar to the gas liquid solid method proposed by Huang *et al.* [222]. For a typical zinc oxide nanorod synthesis a silica support was coated with 0.8 nanometer gold using a sputter-coater. The coated silica plate was placed in an oven with zinc oxide and carbon deposited in a tray underneath it. The sample was then degassed at 500 °C for 1 hour and the nanorods were grown by heating to 910 °C over during 1 hour, in a tube-oven with a 1 % oxygen and 99 % nitrogen flow.

7.3.6 Sample preparation

To deposit the QDSPs on a TEM grid $\sim 3 \mu\text{L}$ of suspension was drop cast on a 200 copper mesh TEM grid with a ~ 25 nm thick Solutia support film, which were carbon coated for 7 sec using a Cressington 208 carbon coater, Fig. 7.2a, b and c. The QDSPs in Fig. 7.2d, e were imaged suspended in water in a glass capillary. To measure the state filling showing in Fig. 7.4 the QDSPs were deposited from water on a silicon wafer with a 600 nm thick silica layer. The state filling of the QDs was measured in cyclohexane. To "suspend" QDSPs in a field of ZnO nanowires the plates with the grown nanowires, described above, were rubbed together dislodging the nanowires. The wires were then collected on a glass support on which a drop of the QDSPs suspension in water was allowed to dry, the resulting images and measurements belonging to this sample are shown in Fig. 7.5 and Fig. 7.6.

7.4 Results & Discussion

7.4.1 Photoluminescent quantumdot supraparticles

The 12.4 nm QDs used for the experiments in this chapter, and presented in section 2.5.3, showed photoluminescence at an energy of 1.96 eV (633 nm), and could be excited at any wavelength above the photoluminescence with increased absorption at shorter wavelengths as is shown in Fig. 7.1.

Self-assembling the QDs in emulsion droplets resulted in dense packed QD colloidal supraparticles (QDSPs) similar to those presented in Ch. 3 but with bright photoluminescence. These SPs were mostly spherical and consisted of highly ordered colloidal crystals of QDs, see Fig, 7.2. In Fig. 7.2a a SE-STEM image of a 275 nm QDSP is shown consisting of 8.8 nm_{eff} QDs, with similar packing as was observed in the hard sphere packings discussed in Ch. 6. The number of QDs in the assembly, based on the effective diameter and a packing fraction of $\phi = 0.74$, is $\sim 22,000$ which is in line with the observed trend for icosahedral and bulk-like FCC ordering described in the previous chapter. This ordering is more clear in Fig. 7.2b where a STEM electron micrograph of this QDSP is shown, showing the dense and highly ordered wedge shaped domains pointing to the center of the QDSP.

By using a lower shear stress, by using 2600 RPM instead of 7500 RPM and a wider gap of 0.4 mm instead of 0.1 mm, QDSPs with diameters between 1 μm and 3 μm were made. a TEM image of the sample is shown in Fig.7.2c. It is likely that these larger QDSPs, Fig. 7.2c have a different colloidal crystal packing than observed for the QDSP in Fig. 7.2a and b, as these consist of well over 100,000 particles, suggesting an bulk-like FCC packing. Also note that trying to make even larger clusters will likely result in hollow shells instead as described in section 3.9.

Imaging the solid QDSPs with optical and confocal microscopy showed colloidal spheres with bright red photoluminescence, around 1.96 eV ($\lambda = 630$ nm). In Fig. 7.2d an optical microscopy image of the QDSPs is shown, excited with a $\lambda=305$ nm laser using optical setup 2. Fig. 7.2e shows a confocal microscopy image of the QDSPs, using optical setup 3, excited at $\lambda=450$ nm. In the confocal images the spherical shapes of the assemblies could clearly be identified as is shown here. This bright red photoluminescence suggested that the QDs and their confinement were preserved in-spite of the self-assembly into

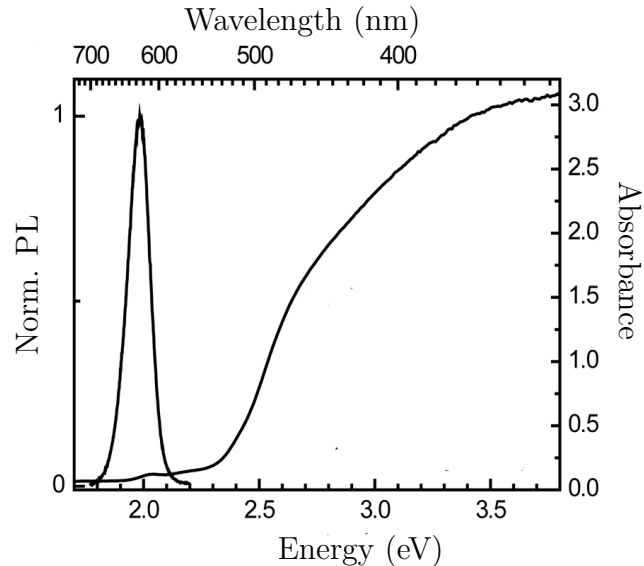


Figure 7.1: Excitation and absorption graph for the CdSe@ZnS quantumdots (QDs) used in this chapter.

micron-sized QDSPs and being heated to 68 °C in the presence of oxygen and water for 4 h.

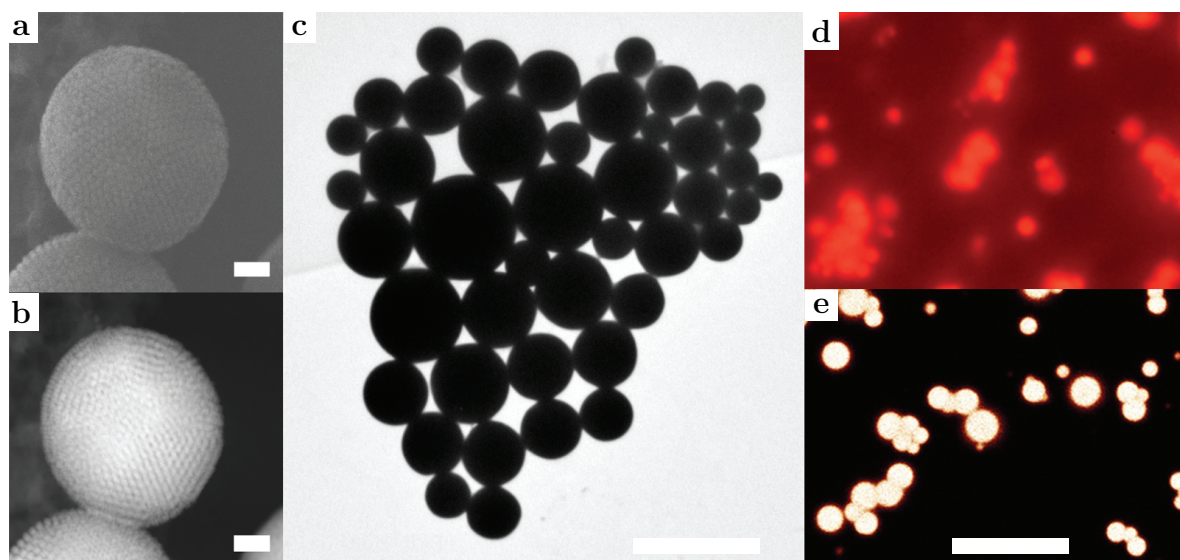


Figure 7.2: Electron and optical microscopy analysis of quantumdot supraparticles (QDSPs). **a)** SE-STEM electron micrograph showing ordered arrangement of the semiconductor nanoparticles on the surface of the QDSP (scale bar = 50 nm). **b)** STEM images of the QDSP showing an ordered internal structure with wedge shape colloidal crystalline domains formed by the QDs (scale bar = 50 nm). **c)** TEM electron micrograph of larger, 1 - 3 μm , QDSPs deposited on a TEM grid (scale bar = 2.5 μm). **d)** Optical microscopy image using optical setup 2 of the QDSPs sample shown in panel **c** showing bright red photoluminescence when excited with a $\lambda = 305$ nm laser (scale bar = 10 μm). **e)** Confocal microscopy image of the same batch of QDSPs, using optical setup 3, showing bright photoluminescent spherical assemblies when exciting between $\lambda = 450$ nm - $\lambda = 650$ nm (scale bar = 10 μm).

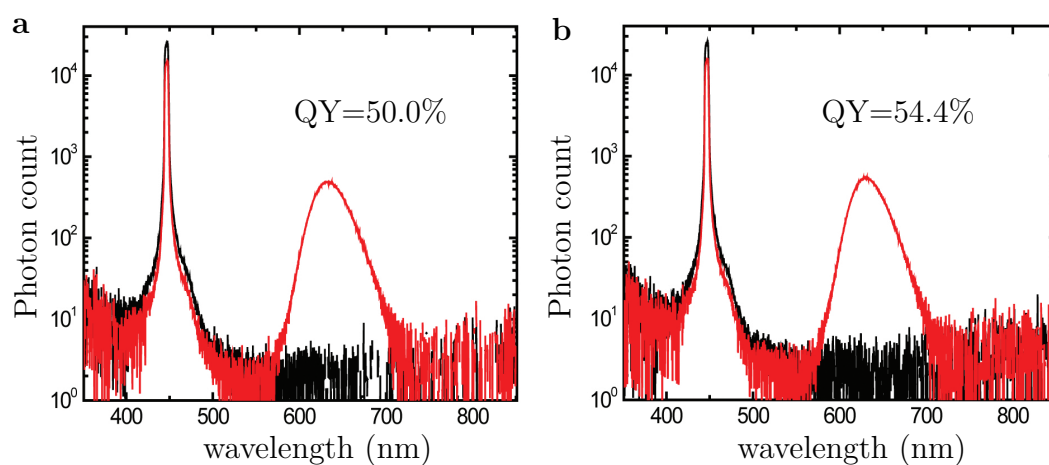


Figure 7.3: Quantum yield measurements using optical setup 1. **a)** CdSe@ZnS QDs in chloroform with a quantum yield of 50.0 %. **b)** QDSPs self-assembled from these QDs, showing a quantum yield of 54.4 %.

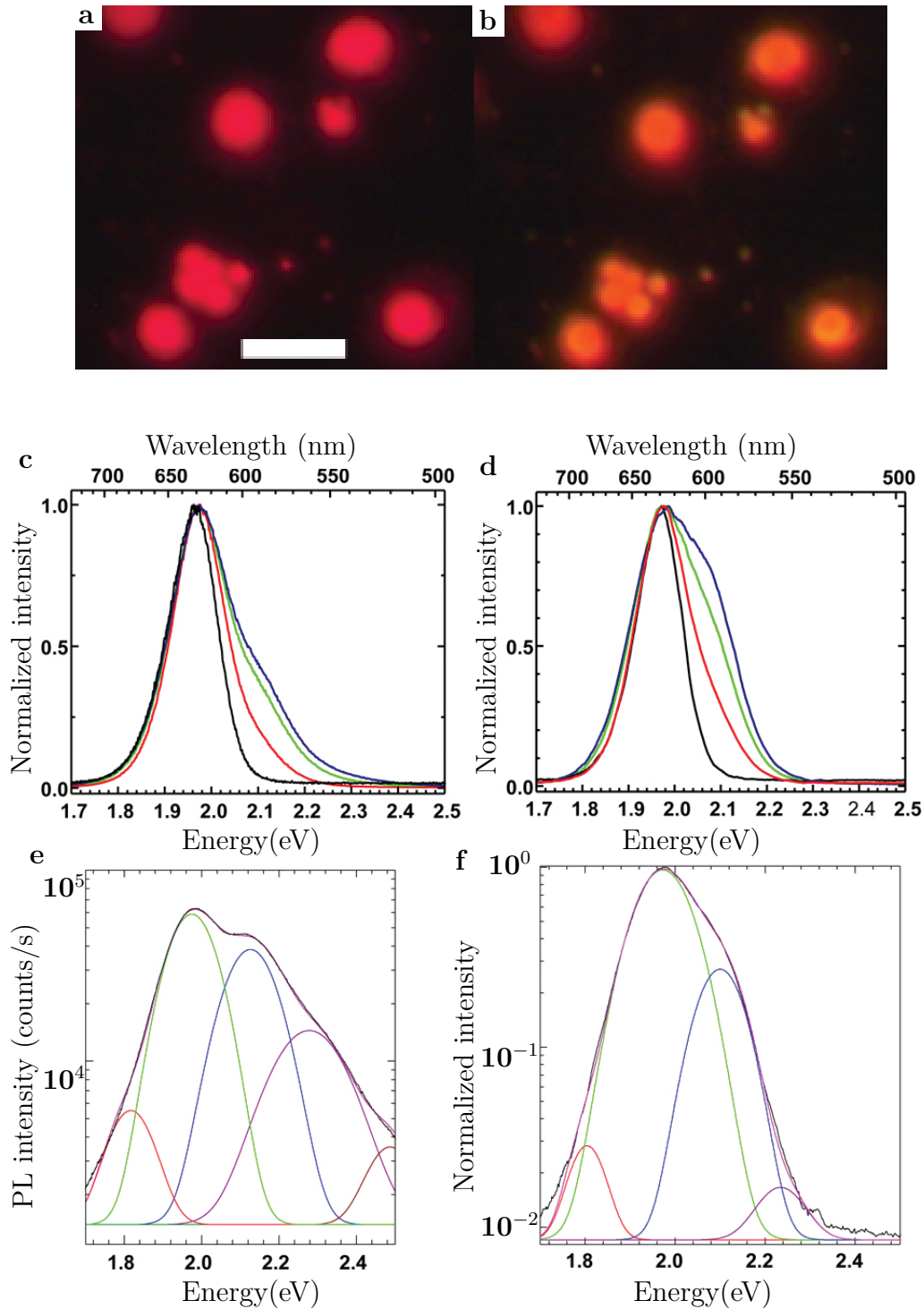


Figure 7.4: In the top 2 images optical microscopy images of QDSPs with an excitation fluence rates of $1.1 \cdot 10^{-6} \text{ J/cm}^2$ (panel a) and $1.9 \cdot 10^{-3} \text{ J/cm}^2$ (panel b) are shown (scale bar = $10 \mu\text{m}$). In the the bottom four graphs photoluminescence spectra for QDs (panel c and e) and QDSPs (panel d and f) at an excitation fluence rates of $1.1 \cdot 10^{-6} \text{ J/cm}^2$, $1.0 \cdot 10^{-4} \text{ J/cm}^2$, $1.0 \cdot 10^{-3} \text{ J/cm}^2$ and $1.9 \cdot 10^{-3} \text{ J/cm}^2$. Graph e and f show the photoluminescence on a Log scale with multi-Gaussian fits showing peaks at higher energies.

7.4.2 Quantum yield measurements

Measuring the quantum yield of both: the initial CdSe@ZnS QD suspension and the self-assembled QDSP suspension resulted in quantum yields of 50.0 % ($\lambda_{max} = 633$ nm) and 54.4 % ($\lambda_{max} = 628$ nm) respectively, see Fig. 7.3. This shows that even though the QDs were self-assembled into dense close packed structures, as shown in Fig. 7.2a, b and 7.5a, the quantum yield was preserved unlike in self-assembled solids of bare CdSe QDs where nearly all luminescence is quenched [203]. On the contrary, a small increasing of 4 % was observed. What caused this increase in the quantum efficiencies was not yet determined and could be the result of a scattering process of the colloidal spheres or could be due to a collective behavior like stimulated emission, and should be the subject of further investigation.

7.4.3 Power dependence and State filling

Under high intensity excitation, fluence rates of $1.0 \cdot 10^{-4}$ J/cm² and above, using optical setup 2, a color change from red (Fig. 7.4a) to orange (Fig. 7.4b) was observed for the QDSPs in optical microscopy. This change is seen in the photoluminescence spectra as a extra shoulder appearing at higher energies as is shown in Fig. 7.4c for QDs in cyclohexane and Fig. 7.4d for QDSPs. The fluence rate shown in these images were $1.1 \cdot 10^{-6}$ J/cm², $1.0 \cdot 10^{-4}$ J/cm², $1.0 \cdot 10^{-3}$ J/cm² and $1.9 \cdot 10^{-3}$ J/cm². This broadening of the spectra, extending into higher energies, indicating photon emission of excitons recombining from a higher energy state. This suggests that multiple excitons are generated per QD forcing the excitons to occupy a higher energy state in both the QDs and the QDSPs, see for example reference [214] for more detail on the state filling behavior in QDs.

In addition to the state filling, a small peak at lower energies was observed as well. This peak was observed in most spectra except for the high power emission spectrum of the QDSPs. This peak is likely caused by exciton recombination but where energy is transferred to an additional electron hole in the valence band, bringing the electron hole in a hot state, from which it cools down by phonon emission. This can only occur if initially more than one hole is present in the QD [212].

These findings shows that during the self-assembly not only the photoluminescence with an equal quantum efficiency was retained, but also the characteristic state filling mechanism observed for the CdSe@ZnS QDs. This showed that the quantum confinement was still present in the assemblies even though the nanoparticles were densely packed.

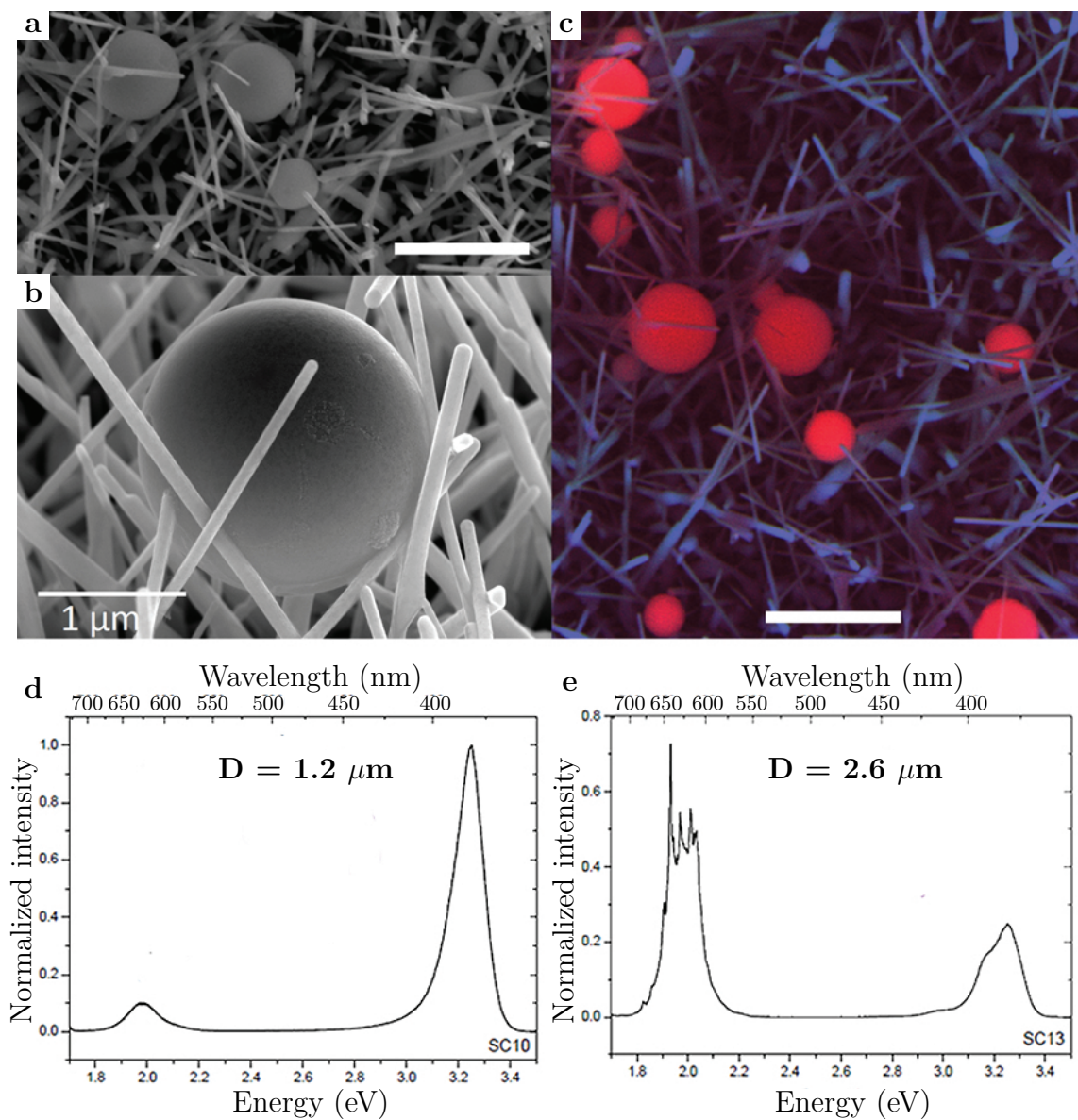


Figure 7.5: QDSPs "suspended" on ZnO nanowires for a nearly isotropic refractive index difference (between the QDSPs and air). **a)** SEM image of several QDSPs on ZnO wires (scale bar = 5 μm). **b)** SEM image of a single "suspended" QDSP (scale bar = 1 μm). **c)** Cathode luminescence image showing bright red luminescence for QDSPs and blue luminescence for the ZnO nanowires as a result of the different band gaps (scale bar = 5 μm). **d)** Photoluminescence spectra of a 1.2 μm QDSP. **e)** Photoluminescence spectrum of a 2.6 μm suspended QDSP showing sharp peaks in the emission as a result of Mie modes. **f)** Seven different emission spectra for QDSPs of diameters between $D = 1.73 \mu\text{m}$ to $D = 2.87 \mu\text{m}$.

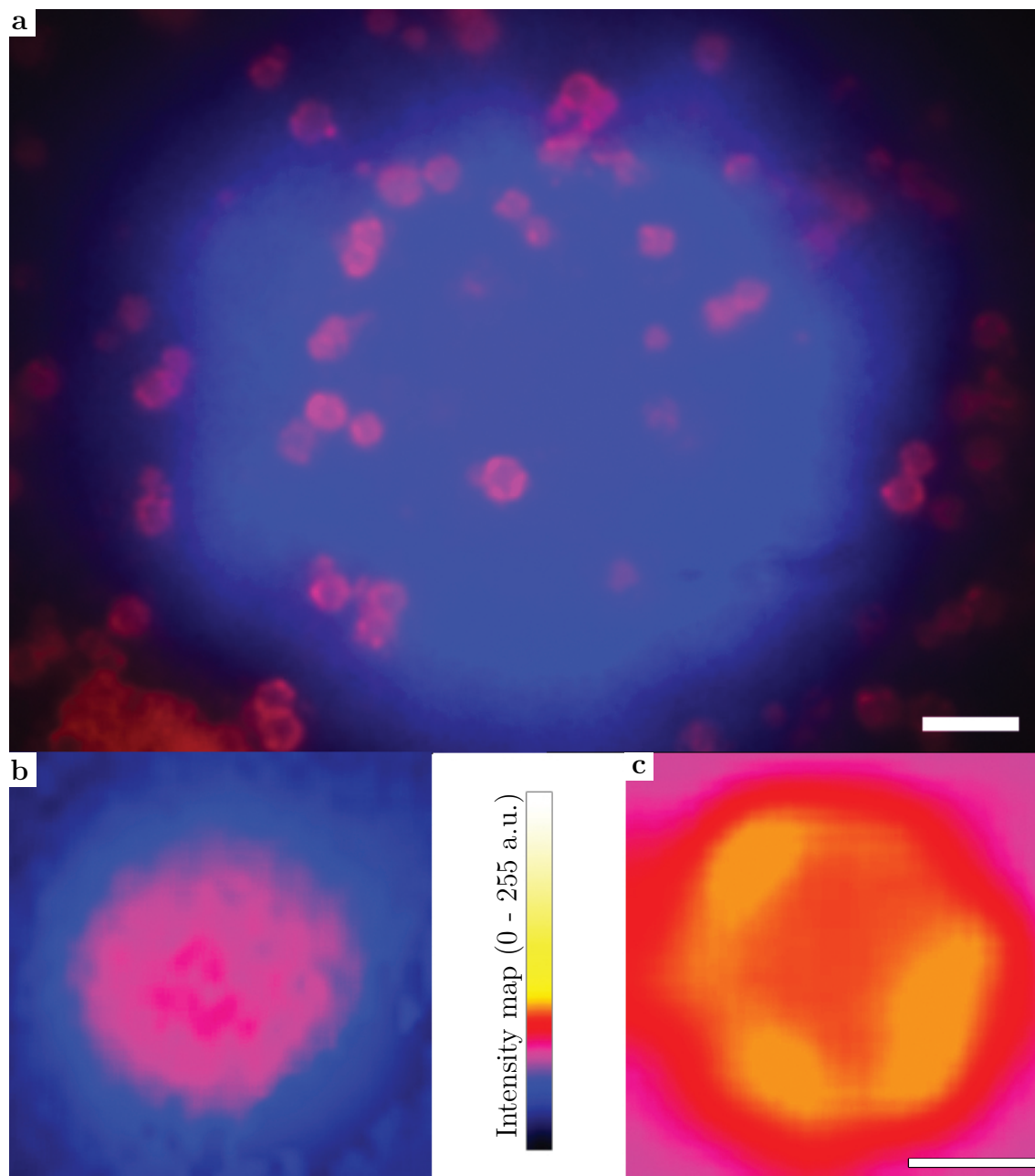


Figure 7.6: Optical microscopy images, made using optical setup 2, of QDSPs on ZnO nanowires. **a)** Suspended QDSPs showing ring like modulated emission (scale bar = $10 \mu\text{m}$). **b)** An intensity map of a non-"suspended" QDSP, showing a Gaussian emission pattern (scale bar = $1 \mu\text{m}$). **c)** An intensity map of a QDSP "suspended" on ZnO nanowires showing emission hotspots on the edge of the QDSP, either caused by Mie resonance modes or by excitation through the ZnO nanowires (scale bar = $1 \mu\text{m}$).

7.4.4 In air "suspended" SPs and Mie resonance modes

QDSPs were deposited on a bed of ZnO nanowires to "suspend" them in air for a nearly isotropic refractive index difference around the QDSPs, Fig. 7.5a. After suspension the QDSPs were mostly intact and showed little to no deformations despite the wet deposition, Fig. 7.5b. Using cathode luminescence the QDSPs were easy to distinguish from the ZnO nanowires as a result of the energy difference in the band gaps between the CdSe@ZnS QDs (red) and the ZnO wires (blue), see Fig. 7.5c.

Measuring the photoluminescence spectra of "suspended" QDSPs, using optical setup 3, showed a distinct size effect in the emission from the QDSPs, suggesting a collective effect of the QDs as a result of the self-assembly. Small, meaning in this case $\sim 1\text{-}2\ \mu\text{m}$, QDSPs on ZnO nanowires showed a Gaussian photoluminescence peak at $1.95\ \text{eV}$ ($636\ \text{nm}$) without any extra features, Fig. 7.5d, the peak at $3.25\ \text{eV}$ belongs to the photoluminescence of the ZnO nanowires. For larger QDSPs, in this case $\sim 2.6\ \mu\text{m}$, high narrow peaks between 1.9 and $2.1\ \text{eV}$ on top of the photoluminescence were observed. These modulated emissions were observed in most of the QDSPs of similar sizes as is shown in Fig. 7.7**Top**. Here a series of emission spectra measured on differently sized QDSPs are plotted with an offset. Interestingly the features on the QDSPs were not similar but instead showed sharp peaks at seemingly random positions over the photoluminescence curve, i.e. between $1.9\ \text{eV}$ and $2.1\ \text{eV}$. This is indicative of optical Mie resonant modes on the surface of the assemblies modulating the photoluminescence of the QD constituents via stimulated emission as these depend sensitively on the exact size parameter of each sphere. The photoluminescence spectra did not change with a higher fluence rate, as is shown in Fig. 7.7**Bottom**. With fluence rates over a range of 5 orders of magnitude the "suspended" QDSPs did not show any significant change in the photoluminescence spectra. This is in sharp contrast with

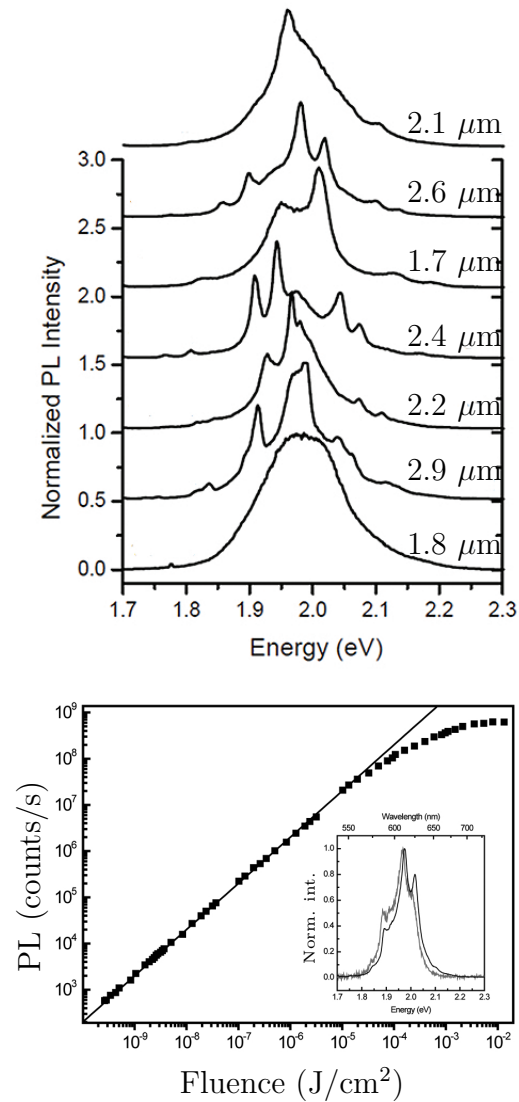


Figure 7.7: Modulated photoluminescence in QDSPs suspended on ZnO nanowires, **Top**) Modulation in the photoluminescence of the "suspended" QD, bigger QDSPs show more modulation. **Bottom**) Photoluminescence as a function of the excitation power showing no change in the shape of the photoluminescence spectra.

the same QDSPs but then deposited on a glass substrate, as described earlier, where these QDSPs showed state filling behavior at high fluence rates similar to the constituent QDs. The reason behind this is not yet known, however, this does show that there are strong collective effects of the QDs in the QDSPs.

In addition to the modulated photoluminescence spectra, inhomogeneous emission was observed when imaging the QDSPs on ZnO nanowires with optical setup 2, a typical image is shown in Fig. 7.6. Where QDSPs on a glass substrate showed a normal brightness distribution, visualized in Fig. 7.6b by using an intensity gradient map, the QDSPs on ZnO nanowires showed hotspots and ringlike features in the intensity map as is shown in Fig. 7.6a. What causes these hotspots could not yet be determined. They could be the result of Mie modes or whispering gallery modes but an effect caused by contact points with the ZnO nanowires can not yet be excluded. Nonetheless, both of these causes for photoluminescent hotspots would be interesting for follow-up research. The narrow peaks in the luminescence is likely the onset of laser action, but should be confirmed by measurements showing e.g. a non-linear (quadratic) dependence of these emissions on the excitation power.

7.5 Conclusions & Outlook

In this chapter it was shown that supraparticles (SPs) consisting of high quantum-efficiency luminescent quantumdots (QDs) were made by self-assembly in slowly drying emulsion droplets. These SPs made with core-multishell CdSe@ZnS QDs maintained the photoluminescence of the QDs with at least equal efficiency as the individual constituents with no significant shift in the photoluminescence spectra. Both the QDs and the QD SPs showed extra peaks at higher fluence rates indicating state filling behavior. From these findings we can conclude that the QD properties inherent to the quantum confinement in the semiconductor nanoparticles were preserved in the densely packed QDSPs. Depositing QDSPs with diameters above $\sim 1.7 \mu\text{m}$ on a bed of ZnO nanowires showed sharp peaks on top of the photoluminescence spectra, most like due to the onset of lasing, possibly caused by Mie resonances or whispering gallery modes. In addition, photoluminescence hotspots were observed in these "suspended" QDSPs but what caused these inhomogeneities in the photoluminescence intensities was not yet determined and will be interesting for follow-up research. It will be interesting to study this self-assembly with QDs of even higher quantum efficiencies and by making larger QDSPs to possibly induce lasing.

7.6 Acknowledgments

Bert van Vugt and Henriette Bakker are gratefully acknowledged for their hard work on the measurements of quantumdots and quantumdot supraparticles. Bert van Vugt is also thanked for growing the zinc oxide nanowires used for this chapter. Relinde Moes is gratefully acknowledged for her hard work on the synthesis of the core-multishell quantumdots that were used for this research. Patrick Beasjou is thanked for the quantum efficiency measurements and Daniel Vanmaekelbergh and Alfons van Blaaderen are thanked for the time and effort they put into this research.

References

- [1] H. G. Moon, Y.-S. Shim, D. H. Kim, H. Y. Jeong, M. Jeong, J. Y. Jung, S. M. Han, J. K. Kim, J.-S. Kim, H.-H. Park, J.-H. Lee, H. L. Tuller, S.-J. Yoon, and H. W. Jang, *Self-activated ultrahigh chemosensitivity of oxide thin film nanostructures for transparent sensors*. *Sci. Rep.*, 2:1–7, 2012.
- [2] G. K. Darbha, A. Ray, and P. C. Ray, *Gold nanoparticle-based miniaturized nanomaterial surface energy transfer probe for rapid and ultrasensitive detection of mercury in soil, water, and fish*. *ACS Nano*, 1(3):208–214, Oct 2007.
- [3] C. K. Chan, X. F. Zhang, and Y. Cui, *High capacity Li Ion battery anodes using Ge nanowires*. *Nano Lett.*, 8(1):307–309, Dec 2007.
- [4] Y. Li, B. Tan, and Y. Wu, *Mesoporous Co_3O_4 nanowire arrays for lithium ion batteries with high capacity and rate capability*. *Nano Lett.*, 8(1):265–270, Dec 2007.
- [5] M. Ferrari, *Cancer nanotechnology: opportunities and challenges*. *Nat Rev Cancer*, 5(3):161–171, 2005.
- [6] M. Mahmoudi, M. Sahraian, M. Shokrgozar, and S. Laurent, *Superparamagnetic iron oxide nanoparticles: promises for diagnosis and treatment of multiple sclerosis*. *ACS Chem Neurosci*, 2(3):118–140, Mar 2011.
- [7] R. Chau, B. Doyle, S. Datta, J. Kavalieros, and K. Zhang, *Integrated nanoelectronics for the future*. *Nat Mater*, 6(11):810–812, 2007.
- [8] T. Ito and S. Okazaki, *Pushing the limits of lithography*. *Nature*, 406(0028-0836):1027–1031, 2000.
- [9] G. M. Whitesides and B. Grzybowski, *Self-assembly at all scales*. *Science*, 295(5564):2418–2421, Mar 2002.
- [10] H.-w. Zhang, Y. Liu, and S.-h. Sun, *Synthesis and assembly of magnetic nanoparticles for information and energy storage applications*. *Frontiers of Physics in China*, 5:347–356, 2010. 10.1007/s11467-010-0104-9.
- [11] H. G. Craighead, *Nanoelectromechanical systems*. *Science*, 290(5496):1532–1535, Nov 2000.
- [12] P. Bolhuis, D. Frenkel, S. Mau, and D. Huse, *Entropy difference between crystal phases*. *Nature*, 388:235–236, 1997.
- [13] W. G. Hoover and F. H. Ree, *Melting transition and communal entropy for hard spheres*. *J. Chem. Phys.*, 49(8):3609–3617, 1968.
- [14] P. N. Pusey and W. van Meegen, *Phase behaviour of concentrated suspensions of nearly hard colloidal spheres*. *Nature*, 320:340–342, 1986.
- [15] Z. Cheng, W. B. Russel, and P. Chaikin, *Controlled growth of hard-sphere colloidal crystals*. *Nature*, 401(6756):893–895, 1999.
- [16] J.-M. Meijer, D. V. Byelov, L. Rossi, A. Snigirev, I. Snigireva, A. P. Philipse, and A. V. Petukhov, *Self-assembly of colloidal hematite cubes: a microradian X-ray diffraction exploration of sedimentary crystals*. *Soft Matter*, 9(45):10729–10738, 2013.
- [17] A. Kuijk, D. V. Byelov, A. V. Petukhov, A. van Blaaderen, and A. Imhof, *Phase behavior of colloidal silica rods*. *Faraday Discuss.*, 159(0):181–199, 2012.

- [18] C. Meltzer, J. Paul, H. Dietrich, C. M. Jäger, T. Clark, D. Zahn, B. Braunschweig, and W. Peukert, *Indentation and self-healing mechanisms of a self-assembled monolayer—a combined experimental and modeling study*. *Journal of the American Chemical Society*, 136(30):10718–10727, 2014.
- [19] S. Auer and D. Frenkel, *Prediction of absolute crystal-nucleation rate in hard-sphere colloids*. *Nature*, 409(6823):1020–1023, 2001.
- [20] L. Fillion, M. Hermes, R. Ni, and M. Dijkstra, *Crystal nucleation of hard spheres using molecular dynamics, umbrella sampling, and forward flux sampling: A comparison of simulation techniques*. *The Journal of Chemical Physics*, 133(24):244115, 2010.
- [21] A. Einstein, *Über die von der molekularkinetischen theorie der wärme geforderte bewegung von in ruhenden flüssigkeiten suspendierten teilchen*. *Annalen der Physik*, 322(8):549–560, 1905.
- [22] F. Perrin, *Mouvement brownien d’un ellipsoïde (II). rotation libre et dâ polarisation des fluorescences. translation et diffusion de molâ cules ellipsoïdales*. *J. phys. radium*, 7(1):1–11, 1936.
- [23] C. Royall, R. van Roij, and A. van Blaaderen, *Extended sedimentation profiles in charged colloids: the gravitational length, entropy, and electrostatics*. *Journal of Physics: Condensed Matter*, 17(15):2315, 2005.
- [24] S. Eustis and M. A. El-Sayed, *Why gold nanoparticles are more precious than pretty gold: noble metal surface plasmon resonance and its enhancement of the radiative and nonradiative properties of nanocrystals of different shapes*. *Chemical Society Reviews*, 35(3):209–217, 2006.
- [25] A. Alsivisatos, *Semiconductor clusters, nanocrystals, and quantum dots*. *Science*, 271:933, 1996.
- [26] L. Néel, *Théorie du traînage magnétique des ferromagnétiques en grains fins avec application aux terres cuites*. *Ann. Géophys. (1949)*., 5:99, 1949.
- [27] C. P. Bean and J. D. Livingston, *Superparamagnetism*. *Journal of Applied Physics*, 30(4):S120–S129, 1959.
- [28] A. I. Ekimov and A. A. Onushchenko, *Quantum size effect in three-dimensional microscopic semiconductor crystals*. *American Institute of Physics*, 34(6):363–366, 1981.
- [29] M. G. Bawendi, M. L. Steigerwald, and L. E. Brus, *The quantum mechanics of larger semiconductor clusters ("quantum dots")*. *Annual Review of Physical Chemistry*, 41(1):477–496, 1990.
- [30] W. Griffin, *Hydrophilic-lipophilic balance*. *J. Soc. Cosmet. Chem*, 1:311, 1949.
- [31] W. Griffin, *Calculation of hlb values of non-ionic surfactants*. *J. Soc. Cosmet. Chem*, 5:249, 1954.
- [32] P. M. Kruglyakov. *Hydrophile-lipophile balance of surfactants and solid particles: physicochemical aspects and applications*, volume 9. Elsevier, 2000.
- [33] V. N. Manoharan, M. T. Elsesser, and D. J. Pine, *Dense packing and symmetry in small clusters of microspheres*. *Science*, 301(5632):483–487, 2003.
- [34] Y. Xia and Z. Tang, *Monodisperse inorganic supraparticles: formation mechanism, properties and applications*. *Chemical Communications*, 48(51):6320–6336, 2012.

- [35] F. Bai, D. Wang, Z. Huo, W. Chen, L. Liu, X. Liang, C. Chen, X. Wang, Q. Peng, and Y. Li, *A versatile bottom-up assembly approach to colloidal spheres from nanocrystals*. *Angewandte Chemie International Edition*, 46(35):6650–6653, 2007.
- [36] J. Guo, W. Yang, and C. Wang, *Magnetic colloidal supraparticles: Design, fabrication and biomedical applications*. *Advanced Materials*, 25(37):5196–5214, 2013.
- [37] Y. Xia, T. D. Nguyen, M. Yang, B. Lee, A. Santos, P. Podsiadlo, Z. Tang, S. C. Glotzer, and N. A. Kotov, *Self-assembly of self-limiting monodisperse supraparticles from polydisperse nanoparticles*. *Nature Nanotechnology*, 6(9):580–587, 2011.
- [38] J. Zhuang, H. Wu, Y. Yang, and Y. C. Cao, *Controlling colloidal superparticle growth through solvophobic interactions*. *Angewandte Chemie International Edition*, 47(12):2208–2212, 2008.
- [39] T. Wang, J. Zhuang, J. Lynch, O. Chen, Z. Wang, X. Wang, D. LaMontagne, H. Wu, Z. Wang, and Y. C. Cao, *Self-assembled colloidal superparticles from nanorods*. *Science*, 338(6105):358–363, 2012.
- [40] M. Grzelczak, J. Vermant, E. M. Furst, and L. M. Liz-Marzán, *Directed self-assembly of nanoparticles*. *ACS nano*, 4(7):3591–3605, 2010.
- [41] J. Lacava, P. Born, and T. Kraus, *Nanoparticle clusters with lennard-jones geometries*. *Nano Lett.*, 12(6):3279–3282, May 2012.
- [42] T. Watanabe, *Grain boundary design for desirable mechanical properties*. *Le Journal de Physique Colloques*, 49(C5):C5–507–C5–519, 1988.
- [43] D. Dimos, P. Chaudhari, J. Mannhart, and F. LeGoues, *Orientation dependence of grain-boundary critical currents in y Ba_2 Cu_3 $O_{7-\delta}$ bicrystals*. *Physical Review Letters*, 61(2):219, 1988.
- [44] P. Chaudhari, J. Mannhart, D. Dimos, C. Tsuei, J. Chi, M. Oprysko, and M. Scheuermann, *Direct measurement of the superconducting properties of single grain boundaries in Y_1 Ba_2 Cu_3 $O_{7-\delta}$* . *Physical review letters*, 60(16):1653, 1988.
- [45] V. K. LaMer and R. H. Dinegar, *Theory, production and mechanism of formation of monodispersed hydrosols*. *Journal of the American Chemical Society*, 72(11):4847–4854, 1950.
- [46] V. K. LaMer, *Nucleation in phase transitions*. *Industrial & Engineering Chemistry*, 44(6):1270–1277, 1952.
- [47] J. Park, J. Joo, S. G. Kwon, Y. Jang, and T. Hyeon, *Synthesis of monodisperse spherical nanocrystals*. *Angewandte Chemie International Edition*, 46(25):4630–4660, 2007.
- [48] M. T. Swihart, *Vapor-phase synthesis of nanoparticles*. *Current Opinion in Colloid & Interface Science*, 8(1):127–133, 2003.
- [49] J. Turkevich, P. C. Stevenson, and J. Hillier, *A study of the nucleation and growth processes in the synthesis of colloidal gold*. *Discussions of the Faraday Society*, 11:55–75, 1951.
- [50] C. B. Murray, D. J. Norris, and M. G. Bawendi, *Synthesis and characterization of nearly monodisperse CdE ($E =$ sulfur, selenium, tellurium) semiconductor nanocrystallites*. *J. Am. Chem. Soc.*, 115(19):8706–8715, Sep 1993.
- [51] J. Park, K. An, Y. Hwang, J.-G. Park, H.-J. Noh, J.-Y. Kim, J.-H. Park, N.-M. Hwang, and T. Hyeon, *Ultra-large-scale syntheses of monodisperse nanocrystals*. *Nat Mater*, 3(12):891–895, 2004.

- [52] A. K. Gupta and M. Gupta, *Synthesis and surface engineering of iron oxide nanoparticles for biomedical applications*. *Biomaterials*, 26(18):3995–4021, 2005.
- [53] T. Hyeon, S. S. Lee, J. Park, Y. Chung, and H. B. Na, *Synthesis of highly crystalline and monodisperse maghemite nanocrystallites without a size-selection process*. *Journal of the American Chemical Society*, 123(51):12798–12801, 2001.
- [54] M. I. Bodnarchuk, M. V. Kovalenko, H. Groiss, R. Resel, M. Reissner, G. Hesser, R. T. Lechner, W. Steiner, F. Schäffler, and W. Heiss, *Exchange-coupled bimagnetic wüstite/metal ferrite core/shell nanocrystals: Size, shape, and compositional control*. *Small*, 5(20):2247–2252, 2009.
- [55] D. Napper, *Steric stabilization*. *Journal of Colloid and Interface Science*, 58(2):390–407, 1977.
- [56] A. Puzder, A. J. Williamson, N. Zaitseva, G. Galli, L. Manna, and A. P. Alivisatos, *The effect of organic ligand binding on the growth of CdSe nanoparticles probed by ab initio calculations*. *Nano Letters*, 4(12):2361–2365, 2004.
- [57] M. V. Kovalenko, M. I. Bodnarchuk, R. T. Lechner, G. Hesser, F. Schäffler, and W. Heiss, *Fatty acid salts as stabilizers in size-and shape-controlled nanocrystal synthesis: the case of inverse spinel iron oxide*. *Journal of the American Chemical Society*, 129(20):6352–6353, 2007.
- [58] A. Shavel and L. M. Liz-Marzán, *Shape control of iron oxide nanoparticles*. *Phys. Chem. Chem. Phys.*, 11(19):3762–3766, 2009.
- [59] G. Wulff. *Z. Kristallogr.*, 34:449, 1901.
- [60] Y. Hou, Z. Xu, and S. Sun, *Controlled synthesis and chemical conversions of FeO nanoparticles*. *Angewandte Chemie*, 119(33):6445–6448, 2007.
- [61] R. M. Cornell and U. Schwertmann. *The iron oxides: structure, properties, reactions, occurrences and uses*. Wiley-Vch, 2003.
- [62] R. Zboril, M. Mashlan, and D. Petridis, *Iron (iii) oxides from thermal processes synthesis, structural and magnetic properties, mössbauer spectroscopy characterization, and applications*. *Chemistry of materials*, 14(3):969–982, 2002.
- [63] S. Saini, R. Frankel, D. Stark, and J. Ferrucci Jr, *Magnetism: a primer and review*. *American Journal of Roentgenology*, 150(4):735–743, 1988.
- [64] J. Kimling, M. Maier, B. Okenve, V. Kotaidis, H. Ballot, and A. Plech, *Turkevich method for gold nanoparticle synthesis revisited*. *The Journal of Physical Chemistry B*, 110(32):15700–15707, 2006.
- [65] M. Brust, M. Walker, D. Bethell, D. J. Schiffrin, and R. Whyman, *Synthesis of thiol-derivatised gold nanoparticles in a two-phase liquid-liquid system*. *J. Chem. Soc., Chem. Commun.*, (7):801–802, 1994.
- [66] R. Xie, U. Kolb, J. Li, T. Basch, and A. Mews, *Synthesis and characterization of highly luminescent CdSe-core CdS/Zn_{0.5}Cd_{0.5}S/ZnS multishell nanocrystals*. *J. Am. Chem. Soc.*, 127(20):7480–7488, Apr 2005.
- [67] W. G. van Sark, P. L. Frederix, D. J. van den Heuvel, H. C. Gerritsen, A. A. Bol, J. N. van Lingen, C. de Mello Donega, and A. Meijerink, *Photooxidation and photobleaching of single CdSe/ZnS quantum dots probed by room-temperature time-resolved spectroscopy*. *The Journal of Physical Chemistry B*, 105(35):8281–8284, 2001.

- [68] P. Pusey, *The effect of polydispersity on the crystallization of hard spherical colloids*. Journal de physique, 48(5):709–712, 1987.
- [69] A. O. Yalcin, B. de Nijs, Z. Fan, F. D. Tichelaar, D. Vanmaekelbergh, A. van Blaaderen, T. J. Vlugt, M. A. van Huis, and H. W. Zandbergen, *Core@shell reconfiguration through thermal annealing in $Fe_xO/CoFe_2O_4$ ordered 2d nanocrystal arrays*. Nanotechnology, 25(5):055601, 2014.
- [70] A. van Blaaderen, J. van Geest, and A. Vrij, *Monodisperse colloidal silica spheres from tetraalkoxysilanes: particle formation and growth mechanism*. Journal of colloid and interface science, 154(2):481–501, 1992.
- [71] P. N. Pusey, E. Zaccarelli, C. Valeriani, E. Sanz, W. C. K. Poon, and M. E. Cates, *Hard spheres: crystallization and glass formation*. Philosophical Transactions of the Royal Society A: Mathematical, Physical and Engineering Sciences, 367(1909):4993–5011, Dec 2009.
- [72] W. H. Evers, B. D. Nijs, L. Filion, S. Castillo, M. Dijkstra, and D. Vanmaekelbergh, *Entropy-driven formation of binary semiconductor-nanocrystal superlattices*. Nano letters, 10(10):4235–4241, 2010.
- [73] K. Overgaag, W. Evers, B. de Nijs, R. Koole, J. Meeldijk, and D. Vanmaekelbergh, *Binary superlattices of PbSe and CdSe nanocrystals*. Journal of the American Chemical Society, 130(25):7833–7835, 2008.
- [74] R. Shannon, *Revised effective ionic radii and systematic studies of interatomic distances in halides and chalcogenides*. Acta Crystallographica Section A, 32(5):751–767, 1976.
- [75] B. A. Korgel, S. Fullam, S. Connolly, and D. Fitzmaurice, *Assembly and self-organization of silver nanocrystal superlattices: Ordered soft spheres*. J. Phys. Chem. B, 102(43):8379–8388, 1998.
- [76] Y. C. Han, H. G. Cha, C. W. Kim, Y. H. Kim, and Y. S. Kang, *Synthesis of highly magnetized iron nanoparticles by a solventless thermal decomposition method*. J. Phys. Chem. C, 111(17):6275–6280, 2007.
- [77] E. V. Shevchenko, D. V. Talapin, N. A. Kotov, S. O’Brien, and C. B. Murray, *Structural diversity in binary nanoparticle superlattices*. Nature, 439(7072):55–59, 2006.
- [78] S. H. Joo, J. Y. Park, C.-K. Tsung, Y. Yamada, P. Yang, and G. A. Somorjai, *Thermally stable Pt/mesoporous silica coreshell nanocatalysts for high-temperature reactions*. Nature materials, 8(2):126–131, 2008.
- [79] F. X. Redl, C. T. Black, G. C. Papaefthymiou, R. L. Sandstrom, M. Yin, H. Zeng, C. B. Murray, and S. P. O’Brien, *Magnetic, electronic, and structural characterization of non-stoichiometric iron oxides at the nanoscale*. Journal of the American Chemical Society, 126(44):14583–14599, 2004.
- [80] Z. Tang, Z. Zhang, Y. Wang, S. C. Glotzer, and N. A. Kotov, *Self-assembly of CdTe nanocrystals into free-floating sheets*. Science, 314(5797):274–278, 2006.
- [81] Z. Yu, C.-F. Wang, L. Ling, L. Chen, and S. Chen, *Triphase microfluidic-directed self-assembly: Anisotropic colloidal photonic crystal supraparticles and multicolor patterns made easy*. Angewandte Chemie International Edition, 51(10):2375–2378, 2012.
- [82] J. Zhuang, H. Wu, Y. Yang, and Y. C. Cao, *Supercrystalline colloidal particles from artificial atoms*. Journal of the American Chemical Society, 129(46):14166–14167, 2007.

- [83] Y.-F. Maa and C. C. Hsu, *Performance of sonication and microfluidization for liquid-liquid emulsification*. *Pharmaceutical development and technology*, 4(2):233–240, 1999.
- [84] K. Landfester, F. Schork, and V. A. Kusuma, *Particle size distribution in mini-emulsion polymerization*. *Comptes Rendus Chimie*, 6(11-12):1337–1342, 2003.
- [85] K. Landfester, J. Eisenblätter, and R. Rothe, *Preparation of polymerizable miniemulsions by ultrasonication*. *JCT Research*, 1(1)(1):65–68, 2004.
- [86] T. G. Mason and J. Bibette, *Emulsification in viscoelastic media*. *Phys. Rev. Lett.*, 77(16):3481–3484, 1996.
- [87] T. Mason and J. Bibette, *Shear rupturing of droplets in complex fluids*. *Langmuir*, 13(17):4600–4613, 1997.
- [88] C. Mabile, V. Schmitt, P. Gorria, F. Leal Calderon, V. Faye, B. Deminiere, and J. Bibette, *Rheological and shearing conditions for the preparation of monodisperse emulsions*. *Langmuir*, 16(2):422–429, 2000.
- [89] C. Mabile, F. Leal-Calderon, J. Bibette, and V. Schmitt, *Monodisperse fragmentation in emulsions: Mechanisms and kinetics*. *EPL (Europhysics Letters)*, 61(5):708, 2003.
- [90] D. Zerrouki, B. Rotenberg, S. Abramson, J. Baudry, C. Goubault, F. Leal-Calderon, D. J. Pine, and J. Bibette, *Preparation of doublet, triangular, and tetrahedral colloidal clusters by controlled emulsification*. *Langmuir*, 22(1):57–62, 2006.
- [91] J. M. Rallison, *The deformation of small viscous drops and bubbles in shear flows*. *Annu. Rev. Fluid Mech.*, 16(1):45–66, 1984.
- [92] E. M. Purcell, *Life at low reynolds number*. *Am. J. Phys*, 45(1):3–11, 1977.
- [93] C. Tropea, A. L. Yarin, and J. F. Foss. *Springer handbook of experimental fluid mechanics*, volume 1. Springer, 2007.
- [94] U. Gündüz, *Viscosity prediction of polyethylene-glycol-dextran-water solutions used in aqueous two-phase systems*. *Journal of Chromatography B: Biomedical Sciences and Applications*, 743(1&2):181–185, 2000.
- [95] M. Tjahjadi, H. Stone, and J. Ottino, *Satellite and subsatellite formation in capillary breakup*. *Journal of Fluid Mechanics*, 243(1):297–317, 1992.
- [96] D. M. Henderson, W. G. Pritchard, and L. B. Smolka, *On the pinch-off of a pendant drop of viscous fluid*. *Physics of Fluids*, 9(11):3188–3200, 1997.
- [97] X. Zhang, *Dynamics of drop formation in viscous flows*. *Chemical Engineering Science*, 54(12):1759–1774, 1999.
- [98] V. Cristini, S. Guido, A. Alfani, J. Blawdziewicz, and M. Loewenberg, *Drop breakup and fragment size distribution in shear flow*. *Journal of Rheology*, 47(5):1283–1298, 2003.
- [99] C. D. Andereck, S. Liu, and H. L. Swinney, *Flow regimes in a circular couette system with independently rotating cylinders*. *Journal of Fluid Mechanics*, 164(3):155–183, 1986.
- [100] C. Graf, D. L. J. Vossen, A. Imhof, and A. van Blaaderen, *A general method to coat colloidal particles with silica*. *Langmuir*, 19(17):6693–6700, 2003.
- [101] ISCO. *ISCOTABLES: A handbook of data for biological and physical scientist*. Isco. 1982.
- [102] A. Mackay, *A dense non-crystallographic packing of equal spheres*. *Acta Cryst.*, 15(9):916–918, 1962.

- [103] T. Brugarolas, F. Tu, and D. Lee, *Directed assembly of particles using microfluidic droplets and bubbles*. *Soft Matter*, 9(38):9046–9058, 2013.
- [104] V. Lucic, F. Förster, and W. Baumeister, *Structural studies by electron tomography: from cells to molecules*. *Annu. Rev. Biochem.*, 74:833–865, 2005.
- [105] J. Frank. *Electron tomography*. Springer, 1992.
- [106] T. G. Frey and C. A. Mannella, *The internal structure of mitochondria*. *Trends in biochemical sciences*, 25(7):319–324, 2000.
- [107] J. L. Milne and S. Subramaniam, *Cryo-electron tomography of bacteria: progress, challenges and future prospects*. *Nature Reviews Microbiology*, 7(9):666–675, 2009.
- [108] H. Friedrich, P. E. de Jongh, A. J. Verkleij, and K. P. de Jong, *Electron tomography for heterogeneous catalysts and related nanostructured materials*. *Chemical reviews*, 109(5):1613–1629, 2009.
- [109] I. Florea, A. Demortiere, C. Petit, H. Bulou, C. Hirlimann, and O. Ersen, *3D quantitative analysis of platinum nanocrystal superlattices by electron tomography*. *ACS nano*, 6(3):2574–2581, 2012.
- [110] H. Friedrich, C. J. Gommers, K. Overgaag, J. D. Meeldijk, W. H. Evers, B. d. Nijs, M. P. Boneschanscher, P. E. de Jongh, A. J. Verkleij, and K. P. de Jong, *Quantitative structural analysis of binary nanocrystal superlattices by electron tomography*. *Nano letters*, 9(7):2719–2724, 2009.
- [111] W. H. Evers, H. Friedrich, L. Filion, M. Dijkstra, and D. Vanmaekelbergh, *Observation of a ternary nanocrystal superlattice and its structural characterization by electron tomography*. *Angewandte Chemie International Edition*, 48(51):9655–9657, 2009.
- [112] T. Altantzis, B. Goris, A. Sánchez-Iglesias, M. Grzelczak, L. M. Liz-Marzán, and S. Bals, *Quantitative structure determination of large three-dimensional nanoparticle assemblies*. *Particle & Particle Systems Characterization*, 30(1):84–88, 2013.
- [113] J. E. Galván-Moya, T. Altantzis, K. Nelissen, F. M. Peeters, M. Grzelczak, L. M. Liz-Marzán, S. Bals, and G. van Tendeloo, *Self-organization of highly symmetric nanoassemblies: A matter of competition*. *ACS nano*, 8(4):3869–3875, 2014.
- [114] B. Goris, S. Bals, W. van den Broek, E. Carbó-Argibay, S. Gómez-Graña, L. M. Liz-Marzán, L. M.n, and G. van Tendeloo, *Atomic-scale determination of surface facets in gold nanorods*. *Nature materials*, 11(11):930–935, 2012.
- [115] P. Yuan, J. Sun, H. Xu, L. Zhou, J. Liu, D. Zhang, Y. Wang, K. S. Jack, J. Drennan, and D. Zhao, *Extensive inspection of an unconventional mesoporous silica material at all length-scales*. *Chemistry of Materials*, 23(2):229–238, 2010.
- [116] S. R. Deans. *The Radon Transform and Some of Its Applications*. Dover Publications Inc., 1983.
- [117] J. Frank. *Introduction: Principles of electron tomography*. In *Electron Tomography*, pages 1–15. Springer, 2006.
- [118] A. van Blaaderen. *Quantitative real-space analysis of colloidal structures and dynamics with confocal scanning light microscopy*. In *Optical Methods and Physics of Colloidal Dispersions*, pages 59–65. Springer, 1997.
- [119] V. Prasad, D. Semwogerere, and E. R. Weeks, *Confocal microscopy of colloids*. *Journal of Physics: Condensed Matter*, 19(11):113102, 2007.

- [120] T. Besseling, M. Hermes, A. Kuijk, B. de Nijs, T.-S. Deng, M. Dijkstra, A. Imhof, and A. van Blaaderen, *Determination of the positions and orientations of concentrated rod-like colloids from 3d microscopy data*. arXiv preprint arXiv:1406.4985, 2014.
- [121] J. Radon, *On determination of functions by their integral values along certain multiplicities*. Ber. der Sachische Akademie der Wissenschaften Leipzig,(Germany), 69:262–277, 1917.
- [122] R. R. Roth, *CCD Camera*. Washington, DC: U.S. Patent and Trademark Office, No. 4,396,950, 1983.
- [123] B. F. McEwen and M. Marko, *The emergence of electron tomography as an important tool for investigating cellular ultrastructure*. Journal of Histochemistry & Cytochemistry, 49(5):553–563, 2001.
- [124] W. Rudin, *Real and complex analysis*. Tata McGraw-Hill Education, third ed., 1987.
- [125] R. N. Bracewell, *Strip integration in radio astronomy*. Australian Journal of Physics, 9(2):198–217, 1956.
- [126] R. Crowther, D. DeRosier, and A. Klug, *The reconstruction of a three-dimensional structure from projections and its application to electron microscopy*. Proceedings of the Royal Society of London. A. Mathematical and Physical Sciences, 317(1530):319–340, 1970.
- [127] P. Gilbert, *Iterative methods for the three-dimensional reconstruction of an object from projections*. Journal of Theoretical Biology, 36(1):105–117, 1972.
- [128] J. R. Kremer, D. N. Mastrorarde, and J. R. McIntosh, *Computer visualization of three-dimensional image data using IMOD*. Journal of structural biology, 116(1):71–76, 1996.
- [129] *Soft condensed matter (SCM) group, Debye Institute for Nanomaterials Science, Ornstein lab. Princetonplein 1, 3584 cc Utrecht, the Netherlands*.
- [130] A. van Blaaderen, M. Dijkstra, R. van Roij, A. Imhof, M. Kamp, B. Kwaadgras, T. Vissers, and B. Liu, *Manipulating the self assembly of colloids in electric fields*. The European physical journal. Special topics, 222(11):2895–2909, 2013.
- [131] L. Wang, L. Xia, G. Li, S. Ravaine, and X. e. Zhao, *Patterning the surface of colloidal microspheres and fabrication of nonspherical particles*. Angewandte Chemie International Edition, 47(25):4725–4728, 2008.
- [132] D. A. Wilson, R. J. M. Nolte, and J. C. M. van Hest, *Autonomous movement of platinum-loaded stomatocytes*. Nature Chemistry, 4:268–274, 2012.
- [133] A. Brown and W. Poon, *Ionic effects in self-propelled Pt-coated janus swimmers*. Soft matter, 10(22):4016–4027, 2014.
- [134] C. Zoldesi and A. Imhof, *Synthesis of monodisperse colloidal spheres, capsules, and microballoons by emulsion templating*. Adv. Mater., 17(7):924–928, 2005.
- [135] C. Zoldesi, P. Steegstra, and A. Imhof, *Encapsulation of emulsion droplets by organo-silica shells*. Journal of Colloid and Interface Science, 308(1):121–129, 2007.
- [136] A. Kuijk, A. van Blaaderen, and A. Imhof, *Synthesis of monodisperse, rodlike silica colloids with tunable aspect ratio*. J. Am. Chem. Soc., 133(8):2346–2349, 2011.
- [137] A. Kuijk, A. Imhof, M. H. Verkuijlen, T. H. Besseling, E. R. van Eck, and A. van Blaaderen, *Colloidal silica rods: Material properties and fluorescent labeling*. Particle & Particle Systems Characterization, 2014.

- [138] B. Peng, G. Soligno, M. Kamp, B. de Nijs, J. de Graaf, M. Dijkstra, R. van Roij, A. van Blaaderen, and A. Imhof, *Site-specific growth of polymer on silica rods*. Submitted to Soft Matter.
- [139] J. de Graaf, M. Dijkstra, and R. van Roij, *Adsorption trajectories and free-energy separatrixes for colloidal particles in contact with a liquid-liquid interface*. The Journal of chemical physics, 132(16):164902–164902, 2010.
- [140] X. Ye, C. Zheng, J. Chen, Y. Gao, and C. B. Murray, *Using binary surfactant mixtures to simultaneously improve the dimensional tunability and monodispersity in the seeded growth of gold nanorods*. Nano Lett., 13(2):765–771, 2013.
- [141] I. Gorelikov and N. Matsuura, *Single-step coating of mesoporous silica on cetyltrimethyl ammonium bromide-capped nanoparticles*. Nano letters, 8(1):369–373, 2008.
- [142] W. Wang, B. Gu, L. Liang, and W. Hamilton, *Fabrication of two-and three-dimensional silica nanocolloidal particle arrays*. The Journal of Physical Chemistry B, 107(15):3400–3404, 2003.
- [143] L. Fillion and M. Dijkstra, *Prediction of binary hard-sphere crystal structures*. Physical Review E, 79(4):046714, 2009.
- [144] N. Zheng, J. Fan, and G. D. Stucky, *One-step one-phase synthesis of monodisperse noble-metallic nanoparticles and their colloidal crystals*. Journal of the American Chemical Society, 128(20):6550–6551, 2006.
- [145] E. A. Avallone, T. Baumeister, and A. M. Sadegh. *Marks’ standard handbook for mechanical engineers*, volume 6. McGraw-Hill New York, 1996.
- [146] D. A. Wilson, B. de Nijs, A. van Blaaderen, R. J. M. Nolte, and J. C. M. van Hest, *Fuel concentration dependent movement of supramolecular catalytic nanomotors*. Nanoscale, pages 1315–1318, 2013.
- [147] L. Zhang, M. D’Acunzi, M. Kappl, A. Imhof, A. van Blaaderen, H.-J. Butt, R. Graf, and D. Vollmer, *Tuning the mechanical properties of silica microcapsules*. Physical Chemistry Chemical Physics, 12(47):15392–15398, 2010.
- [148] H. Friedrich, M. McCartney, and P. Buseck, *Comparison of intensity distributions in tomograms from BF TEM, ADF STEM, HAADF STEM, and calculated tilt series*. Ultramicroscopy, 106(1):18–27, 2005.
- [149] P. A. Midgley and R. E. Dunin-Borkowski, *Electron tomography and holography in materials science*. Nature materials, 8(4):271–280, 2009.
- [150] E. Rabani, D. R. Reichman, P. L. Geissler, and L. E. Brus, *Drying-mediated self-assembly of nanoparticles*. Nature, 426(6964):271–274, 2003.
- [151] T. P. Bigioni, X.-M. Lin, T. T. Nguyen, E. I. Corwin, T. A. Witten, and H. M. Jaeger, *Kinetically driven self assembly of highly ordered nanoparticle monolayers*. Nature Materials, 5(4):265–270, 2006.
- [152] A. Tao, F. Kim, C. Hess, J. Goldberger, R. He, Y. Sun, Y. Xia, and P. Yang, *Langmuir-blodgett silver nanowire monolayers for molecular sensing using surface-enhanced raman spectroscopy*. Nano Letters, 3(9):1229–1233, 2003.
- [153] K. P. Velikov, C. G. Christova, R. P. Dullens, and A. van Blaaderen, *Layer-by-layer growth of binary colloidal crystals*. Science, 296(5565):106–109, 2002.

- [154] E. Lauga and M. P. Brenner, *Evaporation-driven assembly of colloidal particles*. Physical review letters, 93(23):238301, 2004.
- [155] D. Chandra and S. Yang, *Capillary-force-induced clustering of micropillar arrays: is it caused by isolated capillary bridges or by the lateral capillary meniscus interaction force?* Langmuir, 25(18):10430–10434, 2009.
- [156] T. Young, *An essay on the cohesion of fluids*. Philosophical Transactions of the Royal Society of London, 95:65–87, 1805.
- [157] H.-J. Butt and M. Kappl, *Normal capillary forces*. Advances in Colloid and Interface Science, 146(1-2):48–60, 2009.
- [158] D. Miksa, E. R. Irish, D. Chen, R. J. Composto, and D. M. Eckmann, *Dextran functionalized surfaces via reductive amination: morphology, wetting, and adhesion*. Biomacromolecules, 7(2):557–564, 2006.
- [159] F. Frank, *Supercooling of liquids*. Proceedings of the Royal Society of London. Series A, Mathematical and Physical Sciences, pages 43–46, 1952.
- [160] J. Conway and N. Sloane, *Sphere packings*. 1998.
- [161] J. T. McGinley, I. Jenkins, T. Sinno, and J. C. Crocker, *Assembling colloidal clusters using crystalline templates and reprogrammable DNA interactions*. Soft Matter, 9(38):9119–9128, 2013.
- [162] D. R. Nelson and B. I. Halperin, *Pentagonal and icosahedral order in rapidly cooled metals*. Science, 229(4710):233–238, 1985.
- [163] P. J. Steinhardt, D. R. Nelson, and M. Ronchetti, *Bond-orientational order in liquids and glasses*. Physical Review B, 28(2):784, 1983.
- [164] J. P. Doye and D. J. Wales, *The structure and stability of atomic liquids: From clusters to bulk*. Science, 271(5248):484–487, 1996.
- [165] N. C. Karayiannis, R. Malshe, M. Kröger, J. J. de Pablo, and M. Laso, *Evolution of fivefold local symmetry during crystal nucleation and growth in dense hard-sphere packings*. Soft Matter, 8(3):844–858, 2012.
- [166] S. C. Hendy and J. P. Doye, *Surface-reconstructed icosahedral structures for lead clusters*. Physical Review B, 66(23):235402, 2002.
- [167] Y. Wang, S. Teitel, and C. Dellago, *Melting of icosahedral gold nanoclusters from molecular dynamics simulations*. The Journal of chemical physics, 122(21):214722, 2005.
- [168] H. Hubert, B. Devouard, L. A. Garvie, M. O’Keeffe, P. R. Buseck, W. T. Petuskey, and P. F. McMillan, *Icosahedral packing of B_{12} icosahedra in boron suboxide (B_6O)*. Nature, 391(6665):376–378, 1998.
- [169] J. P. Doye and F. Calvo, *Entropic effects on the structure of lennard-jones clusters*. The Journal of chemical physics, 116:8307–8317, 2002.
- [170] H. Hofmeister, *Forty years study of fivefold twinned structures in small particles and thin films*. Crystal Research and Technology, 33(1):3–25, 1998.
- [171] M. R. Langille, J. Zhang, M. L. Personick, S. Li, and C. A. Mirkin, *Stepwise evolution of spherical seeds into 20-fold twinned icosahedra*. Science, 337(6097):954–957, 2012.
- [172] J. Tang, X. Zhou, D. Zhao, G. Q. Lu, J. Zou, and C. Yu, *Hard-sphere packing and icosahedral assembly in the formation of mesoporous materials*. Journal of the American Chemical Society, 129(29):9044–9048, 2007.

- [173] J. Doye and D. Wales, *Thermally-induced surface reconstructions of mackay icosahedra*. Zeitschrift für Physik D Atoms, Molecules and Clusters, 40(1):466–468, 1997.
- [174] G. Meng, N. Arkus, M. P. Brenner, and V. N. Manoharan, *The free-energy landscape of clusters of attractive hard spheres*. Science, 327(5965):560–563, 2010.
- [175] D. J. Wales, *Surveying a complex potential energy landscape: Overcoming broken ergodicity using basin-sampling*. Chemical Physics Letters, 584:1–9, 2013.
- [176] A. Fortini and M. Dijkstra, *Phase behaviour of hard spheres confined between parallel hard plates: manipulation of colloidal crystal structures by confinement*. Journal of Physics: Condensed Matter, 18(28):L371, 2006.
- [177] H. Löwen, E. Oguz, L. Assoud, and R. Messina, *Colloidal crystallization between two and three dimensions*. Advances in Chemical Physics, 148:225, 2012.
- [178] A. van Blaaderen and A. Vrij, *Synthesis and characterization of colloidal dispersions of fluorescent, monodisperse silica spheres*. Langmuir, 8(12):2921–2931, 1992.
- [179] H. Giesche, *Synthesis of monodispersed silica powders II. controlled growth reaction and continuous production process*. Journal of the European Ceramic Society, 14(3):205–214, 1994.
- [180] J. C. Crocker and D. G. Grier, *Methods of digital video microscopy for colloidal studies*. Journal of colloid and interface science, 179(1):298–310, 1996.
- [181] U. Dassanayake, S. Fraden, and A. van Blaaderen, *Structure of electrorheological fluids*. The Journal of Chemical Physics, 112:3851, 2000.
- [182] P. R. ten Wolde, M. J. Ruiz-Montero, and D. Frenkel, *Numerical calculation of the rate of crystal nucleation in a lennard-jones system at moderate undercooling*. J. Chem. Phys., 104(24):9932–9947, Jun 1996.
- [183] P. t. ten Wolde, M. Ruiz-Montero, and D. Frenkel.
- [184] J. Van Duijneveldt and D. Frenkel, *Computer simulation study of free energy barriers in crystal nucleation*. The Journal of chemical physics, 96(6):4655–4668, 1992.
- [185] P. R. Ten Wolde and D. Frenkel, *Computer simulation study of gas-liquid nucleation in a lennard-jones system*. The Journal of chemical physics, 109(22):9901–9918, 1998.
- [186] P. R. Ten Wolde, M. J. Ruiz-Montero, and D. Frenkel, *Numerical evidence for bcc ordering at the surface of a critical fcc nucleus*. Physical review letters, 75(14):2714, 1995.
- [187] K. Kuo, *Mackay, anti-mackay, double-mackay, pseudo-mackay, and related icosahedral shell clusters*. Structural Chemistry, 13(3-4):221–230, 2002.
- [188] A. L. Efros and M. Rosen, *The electronic structure of semiconductor nanocrystals*. Annual Review of Materials Science, 30(1):475–521, 2000.
- [189] C. de Mello Donegá, *Synthesis and properties of colloidal heteronanocrystals*. Chemical Society Reviews, 40(3):1512–1546, 2011.
- [190] P. V. Kamat, *Quantum dot solar cells. semiconductor nanocrystals as light harvesters*. The Journal of Physical Chemistry C, 112(48):18737–18753, 2008.
- [191] J. Bomm, A. Büchtemann, A. J. Chatten, R. Bose, D. J. Farrell, N. L. Chan, Y. Xiao, L. H. Slooff, T. Meyer, and A. Meyer, *Fabrication and full characterization of state-of-the-art quantum dot luminescent solar concentrators*. Solar Energy Materials and Solar Cells, 95(8):2087–2094, 2011.

- [192] W. G. van Sark, K. W. Barnham, L. H. Slooff, A. J. Chatten, A. Büchtemann, A. Meyer, S. J. McCormack, R. Koole, D. J. Farrell, R. Bose, E. E. Bende, A. R. Burgers, T. Bude, J. Quilitz, M. Kennedy, T. Meyer, C. d. M. Donegá, A. Meijerink, and D. Vanmaekelbergh, *Luminescent solar concentrators-a review of recent results*. Optics Express, 16(26):21773–21792, 2008.
- [193] A. Nozik, *Quantum dot solar cells*. Physica E: Low-dimensional Systems and Nanostructures, 14(1):115–120, 2002.
- [194] X. Michalet, F. F. Pinaud, L. A. Bentolila, J. M. Tsay, S. Doose, J. J. Li, G. Sundaresan, A. M. Wu, S. S. Gambhir, and S. Weiss, *Quantum dots for live cells, in vivo imaging, and diagnostics*. science, 307(5709):538–544, 2005.
- [195] R. Gill, M. Zayats, and I. Willner, *Semiconductor quantum dots for bioanalysis*. Angewandte Chemie International Edition, 47(40):7602–7625, 2008.
- [196] A. L. Rogach, N. Gaponik, J. M. Lupton, C. Bertoni, D. E. Gallardo, S. Dunn, N. Li Pira, M. Paderi, P. Repetto, and S. G. Romanov, *Light-emitting diodes with semiconductor nanocrystals*. Angewandte Chemie International Edition, 47(35):6538–6549, 2008.
- [197] H.-J. Eisler, V. C. Sundar, M. G. Bawendi, M. Walsh, H. I. Smith, and V. Klimov, *Color-selective semiconductor nanocrystal laser*. Applied physics letters, 80(24):4614–4616, 2002.
- [198] S. Hoogland, V. Sukhovatkin, I. Howard, S. Cauchi, L. Levina, and E. Sargent, *A solution-processed 1.53 μm quantum dot laser with temperature-invariant emission wavelength*. Optics Express, 14(8):3273–3281, 2006.
- [199] P. Michler, A. Kiraz, C. Becher, W. Schoenfeld, P. Petroff, L. Zhang, E. Hu, and A. Imamoglu, *A quantum dot single-photon turnstile device*. Science, 290(5500):2282–2285, 2000.
- [200] R. Rossetti, S. Nakahara, and L. E. Brus, *Quantum size effects in the redox potentials, resonance raman spectra, and electronic spectra of CdS crystallites in aqueous solution*. The Journal of Chemical Physics, 79:1086–1088, 1983.
- [201] W. L. Ng, M. Lourenco, R. Gwilliam, S. Ledain, G. Shao, and K. Homewood, *An efficient room-temperature silicon-based light-emitting diode*. Nature, 410(6825):192–194, 2001.
- [202] M. A. Green, *Radiative efficiency of state-of-the-art photovoltaic cells*. Progress in Photovoltaics: Research and Applications, 20(4):472–476, 2012.
- [203] S. Crooker, J. Hollingsworth, S. Tretiak, and V. Klimov, *Spectrally resolved dynamics of energy transfer in quantum-dot assemblies: Towards engineered energy flows in artificial materials*. Physical Review Letters, 89(18):186802, 2002.
- [204] C. Kagan, C. Murray, M. Nirmal, and M. Bawendi, *Electronic energy transfer in CdSe quantum dot solids*. Physical Review Letters, 76(9):1517, 1996.
- [205] R. Heitz, M. Veit, N. N. Ledentsov, A. Hoffmann, D. Bimberg, V. M. Ustinov, P. S. Kop'ev, and Z. I. Alferov, *Energy relaxation by multiphonon processes in InAs/GaAs quantum dots*. Physical Review B, 56(16):10435, 1997.
- [206] H. Yang and P. H. Holloway, *Enhanced photoluminescence from CdS: Mn/ZnS core/shell quantum dots*. Applied physics letters, 82(12):1965–1967, 2003.
- [207] L. Meitner, *Über die entstehung der β -strahl-spektren radioaktiver substanzen*. Zeitschrift für Physik A Hadrons and Nuclei, 9(1):131–144, 1922.
- [208] P. Auger, *Sur l'effet photoélectrique composé*. J. Phys. Radium, 6(6):205–208, 1925.

- [209] P. Frantsuzov, M. Kuno, B. Janko, and R. A. Marcus, *Universal emission intermittency in quantum dots, nanorods and nanowires*. *Nature Physics*, 4(7):519–522, 2008.
- [210] W. G. van Sark, P. L. Frederix, A. A. Bol, H. C. Gerritsen, and A. Meijerink, *Blueing, bleaching, and blinking of single CdSe/ZnS quantum dots*. *ChemPhysChem*, 3(10):871–879, 2002.
- [211] G. E. Cragg and A. L. Efros, *Suppression of auger processes in confined structures*. *Nano Lett.*, 10(1):313–317, Dec 2009.
- [212] X. Wang, X. Ren, K. Kahen, M. A. Hahn, M. Rajeswaran, S. Maccagnano-Zacher, J. Silcox, G. E. Cragg, A. L. Efros, and T. D. Krauss, *Non-blinking semiconductor nanocrystals*. *Nature*, 459(7247):686–689, 2009.
- [213] F. García-Santamaría, Y. Chen, J. Vela, R. D. Schaller, J. A. Hollingsworth, and V. I. Klimov, *Suppressed auger recombination in "giant" nanocrystals boosts optical gain performance*. *Nano letters*, 9(10):3482–3488, 2009.
- [214] V. I. Klimov, *Spectral and dynamical properties of multiexcitons in semiconductor nanocrystals*. *Annu. Rev. Phys. Chem.*, 58:635–673, 2007.
- [215] J. Knight, T. Birks, P. S. J. Russell, and D. Atkin, *All-silica single-mode optical fiber with photonic crystal cladding*. *Optics letters*, 21(19):1547–1549, 1996.
- [216] S. McCall, A. Levi, R. Slusher, S. Pearton, and R. Logan, *Whispering-gallery mode microdisk lasers*. *Applied physics letters*, 60:289, 1992.
- [217] A. C. Tamboli, E. D. Haberer, R. Sharma, K. H. Lee, S. Nakamura, and E. L. Hu, *Room-temperature continuous-wave lasing in GaN/InGaN microdisks*. *Nature photonics*, 1(1):61–64, 2006.
- [218] S. Spillane, T. Kippenberg, and K. Vahala, *Ultralow-threshold raman laser using a spherical dielectric microcavity*. *Nature*, 415(6872):621–623, 2002.
- [219] M. Jouravlev, D. R. Mason, and K. S. Kim, *Ultralow raman lasing threshold and enhanced gain of whispering gallery modes in silica microspheres*. *Physical Review A*, 85(1):013825, 2012.
- [220] V. Sandoghdar, F. Treussart, J. Hare, V. Lefevre-Seguin, J. Raimond, and S. Haroche, *Very low threshold whispering-gallery-mode microsphere laser*. *Physical Review-Section A-Atomic Molecular and Optical Physics*, 54(3):R1777, 1996.
- [221] G. Mie, *Beiträge zur optik trüber medien, speziell kolloidaler metallösungen*. *Annalen der physik*, 330(3):377–445, 1908.
- [222] M. H. Huang, Y. Wu, H. Feick, N. Tran, E. Weber, and P. Yang, *Catalytic growth of zinc oxide nanowires by vapor transport*. *Advanced Materials*, 13(2):113–116, 2001.

Summary

Nanometer sized objects are typically close to a billionth of a meter in size and at such length-scales the properties of materials are different. This changes can result in unique properties such as the tunable photoluminescence and light absorbing properties of semiconductor nanoparticles, useful for example in photovoltaics such as solar cells and LEDs; extremely sensitive magnetism in ferro-oxide nanoparticles, useful for e.g. high density data storage; and localized plasmon resonance which is the transfer of the energy of incoming light to the localized collective oscillation of electrons which in turn can be used for example in ultra sensitive bio-sensors and is commonly used in surface enhanced Raman scattering. This has resulted in nanoparticles to be the subject of extensive study for practical applications.

However, physically manipulating anything on such a small length-scale is difficult, time consuming, and prone to failure. Therefore, the behavior of such particles must be studied so that ultimately functional components can be formed by self-assembly. This is a bottom-up fabrication process which can serve as an alternative to the conventional top-down manufacturing process typically used today.

In this thesis we present a study into several published methods for synthesizing nanometer sized colloidal particles with which the size can be tuned between 6 to 35 nm with typical polydispersities of 4 % or lower. In addition, a method, based in part on literature, to control the shape of the nanoparticles by using different ligands during the synthesis is presented. Self-assembling these nanoparticles inside emulsion droplets resulted in highly ordered spherical supraparticles typically consisting of well over thousands of particles. We show that such superstructures can be formed with relatively low polydispersities of <15 % when using a shear cell as emulsification method.

In this thesis we show that by using the 3D analysis technique: electron tomography, the internal and external structures of self-assembled systems and colloids intended for self assembly could be resolved in detail. Using this technique we study the effects of drying on such systems and how they deform self-assembled nanoparticles structures. It was found that self-assembly in spherical confinements resulted in icosahedral ordering for both nanoparticles and micrometer sized colloids. Event driven molecular dynamic simulations showed that the these structures form by hard-spheres interactions alone if spheres are self-assembled in a spherical confinement. In both the simulations and the experiments it was found that the amount of spheres in the confinement determined whether an icosahedral or bulk-like face centered cubic packing is formed.

Finally, we show that by using photoluminescent nanoparticles as constituents in the supraparticles self-assembly, micrometer sized photoluminescent supraparticles were formed. At high excitation fluence rates the quantumdot supraparticles showed state-filling similar to the quantumdot constituents. Depositing the quantumdot supraparticles on a bed of ZnO nanowires the SPs exhibited narrow peaks on the photoluminescence indicative of laser action.

Samenvatting

Nanometer objecten hebben groottes van bijna een miljardste van een meter. Bij zulke kleine afmetingen zijn de eigenschappen van veel materialen anders dan wij gewend zijn op grote schaal en worden er vaak nieuwe en unieke eigenschappen waargenomen. Voorbeelden hiervan zijn de licht uitzendende en absorberende eigenschappen van halfgeleider nanodeeltjes, wat deze geschikt maakt voor bijvoorbeeld zonnecellen en LEDs; de magnetische eigenschappen in ijzeroxide nanodeeltjes maken deze weer bijzonder geschikt voor digitale data opslag zoals gebruikt wordt in bijvoorbeeld hardeschijven; en de bijzondere eigenschappen van metalen nanodeeltjes die de energie van licht kunnen omzetten in zeer gelokaliseerde collectieve golf bewegingen van electronen wat deze deeltjes geschikt maakt voor extreem gevoelige sensoren. Vanwege dit soort eigenschappen worden nanodeeltjes tegenwoordig uitgebreid bestudeerd voor mogelijke toepassing in de praktijk.

Echter, het plaatsen en verplaatsen van zulke kleine objecten is moeilijk, tijdrovend en duur. Daarom is het belangrijk om meer te weten te komen over hoe deze deeltjes zich bewegen en hoe we ze kunnen sturen om zo ze zelf de gewenste structuren te laten vormen. Als er uiteindelijk genoeg over de beweging van dit soort nanodeeltjes bekend is dan wordt het mogelijk om structuren met een specifieke functie te laten vormen door zelforganisatie.

Voor dit onderzoek zijn verscheidene soorten nanodeeltjes gesynthetiseerd bestaande uit ijzeroxide, goud en cadmiumselanide. Deze deeltjes zijn daarna gebruikt om de zelforganisatie eigenschappen van deze deeltjes te bestuderen.

Het onderzoek in dit proefschrift is voornamelijk gericht op de zelforganisatie van nanodeeltjes in een spherische ruimte, omdat nog zeer weinig bekend is over het zelforganisatie gedrag van deze deeltjes binnen in zo een ruimte. Er is ontdekt dat de beste methode om dit te bestuderen de zelforganisatie in emulsie druppeltjes van een vloeistof met een laag kookpunt was. Wanneer de emulsie wordt verwarmd verdampt de vloeistof en worden de deeltjes samengedrukt. Dit resulteerde in spherische verzamelingen van samengepakte en zeer geordende nanodeeltjes, deze deeltjes worden ook wel superdeeltjes genoemd. De groottes van zulke superdeeltjes kon worden bepaald door de grootte van de gebruikte emulsie druppeltjes en de initiële concentratie van de nanodeeltjes. Op deze manier konden er superdeeltjes gevormd worden met diameters van enkele nanometers tot enkele micrometers.

Voor gedetailleerde analyse van nanometer grote objecten werd een 3D electronen microscopy techniek gebruikt. Met deze analyse techniek worden er projecties van een object genomen van zoveel mogelijk invalshoeken door de te analyseren structuren te kantelen in the electronen microscoop. Door deze projecties te combineren kan een 3D reconstructie van het object gemaakt worden. Tevens kon deze techniek gebruikt worden om de individuele posities van nanodeeltjes binnenin superdeeltjes te bepalen. Met deze gegevens gecombineerd met conventionele electronen microscopie kon het zelforganisatie gedrag van de nanodeeltjes in een spherische ruimte met detail bestudeerd worden. Er is ontdekt dat door de beperkte hoeveelheid deeltjes in een superdeeltjes en de kromming van de ruimte waarin de nanodeeltjes moeten ordenen een icosahedrale symmetry gevormd

word. Dit gedrag voor ronde deeltjes in een sferische ruimte wordt ook gevonden wanneer er micrometer grote deeltjes gebruikt werden in plaats van nanodeeltjes. Vergelijkbaar gedrag werd ook gevonden in simulaties voor hard bollen. Doordat dit gedrag over deze verschillende systemen hetzelfde was werd er vastgesteld dat dit zelforganisatie gedrag karakteristiek is voor bollen die worden samengedrukt in een sferische ruimte.

Tot slot, wanneer er halfgeleider deeltjes gebruikt werden in deze zelforganisatie experimenten werden er superdeeltjes gevormd met heldere fotoluminescentie. De unieke eigenschappen karakteristiek voor nanometer grote halfgeleider deeltjes bleef behouden in de superdeeltjes ondanks dat deze tot enkele micrometers groot gemaakt konden worden. Dankzij de hoge brekingsindex van de nanodeeltjes was het mogelijk om het uitgezonde licht van de fotoluminescente deeltjes te vangen aan het oppervlak van de superdeeltjes, en kan mogelijk leiden tot zeer zuinige lasercomponenten.

Acknowledgements

The work presented in this thesis is not just my work but the result of extensive collaborations, discussions, and with support of many people with which I had the pleasure of working with. Without them this research would not have been where it is at today. I will now like to express my gratitude and try to acknowledge everyone who has helped me in one way or another during these years.

First I like to thank my supervisors Prof. Alfons van Blaaderen and Dr. Arnout Imhof for giving me this great opportunity and for their supervision during my project. Second I would like to thank Prof. Marjolein Dijkstra, Dr. Marijn van Huis, Prof. René van Rooij and Prof. Daniel Vanmaekelbergh who took the effort and time to help with my thesis and provided advice and constructive criticism even on such a short notice. Then I would like to thank Marlous Kamp for all her tremendous help and dedication, she has been invaluable in the completion of this this work. Additionally, Johan Stiefelhagen and Joost de Graaf have been amazing friend and colleagues and are also gratefully acknowledged for all their help with writing. Hans Meeldijk and Chris Schneijdenberg are gratefully acknowledged for all their help and hard work with the electron microscopy and electron tomography and for putting up with me on an almost daily basis. Frank Smalenburg and Simone Dussi without your work on the event driven molecular dynamic simulations we would not have come to the results and conclusions we are now. Simone thank you for the help with all the images as well. Laura Fillion thank you for the your help and insights in this projects, you have been invaluable. Tian-Song Deng and Da Wang thank you for very nice collaboration on the self-assembly of rods and the binary self-assembly of spheres in spherical confinement, this is already producing very nice results and I am convinced there will be much more to come. Best of luck to both of you with future research in this area. Then I would like to express my deepest appreciation for Carlos van Kats, Judith Wijnhoven and Peter Helfferich who support me and helping me getting started. Relinde Moes is gratefully acknowledged for her hard work on quantumdot syntheses and quantum yields measurements. Bert van Vugt is gratefully acknowledged for all his hard work characterizing the quantumdot supraparticles. Hanriette Bakker is gratefully acknowledged for her hard work on imaging the quantumdot supraparticles with confocal microscopy and measuring the absorption and emission characteristics. My gratitude to Hanumantha Rao Vutukuri for performing fluidics experiments. Bo Peng thank you for the great collaboration and always being cheerful. Bing Liu thank you for helping me with the colloidal self-assembly experiments. Thijs Besseling thank you for the collaboration and help with tracking of nanoparticles and nanorods. I have also had the pleasure of collaborating with Anil Yalcin and Marijn van Huis on detailed nanoparticle analysis. I would also like to thank Naomi Winkelman, Bart van Goor and Sarah Balls for their very nice collaboration. To my roommates: Teun Vissers, Allisandro patti, Douglas Ashton, Weikai Qi, and Da wang with whom I had the pleasure of sharing a room with. I would also like to express my gratitude for the work Dirk Groenendijk and Kyo Beyeler performed, who worked hard on the self-assembly of micrometer sized colloids in spherical confinements. Nina Elbers, Marjolein van der Linden, Michiel Hermes,

Matthieu Marechal, Anjan Gantapara, Jissy Jose, Bas Kwaadgras, Wessel vlug, Wiebke Albrecht, Anke Kuijk, Arjen van de Glind and John Edison thank you for all your help and making the time in the soft condensed matter group an amazing time. The following people I would like to thank for fruitful discussions and great scientific input: Daniel Vanmaekelbergh, Heiner Friedrich, Ben Ern e, Patrick Baesjou, and Krassimir Velikov. In addition, my thanks to everyone from the soft condensed matter group for the great time and made the workplace feel like a second home.

Then I would like to gratefully acknowledge my friends who have been always there for me: Remko van Hierden, Suzanne van der Veer, Bart van Vliet, Anouk Stigter, Jeroen van Oort, Lidewij van Dijck, Marten Verhoog, Emiel Bosman, Naomi van Wijck, Peter Bouwman, Paul Wiggers, Anja Schaapman. I would also like to thank my sister Maaike de Nijs voor all her help and support and for always being there for me. Finally, I would like to thank my parents for supporting me and making this all possible, without them I would not have been where I am now, thank you.

List of Peer-Reviewed Publications

The presented work is based in part on the following peer reviewed publications:

- *Steady bright multi-exciton emission and whispering gallery modes in supra-particles of CdSe/multi-shell quantum dots* Daniël Vanmaekelbergh, Lambert K. van Vugt, Henriëtte E. Bakker, Bart de Nijs, Relinde J. A. van Dijk - Moes, Marijn A. van Huis, Patrick J. Baesjou, and Alfons van Blaaderen, submitted.
- *Entropy-driven formation of large icosahedral colloidal clusters by spherical confinement* Bart de Nijs, Simone Dussi, Frank Smalenburg, Johannes D. Meeldijk, Dirk J. Groenendijk, Laura Filion, Arnout Imhof, Alfons van Blaaderen and Marjolein Dijkstra, *Nature Materials* (2014).
- *Site-Specific Growth of Polymer on Bullet-Shaped Silica Rods*, B. Peng, B. de Nijs *et al.* Bo Peng, Giuseppe Soligno, Marlous Kamp, Bart de Nijs, Joost de Graaf, Marjolein Dijkstra, Ren-ÅI van Roij, Alfons van Blaaderen and Arnout Imhof, submitted.
- *Core-shell Reconfiguration Through Thermal Annealing in $\text{Fe}_x\text{O}/\text{CoFe}_2\text{O}_4$ ordered 2D Nanocrystal arrays*, Anil O. Yalcin, Bart de Nijs, Zhaochuan Fan, Frans D. Tichelaar, Daniël Vanmaekelbergh, Alfons van Blaaderen, Thijs J.H. Vlugt, Marijn A. van Huis, Henny W. Zandbergen, *Nanotechnology* **25(5)** (2014) 055601
- *Fuel Concentration Dependent Movement of Supramolecular Catalytic Nanomotors*, Daniela A. Wilson, Bart de Nijs, Alfons van Blaaderen, Roeland J. M. Nolte and Jan C. M. van Hest, *Nanoscale* **5(4)** (2013) 1315-1318.
- *Entropy-driven Formation of Binary Semiconductor-Nanocrystal Superlattices*, Wiel H. Evers, Bart de Nijs, Laura Filion, Sonja Castillo, Marjolein Dijkstra, and Daniël Vanmaekelbergh, *Nano Lett.* **10(10)** (2010) 4235-4241.
- *Quantitative Structural Analysis of Binary Nanocrystal Superlattices by Electron Tomography*, Heiner Friedrich, Cedric J. Gommès, Karin Overgaag, Johannes D. Meeldijk, Wiel H. Evers, Bart de Nijs, Mark P. Boneschanscher, Petra E. de Jongh, Arie J. Verkleij, Krijn P. de Jong, Alfons van Blaaderen and Daniël Vanmaekelbergh, *Nano Lett.* **9(7)** (2009) 2719-2724.
- *Binary Superlattices of PbSe and CdSe Nanocrystals*, Overgaag, K.; Wiel H. Evers, Bart de Nijs, Laura Filion, Sonja Castillo, Marjolein Dijkstra, and Daniël Vanmaekelbergh, *J. Am. Chem. Soc.* **130** (2008) 7833-7835.

Oral and Poster Presentations

The contents of this thesis was presented at the following:

- Oral presentation at Nanophotonics group, 2013, Cambridge
- Oral presentation at "Physics at FOM, 2013" conference Veldhoven
- Oral presentation at "NWO - Chemical Sciences, 2013" conference Veldhoven
- Oral presentation at "FOM functional nanoparticle meeting, 2012" Delft
- Poster presentation at "Physics at FOM, 2012" conference Veldhoven
- Oral presentation at "FOM functional nanoparticle meeting, 2011", Utrecht
- Poster presentation at "NWO - CHAINS, 2011", Utrecht
- Poster presentation at "Physics at FOM, 2011" conference Veldhoven
- Oral presentation at "FOM functional nanoparticle meeting, 2010" Delft
- Poster presentation at "Physics at FOM, 2009" conference Veldhoven
- Poster presentation at "NWO - Chemical Sciences, 2009" conference Veldhoven

Curriculum Vitae

Bart de Nijs was born in Utrecht on the twentieth of February 1981. He finished his high school at HAVO level in 1999 and received his bachelor of applied science in chemistry at the Utrecht school for Life Sciences and Chemistry in 2004. For this bachelor he worked on the synthesis of iron complexed phosphinidenes at the inorganic chemistry department at the Free University of Amsterdam in the group of Koop Lammertsma. In the subsequent two years he completed a premaster at the university of Utrecht for the master: Chemistry & Physics. He attained his master degree in Chemistry & Physics at the University of Utrecht in 2008. For this master he worked on the binary self-assembly of lead selenite, cadmium selenite and gold nanoparticles. Shortly after in 200 he started his PhD research on the self-assembly in spherical confinement in the Group of Alfons van Blaaderen where he specialized on nanoparticle synthesis, their self-assembly behavior, and electron microscopy and tomography on the resulting nanostructured materials.